UNIVERSITY OF SOUTHAMPTON

FACULTY OF ENGINEERING AND THE ENVIRONMENT

FLUID STRUCTURE INTERACTIONS GROUP

A Particle Based Method for Flow Simulations in Hydrodynamics and Hydroelasticity

by

Muhammad Zahir Bin Ramli

Prof. Pandeli Temarel

Dr Mingyi Tan

A thesis submitted for the Degree of

Doctor of Philosophy

September_2016

UNIVERSITY OF SOUTHAMPTON
<u>**ABSTRACT**</u>

FACULTY OF ENGINEERING AND THE ENVIRONMENT
<u>Fluid Structure Interactions Group</u>

Thesis for the degree of Doctor of Philosophy

A PARTICLE BASED METHOD FOR FLOW SIMULATIONS IN
HYDRODYNAMICS AND HYDROELASTICITY

by Muhammad Zahir Bin Ramli

Seakeeping analysis involving violent flows is still quite challenging because the conventional Reynolds Averaged Navier-Stokes (RANS) approaches are not effective for such flow simulations. Different techniques and numerical tools are required to obtain approximate solutions. This research aims to apply Smoothed Particle Hydrodynamics (SPH), a fully Lagrangian meshless method to investigate the behaviour of ships in realistic waves. SPH has been used in a wide variety of hydrodynamic problems overcoming the limitation of finite volume or element type methods. This makes it a suitable alternative for simulating a range of hydrodynamic problems, especially those involving severe flow discontinuities, such as deformable boundary, wave breaking and fluid fragmentation, around complex hull shapes. The main goal of this research is to investigate the possibility of implementing SPH in 3-dimensional problems for the seakeeping analysis of ships treated as rigid and flexible bodies operating in reasonably rough seas. The outcomes of the research will focus on predicting wave-induced motions, distortions and loads with particular references to response in waves of reasonably large amplitude. The initial work deals with modifying standard Incompressible SPH (ISPH) formulation in generating free surface waves. It was observed that the kernel summation of standard ISPH formulation is not sufficiently accurate in obtaining the velocity and pressure fields. Therefore, a range of solutions were proposed to improve the prediction and the following were considered: i) employing collision control, ii) shifting technique to maintain uniform particle distribution, iii) improving the accuracy of gradient estimations up to 2nd order with kernel renormalization technique, iv) applying an artificial free surface viscosity and v) adapting new arc method for accurate free surface recognition. In addition, the weakly compressible SPH (WCSPH) from DualSPHysics was also applied to similar problems. It was found that WCSPH performed better in accuracy and was then adopted further in the analysis of hydrodynamic and hydroelasticity. The research studies were extended to investigate 2-D problems of radiation, diffraction and wave-induced motion. Comparisons were made with available potential flow solutions, numerical results and experimental data. Overall, a satisfactory agreement has been achieved in determining i) added mass and damping coefficients and ii) responses of fixed and floating body in waves. Convergence studies were carried out for particle density influences, as well as sensitivity and stability of implemented parameters. In the extension of the model to 3-D framework, both cases of floating rigid and flexible barges in regular waves were modelled. For this particular case, vertical bending moment (VBM) was obtained using the one-way coupling approach. Comparisons to two other numerical methods and experimental data in the prediction of RAOs, motion responses and vertical bending moments have shown consistent performance of WCSPH. Finally, the success of WCSPH was highlighted by solving the hydrodynamic coefficients for a 3-D flexible structure oscillating in rigid body motions of heave and pitch, as well as 2-node and 3-node of distortion modes.

Table of Contents

List of tables

List of figures

DECLARATION OF AUTHORSHIP

I, **Muhammad Zahir bin Ramli**

declare that this thesis and the work presented in it are my own and has been generated by me as the result of my own original research.

A PARTICLE BASED METHOD FOR FLOW SIMULATIONS IN HYDRODYNAMICS AND HYDROELASTICITY

I confirm that:

1. This work was done wholly or mainly while in candidature for a research degree at this University;
2. Where any part of this thesis has previously been submitted for a degree or any other qualification at this University or any other institution, this has been clearly stated;
3. Where I have consulted the published work of others, this is always clearly attributed;
4. Where I have quoted from the work of others, the source is always given. With the exception of such quotations, this thesis is entirely my own work;
5. I have acknowledged all main sources of help;
6. Where the thesis is based on work done by myself jointly with others, I have made clear exactly what was done by others and what I have contributed myself;
7. Parts of this work have been published as in the reference:

Signed:...

Date:...

Dedication

This thesis is dedicated to the loving memory of my father, Ramli bin Ismail. I love you and will always miss you, to all the supports through good times and bad, for which I am eternally grateful.

"My Lord! Bestow on them Your Mercy as they did bring me up when I was young."

Al-Isra verse 24

Acknowledgements

First of all, Alhamdulillah I am grateful to Allah for providing me with the health and blessings to undertake this task. Behind every successful PhD, there is always a well of vision, experiences and supports. I would like to express my deepest gratitude to both of my supervisors, Prof Temarel and Dr Tan who has helped me through the completion of my PhD work. To both, I need to acknowledge the great opportunities that I was presented with. Guidance from the beginning point of my research up to this level of my progress so far which enabled me to overcome difficulties in hydrodynamic, hydroelasticity, mathematics and computing problems. And also thanks again for agreeing to proofread my thesis.

Thanks to the International Islamic University Malaysia (IIUM) and Ministry of Higher Education of Malaysia (MOHE) for their financial support in my research.

I would like to express my appreciation to Malaysian community (KS) since they made me feel at home from the very first time in Southampton. In Southampton, special thanks go to all my friends (Pansy boys, Honeysuckle boys, Pansy girls and 307 Burgess boys) that have been a great companion. In general, I had a very good time in Southampton.

Thanks to my friend Sun Zhe for all the important suggestions given whenever I got problems with SPH. I am deeply grateful for his guidance and, above all, for his true friendship which significantly helped me in scientific difficulties.

I will not forget the people I was sharing office with at Boldrewood campus and I thank them for their daily support and for brightening up my day, especially for making this whole experience an enjoyable one. And last, but not least, I dedicate this thesis, with love and appreciation, to my brothers and sisters, who provided me with enormous emotional support and encouragement over the years.

I have to thank my dearest mother, Siti Ajar binti Abdul Rahman, who always gives an unconditional love in everything I do.

The amount of knowledge, patience and dedication devoted to this project make me proud, humbled and thankful.

Definitions and Abbreviations

ALE   Arbitrary Lagrange Euler

BC   Boundary Conditions

BPs   Boundary particles

BEM   Boundary Element Method

CSM   Computational Solid Mechanics

CEL   Coupled Eulerian-Lagrangian

CFD   Computational Fluid Dynamic

CFL   Courant-Friedrichs-Levy Criteria

CUDA   Compute Unified Device Architecture

DOF   Degree of Freedom

EOS   Equation of State

FSI   Fluid Structure Interactions

FEA   Finite Element Analysis

FEM   Finite Element Method

FDM   Finite Difference Method

FFT   Fast Fourier Transform

FPs   Fluid Particles

FVM   Finite Volume Method

GPU   Graphical Processing Unit

ISPH   Incompressible Smoothed Particle Hydrodynamics

MARS   Modal Analysis of Ship Response to Symmetric Excitation

MPS   Moving Particle Semi-implicit

MPM   Meshfree particle methods

N-S   Navier-Stokes Equation

NWT   Numerical Wave Tank

ODE   Ordinary Differential Equations

PDE   Partial Differential Equations

RAO   Response Amplitude Operator

RANS   Reynolds Averaged Navier-Stokes Equation

SPH   Smoothed Particle Hydrodynamics

SWL   Still Water Level

VBM   Vertical Bending Moment

VIC   Vortex-in-Cell

VOF   Volume-of-Fluid

WCSPH   Weakly Compressible Smoothed Particle Hydrodynamics

WSI   Wave – Structure Interactions

2VB   2-node distortion mode

2-D   2 Dimensional

3VB   3-node distortion mode

3-D   3 Dimensional

Notations

a_{yy}/b_{yy} Added mass and damping coefficient in swaying

a_{zz}/b_{zz} Added mass and damping coefficient in heaving

$a_{\varphi\varphi}/b_{\varphi\varphi}$ Added mass and damping coefficient in rolling

$a_{\varphi y}/b_{\varphi y}$ Coupling coefficients of sway into roll

$a_{y\varphi}/b_{y\varphi}$ Coupling coefficients of roll into sway

α_c Distance reduction coefficient

α_d Damping layer coefficient

α_Π Constant in artificial viscosity

φ Coefficient in viscous term

$A(x)$ Cross sectional area

B   Constant related to bulk modulus

β_c Collision boundary coefficient

β_d Damping layer coefficient

β_Π Constant in artificial viscosity

b_{ii} Damping coefficient against motion in the i-th mode

$\bar{c}_{ab}$ Speed of sound

d Depth

dt Time step

dx Initial particle spacing

δ Dirac Delta Function

δ-SPH   Delta-SPH

∇	Gradient Operator
∇^2	Laplacian Operator
Δ	Delta denoting a small increment over a variable
EI	Flexural rigidity
ε	XSPH velocity correction factor
ε_r	Relative error
f	Force per unit mass
F_x	Horizontal force
F_z	Vertical force
$\bar{F}$	Drift force
F_{rs}	Generalised force
G	Shear modulus
g	Acceleration due to gravity
h	Smoothing length
H	Wave height
H_σ	Sum of reflected and scattered wave height
k	Kernel support size
k_n	Wave number
$\mathbf{L(r)}$	Kernel renormalisation
M	Mass of the object
M_y	Roll moment
M_m	Corresponding moment
m	Mass

mr^2	Mass moment of inertia
$\mathbf{n}_{ab}$	Unit distance vector between 2 particles
N	Number of particles
$\mathbf{\Omega}$	Rotational velocity of the object
ϕ	General variable
$\phi(x,t)$	Angular displacement
P	Pressure
Pt.	Corresponding points on the barge
P_r	Principal coordinate
ρ_0	Reference density
Pe_{max}	Global maximum Peclet number
$\mathbf{R}_0$	Position of the centre of mass
R_y	Rotational vector
$\mathbf{r}$	Distance between particle a and b
S	Stroke of the wavemaker
T_y	Translational vector
τ	Viscous stress tensor
U_x	Horizontal velocity
U_z	Vertical velocity
U_r	Roll velocity
u	Piston velocity
u_j	Dry mode shapes
u_{max}	Global maximum velocity

μ	Dynamic viscosity
$\mathbf{V}$	Velocity of the object
v	Kinematic viscosity
$v(x,t)$	Vertical deflection
v_d	Free surface viscosity
$\mathbf{v}$	Velocity
W_{ab}	Weighting function for higher order convergence
ω	Angular frequency of wave
ω_{ab}	Weighting function
w_j	Time dependent modal coefficient
$\mathbf{x}$	Displacement of particles
y_a	Sway amplitude
z_a	Heave amplitude
Π_{ab}	Artificial viscosity term
Ω	Support domain

Chapter 1

Introduction

Contrary to the work of craftsmen which relies on pre-scientific rules based on trial and error, the power of engineers is to provide models in order to study dimensions and then build artefacts that will be used in a certain context. Therefore, it is necessary to take into account the effects of environmental physics on the studied object. Over the years, many steps have been taken towards a deeper understanding of water-ship interactions and of related phenomena. It is agreed that proper ship design such as the ship's capability to operate, its survivability and comfort are crucial aspects to consider. Recently, the interactions of ships with very large ocean waves when underway have been the subject of interest to naval architects and have been the motivation for a number of new studies. For example, when slamming in heavy seas, the hydrodynamic impact may result in damage to a ship's structure. The tragedy of MV Estonia in the Baltic Sea on 28 September 1994, one of the deadliest marine disasters of the 20th century, resulted from the breaking of the bow door due to severe slamming. Another phenomenon that can lead to the large-scale deformation of the free surface in ocean waves is known as green water loading or shipping of water, as well as sloshing, which may cause structural damage as well (Paik and Shin, 2006). As water-ship interactions and related phenomena problems became more serious, in the mid-1950s rapid expansion began in the application of hydrodynamic theory, the use of experimental model techniques and the collection of full-scale empirical data. These important developments led to a better understanding of the problems and ways of dealing with them. In experimental studies, most of the time, the ship model is built and tests are performed in a numerical towing tank (NWT). The aim of the tests is to measure ship responses to different wave

conditions, ship speeds, relative wave headings, and sea states etc. Although model tests are considered to be reliable tools, they are rather expensive and time-consuming, thus the test conditions need to be carefully chosen and well planned. Most of the data from these tests have been published with continuous effort spent to develop suitable tools as important assessment work of verification and validation to handle more complex relevant phenomena involved and to give valuable data. Therefore, efforts in developing numerical approaches are focused on filling the gap, in terms of the reliability, efficiency, and robustness of the solvers.

1.1 Fluid-structure interactions in seakeeping

Fluid-structure interactions (FSI) is the physical phenomenon when a fluid force acts on the structure, the structure will deform or move and this, in turn, changes the boundary conditions of the fluid; which will affect the fluid motion. This interaction generates a variety of physical phenomena with applications in many fields of engineering, such as the stability and response of aircraft wings, the impact of landing aircraft, the flow of blood through arteries, the response of bridges and tall buildings to the wind, the vibration of turbines etc. In general, FSI problems can be divided into 2 areas; small deformation regimes and large deformation regimes. Small deformation regimes, i.e. aeroelasticity and acoustic vibrations, deal with the analysis of small vibrations of the structure and often a simplified fluid dynamic theory *(potential flow etc.)* may be applied as the fluid domain can be kept fixed (Xing and Price, 1991). On the other hand for large deformation regimes in a strong coupling between fluid and structure, fluid domain changes considerably over time which require different numerical techniques to enforce the kinematic compatibility at the fluid-structure interface and to update the geometry of the domain. Among the techniques was by Tallec and Mouro, (2001) where they introduced an additive decomposition technique which considered fluid and solid as a unique continuous medium to be studied in a fixed reference configuration.

In this study, fluid-structure interaction is investigated in the context of the seakeeping analysis. Seakeeping can be understood as the ability of a ship to navigate safely at sea and can proceed on course under severe conditions successfully. In engineering terms, it can also be defined as the investigation of a ship's motion, which possesses six degrees of freedom in a seaway; surge, sway, heave, roll, pitch and yaw. The seakeeping performance assessment of a ship is mainly related to the weather conditions, the manoeuvring and navigation conditions, the ship's response to the wave and other additional criteria needed to evaluate the safety and well-being of passengers and crew (Giron et al, 2005). In ship design, the relative motion between ship

structure and the water surface is critical, particularly in severe sea states. Nonlinear effects on wave-induced loads, ship motions and structural responses such as slamming and green water are often significant for a ship travelling in moderate and severe waves. This nonlinear effects may cause failure of the marine structure, damage to ships and cargo, and loss of lives. Until recently, investigation on ship motions and wave-induced loads were barely considered in the design procedure. Over the past two decades, ship designing has started to focus in the effort of reducing the ship motions and minimising the effect of wave-induced loads. The real situations are highly complex, involving the non-linearity of the wave breaking, the non-linear interaction between wave and structure and the structural behaviour of ship plating in relation to the wave loads.

St.Dinis and Pierson, (1958) first applied the principle of superposition in the prediction of ship motions and loads in regular waves which use statistical responses to determine the distribution of sea conditions which a ship may encounter in its lifespan. However, inadequate information on the sea environment has made this seaworthiness analysis less accurate for a ship in a seaway. In the evolutionary approach, information on the wave-induced loads is gradually gathered through trial and experience based on rules specified by classification societies. With the help of service data and some knowledge from theoretical and model tests, future design of similar ships is gathered and interpreted in the form of codes though it is really at disadvantages for cases in the absence of relevant previous experience. In order to sustain and improve the human condition, while minimising direct or collateral damage to the environment and losses from accidents i.e. casualties, injuries etc, evaluation in seakeeping at a higher level of accuracy is essential. Since then, the studies of the behaviour of ships in waves have gained great interest in both theoretical and experimental aspects (Vossers et al., 1961). Among those are full-scale measurements and model tests of slamming effects and green water impact on ship structures which allow the determination of design loads and the validation of prediction methods of loads and responses (Jensen and Mansour, 2003; Ciappi et al., 2003). While Wu et al., (2003) use full flexible models for a barge, destroyer and for the S-175 container ship in the validation of hydroelastic codes at CSSRC (China Ship Scientific Research Centre). It is not very easy to find well-presented linear or nonlinear measurements from sea trial and model tests. Hull form for which there exists substantial experiment information about the ship motion, wave-induced and nonlinear effects is presented later in this thesis.

1.2 Numerical approaches in seakeeping

In seakeeping, experiments are extremely costly and time-consuming, so it is not usually practical to execute these experiments for individual ship designs. Thus, to investigate the complexity involved in the interaction between fluids and solids, many researchers emphasised the importance of the development of theoretical and numerical methods. Numerical simulations, with the help of increasing computational power, plays a valuable role in providing a validation for theories and offers insights into experimental results while assisting in the interpretation of theoretical predictions. In this process, physical phenomena are expressed by mathematical models, consisting of governing equations with proper boundary conditions and/or initial conditions. The most common governing equations used in computational methods are sets of ordinary differential equations (ODE) or partial differential equations (PDE). These governing equations can be approximated for numerical computations when the geometry of problem domain is discretised.

Within the theoretical approach, in many circumstances the waves-ship interaction can be efficiently described in a large variety of methods ranging from linear theories to fully nonlinear methods. Besides that, combination or partial linear and nonlinear methods are also developed to optimise the results involving nonlinear effects. In traditional ship problems, strip theories, both linear and nonlinear, are one of the most significant contributions in the field of seakeeping. It was initially introduced by Kroukovsky and Jacobs in 1957 and mostly employed for conceptual design and risk assessment procedures (Jensen et al., 2004). These methods are proven to be reliable in predicting ship motion for both model tests and full-scale trials. In general, linear methods provide adequate prediction of vertical ship motion and wave-induced loads particularly in low and moderate regular waves (Bishop et al., 1979; Faltinsen et al., 1991). Their mathematical formulation is within the framework of potential flow theory and the problem is solved in the frequency domain by either two or three-dimensional works. In most linear cases, boundary condition problem is solved by correction due to the forward speed which is also a common approach in the linear three-dimensional methods such as Green's function panel methods. Further details on the comparison of frequency domain between Green's function methods of pulsating source (PS) and translating source (TPS) can be found in Chapchap et al., (2011). However, panel methods have serious limitations when dealing with the complicated geometrical approximation of free surface, severe flow separation, and evaluation of the free surface Green's function which often rely heavily on complex equations (Cartwright et al., 2004). Further, in some situations, qualitative information may be obtained, but the linear methods

cannot give any suitable information when the phenomena involved can be excited only by a nonlinear mechanism. For example, ordinary linear strip theories cannot be applied to very large wave conditions where breaking water occurs e.g. sloshing, because the ship motion and the fluid force must be treated as non-linear in such conditions (Landrini et al., 2003; Kazuya et al., 2007; Le et al., 2010).

In such cases, there have been ideas about solving the nonlinear part partially *(coupling of linear and nonlinear)* where nonlinear terms may be included in the equation of motions in addition to nonlinear Froude-Krylov and restoring force in order to account for slamming forces and water-on-deck forces. Time domain strip theories and panel methods have implemented these techniques, using Green functions and discretizing only the hull surface (Lin et al., 1996; Lin et al., 2007) or using Rankine sources distributed over the hull and free surface (Huang et al., 1998). In these methods, some degree of linearization is done at the free surface, but the body boundary condition may be treated as nonlinear since it is satisfied with the exact position at each time instant. As a result, nonlinear effects are well identified with the limitation of lower Froude number, but the results show discrepancies for higher wave amplitudes (Fonseca and Guedes, 2002). A hybrid of time-domain potential theory by Liu and Papanikolaou (2010, 2011) has proven to provide good predictions in nonlinear motions and loads in waves. Similarly, a hybrid nonlinear NS method made of the Eulerian level set approach and Lagrangian markers for the body motion are coupled with linear potential flow solver for steady flow validation is implemented in Greco et al., (2013).

Nonlinear strip methods are used mostly to estimate the seakeeping behaviour of a ship in sea states where nonlinearities occur due to large amplitude motions. In this case, boundary integral methods can be used to improve the computational efficiency. In general, in order of significance, nonlinearities in seakeeping problems may be classified as i) the steepness of the ambient wave train; ii) nonlinearity of hydrostatic and Froude Krylov forces resulting from the interaction of a steep wave train with the ship hull; iii) roll damping mechanism arising from viscous separation, viscous lift forces from appendages and transom sterns; iv) slamming and sloshing and v) nonlinearities in the radiated and diffracted wave disturbance. In most cases, these fully nonlinear methods assume that the flow is irrotational and smooth, so there is no breaking or fragmentation on the free surface (Sun and Faltinsen, 2009; Yan and Liu, 2010; Chapchap, 2015). There have been several attempts to solve nonlinear seakeeping problems and recent progress in RANS code development in incorporating both viscous and rotational effects in the flow and free surface waves make RANS solver method widely popular. With the increasing power of modern

computers, application has been extended not only to seakeeping but also to resistance and propulsion, manoeuvring and ship design (Weymouth et al., 2005; Wilson et al., 2006; Castiglione et al., 2011; Hochkirch and Mallol, 2013; Tezdogan et al., 2015). Most of these methods which are based on boundary integral method are ineffective in the case of green water effect, breaking waves or water spray. This is the reason why the meshless method is also applied in solving the Navier-Stokes equations for nonlinear seakeeping problems. More details on the meshless method in seakeeping applications will be given in the literature review.

Local phenomena such as springing or slamming (Faltinsen, 2001), may cause local elastic deformation of the structure e.g. whipping. In this context, the complexity of the interaction between violent free surface flow and structural deformation *(i.e. hydroelasticity)* can be a matter of concern. The linear hydroelasticity theory was first developed for seakeeping problems in the 1950s and modern studies conducted by Bishop and Price (1979) have been employed to predict the responses of a wide range of marine structures. The well-known linear strip theories of modal superposition method provide an efficient tool for calculating the hydrodynamic forces acting on flexible ship's hull and this also provided a base for the hydroelasticity theories for the symmetric and antisymmetric responses of hulls (Hirdaris et al., 2003; Hirdaris and Temarel, 2009). The theories treat the hull as a non-uniform Euler or Timoshenko beam where the structural responses of the beam represent the effect of the structure on its hydrodynamic loads. The problem is then solved through a generalised equation of motion derived from a strip theory. A number of numerical methods have also been developed based on the theories (Wu and Moan, 2005; Hirdaris et al., 2010). In nonlinear cases where ships experience potentially large amplitude motions in the sea, two approaches to solving the nonlinear hydroelasticity problems have been investigated. The first approach deals with solving the rigid body motion and structural response separately (Baum and Taylor, 2009), while a coupling method to treat the structure and the surrounding fluid is adopted in the second approach (Tuitman and Malenica, 2009; Moctar et al., 2011). An efficient nonlinear hydroelastic method based on linear frequency domain strip theory was introduced by Song et al., (1994). Two-dimensional and three-dimensional linear theories are very well established in the frequency domain but not in terms of hydroelasticity for nonlinear structural behaviour (Taylor, 2009). Following that, research has been extended from frequency domain methods to time domain methods, which have proved to be more suitable for fully nonlinear hydroelasticity problems. Further examples of fully nonlinear flow solutions based on solving Navier-Stokes equations which are applied to investigate the interaction between free surface flow and elastic structures are presented in the studies by Wlhorn et al., (2005) , Potapov et al, (2009) and Das and Cheung, (2012).

1.3 The Aim and Objectives

The aim of this research is to present a practical meshless or particle-based numerical method with sufficient engineering accuracy for the solution of hydrodynamics/seakeeping and hydroelasticity in seakeeping problems. Despite extensive numerical works done on seakeeping area mentioned in the previous section, development of fluid-structure interactions computation with a focus on implementing meshless based methods i.e. Smoothed Particle Hydrodynamics (SPH) in seakeeping analysis of ships, operating in reasonably rough seas is still open to lots of improvements. In contrast to the traditional mesh-based methods, SPH is found to be an attractive and well-suited method due to its simple algorithm and many other attractive features that will be explained further in chapter 2. Further, SPH is still being developed into a mature numerical tool and rather limited application in seakeeping problem using this approach is noted until now. Thus, SPH plays a role in becoming a suitable method in many viable research directions, from novel applications to method improvements. Hence, the outcomes of this research will be based on the objectives in developing a method as follows;

- Three-dimensional seakeeping simulation method and software i.e. rigid body motions in waves encountered at arbitrary heading.
- Three-dimensional simulation method and software of the dynamic behaviour of a flexible barge, predicting wave-induced motions, distortions (VBM) and loads.

1.4 Novelties

In particular, the first contribution in terms of novel applications includes the demonstration of SPH as a reliable numerical tool by validation of two-dimensional hydrodynamics tests. The ability to predict hydrodynamic coefficients can serve as one of solution for ship motion problem at sea which requires the determination of the dynamic equilibrium of forces and moment. An extensive study is also presented in the interaction of fixed and floating body in waves encountered at arbitrary heading. A study presented herein has shown a correlation between nonlinearity of water waves, responses and hydrodynamic loads.

The second novel implementation of this study is extending three-dimensional simulation method in predicting wave-induced motions and vertical bending moment of a rigid body. Assessment of the dynamic behaviour of the floating body and the importance of flexibility on the structural response in waves provide significant findings in realistic seaways and operational

conditions. Limited literature has been shown in the study of hydroelasticity in seakeeping by SPH. Along with code provided by DualSPHysics, hydroelasticity part is integrated to solve the hydrodynamics of oscillating flexible body. Results are validated against numerical and experimental works of similar nature, suggesting that SPH is reliable in modelling wave-body interaction of seakeeping computation. The used of large domain has validated the applicability of SPH towards much complex engineering problems.

1.5 Report Outline

In this thesis, literature reviews of meshless particle methods and their applications will be presented in Chapter 2. The basics of SPH methodologies will be fully described in Chapter 3. In Chapter 4, improvements to tackle the issues of standard SPH formulation are discussed for propagating free surface simulation and the employment of weakly compressible SPH (WCSPH) from DualSPHysics. In Chapter 5, WCSPH is validated through benchmark test cases, which involve two-dimensional hydrodynamic problems including radiation, incident wave and diffraction cases. Chapter 6 presents the three-dimensional test cases of a rigid barge in regular waves and radiation problem of a flexible barge. All results are compared to available numerical, potential flow and experimental results. Finally, conclusions are drawn and further work is proposed in detail in Chapter 7. **Appendix A** provides additional results for all test cases while **Appendix B** presents the details of additional SPH mathematical formulations.

Chapter 1 Introduction

Chapter 1

Motivation and background of numerical approaches in seakeeping

Chapter 2

Literature review

History and development of meshless methods and particle methods.

Chapter 3

SPH theory and implementations

- SPH formulations (ISPH and WCSPH)
- kernel functions
- boundary conditions
- computational strategies
- timing algorithm

Investigation of issues in standard SPH formulation in seakeeping problems

2-D problems

3-D problems

Hydrodynamic aspects

Hydroelasticity aspects

Chapter 4

Modelling a propagating free surface with SPH

Validating SPH as reliable tool by
1) Modifying standard ISPH
2) Implementing DualSPHysics WCSPH

Chapter 6.1 a,b

- Wave generation
- motion response of rigid body in waves

Chapter 6.1 c

Vertical Bending Moment (VBM) of 1 way coupled solution

Chapter 6.2

Hydrodynamic coefficients for a uniform flexible barge

Chapter 5

Benchmark tests of simple fluid structure interaction

1) Predicting hydrodynamic coefficients (radiation problems)
2) Diffraction problems
3) Floating body problems

Chapter 7

Conclusion and future works

Figure 1-1-1 Flowchart of thesis

Chapter 2

Literature review

In this chapter, a literature review on the current improvements of meshless methods in engineering applications particularly in the area of marine engineering and seakeeping is carried out. Detailed analysis is given to the differences between meshless methods and a review of the evolution of particle methods especially smoothed particle hydrodynamics (SPH) is provided. Basic background of SPH is then covered together with its applications in fluid mechanics and wave-structure interaction problems.

2.1 Meshless methods

Many fluid dynamics problems of practical interest involve irregularly shaped boundaries where the boundaries move and change shape. In the past, considerable efforts have been put into simulating the fluid flows in the presence of such boundaries. In fluid flows which deal with moving structures, the situation can be further complicated. Treatments of two fluid phases need to be considered; between water and air and between boundaries of structure that follows the structure motion. Based on real physical situations, moving boundaries should be treated as defined interfaces between the different phases without mixing the information in the neighbourhood of the interfaces. When the interface between fluid-structure and free surface is not highly deformed, a single boundary-conforming grid arrangement is convenient for obtaining solutions to the transport equations. However, the movement of the free surface is

much more complex than that of rigid structure because free surface may experience large discontinuities which may lead to nonlinearities and start to fragment. There are several methods used for representing/tracking the moving interfaces and they can be classified as a Lagrangian method (Liu and Quek, 2003; Lin, 2009; Belibassaki, 2010), a Eulerian method (Wilkins, 1999) or a mixed Eulerian-Lagrangian method. Among Eulerian methods is the volume of fluid (Rider and Kothe, 1998; Yang et al., 2006) and the level set method (Osher and Fedkiw, 2001; Sethian, 2001). While most efficient Eulerian-Lagrangian methods in practice are the Arbitrary Lagrangian Eulerian (ALE) (Noh, 1964; Hirt et al., 1974; Benson, 1992).Since each method has unique advantages and disadvantages, the choice of which method to use depends on the characteristics of the problem to be solved. Lagrangian methods have not been as widely developed as Eulerian methods but they offer a viable alternative. In practice, Eulerian methods are not suitable when dealing with problems where details of the interface geometry are to be explicitly tracked, which limits their application in many complex problems (Xie et al., 2009). The major disadvantage of the ALE method is that an additional remeshing step is required which can be time-consuming and introduces numerical errors if the remeshing step is not well designed (Ahn and Kallinderis, 2006). Grid based numerical methods often experience difficulty where the grid generation is not always straightforward when dealing with complex problems and this may result in a breakdown of the computation (Jenssen et al., 1998). Therefore, in order to find a better approximation method in tracking highly distorted interface and free surface, meshless Lagrangian methods are preferable.

The aim of meshless methods is to provide accurate and stable numerical solutions without any mesh constraints because they are initially designed to improve the inadequacy of FEM discretization. Some advantages of meshless particle methods can be summarised as follows (Shaofan and Liu, 2007);

- They can easily handle simulations of very large deformations since the connectivity among particles is generated as part of the computation, which evolves with time (Chen et al., 1996; Chen et al., 1997).

- They support a very flexible adaptive refinement procedure, such that computational accuracy can be easily controlled, because, in areas where more refinement is needed, particles can be added without any restraints *(h-adaptivity)* (Krongauz and Belytschko, 1996; Huerta and Fernandez-Mendez, 2000).

- They allow researchers to use three-dimensional continuum models to simulate the large deformation of plates and shells, such as thin shell structures and nanotubes (Krongauz and Belytschko, 1996; Li et al., 2000).

- The meshless method is a better computational paradigm for multi-scale computations than the mesh based discretization method because it is a non-local interpolation and it can easily incorporate an enrichment of fine-scale solutions of features into the coarse scale (Liu et al., 1997).

- Meshless discretization can provide an accurate representation of geometric objects (Li et al., 2000).

A number of meshless methods have been proposed to analyse rigid bodies and free surface flows. Most of the meshless methods are Lagrangian and can be categorised into three types which are i) methods based on strong form of formulations, ii) methods based on weak form of formulations, and iii) particle-based methods. A strong form of system equation expressed in ODE or PDE is derived based on the theory of continuum mechanics. The strong form methods normally use the collocation technique and the system is represented by collocation points. They are known for being computationally efficient but often unstable for irregularly distributed particles. Meanwhile, for a weak form, an integral operation is applied to generate the discrete system equations. Formulation based on weak forms can usually produce stable and accurate results. However, compared to strong form, a background mesh is required for the integration of the weak forms so it does not entirely mesh free. In a particle-based method, the system equation belongs to the strong form where no background mesh is required but its implementation is very similar to the weak form method. This is because the integral operation is applied in the stage when the function is approximated rather than in the stage when the discrete system equations are generated.

2.2 Meshless particle methods (MPMs)

In general, MPM refers to a class of meshless methods that implement a set of finite numbers of discrete particles to represent the state of a system and to record the movement of the system. Each particle can either be directly associated with one discrete physical object or be generated to represent a part of the continuum problem domain. For all problems, the evolution of a physical system is determined by the conservation of mass, momentum and energy of the discrete particles. Almost all meshless particle methods share a similar fundamental concept, but they

implement different approximation formulations and require specific implementation techniques. In brief, MPMs can be categorised as shown in Fig.2.1;
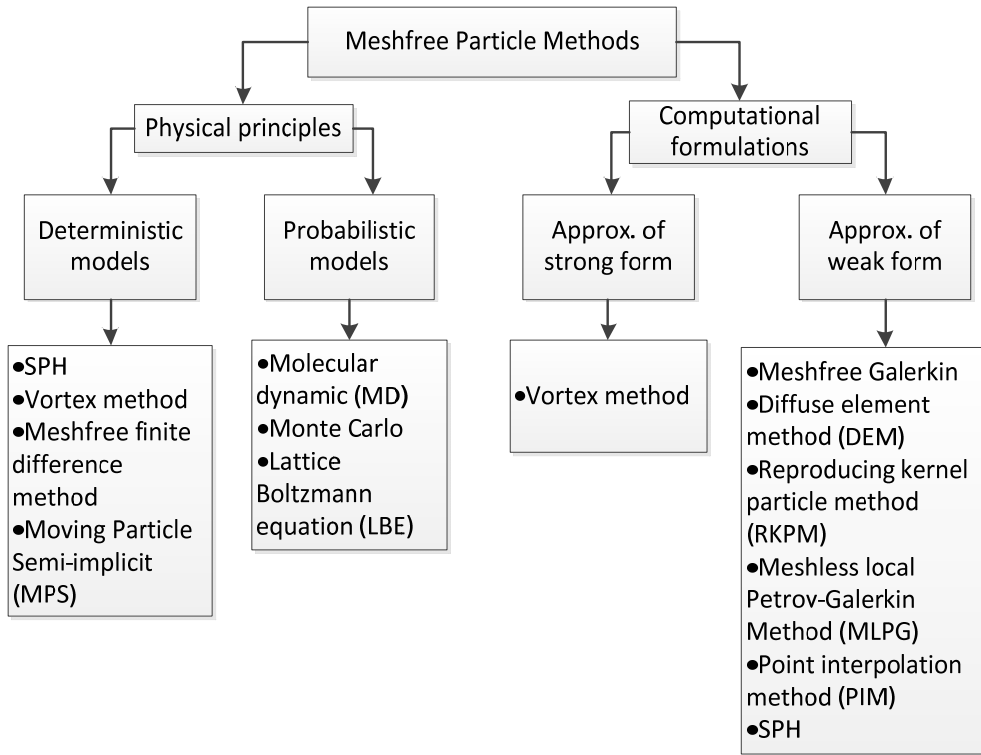
Figure 2-1 Flowchart on Meshfree Particle Methods (MPM)

The deterministic models deal directly with the governing system equation of physical law while probabilistic models deal with statistical principles. The most widely used particle methods under probabilistic models are the molecular dynamic, Monte Carlo, lattice Boltzmann and Particle-in-Cell methods. The molecular dynamics method is an atomistic method and is still not accurate enough to reproduce the realistic dynamic of mesoscopic and macroscopic systems (Stilinger and Rahman, 1974). On the other hand, the Monte Carlo method requires an iterative process based on proper random sampling techniques (Rubinstein and Kroese, 2011). The lattice Boltzman method uses a series of imaginary particles to model the fluid domain that moves through a background lattice mesh while the viscous flow behaviour is modelled by inter-particle interaction forces (Chen and Doolen, 1998). The SPH method has mixed features of both and has been widely developed for both discrete particle systems and continuum systems. Unlike the Particle-in-Cell method, SPH does not use the grid to calculate the spatial derivatives and thus the back and forth interpolations between the grid and particle information are avoided. Most meshless particle methods are based on Lagrangian methods and most of them use explicit methods for the time integration *(except MPS)*. However, although most of the particle methods

are mesh free, in using particles to represent a continuum domain, some kind of mesh may be needed to generate the initial distribution of particles.

Fluid-structure interaction represents a very challenging problem. Despite the amount of experimental and numerical modelling that has been undertaken to date, it is fair to say that no fully consistent numerical solution has yet been developed. This allows for new numerical techniques and the development of new numerical approaches. The choice of numerical methods can be dependent on the problem to be considered. Meshfree particle methods have evolved along with the emergence of new technologies. Subjects such as meshless-based quasi-continuum discretization, meshless multi-scale methods, nodal integration technique, hybrid meshless element methods, and mixed meshless finite element refinement technique, are the key technical components that have been developed so far in computational fields. Moreover, with its multi-scale and interdisciplinary character, the meshless multi-scale paradigm is a perfect embodiment of concurrent multi-scale modelling and simulation, which is the focus of today's research in computational mechanics in general. This again will be discussed in detail through the Smoothed Particle Hydrodynamics (SPH) scheme.

2.3 Smoothed Particle Hydrodynamics (SPH)

Smoothed Particle Hydrodynamics (SPH) which is a purely Lagrangian method developed during the seventies by Lucy (1977) and Gingold and Monaghan (1977) was an attempt to model continuum physics to overcome the limitations of finite difference methods. It is based on the theory of integral interpolant and the PDE are approximated by integral formulation involving a kernel function. The interpolation method used in the particle method is closely related to the standard interpolation methods used in other more traditional numerical methods such as finite element method (Monaghan, 1982). Besides interpolation methods, Bonet, et al., (2004) shows how SPH formulae for governing equations can be derived based on Lagrangian formulation.

The Lagrangian method is a meshless method whereby the computational domain is represented by a set of interpolation points called particles where the fluid medium is discretized by the interaction between particles rather than grid cells. Each particle carries an individual mass, position, velocity, internal energy and any other physical quantity, which evolve over time according to the governing equations. All particles have a kernel function to define their range of interaction, while the hydrodynamic variables are approximated by integral approximations. More discussion on this will be given in Chapter 3. This method, in which the main idea is to

substitute the grid with a set of arbitrarily distributed particles, are expected to be more adaptable and versatile than conventional grid-based methods, especially for those applications with severe discontinuities in free surface. This method has been extended to the study of solid mechanics for dynamic phenomena and more recently to complex fluid mechanics problems such as dam breaking and wave propagation.

2.3.1 Applications in Fluid Mechanics

Mesh-based methods such as Volume of Fluid (VOF) (Hirt and Nichols, 1981) and BEM offer good performance in free-surface simulations (Darwish, 1993; Lafaurie et al., 1994). However, drawbacks in capturing sharp interfaces of free surface with rapid changes have left openings for better alternatives (Ubbink, 1997). The ability of SPH to capture details of fluid motion is the main advantage in free surface flow simulations.

In general, SPH has shown good performance in the simulation of compressible flow (Tiwari, 2001). However, the SPH technique has some difficulties dealing with the incompressible flow and this is an interesting subject for researchers. The first approach to this case was introduced by Monaghan (1994) and has been brought into wider application since. There are two methods of applying incompressibility in flows simulation, which is 1) incompressible fluid with a small compressibility, namely Weakly Compressible SPH (WCSPH) or by 2) enforcing true incompressibility, namely Incompressible SPH (ISPH). In WCSPH, the fluid is considered to be slightly compressible with a state equation for the pressure calculation (Lee et al., 2008; Lee et al., 2010b). In WCSPH, a high speed of pressure wave has to be assumed so that the corresponding density fluctuation can be kept to within a small fraction of the actual fluid density, but the high sound speed can lead to a very stringent CFL (Courant-Friedrichs-Lewy condition) time step constraint. WCSPH is simple in concept and much easier to implement in applications. However, it does encounter pressure oscillation with the standard SPH formulation. Although WCSPH predicts some highly transient flows quite well, notably in dam break flows; it has a particular weakness relating to noise in the pressure field, since a small perturbation in the local density will yield a large variation in the local pressure. Even small changes in density will result in a large pressure oscillation (Antuono et al, 2012). At a higher number of Reynolds number, pressure gradient becomes dominant over viscous force and this results in a nonphysical pressure distribution (Liang et al., 2012).

In recent years, a number of researches have been conducted into WCSPH, and the previous drawbacks call for further improvements to WCSPH. The XSPH method introduced by Monaghan (1989) applies to the flow fields, keeping the particles more orderly by modifying the velocity closer to the average velocity of neighbouring particles, and thus overcoming the oscillation in the pressure fields. This technique works to some extent with additional numerical dispersion too. Implementation of high order approximation schemes by Chen and Beraun (2000) resolves pressure oscillation quite well. Meanwhile, as Colagrossi and Landrini (2003) noted, increasing the artificial viscosity may reduce noise in pressure but this approach can lead to inaccuracy in the solution. Research on the accuracy of density estimation by Antuono et al, (2012) presents a modified SPH equation with additional artificial diffusive terms in the continuity equation in order to remove the large pressure oscillation. Other alternatives, such as the density re-initialization suggested by Dilts (2000), help to reduce large oscillation of the particle pressure and can be used with low computational cost. Important developments made by Zheng et al., (2012) have also contributed to WCSPH in better modelling free surface incompressible flows. Meanwhile, Gao et al., (2012) show that pressure noise can be reduced with the application of the corrected smoothed particle method (CSPM) and implementation of the Riemann formulation between interacting particles (Vila, 1999). Furthermore, many modified SPH methods with a Riemann solver have been introduced to reduce the numerical noises and avoiding the use of artificial viscosity term. This improves the accuracy without compromising the computational cost (Inutsuka, 2002; Roubtsova and Kahawita, 2006; Omidvar, 2010; Rafiee et al., 2012; Sirotkin and Yoh, 2013).

In order to overcome the limitations of WCSPH, the ISPH method with properties of noise-free pressure field and bigger time step limits is preferable. The incompressible SPH (ISPH) method introduced by Cummins and Rudman, (1999) was developed based on a strict hydrodynamic formulation and a two-step semi-implicit solution process. The incompressibility is enforced by solving the Poisson`s equation for the pressure field. In this method, prediction-correction fractional time steps are implemented when updating all physical properties. At the first step, the intermediate velocity field is integrated forward in time without considering the pressure effect. Unlike WCSPH, the density and mass remain constant and this ensures the incompressibility of the fluid. Then, pressure is calculated through Poisson`s equation implicitly. Therefore, ISPH methods usually obtain much smoother pressure fields though they are not as flexible as WCSPH methods (Liu et al., 2013). A study by Shao and Lo (2003) suggests the alternative of a projection-based incompressible method that directly imposes density invariance rather than a divergence-free velocity field. However, it still suffers from noisy pressure fluctuation (Xu et al., 2009). Hu

and Adams (2007) suggest using a combination of density invariance and a divergence-free velocity field, which requires solving two pressures Poisson equations at each time step. The process of obtaining pressure and corresponding gradient fields are doubled but do not affect the velocity results. However, the computational cost is higher although the simulation appears to be much more stable. In other alternatives, the incompressibility can be enforced by using a constant density, thus only the divergence-free velocity condition is considered according to the continuity equation (Lee et al., 2010b). In general, Lee et al., (2008) showed that the ISPH technique may improve the computational efficiency and pressure stability of a simulation. However, one drawback could be that particle distributions may become highly distorted as a result of simulation errors and consequently instability could arise. This issue has been investigated by Xu et al., (2009) who followed the same approach as Cummins and Rudman, (1999) with new additional techniques. Fluid particles are slightly shifted away from the streamlines at the end of every time step, with their hydrodynamic variables being corrected as they move to a new position (Lind et al., 2012). This avoids highly distorted particle spacings which cause instability. Xu et al., (2009) showed that the technique yields high accuracy with regard to pressure and noiselessness without increasing the computational cost. The works have been extended by Xenakis et al., (2015) in designing a new approach to solving inelastic non-Newtonian flows for much accurate prediction of the pressure field. Kernel correction term is then introduced by Oger et al., (2007) where a 2nd order accuracy of convergence is implemented to exploit fully all the particle information in the kernel domain. Thus, pressure and velocity field can be accurately calculated without increasing the computational cost. Gotoh et al., (2014) proposed two new schemes to improve the performance of ISPH, particularly on sloshing induced impact pressure. Some of these techniques are adopted in the standard SPH formulation in this research and the performance of ISPH is improved accordingly. However, the implementation is rather complicated at a certain degree. Hence, research has been focused on how to incorporate different technique of modifications which may improve the performance of ISPH in the free surface prediction which is explained in Chapter 4. Further comparison between WCSPH and ISPH in free surface flows can be found in Lee et al., (2008), Hughes and Graham (2010), Shadloo et al., (2012) and Chen et al., (2013).

2.3.2 Applications in Wave-Structure Interactions

The wave structure interactions (WSI) play a major role in applications of free surface flow hydrodynamics. A sound physical understanding and robust numerical computation of the wave-structure interactions are crucial to assess the wave impact on structures as well as the structural responses to these wave attacks. For SPH application in WSI problems, many questions such as boundary treatment; numerical stability of pressure and turbulence models are still progressing due to the complexity of wave transformation and the interaction between wave and structures. SPH began to address the issue in 1995 where Benz and Asphaug modelled a material with strength in high-speed impacts. Since the mid-1990s the method has been applied to the study of free-surface hydrodynamics problems. In particle methods, it is difficult to simulate water waves in the domain that are large enough to avoid the effect of reflection waves because of the calculation cost. Therefore, artificial boundaries (open boundaries) are placed in the simulation domain to limit it to a finite size. The application of SPH to water waves was started by Monaghan, (1996) who performed two-dimensional simulations of wave propagation onto a shallow beach. SPH simulations have been further compared with published experimental results, the most famous example being the investigation of flow around the wave maker in Scott Russel`s experimental apparatus for producing solitary waves (Monaghan, 2000). In these simulations, he used an artificial equation of state to produce a quasi-incompressible fluid. SPH has also been used for wave mechanics with exact enforcement of incompressibility (Lo and Shao, 2002), in particular, the model was applied to the study of wave-breakwater interaction (Gotoh et al., 2004). This model uses an implicit pressure update that allows a larger time step but requires more computational work per time step. The use of SPH has also been extended to simulating ocean waves (Dalrymple and Rogers, 2006; Didier and Neves, 2012). Antuono et al., (2011) introduced a diffusive term to model propagating gravity waves, while a modification in SPH solver by Colagrossi et al., (2013) can correctly simulate dissipation phenomena for viscous flows. With the advancement of qualitative methods in modelling free surface and wave motion, SPH has been applied to analyse wave impact on offshore structures. The interaction between a single wave and an isolated structure is presented in Gomez and Dalrymple (2004), as the first approach to 3D calculation. Then in 2007, the presence of 3D dykes to mitigate the effect of large waves on coastal structures was considered (Crespo et al., 2007). Manenti et al., (2008) investigated the behaviour of a floating box in periodic waves offshore of the breaker line, while Roger et al., (2010) did the same in a surf zone. Panizzo and Dalrymple (2004) and Xie et al., (2007) successfully generates a propagating tsunami wave through simulating a landslide deformations

treated as rigid bodies sliding down inclines into the towing tank. Weiss et al., (2011) utilised a GPU-based SPH model to numerically simulate the conical island experiment and shallow water equation solved by Vacondio et al., (2012) and he simulated the 1983 Okushiri Island Tsunami. Most recently, rapidly advancing tsunamis induced by the impact of hydrodynamic forces have been investigated by St-Germain et al. (2014). Within the field of coastal engineering, Landrini et al., (2007) show that SPH can simulate near-shore bore propagation both at a uniform depth and over a beach with a constant slope. Research by Shao, (2010) used a periodic wave to simulate the wave damping over a porous medium while Ren et al., (2014) compared them with different levels of permeability. In the same field, Li et al., (2012) conducted a series of tests using a solitary wave over different seabeds. Since SPH is able to capture details of discontinuities of the free surface, many successful applications have been published. Wave breaking analysis by Lo and Shao (2002) studied the forces generated by regular and irregular waves overtopping the decks of offshore structures (Gomez et al., 2005; Shao et al., 2006). A study on the dynamics of breaking water waves on beaches in 2-D and 3-D by Dalrymple and Rogers (2006) suggested improvements concerning handling turbulence, fluid viscosity and density, while an investigation of wave interaction with a vertical wall of a breakwater was completed by Didier et al., (2014). In this research, the interaction between waves and rigid body is demonstrated in Chapter 5. The reliability of SPH as a numerical tool is tested through a series of 2-D validation benchmark tests of predicting radiation, diffraction and floating body problems.

The motion of ship can be considered complex which involve influent, ship hull and other numerous external loads. Various numerical studies has been implemented to study the complex motion. However, there are limited quantitative studies found relating to SPH particularly in seakeeping analysis. Shibata et al., (2009) used particle method (MPS) in simulating shipping water to validate the fluid behaviour and impact force on the deck of a moving ship. Similar validation case of slamming events were also done where accurate slamming pressure can be estimated using SPH algorithm (Veen, 2010; Veen and Gourlay, 2012). Famous works in the study of behaviour and motion of ships in waves were shown by Cartwright et al., (2006) and Patel et al., (2009). Then recently Kawamura et al., (2016) managed to predict 6DoF ship motions in severe, water-shipping condition using a GPU-accelerated SPH simulations. Coupling method between a SPH flow solver and a FEM seakeeping solver were shown by Servan et al., (2016) in simulating seakeeping dynamics and internal flows in tanks. Marrone et al., (2011, 2012) proposed a 2-D+t and 3-D SPH solver to analyse wave pattern generated by ship with good qualitative description of the breaking phenomenon. Wave height above deck is then predicted by Le Touze (2010) when the ship moves in waves. With respect to ship collision, Zhang et al., (2013) showed transient

height of water after two ship collisions while coupling nonlinear motion of ship hull with complex internal liquid of a damaged ship. In similar way, influent problems of a simple damaged ship model under the condition of roll and heave respectively was also simulated by Skaar et al., (2006). The behaviour of a 3-D rigid body in waves is investigated in Chapter 6.1. Studies are conducted on the topic of the motion response problem, with the task of estimating the vertical bending moment at amidships. However, the analysis of seakeeping using SPH is still not common due to the request for a large size of fluid domain involved to avoid wave reflection at the boundaries. The investigation on hydroelasticity is also rarely mentioned. In order to capture details on the free surface with high resolution, suitable particle distributions need to be considered. The prediction of hydrodynamic coefficients of a flexible barge in Chapter 6.2 requires more than 8 million particles for a single case. Without suitable hardware acceleration or effective parallel computing techniques, the method is computationally expensive and very slow, particularly in 3-D applications. Therefore, a highly optimised open-source SPH code by DualSPHysics is utilised in this research. DualSPHysics is developed by researchers at the University of Manchester (UK), University of Vigo (Spain) and Universita Degli Studi Di Parma (Italy) to solve both 2-D and 3-D Navier-Stokes equations using either central processing units (CPUs) with OpenMPI and graphics processing unit (GPUs). With continuing modifications and improvements, the code is approaching its mature stage where many practical engineering problems have been investigated (Crespo et al., 2011; Gomez-Gesteira et al., 2012a, 2012b; Crespo et al., 2015). Due to its open source nature, modifications have been done to suit the need for seakeeping problems, both for rigid and flexible barge in Chapter 6. In comparison to CPU performance, GPUs offer much more powerful computing performance at an affordable price (Dalrymple et al., 2010). GPUs are also built and designed to handle a huge amount of data in simulations. Therefore, the need of using supercomputer such as IRIDIS of the University of Southampton is not necessary as all the simulations can be executed on a personal computer.

Chapter 3

SPH Methodology

In this chapter, basic concepts and fundamental theory in SPH method are presented and explained. The main differences between 2 types of SPH formulations, namely, incompressible SPH (ISPH) and the weakly compressible SPH (WCSPH) formulations, are highlighted. Then, the implementation of SPH schemes, especially treatments between boundary, floating body and fluid domain, are presented. Further details on the mathematical formulation can be found in **Appendix B**.

3.1 SPH theory

3.1.1 Basic SPH operator

SPH is based on the theory of integral interpolants (Monaghan, 1987; 1988). It is a method for obtaining approximate numerical solutions of the equations of fluid dynamics by replacing the fluid with a set of particles (Gingold and Monaghan, 1977). The equations of motion and properties of these particles are determined from the continuum equations of fluid dynamics by interpolation from the particles.

The fundamental concept starts with the consideration of a set of SPH particle (e.g. particle b) that has mass m, density ρ, and position $\mathbf{x}$, with $\mathbf{x} = (x, y)$ and the interpolation for any general

25

function $A(x)$ can be reproduced by a kernel approximation as $\langle A(\mathbf{r}) \rangle$, (Monaghan, 1982; Monaghan and Gingold, 1983; Monaghan and Poinracic, 1985).

$$\langle A(\mathbf{x}) \rangle = \int_{\Omega} A(\mathbf{x}')\omega(\mathbf{x} - \mathbf{x}', h)\mathbf{dx}' \tag{3.1}$$

where $\mathbf{dx}'$ denotes a volume element. ω is the weighting function or kernel; h is called smoothing length and it controls the influence domain Ω. Normally, the value of h must be higher than initial particle separation. Straightforwardly, the gradient and divergence can be respectively written as,

$$\langle \nabla A(\mathbf{x}) \rangle = \int_{\Omega} A(\mathbf{x}')\nabla\omega(\mathbf{x} - \mathbf{x}', h)\mathbf{dx}' \tag{3.2}$$

$$\langle \nabla \cdot A(\mathbf{x}) \rangle = \int_{\Omega} A(\mathbf{x}') \cdot \nabla\omega(\mathbf{x} - \mathbf{x}', h)\mathbf{dx}' \tag{3.3}$$

In order to facilitate numerical approximation, the infinitesimal volume $\mathbf{dx}'$ is replaced by the particle volume, which can be expressed using mass and density.

$$\mathbf{dx}' = \frac{m_b}{\rho_b} \tag{3.4}$$

The approximation in equation (3.4), in discrete notation, leads to the following approximation of the function at a particle a, (particle approximation), where the integration is approximated by a summation over the neighbouring particles that are located within the smoothing length domain.

$$\langle A(\mathbf{x}) \rangle_a = \sum_b m_b \frac{A(\mathbf{x}_b)}{\rho_b}\omega(|\mathbf{x} - \mathbf{x}_b|, h), \tag{3.5}$$

Although the summations are formally overall the particles, the only particles b that make a contribution to the density of particle a are those for which $|\mathbf{r}_a - \mathbf{r}_b| \leq 2h$. By using SPH kernel approach, the interpolant can be constructed using analytical function and spatial derivatives of the interpolated quantities can then be found by differentiating the kernel, as opposed to a method like finite differences, where the derivatives are calculated from neighbouring points using the spacing between them. There is no need for grid and mesh and the description of free surfaces, however complicated, is trivial. The approximation for spatial derivatives can be expressed as

$$\langle \nabla A(\mathbf{x}) \rangle_a \approx \sum_b m_b \frac{A(\mathbf{x}_b)}{\rho_b} \nabla \omega(\mathbf{x} - \mathbf{x}_b, h), \tag{3.6}$$

$$\langle \nabla \cdot A(\mathbf{x}) \rangle_a \approx \sum_b m_b \frac{A(\mathbf{x}_b)}{\rho_b} \cdot \nabla \omega(\mathbf{x} - \mathbf{x}_b, h), \tag{3.7}$$

With this equation, only ordinary differential equations need to be solved instead of solving partial differential equations for hydrodynamic problems. The derivative of the kernel function can be expressed as

$$\nabla_a \omega_{ab} = \frac{\mathbf{x}_a - \mathbf{x}_b}{\mathbf{r}_{ab}} \frac{\partial \omega_{ab}}{\partial \mathbf{r}_{ab}} \tag{3.8}$$

where $\mathbf{r}_{ab}$ is the distance between particle a and b, ω_{ab} is the associated kernel function and ∇_i implies spatial derivative with respect to coordinates of the generic particle i. From equation (3.8) it is clear that the gradient of a function at particle a is approximated with a summation of the function values at each neighbouring particle times the gradient of the kernel function. This smoothing kernel ω_{ab} is explained in more detail in **Appendix B**.

3.1.2 Smoothing kernel

The performance of an SPH model is critically dependent on the choice of the kernel functions. The selection of kernel has to be constructed for a successful SPH simulation. An improper choice of the kernel function may lead to unphysical structures of the system (Schussler and Schmitt, 1981). They should satisfy several conditions such as positivity, normalisation and compact support. Being positive is important to prevent any unphysical parameters such as negative density and energy. While the normalisation condition ensures that a continuum function can be approximated to the zeroth order. The compact support condition transforms a SPH approximation from global operation to a local operation. In addition, ω_{ab} must be monotonically decreasing with increasing distance from particle a and behave like a delta function as the smoothing length, h, tends to zero (Benz, 1990; Monaghan, 1992; Liu, 2003). Kernels depend on the smoothing length, h, and the non-dimensional distance between particles given by $q = \mathbf{r}/h$ where $\mathbf{r}$ is the distance between particles a and b. The parameter h, often called influence domain or smoothing domain, controls the size of the area around particle a where contribution from the rest of the particles cannot be neglected. It is possible to use different kernels for different property calculations. There are several examples of kernel function that are commonly used in SPH computations and all are described in Monaghan (1992), Liu and Liu

(2003), and Monaghan (2005). Quartic smoothing function is used in this work for ISPH and WCSPH by DualSPHysics employs a quintic kernel by Wendland (1995).

Quartic

$$\omega(\mathbf{r}, h) = \alpha_D[1 - 6q^2 + 8q^2 - 3q^4] \quad 0 \leq q \leq 1 \tag{3.9}$$

where α_D is $5/(\pi h^2)$ in 2-D and $105/(16\pi h^3)$ in 3-D. $q = |\mathbf{r}_{ab}|/k$. k is the kernel support size, $k = 2 \cdot h$, with $h = c \cdot dx$ where dx is the initial particle distance and c a constant, equal to 1.0. Details of other kernels can be found in the appendices. This kernel is used by Lucy (1977) in his original SPH paper.

Wendland quintic

$$\omega(\mathbf{r}, h) = \alpha_D \left(1 - \frac{q}{2}\right)^4 (2q + 1) \quad 0 \leq q \leq 2 \tag{3.10}$$

where α_D is $7/(4\pi h^2)$ in 2-D and $7/(8\pi h^3)$ in 3-D.

This was used by Panizzo et al. (2007) and the results showed that the best compromise between accuracy and time computation cost is reached by the use of the Wendland kernel (Wendland, 1995). In general, the higher the order of the kernels, the greater the accuracy of the SPH scheme and the higher the computational cost. In this study, it is necessary to capture detailed of complex phenomena, so using a kernel approximation of fourth order accuracy become a necessity.

3.1.3 Governing equations

Fluid can be treated as a continuum enclosed in a volume bounded by an arbitrary closed surface. In order to describe the motion of the continuum, governing equations can be developed based on the principles of conservation of mass and conservation of momentum of Navier-Stokes equations, which are solved in a Lagrangian framework. The governing equations for fluid include the conversation of mass. In a Lagrangian framework, these can be written as follows,

$$\frac{1}{\rho}\frac{D\rho}{Dt} + \nabla.\mathbf{v} = 0 \tag{3.11}$$

Implementation of incompressibility in this work is divided into two types according to incompressible SPH (ISPH) and weakly compressible SPH (WCSPH). In ISPH, incompressibility

is enforced in the projection method by a pressure Poisson equation. In that way, the mass density takes a constant, equation (3.11) reduced as follows;

$$\nabla \cdot \mathbf{v} = 0 \tag{3.12}$$

The body force of the fluid is gravity force, and the stress tensor can be considered as a combination of viscous force and pressure. The conservation of momentum can be written as follows;

$$\frac{D\mathbf{v}}{Dt} = \mathbf{g} + \frac{1}{\rho}\nabla \cdot \tau - \frac{1}{\rho}\nabla P + \Theta \tag{3.13}$$

$$\frac{D\mathbf{x}}{Dt} = \mathbf{v} \tag{3.14}$$

where t is the time, g is the gravitational acceleration, P is the pressure, v is the velocity, τ is the viscous stress tensor, $^D/_{Dt}$ refers to the material derivative and Θ is the diffusion terms which in this case is the artificial viscosity term. Equation (3.14) is solved for the particle positions. The momentum equations include three driving force terms, i.e. body force, forces due to divergence of stress tensor and the pressure gradient. The momentum equation is solved in the presence of the body forces and viscosity forces corresponding to the fluid with consideration of the effects of pressure and incompressibility (Farahani et al., 2009). The SPH equation of motion will be derived based on these governing equations in Lagrangian form.

3.1.3.a   Viscous term and Laplacian operator

Based on the momentum equation (3.13), the 2nd term on the right-hand side (RHS) of the equation relates to forces due to the divergence of stress tensor. Assuming a Newtonian fluid, the viscous stress tensor τ in the momentum conservative equation is related to the rate of strain as follows,

$$\tau_{ij} = \tau_{ji} = \mu\left(\frac{\partial \mathbf{v}_i}{\partial \mathbf{x}_j} + \frac{\partial \mathbf{v}_j}{\partial \mathbf{x}_i}\right) \tag{3.15}$$

where μ is the dynamic viscosity coefficient of the fluid and τ_{ij} is the stress in the j direction exerted on a plane perpendicular to the i axis. So, by implementing the chain rule, the gradients on the RHS is written as

$$\left(\frac{\partial \mathbf{v}_i}{\partial \mathbf{x}_j}\right)_a = \left(\frac{\partial \mathbf{v}_i}{\partial \mathbf{r}_{ab}}\right)\left(\frac{\partial \mathbf{r}_{ab}}{\partial \mathbf{x}_j}\right) = \left(\frac{\mathbf{v}_a^i - \mathbf{v}_b^i}{\mathbf{r}_{ab}}\right)\left(\frac{\mathbf{x}_a^j - \mathbf{x}_b^j}{\mathbf{r}_{ab}}\right) \tag{3.16}$$

The viscosity term is presented in equation (3.17) (Shao and Lo, 2003). In this approximated viscous term, only the first derivative of the kernel function is used. The calculation of the first derivative can be used not only in the divergence or gradient calculation but also for the viscous term which saves more computing time. The viscosity term can be written as,

$$\left(\frac{1}{\rho}\nabla\cdot\tau\right)_a = \left(\frac{\mu}{\rho}\nabla^2\mathbf{v}\right)_a = \sum_{b=1}^{N}\frac{4m_b(\mu_i+\mu_j)}{(\rho_a+\rho_b)^2}\frac{\mathbf{r}_{ab}\cdot\nabla_a\omega_{ab}(\mathbf{v}_a-\mathbf{v}_b)}{|\mathbf{r}_{ab}|^2+\varphi^2} \tag{3.17}$$

where m is the mass of the particle; ρ is the fluid density; $\mathbf{v}_a$ is the velocity of particle a, $\mathbf{v}_{ab} = \mathbf{v}_a-\mathbf{v}_b$; $\mathbf{r}_a$ is the position of particle a, $\mathbf{r}_{ab} = \mathbf{r}_a-\mathbf{r}_b$; φ is a small value used to prevent numerical divergence when two particles are too close to each other. With constant viscosity and density in this thesis, a similar viscosity term is formulated as,

$$\left(\frac{1}{\rho}\nabla\cdot\tau\right)_a = \left(\frac{\mu}{\rho}\nabla^2\mathbf{v}\right)_a = \sum_{b=1}^{N}\frac{2m_b\mu}{\rho_b^2}\frac{\mathbf{r}_{ab}\cdot\nabla_a\omega_{ab}(\mathbf{v}_a-\mathbf{v}_b)}{|\mathbf{r}_{ab}|^2+\varphi^2} \tag{3.18}$$

while an approximate Laplacian operator is used for the force term due to pressure gradient and can be written in a symmetric form as,

$$\left(\frac{1}{\rho}\nabla\sigma\right)_a = \frac{\partial}{\partial\mathbf{x}_a^j}\left(\frac{\sigma_{ij}}{\rho}\right) + \frac{\sigma_{ij}}{\rho^2}\frac{\partial\rho}{\partial\mathbf{x}_a^j}$$

$$= \sum_{b=1}^{N}\frac{m_b}{\rho_b}\frac{\sigma_b^{ij}}{\rho_b}\frac{\partial\omega_{ab}}{\partial\mathbf{x}_a^j} + \frac{\sigma_a^{ij}}{\rho_a^2}\sum_{b=1}^{N}\frac{m_b}{\rho_b}\rho_b\frac{\partial\omega_{ab}}{\partial\mathbf{x}_a^j}$$

$$= \sum_{b=1}^{N}m_b\left(\frac{\sigma_a^{ij}}{\rho_a^2}+\frac{\sigma_b^{ij}}{\rho_b^2}\right)(\mathbf{L}(\mathbf{r})\cdot\nabla_a\omega_{ab})$$

$$= \sum_{b=1}^{N}m_b\left(\frac{\sigma_a^{ij}}{\rho_a^2}+\frac{\sigma_b^{ij}}{\rho_b^2}\right)\nabla_a W_{ab} \tag{3.19}$$

where $\mathbf{L}(\mathbf{r})$ is the kernel correction term which will be explained further in Chapter 4.2. This formula is the most widely used as it conserves angular and linear momentum because of the symmetry of the formula. As the density is constant, the equation is rewritten as,

$$\left(\frac{1}{\rho}\nabla\sigma\right)_a = \sum_{b=1}^{N}\frac{m_b}{\rho_b}\left(\sigma_a^{ij}+\sigma_b^{ij}\right)\frac{\partial W_{ab}}{\partial\mathbf{x}_a^j} \tag{3.20}$$

3.1.3.b Artificial viscosity

The early implementation of SPH equations, a viscosity term was introduced by (Lucy, 1977) as an artificial bulk viscosity was introduced to prevent a slow build-up of acoustic energy from integration errors in an SPH simulation. A different, and more effective viscosity term, which conserves linear and angular momentum was suggested and tested by (Monaghan and Gingold, 1983; Monaghan, 1992). Artificial viscosity is developed to allow shock phenomena to be simulated or to stabilise a numerical algorithm.

The artificial term is necessarily added when calculating the velocity to damp out some unphysical penetration for particles approaching each other (Johnson and Beissel, 1996). When two particles approach each other, the artificial viscosity produces a repulsive force between the particles and when they recede from each other the force becomes attractive. Artificial viscosity can be simulated by adding $\mathbf{\Pi}_{ab}$ term to the pressure term in the equation.

$$\mathbf{\Pi}_{ab} = \begin{cases} \dfrac{-\alpha_\Pi \overline{c_{ab}}\Phi_{ab} + \beta_\Pi \Phi_{ab}^2}{\bar{\rho}_{ab}} & \mathbf{v}_{ab} \cdot \mathbf{x}_{ab} < 0 \\ 0 & \mathbf{v}_{ab} \cdot \mathbf{x}_{ab} > 0 \end{cases} \tag{3.21}$$

where

$$\Phi_{ab} = \frac{\bar{h}_{ab}\mathbf{v}_{ab} \cdot \mathbf{x}_{ab}}{|\mathbf{x}_{ab}|^2 + \varphi^2} \; ; \; \bar{c}_{ab} = \frac{1}{2}(c_a + c_b); \; \bar{\rho}_{ab} = \frac{1}{2}(\rho_a + \rho_b) \tag{3.22}$$

$$\bar{h}_{ab} = \frac{1}{2}(h_a + h_b); \mathbf{v}_{ab} = \mathbf{v}_a + \mathbf{v}_b; \quad \mathbf{x}_{ab} = \mathbf{x}_a + \mathbf{x}_b \tag{3.23}$$

In the above equation, α_Π, β_Π are constant and are typically set around 1.0 and are tested in preliminary runs for confirmation (Rabzuk et al., 2000). The factor $\varphi = 0.1\bar{h}_{ab}$ is inserted to prevent numerical divergences when two particles are approaching each other. $\bar{c}_{ab}$ and $\mathbf{v}$ represent the speed of sound and the particle velocity vector respectively.

3.1.4 Continuity equation

For WCSPH, the fluid density is not constant and changes in the fluid density are calculated using

$$\frac{d\rho_a}{dt} = \sum_b m_b \mathbf{v}_{ab} \cdot \nabla_a \omega_{ab} \tag{3.24}$$

instead of using a weighted summation of mass terms (Monaghan, 1992), since it is known to result in artificial density decrease near the fluid interface.

Within DualSPHysics, it is also possible to apply a delta-SPH formulation (Crespo et al., 2015; Antuono et al., 2016). A diffusive term was introduced by Antuono et al., (2012) to reduce density fluctuations and high-frequency spurious oscillations in the pressure field

$$\frac{d\rho_a}{dt} = \sum_b m_b \mathbf{v}_{ab} \cdot \nabla_a \omega_{ab} + 2\delta h \sum_b m_b \bar{c}_{ab} \times \left(\frac{\rho_a}{\rho_b} - 1\right) \frac{1}{\mathbf{r}_{ab}^2 + \eta^2} \cdot \nabla_a \omega_{ab} \qquad (3.25)$$

where $\bar{c}_{ab} = 0.5(c_a + c_b)$, c_a and c_b are the speed of sound at particles a and b respectively, $\eta^2 = 0.01h^2$ and δ is the delta-SPH coefficient. This technique is designed to filter relatively large wave numbers from the density field while solving the conservation of mass of each particle, therefore reducing noise throughout the system of particles. The term can be expanded into a first and second order contribution, where the second order corresponds to its diffusive nature and the first order is approximately zero if the kernel is complete. However, at open boundaries, where a non-complete interpolation kernel is inevitably present, the first order term initiates a net contribution. For this reason, it is advised that the delta-SPH scheme is disabled for cases that rely on hydrostatic equilibrium. If the case represents a very dynamic situation, the term contributes with a force that may be several orders of magnitude smaller than the pressure and viscous terms, not contributing to a significant degradation of the solution. A delta-SPH coefficient of 0.1 is recommended for most applications (Marrone et al., 2011; Meringolo et al., 2015).

3.1.5 Pressure calculation

In ISPH, computing pressure is calculated by considering the fluid as a truly incompressible flow by solving a Poisson's equation to obtain the pressure values. This can be done by enforcing the velocity divergence free and zero density variation conditions (Shao and Lo, 2003; Hosseini et al., 2007). Alternatively, a straightforward method to ensure incompressibility for the fluid is to use a constant density all through the calculations and the velocity divergence is forced to be zero (Lee et al., 2010b). The advantage of using constant density is that no additional consideration of unphysical density oscillation for the near boundary particles is required.

The momentum equation is split into two parts and in part one, the effect from body force and viscosity are considered

$$\frac{\mathbf{v}^* - \mathbf{v}^n}{\Delta t} = g + \frac{1}{\rho}\nabla \cdot \tau^n \tag{3.26}$$

and in part two, the effect from pressure is accounted for

$$\frac{\mathbf{v}^{n+1} - \mathbf{v}^*}{\Delta t} = \frac{-1}{\rho}\nabla P^{n+1} \tag{3.27}$$

By taking the divergence of equation (3.27) and substituting into equation (3.12), Poisson's pressure equation can be derived

$$\Delta P^{n+1} = \frac{\rho}{\Delta t}\nabla \cdot \mathbf{v}^* \tag{3.28}$$

and this Poisson's equation is converted into SPH formulation method

$$\sum_b \frac{m_b {P_{ab}}^{n+1}{\mathbf{r}_{ab}}^n}{\mathbf{r}_{ab}^2 + \eta^2}\nabla_a \omega_{ab}^n = \frac{\rho}{2\Delta t}\sum_b m_b \mathbf{v}_{ab}^* \nabla_a W_{ab}^n \tag{3.29}$$

Hence, the pressure can be updated using equation (3.29), which can be solved efficiently using the Bi-CGSTAB method.

Then, by adding artificial viscosity term into the momentum equation,

$$\mathbf{v}_a^{n+1} = \mathbf{v}_a^* - \Delta t \Sigma_b m_b \left(\frac{P_a^{n+1}}{\rho^2} + \frac{P_b^{n+1}}{\rho^2} + \mathbf{\Pi}_{ab}\right)\nabla_a W_{ab}^n \tag{3.30}$$

the position can be renewed based on the velocity

$$\mathbf{x}_a^{n+1} = \mathbf{x}_a^n + \mathbf{v}_a^{n+1}\Delta t \tag{3.31}$$

In WCSPH, the incompressible flow is assumed to have a small compressibility. The pressure field is not solved with a pressure Poisson equation, but with a state equation. In the state equation, the speed of sound, whose value should be at least ten times the maximum fluid velocity, is used for the calculation of coefficient. In order to satisfy the CFL condition, the time step is limited to a very small value, which reduces the simulation efficiency. Compressibility causes problems with sound wave reflection at the boundaries. However, due to its simplicity, the state equation is still widely used in pressure calculations in simulations (Batchelor, 1973; Monaghan, 1994). The state equation follows the expression

$$P = B\left[\left(\frac{\rho}{\rho_0}\right)^\gamma - 1\right] \tag{3.32}$$

where, $\gamma = 7$, $B = c_0^2 \rho_0 / \gamma$, with ρ_0 being the reference density and c_0 being the speed of sound at the reference density and $c_0 = c(\rho_0) = \sqrt{\frac{\partial P}{\partial \rho}}$. The parameter B is a constant related to the bulk modulus of elasticity of the fluid; ρ_0 is the reference density, usually taken as the density of the fluid at the free surface, and γ is the polytrophic constant, usually between 1 and 7, the minus one term used in the equation of state is to obtain zero pressure at a surface. It can be seen that a small oscillation in density may result in a large variation in pressure.

3.2 SPH implementation

3.2.1 Boundary conditions

On the boundaries, the problem occurs when fluid particles penetrate the wall particles. The wall modelled by particles must be treated with care in order to prevent any penetration from inner particles. In SPH simulations, the rigid body is also treated as a solid boundary where the boundary conditions use the same approach as wall boundaries. Two types of boundary conditions have been implemented in ISPH and WCSPH in this research. The methods used to implement boundary conditions are either (i) using boundary force particles that repel those in the fluid (Monaghan, 1994; Monaghan and Kajtar, 2009), (ii) mirroring ghost boundary (Colagrossi and Landrini, 2003), (iii) the dummy particle boundary (Adami et al., 2012), or (iv) having layers of fixed wall around the boundaries which is also known as Dynamic Boundary Condition (DBC) (Shao and Lo, 2003; Crespo et al., 2007; Lee et al., 2008). In repulsive boundary conditions, the boundaries are modelled by a set of particles, which exert a repulsive force on the approaching inner fluid particles. The force can take various forms such as a Lennard-Jones force or an empirical function with a singularity so that the force increases as the particle moves nearer to the boundaries. Following this approach, the force can be calculated by

$$f(r) = D \left(\left(\frac{r_0}{r} \right)^{p_1} - \left(\frac{r_0}{r} \right)^{p_2} \right) \frac{\mathbf{r}}{r^2} \tag{3.33}$$

where D is a problem dependent constant and its value can be determined using other parameters of the problem. In this work, one suggestion is to use $D = 5gH$, where H is the water depth (although there will be some differences between bottom particles and side particles. D is used as the unique value for all particles to keep an algorithm simple). Parameters p_1 and p_2 are set as 4 and 2 respectively according to Monaghan (1994), r is the distance from an inner particle to a

boundary particle and r_0 is the cut-off distance normally selected to be the initial particle spacing. The value of $f(r)$ is set to be zero when $r > r_0$ so that the force is purely repulsive.

In the DBC method, boundary particles are forced to have the same properties as corresponding fluid particles. Thus they follow the same momentum equation, continuity equation and the equation of state. Therefore, the kernel domain of fluid particles can remain complete to ensure accurate particle approximation and the physical properties such as density can be calculated correctly. When a fluid particle approaches a boundary, the density of a boundary particles increase due to the contribution of its adjacent fluid particles. Thus, the force exerted on the fluid particle increases due to the pressure term in the momentum equation creating a repulsive mechanism. Their density and pressure update continually during the simulation, but their velocities and their positions remain unchanged. They remain fixed in position or move according to an externally imposed position i.e. a wave maker, imposed velocity, forced oscillation (sway, heave, roll) etc. The DBC method is easy to implement but sometimes becomes unstable when dealing with complex moving solid boundaries i.e. hull structures, wave maker etc. Therefore, to minimise numerical errors and particle lost during the simulation, the implementation of denser boundary particles is also considered. Several layers of boundary particles are organised in either a uniform or a staggered manner, as shown in Fig.3.1. Denser boundary particle contribute to the fully exploitation of the kernel support. However, this is case dependent and several initial tests need to be carried out to observe the behaviour of the boundary particles before real measurement commences. Both the boundary treatments allow for efficient simulations to a certain degree of complex solid boundaries and they simplify the coupling approach for fluid-structural interactions (Sun et al., 2011).
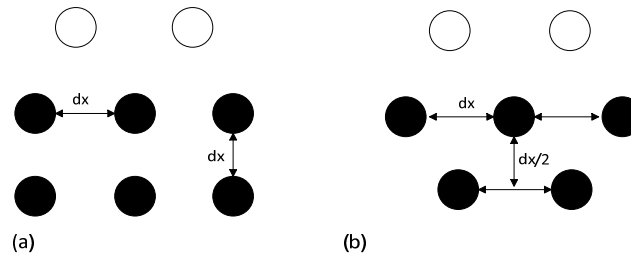
Figure 3-1 Illustration of the interaction between a fluid particle (empty circle) and a set of boundary particles (full circle). (a) boundary particles are placed in a uniform manner and (b) in a staggered manner.

3.2.2 Force and floating bodies

As mentioned earlier in the literature review, boundary particles can be used for simulating rigid body and deformable body for fluid-structure interaction problem. The body might drift freely on the free surface with given initial velocity or it might have a constrained movement along the fluid domain. All boundary particles have similar properties with fluid particles. However, according to DBC, boundary particle is bound to repel approaching fluid particles using repulsive force to prevent any penetration from the fluid particle. The interaction between the boundary and the fluid particle will contribute to the motion of the floating body. Within the same kernel, the force on each boundary particle is computed by adding up the contribution from all the surrounding fluid particles. Hence, boundary particles experience a force per unit mass given by

$$\mathbf{f}_k = \sum_{a \in FPs} \mathbf{f}_{ka} \tag{3.34}$$

where FPs denotes fluid particles and $\mathbf{f}_{ka}$ is the force per unit mass exerted by fluid particle a on boundary particle k. The force exerted by a fluid particle on each boundary particle follows the principle of equal and opposite action and reaction which is,

$$m_k \mathbf{f}_{ka} = -m_a \mathbf{f}_{ak} \tag{3.35}$$

In the simulations, the repulsive force, $\mathbf{f}_{ak}$, exerted by the boundary particle k on fluid particle a is the only force computed but from the equation (3.35), the force exerted on the moving body can be calculated. Equations of rigid body dynamics are used to determine the motion of the floating body. The equations of motion of the body in the translational and rotational degrees of freedom are given by

$$M \frac{d\mathbf{V}}{dt} = \sum_{k \in BPs} m_k \mathbf{f}_k \quad \text{and} \quad I \frac{d\mathbf{\Omega}}{dt} = \sum_{k \in BPs} m_k (\mathbf{r}_k - \mathbf{R}_0) \times \mathbf{f}_k \tag{3.36}$$

where M is the mass of the object, I is the moment of inertia, $\mathbf{V}$ is the velocity of the object, $\mathbf{\Omega}$ is the rotational velocity of the object, $\mathbf{R}_0$ is the position of the centre of mass and BPs denotes boundary particles. The values of $\mathbf{V}$ and $\mathbf{\Omega}$ for the beginning of the next time-step are predicted through the integration of equations (3.37). Each boundary particle that describes the moving body has a velocity given by

$$\mathbf{v}_k = \mathbf{V} + \mathbf{\Omega} \times (\mathbf{r}_k - \mathbf{R}_0) \tag{3.37}$$

By integrating equation (3.37) in time, the position of each boundary particle can be determined and moved accordingly. It can be shown that this technique conserves both linear and angular momentum (Monaghan et al., 2003; Monaghan, 2005).

3.2.3 Linked-list algorithm

In SPH method, the summation is performed over all the particles since the smoothing kernel has a compact support domain. Unlike grid-base method, the neighbouring particles which are used in the particle approximations can vary with time. Therefore, there are several approaches that can be used to determine the nearest neighbouring particles. In this thesis, the cell linked-list approach (CLL) is used for both ISPH and WCSPH models (Monaghan and Lattanzio, 1985; Dominguez et al., 2010). Other examples are the tree search algorithm (Hernquist and Katz, 1989) and the Verlet list algorithm (Dominguez et al., 2010).
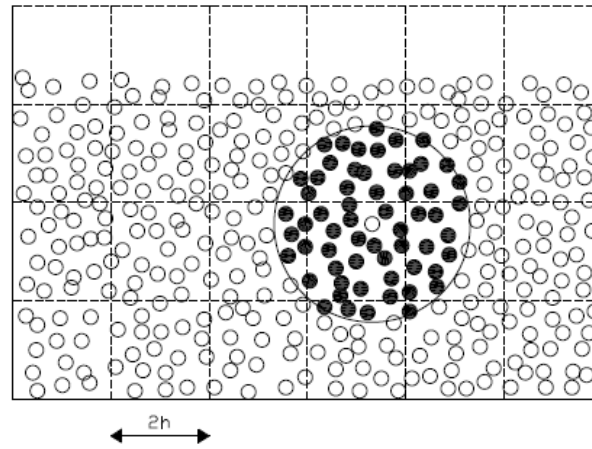
Figure 3-2 Set of neighbouring particles in 2D. The possible neighbours of a fluid particle are in the adjacent cells but it only interacts with particles marked by black dots (Dominguez et al., 2010).

In SPH code, the computational domain is divided into square cells of size *2h* for particles. Thus, only particles that are within the cell are referred to as neighbouring particles and used in the particle approximations. In this way, the number of calculations per time step and, therefore, the computational time reduces considerably, from N^2 operations to $N \cdot \log N$, N being the number of particles. The algorithm sweeps through the grid along the x-direction, for each z-level. Starting from the lower left corner, particles inside the centre cell N interact with adjacent cells only in E,

N, NW and NE directions. The interactions with the rest of the cells W, S, SW and SE direction are computed using reverse interactions.
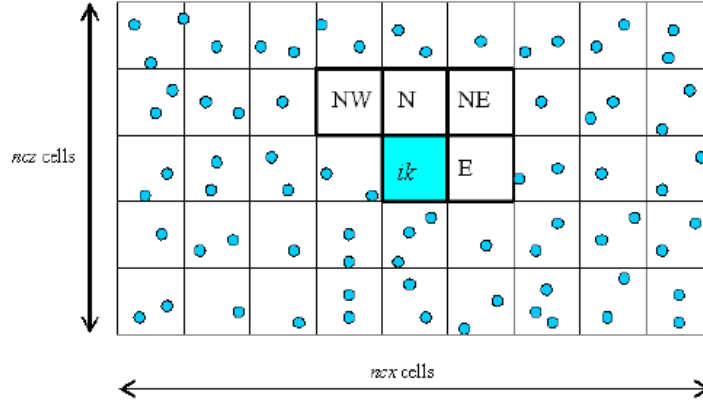
Figure 3-3 Interaction of particle with adjacent cells.

3.2.4 Time stepping algorithm

There are several ways to develop the solution of the SPH equations in time. It is advisable to use at least a second-order accurate scheme in time. The numerical scheme implemented in this paper for ISPH is the Predictor-Corrector algorithm described by Monaghan (1989) and the Sympletic scheme for WCSPH (Monaghan 2005). Other different time integration schemes have been employed in SPH and in other Lagrangian numerical models such as the Leap-Frog algorithm (Bui, 2007), Verlet algorithm (Verlet, 1967), the Two Step Velocity Verlet algorithm (Monaghan, 2006) and the Beeman (Beeman, 1976) algorithm.

The momentum, density and position equations are given in the following form

$$\frac{d\mathbf{v}_a}{dt} = \mathbf{F}_a \tag{3.38}$$

$$\frac{d\rho_a}{dt} = D_a \tag{3.39}$$

$$\frac{d\mathbf{x}_a}{dt} = \mathbf{v}_a \tag{3.40}$$

where $\mathbf{v}_a$ represents the velocity contribution from particle a and from neighbouring particles .

Predictor-corrector scheme

This scheme predicts the evolution in time as,

$$\mathbf{v}_a^* = \mathbf{v}_a^n + \frac{\Delta t}{2} D\mathbf{v}_a^n \qquad (3.41)$$

$$\rho_a^* = \rho_a^n + \frac{\Delta t}{2} D\rho_a^n \qquad (3.42)$$

$$\mathbf{x}_a^* = \mathbf{x}_a^n + \frac{\Delta t}{2} \mathbf{v}_a^n \qquad (3.43)$$

calculating $P_a^* = f(\rho_a^*)$ according to the equation of state.

These values are then corrected using forces at the half step

$$\mathbf{v}_a^* = \mathbf{v}_a^n + \frac{\Delta t}{2} D\mathbf{v}_a^* \qquad (3.44)$$

$$\rho_a^* = \rho_a^n + \frac{\Delta t}{2} D\rho_a^* \qquad (3.45)$$

$$\mathbf{x}_a^* = \mathbf{x}_a^n + \frac{\Delta t}{2} \mathbf{v}_a^* \qquad (3.46)$$

Finally, the values are calculated at the end of the time step following:

$$\mathbf{v}_a^{n+1} = 2\mathbf{v}_a^* - \mathbf{v}_a^n \qquad (3.47)$$

$$\rho_a^{n+1} = 2\rho_a^* - \rho_a^n \qquad (3.48)$$

$$\mathbf{x}_a^{n+1} = 2\mathbf{x}_a^* - \mathbf{x}_a^n \qquad (3.49)$$

Finally, the pressure is calculated from density using $P_a^{n+1} = f(\rho_a^{n+1})$.

Monaghan (1989) used this implementation to show that the SPH method conserves both linear and angular momentum. In practice, they use the midpoint value of the previous time step instead of computing the value at instant n, which saves time and creates only a small error. The overall scheme is in the second order.

Sympletic scheme

Symplectic time integration algorithms are time reversible in the absence of friction or viscous effects (Leimkuhler et al., 1996). It is also often known as the kick-drift-kick scheme where the kick is the velocity changing according to the force and drift is the coordinate changing with the initial velocity. Symplectic methods preserve geometric features, such as the energy time-reversal symmetry, which are present in the equations of motion, leading to improved resolution of long term solution behaviour. The scheme used for WCSPH in DualSPHysics is an explicit symplectic scheme with accuracy up to $O(\Delta t^2)$.

In this case, first, the values of acceleration and density are calculated at the middle of the time step as:

$$\mathbf{r}_a^* = \mathbf{r}_a^n + \frac{\Delta t}{2}\frac{\mathrm{d}\mathbf{r}_a^n}{\mathrm{d}t}; \; \rho_a^* = \rho_a^n + \frac{\Delta t}{2}\frac{\mathrm{d}\rho_a^n}{\mathrm{d}t} \tag{3.50}$$

where the superscript denotes time step and $t = n\Delta t$. In the second stage $d(V_a\rho_a\mathbf{v}_a)^*/dt$ gives the velocity and hence position of the particles at the end of the time step.

$$(V_a\rho_a\mathbf{v}_a)^{n+1} = (V_a\rho_a\mathbf{v}_a)^* + \frac{\Delta t}{2}\frac{\mathrm{d}(V_a\rho_a\mathbf{v}_a)^*}{\mathrm{d}t} \tag{3.51}$$

$$\mathbf{r}_a^{n+1} = \mathbf{r}_a^* + \frac{\Delta t}{2}\mathbf{v}_a^{n+1} \tag{3.52}$$

At the end of the timestep $\mathrm{d}\rho_a^{n+1}/\mathrm{d}t$ is calculated using the updated values of $\mathbf{v}_a^{n+1}$ and $\mathbf{r}_a^{n+1}$ (Monaghan, 2005). The DualSPHysics code provides an option in selecting the sympletic algorithm for simulation and this is based purely on the computational cost.

3.2.5 Time step constraints

In general, the choice of the time step can be based on three limitations which are i) Courant-Friedrichs-Lewy (CFL) condition, ii) condition on the viscous condition (Shao and Lo, 2003) and iii) condition on the inter-particle forces per unit mass. All these three time-step constraints were also adopted by Lee et al. (2008) in the truly incompressible SPH (ISPH) method. However, only the first two conditions are considered to determine the time step in ISPH in this study as the third condition is actually limiting the distance between particles (Morris et al., 1997). The size of the time step must be controlled in order to generate stable and accurate results. The Courant-Friedrichs-Lewy (CFL) condition must be satisfied and written as

$$\Delta t_{CFL} \leq \sigma \frac{h}{u_{ref}} \tag{3.53}$$

where, σ is a constant, (set as 0.2 or 0.1) which ensures that the particle moves only a fraction of the particle spacing per time step; h is the smoothing length, which is proportional to the initial particle spacing dx; u_{ref} is the maximum fluid velocity in the computation. For WCSPH in DualSPHysics, time step constraint is different depending on the condition in the domain along the simulations (Cummins and Rudman, 1999). Therefore, a variable time step is indeed employed. After several tests runs, it has come to our understanding that time step is mainly influenced by either the viscous force or the inter-particle force. The viscous force restriction,

essentially based on particle velocity due to high speed of sound is given by the equation (3.54). Larger value of coefficient of sound would reduce the overall time step.

$$\Delta t_v \leq \min_a \frac{h}{c + \max_b \left| \frac{h\mathbf{u}_{ab} \cdot \mathbf{r}_{ab}}{\mathbf{r}_{ab}^2} \right|} \tag{3.54}$$

Moreover, neighbouring particles that move closer to each other is prevented by controlling forces using the time step given by equation (3.55) where f_a is the internal or external force. The values of times step that meet these two criteria are computed and the smallest one is used for the time step value.

$$\Delta t_f \leq \min_a \sqrt{\frac{h}{|f_a|}} \tag{3.55}$$

3.3 SPH flowchart
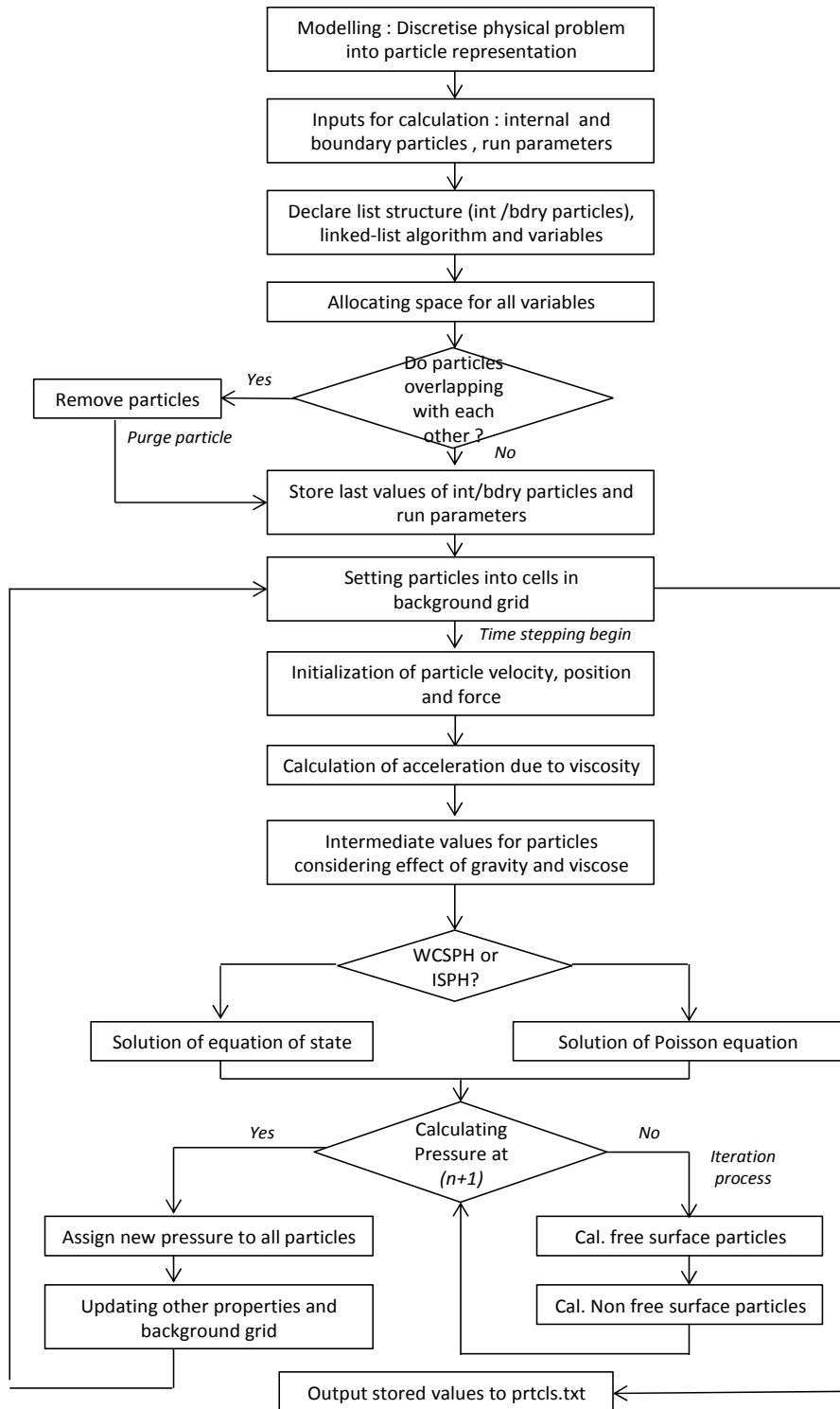
Figure 3-4 Flowchart

Chapter 4

Modelling of free surface wave with SPH (ISPH and WCSPH)

In this chapter, the issues of standard SPH formulation in the prediction of the free surface wave simulation are discussed. Sources of problems are identified along with the improvements and modifications proposed in the incompressible SPH (ISPH) model to incorporate the wave propagation model. Each modification comes with different approaches and their effects on the free surface simulation is further studied in comparison with the prediction from potential flow theory. Moreover, the open source code of DualSPHysics which employs the weakly compressible SPH (WCSPH) method is adopted for similar applications to assess the feasibility of larger 3-D simulations to be undertaken later.

4.1 Introduction

In the standard SPH formulation, SPH is known to perform inaccurately for the prediction of free surface waves particularly in maintaining a good profile of regular waves in wave propagation (Chen et al., 1999; Monaghan, 2000; Antuono et al., 2011). The reason behind this poor behaviour is the kernel summation of fundamental SPH formulation. Due to the deficiency of the integral domain and inconsistency of particle distribution near the free surface boundary, the summation of the kernel is not fully supported, which increases the effect of kernel interpolation errors to the computed results (Swegle et al., 1995; Xu et al., 2009; Lind et al., 2012).

Looking back at equation (3.1) and equation (3.5), two approximation errors are indirectly introduced in the first and last step of the approximation approach (Hu et al., 2014). The first step which is shown by equation (3.1) is called the filtering or smoothing approximation where the error is introduced in the approximation which is called the smoothing error. The second step in equation (3.2) is integration by parts and kernel function is assumed to be zero at the edge of the support domain. Equation (3.5) which calculates integral by the summation over all particles in the support domain introduces the second error in the approximation i.e. integration error. Therefore, errors accumulated by this approximation processes are evitable throughout the simulation. It is worth to mention that the outcomes and behaviour of the SPH simulation are directly determined by the properties of these two approximation errors. In order to minimise these errors, researchers have been looking into various modifications, boundary treatments and additional terms to improve the performance of SPH particularly in the prediction of the free surface. These have been explained in details in the literature review. Therefore, based on some ideas from other works, this chapter summarised the effect of ISPH modifications from available literature in simulating propagating waves. List of modifications and their abbreviations are shown in Table 4.1. The same reference will be used in all results and graphs in this chapter. Then, results from incompressible SPH (ISPH) and weakly compressible SPH (WCSPH) by DualSPHysics are compared through the validation with potential flow theory.

Table 4-1 Different models of modifications

Model	Modifications with characteristic features
ISPH-C	Collision model technique and arc method
ISPH-CS	ISPH-C with particle shifting technique
ISPH-R	ISPH-CS with kernel renormalization
ISPH-RD	ISPH-R with artificial viscosity on the free surface
Flow	Solution based on potential flow
FlowD	Solution based on potential flow with increased depth

4.2 Simulation based on the ISPH

4.2.1 Numerical wave tank setup

In this study, simulations are carried out using a 2-D model intended to test suitable approaches to employ in the WSI. At the same time, initial insight into domain size, damping zones and particle refinements can be obtained. Regular waves with 2 conditions of wave heights are simulated using the ISPH method. The wave conditions employed in the simulation are listed in Table 4.2. The original $x = 0$ and $y = 0$ are located at the still water surface at the left side of the numerical wave tank (NWT). The initial still water depth is $d = 0.6$ m. The rectangular tank used is 6 m long with a piston wave maker located at $x = 0.5$ m. The fluid density ρ is 998 kg/m³, the kinematic viscosity v is 10^{-6} m²/s¹. Approximately 17,812 particles are used in the simulations with initial particle spacing dx of 0.015 m.

For most wave generation in SPH, setting up a suitable wave maker is important to keep the generated wave profile accurate in comparison to the analytical solution. A complete study of the wave maker principles was published by Biesel and Suquet (1954). One of the main features of the principle is on how to select a suitable mechanism for generating deep water waves. A good wave maker is supposed to follow as closely as possible the particle motion in the progressive wave to be generated, and for deep water waves, the particle motion decreases exponentially downwards from the surface. The layout of bottom, right and wave maker boundaries is shown in Fig.4.1. In this model, the solid boundaries are simulated by two layers of boundary wall particles similar to the fluid particles. These boundary particles balance the pressure of inner fluid particles and prevent any fluid particles from penetrating the wall. The physical properties of all the boundary particles, except velocity and position, evolve with time, but for moving boundaries, such as the piston, the velocities and the positions/strokes are updated independently by solving the sinusoidal motion for the boundary. Two methods have been implemented in this work to generate a wave profile. The first one is to assign analytical fluid particle trajectories in waves as a function of time to layers of fluid particles located on the left side of the tank; which interact with neighbour particles as a result of pressure. However, this method showed inconsistency in almost all preliminary runs and so the second method is considered as an alternative which is to model the motion of a piston-type wavemaker in the simulations.

Piston-type wave maker which is modelled as moving boundary is placed on the left side of the NWT. Based on the linearized wavemaker theory by Dean and Dalrymple (1991), the piston motion is described as

$$u = \frac{S}{2} \omega \cos(\omega t) \tag{4.1}$$

where u is the piston velocity; S is the stroke of the wavemaker; and ω is the wavemaker frequency. The stroke of the wavemaker S relates to the wave height as follows,

$$\frac{H}{S} = \frac{2(cosh2k_nd - 1)}{sinh2k_nd + 2k_nd} \tag{4.2}$$

d is the water depth and; k_n is the wave number defined as

$$k_n = 2\pi/l \tag{4.3}$$

The angular wave frequency in equation (4.3) relates to the wavenumber as follows,

$$\omega^2 = gk_n \cdot \tanh(k_nd) \tag{4.4}$$
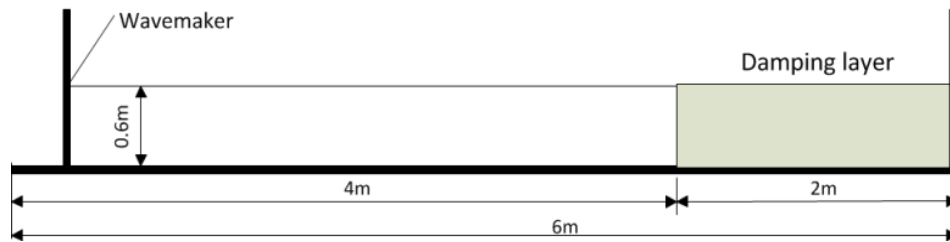
Figure 4-1 Numerical tank setup for wave generation

Table 4-2 Conditions for wave propagation case.

H (m)	T (t)	λ(m)	k_n	ω(rad/s)
0.05	0.995	1.5	4.189	6.369
0.10	1.569	3.0	2.095	4.180
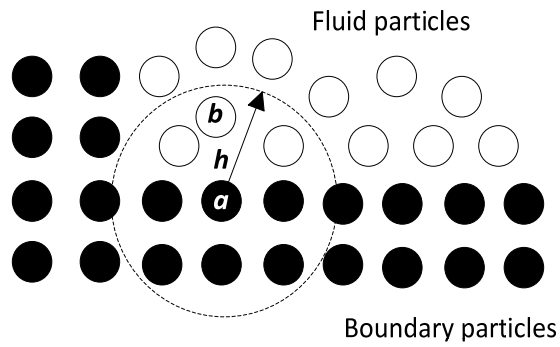
Figure 4-2 Boundary and fluid particles layout

4.2.2 Artificial absorbing layer

In order to absorb the waves that reach the right end of the NWT to reduce reflection, two absorbing methods are implemented in this study. The first method uses an exponential sponge layer or damping zone, which is placed at a distance of at least a wavelength from the wave maker. For the fluid particles in the damping zone, the velocity is re-calculated as follows

$$U' = Uf(\mathbf{x}) \tag{4.5}$$

where and U' is the recalculated fluid velocity, and

$$f(\mathbf{x}) = 1 - e^{(-\alpha(L-\mathbf{x}))} \tag{4.6}$$

α is an coefficient, equal to 2, x are the coordinates of the free surface points and L is the wave tank length. When the particles are getting close to the right end of the wave tank, the velocity U will decrease to zero.

However, because the recalculation is applied numerically to the velocity at every time step, it has been observed in the simulation that this approach does not reduce the reflection of the wave from the right end effectively. As for an alternative method, propagating wave is damp physically in the damping layer by modifying the momentum equation as

$$\frac{D\mathbf{v}}{Dt} = g + \frac{1}{\rho}\nabla \cdot \tau - \frac{1}{\rho}\nabla P - \gamma\mathbf{v} \tag{4.7}$$

rewriting the formula in the predictor step in predictor-corrector-scheme,

$$\mathbf{v}^* = g\Delta t + \frac{1}{\rho}\nabla \cdot \tau\Delta t + (1 - \gamma\Delta t)\mathbf{v}^n \tag{4.8}$$

where γ may be selected as

$$\gamma = \beta_d e^{(-2.0(L-\mathbf{x}))} \tag{4.9}$$

which is an exponential damping or alternatively using a polynomial damping

$$\gamma = \alpha_d\omega(\frac{\mathbf{x} - \mathbf{x_0}}{L})^2 \qquad \mathbf{x} \geq \mathbf{x_0} \tag{4.10}$$

where β_d and α_d are the coefficients determined by pre-test run, ω is the circular frequency of the wave and $\mathbf{x_0}$ is the damping zone starting point. The sensitivity of both artificial coefficients in both exponential and polynomial damping is compared in Fig.4.3.
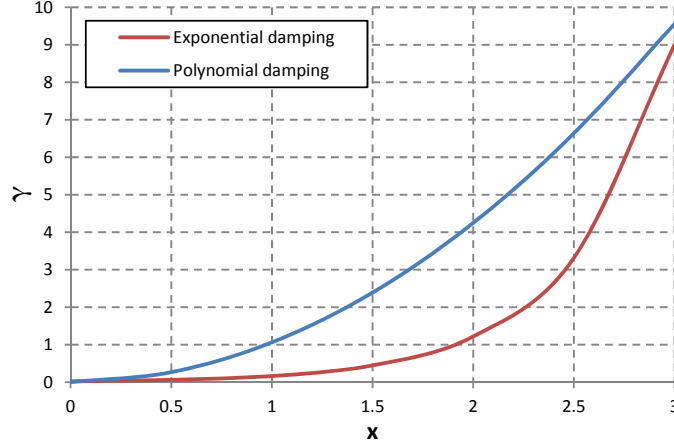
Figure 4-3 Profile of exponential damping and polynomial damping used for wave absorption. $\beta_d = 9; \alpha_d = 1.5$.

It is shown in Fig.4.3 that when particles move into the damping area, the velocity will be forced to damp with the additional term on the right-hand side of equation (4.5). Exponential form damps the velocity gradually compared to polynomial form. However, in order to effectively reduce the reflection of the wave from the right end and damp the incoming waves in the least time possible, the polynomial form is implemented in this study.

4.2.3 Identification of free surface particles

In ISPH, free surface particles are tracked down to set their pressure to zero to simplify the dynamic surface boundary conditions. The following quantity is calculated to identify the free surface particles without kernel correction.

$$\nabla \cdot \mathbf{r}_a = \sum_b \frac{m_b}{\rho_b} \mathbf{r}_{ab} \cdot \omega'_{ab} e_{ab} \tag{4.11}$$

This value equals 2 in 2-D cases or 3 in 3-D cases when the smoothing domain is not truncated. It is far below these values for surface particles and the criterion used is 1.6 in 2-D cases. However, this approach cannot locate the free surface accurately. The problem is that internal fluid particles may have values of $\nabla \cdot \mathbf{r}$ smaller than the criterion, while some other particles may have larger values. This misidentification of free-surface boundary introduces errors with noisy results on the free surface. In order to overcome this problem, a new fast and accurate boundary recognition method called the 'arc' method is applied (Koh et al., 2012). The principle of the arc method is to check if any arc of the circle (with radius R) around a centre particle is not covered by any circle

of its neighbours. If so, the centre particle is treated as a free surface particle. In other words, if the overall covered arc is beyond (0,2π) without gaps, the particle is identified as an inner fluid particle; otherwise it is treated as a free surface particle.
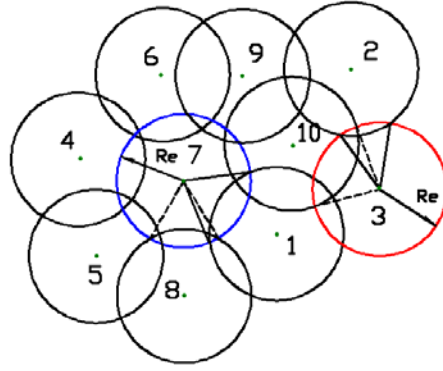
Figure 4-4 Arc method.

Table 4-3 Arc method (Wu et al., 2014).

Particle 3		Particle 7	
Neighbouring Particle	Covered arc （clockwise）	Neighbouring Particle	Covered arc （clockwise）
1	(0, 0.367π)	1	(0, 0.417 π)
10	(0.228 π, 0.706 π)	8	(0.367 π, 0.711 π)
2	(0.617 π, 0.861 π)	5	(0.644 π, 0.989 π)
		4	(0.906 π, 1.311 π)
		6	(1.278 π, 1.678 π)
		9	(1.561 π, 1.844 π)
		10	(1.756 π, 2.11 π)
Overall covered arc： （0, 0.861 π）		Overall covered arc： （0, 2.11 π）	
Conclusion：Particle 3 is a free surface particle		Conclusion：Particle 7 is an inner particle	

Fig.4.5 shows a small part of the fluid domain of a propagating wave. Green colour particles represent free surface particles while the dark blue colour particles represent inner fluid particles. The criteria in standard SPH formulation identification are not enough to effectively distinguish between free surface and inner particles. A single line of green colour particles (free surface particles) confirms the ability of the arc method to identify only the outer layer of particles as free surface particles accurately.
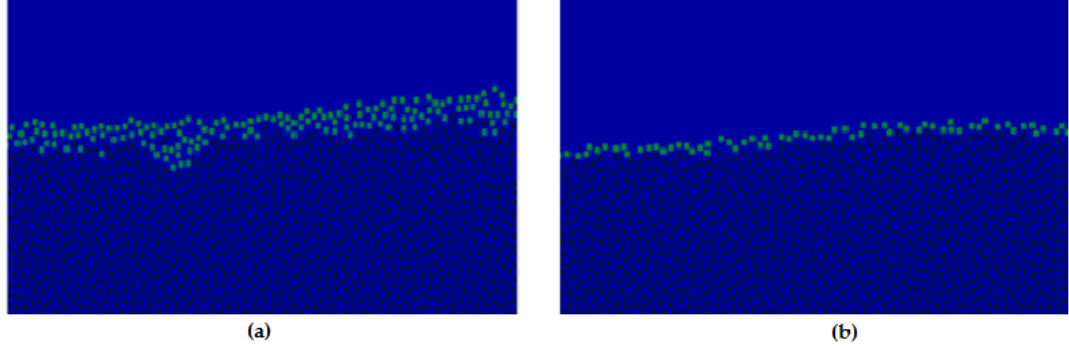
Figure 4-5 Different between 2 free surface identifications. (a) Standard SPH of free surface identification, (b) Arc method of free surface identification.

4.2.4 Incorporation of collision control (ISPH-C)

In order to prevent particles from hitting each other at high speed during simulation, collision control is introduced in SPH. The collision model was introduced by Lee et al., (2011) in the MPS method to simulate violent free-surface motions. On a free surface where pressure is fixed to zero, repulsive forces may not be effectively generated when particles accelerate and get close to each other in high velocity. As a result, free-surface particles may not be recognised and pressure can be suddenly increased. This could lead to numerical instability in the simulation. Therefore, the influence of collision model, enough to prevent collision between particles, is employed to better represent the proper repulsive forces near a free surface. As shown in Fig.4.6, OXY is the global coordinate system, and the coordinate with its origin in the centre of the particle is the local coordinate system. When the distance of two particles $< \beta_c dx$, then the collision model is applied as;

$$m\mathbf{v}_{ax} + m\mathbf{v}_{bx} = m\mathbf{v}'_{ax} + m\mathbf{v}'_{bx} \tag{4.12}$$

where m is the particle mass, $\mathbf{v}'_{ax} = -\alpha_c\mathbf{v}_{ax}$. α_c is the distance reduction coefficient while β_c is the collision boundary coefficient. Based on numerical tests, the optimal combinations are $\alpha_c =$ 0.0001, $\beta_c = 0.99$ (Lee et al., 2011; Sun et al., 2011). In collision control, β_c share similarities with von Neumann viscosity. The value must be set large enough to prevent unphysical penetration particularly for particles that are approaching each other at high velocity and almost head-on. However, value of α_c is kept to the minimum for flow with physical viscosity to avoid any spurious large shear viscosity.
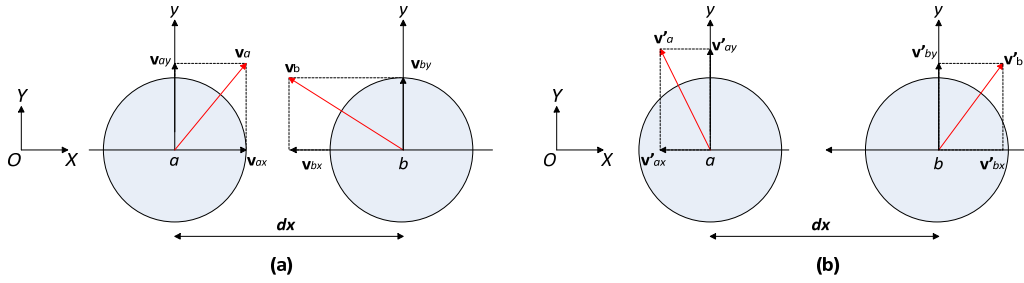
Figure 4-6 Collision model. (a) Before collision, (b) After collision.
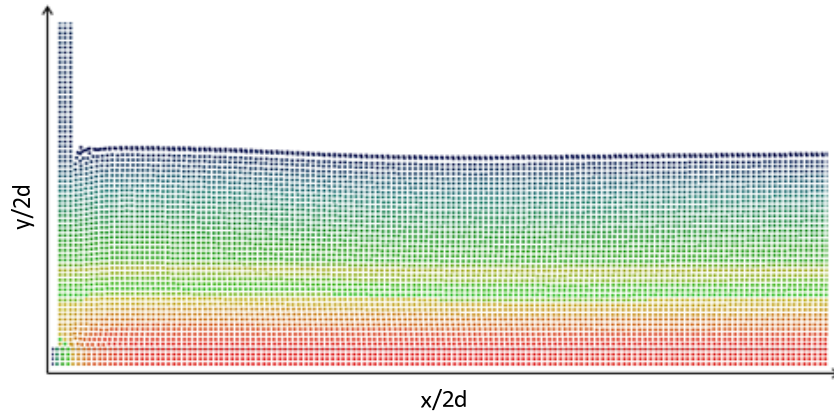
Figure 4-7 Pressure distribution of propagating wave in standard SPH formulation without collision model.

Fig.4.7 shows the pressure field of a fluid domain in NWT without the implementation of collision model technique. The simulation time is set to 10 seconds to reduce computational cost. The wave height and the wavelength of the simulated waves are 0.5 m and 1.5 m, respectively. Without the collision model, adjacent particles would collide with free surface particles at every time step, moving the particles far from their previous positions, stretching and reducing the interaction between particles. Even with the presence of artificial viscosity as a numerical stabiliser which usually solve the instability in dambreaking problem, breaking down of particle distributions in progressing wave problem particularly on the free surface after several time steps are inevitable. Therefore, a collision model is implemented in the simulation with a large enough effect to prevent numerical instability but small enough to avoid additional viscosity in the calculation. From Fig.4.8 to Fig.4.10, steady propagating waves can be observed while the damping layer absorbs the incoming waves effectively with a more stable pressure field and a lower velocity magnitude.
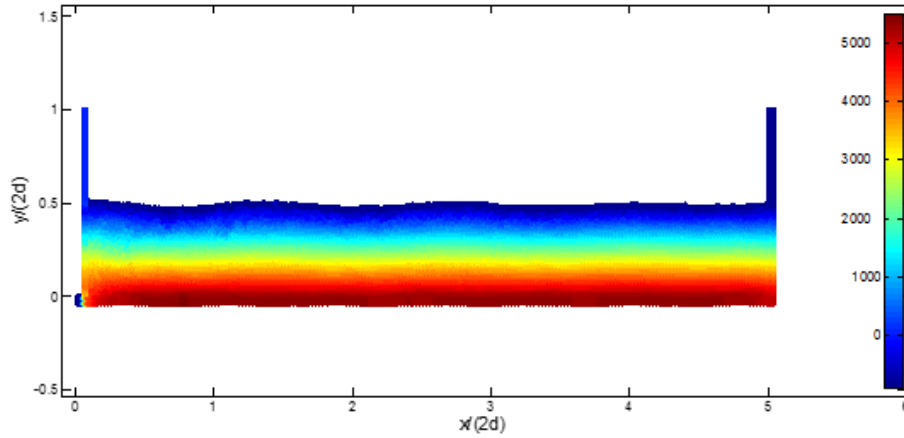
Figure 4-8 Corrected pressure field of simulation with a collision model.
$H = 0.05$ m; $\lambda = 1.5$ m; $t = 14.75$ s.
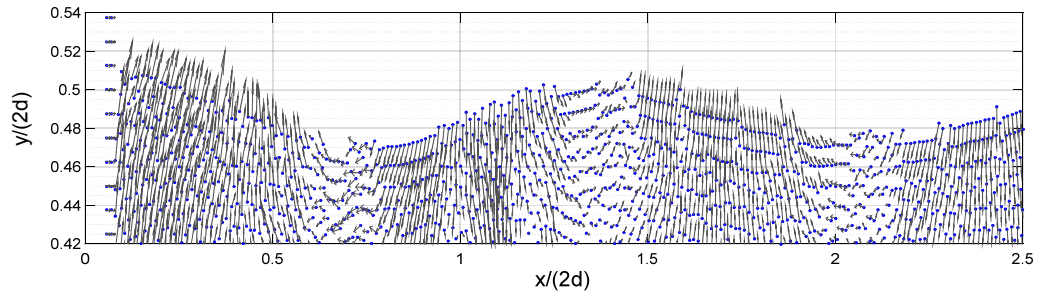
Figure 4-9 Velocity magnitude field at wave crest and wave trough of simulation with collision model. $H = 0.05$ m; $\lambda = 1.5$ m; $t = 14.75$ s.

The resulting velocity plotted in Fig.4.9 shows the behaviour of velocity values in vertical and horizontal direction. A higher value of velocity is demonstrated by the black colour of magnitude arrow. Fig.4.10 shows the comparison of time history at different locations for $H = 0.10$ m between original location of free surface particles with the free surface predicted by post-processing smoothing method. The MATLAB smoothing algorithm based on *moving average filter* is applied, using weights and a smoothing parameter to filter out the unphysical noise. The reason for employing the smoothing technique is to assign a lower weight to outlying particles in the free surface regression in order to obtain a smooth free surface without compromising the agreement between original and smoothed data. The original particle data and approximation data from the smoothing effect in Fig.4.10 are then used to plot Fig.4.9 at $t = 14.75$ s in space to preserve the consistency between data in both graphs. The smoothed data will be used later for other analysis in this thesis. From the graphs, the free surface is in stable condition with the application of collision control but overall not enough to maintain a good wave height.
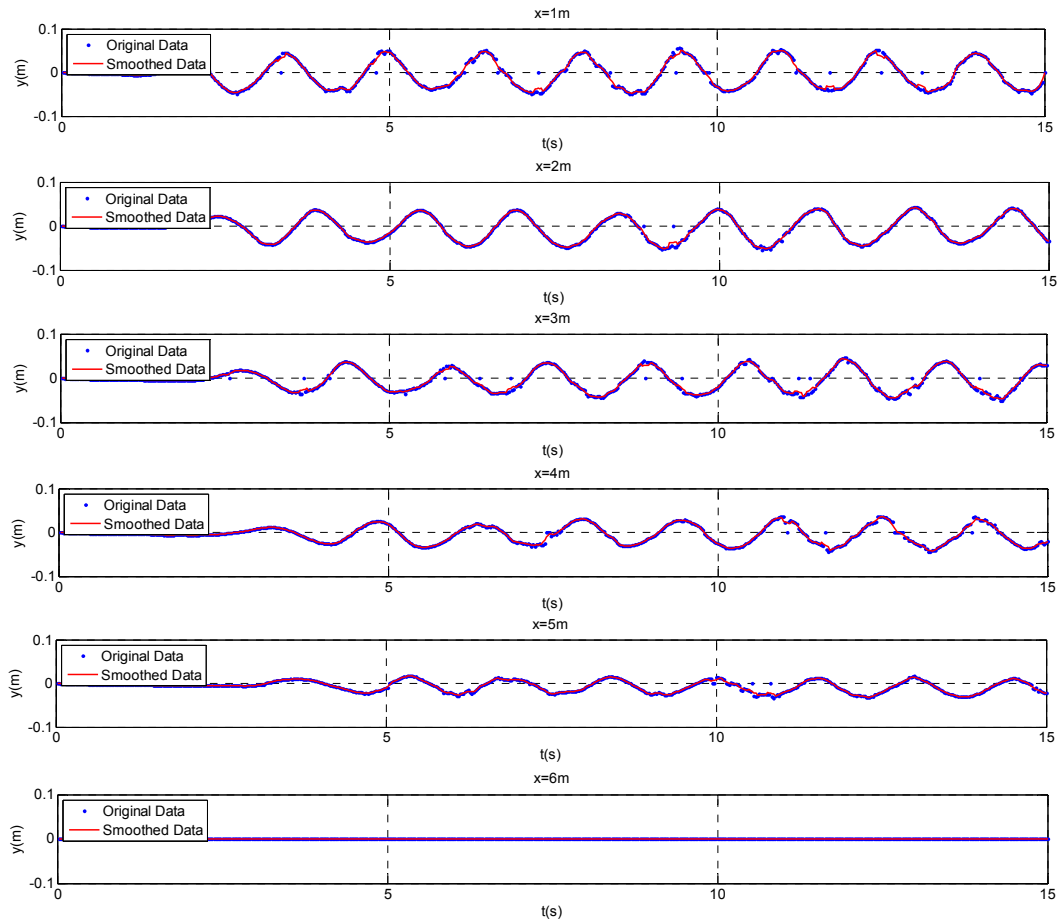
Figure 4-10 Comparing time history of wave surface at different locations between original and smoothed data. $H = 0.10$ m; $\lambda = 3.0$ m; $t = 14.75$ s.

4.2.5 Incorporation of particle shifting (ISPH-CS)

The particle clustering caused by the flow cannot be avoided when ISPH with divergence-free velocity field as introduced by Cummins and Rudman (1999) is employed. With the errors accumulated from the insufficient approximation by the kernel, instability will occur in the ISPH simulation. As mentioned before in section 4.1, in order to preserve consistency in the integration, uniform particle distribution is required and this can be achieved by the incorporation of a particle shifting technique.

This method was first introduced by Xu et al., (2009) where he proposed that particles are slightly shifted across streamlines in the fluid domain when particle distribution is distorted. This technique will prevent instability caused by the anisotropic particle spacing. The instability mentioned happens under certain conditions when there are stretch and compression between interacting particles. New hydrodynamic variables of each shifted particles are then computed at each time step. By applying the shifting method, the particle distribution is well maintained, though this approach violates the momentum conservation due to the interpolation of the hydrodynamic variables (Xu et al., 2009). In this method, particles are advanced according to the projection-based method, then they will be slightly shifted to a new position. Hydrodynamic variables for particles in the new position will be updated accordingly by the Taylor expansion series.

$$\phi_{a\prime} = \phi_a + (\nabla\phi)_a \cdot \delta\mathbf{r}_{aa\prime} + \vartheta(\delta r^2{}_{aa\prime}) \tag{4.13}$$

where, ϕ is a general variable; a and a' are the particle's old and updated positions respectively; $\delta\mathbf{r}_{aa\prime}$ is the distance vector between the updated and the old position after shifting takes place, also known as the amount of position shifting. Based on Xu Rui's works, simulation in this research will only be applied to the first two terms of the Taylor expansion series, giving an order consistent with the Laplacian operator.

The shifting approach is applied to particles inside the fluid domain where the amount of shifting calculated by equation (4.14) is added to the old position. Particle shifting magnitude α , in relation to the particle distance and the particle size, the amount of position shifting would be

$$\mathbf{r}_{a\prime} = \mathbf{r}_a + \delta\mathbf{r}_a \tag{4.14}$$

$$\delta\mathbf{r}_a = C\alpha_s\mathbf{R}_a \tag{4.15}$$

where, C is an empirical constant set as 0.01 to 0.1 and α_s is the shifting magnitude which is the product of $U_{max}dt$, with U_{max} being the maximum particle velocity, and dt the time step. At every time step, fluid particle that possesses the largest velocity value will be used as the value for U_{max}. Based on the results of a number of preliminary tests, value of 0.1 is selected for C so that it is large enough to prevent instability and small enough not to affect the original SPH scheme. In order to determine the shifting vector, $\mathbf{R}_a$, equation (4.16) is applied.

$$\mathbf{R}_a = \sum_{b=1}^{M_a} \frac{\bar{r}_a^2}{\mathbf{r}_{ab}^2} \mathbf{n}_{ab} \tag{4.16}$$

where $\mathbf{n}_{ab}$ is the unit distance vector between particle a and particle b and $\bar{r}_a$ reads,

$$\bar{r}_a = \frac{1}{M_a} \sum_{b=1}^{M_a} \mathbf{r}_{ab} \tag{4.17}$$

where, $\mathbf{r}_{ab}$ is the distance between particle a and particle b; $\bar{r}_a$ is the average particle spacing among the neighbourhood of particle a; M_a is the number of neighbouring particles around a particular particle a within the smoothing length h. Neighbouring particles are treated slightly differently for particle a if it is closer to the free surface. In this approach, only particles which have a smaller distance to the particle a than the distance of particle a to the free surface are considered. In other words, the smallest distance of particle a to the free surface particles will be assumed as the new radius replacing the smoothing length h and only particles within the new radius will be considered as particle a 's neighbouring particles. A simple diagram of this description is shown in Fig.4.11.
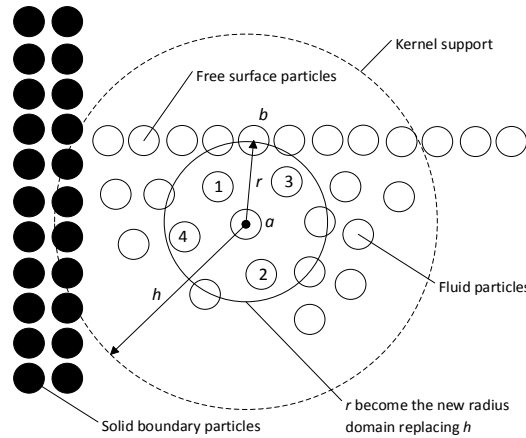
Figure 4-11 Illustration of particle shifting mechanism near the free surface.

R_a is evaluated on a fixed particle distribution obtained after the particle position is advanced in time as shown in equation (4.16) so it is not necessary for internal iteration for a converged particle position. Then, in the same time step, particles are slightly shifted into their new positions. The hydrodynamic variable e.g. velocity field is updated accordingly and calculation continues for the next time step. The shifting distance will always be much less than the smoothing length h. Other research that also implement similar shifting technique can be found in Antuono et al., (2011), Shadloo et al., (2012) , Vacondio et al., (2013) and Mokos (2014). The time history of free surface prediction at different locations for H = 0.10 m is shown in Fig.4.13. The simulation presents results from the combination of collision technique and particle shifting algorithm. Collision technique is only activated when particles are about to collide at high velocity so that it will not affect the original particle shifting scheme. The wave height displayed at x = 3 m is recorded at around 0.07 m, losing almost 30 % of the initial wave height. Then, along the way it starts to lose half of the wave height before completely damped by the damping layer. Although particle shifting manages to contribute to a better particle distribution, thus maintaining wave height better up to $x = 2$ m, the inner fluid particles still produce a viscous flow, forcing the waves to decay. The velocity magnitude shown in Fig.4.12 confirms a rapid decrease of particles velocity at $x = 1$ to 2 m where the waves start to decay. The horizontal velocity and vertical velocity under the wave crest and trough are demonstrated in Fig.4.18 and Fig.4.19. When the particles form a significant height of propagating wave at the crest, fluid particles will move with large horizontal velocities and smaller vertical velocities. Then, when the wave moves, the fluid particles have negative horizontal velocities and the vertical velocities are nearly zero under the trough. This behaviour is consistent with an analytical solution but because of the excessive wave decaying, this approach needs improvements to eliminate additional viscosity for better simulation of propagating waves.
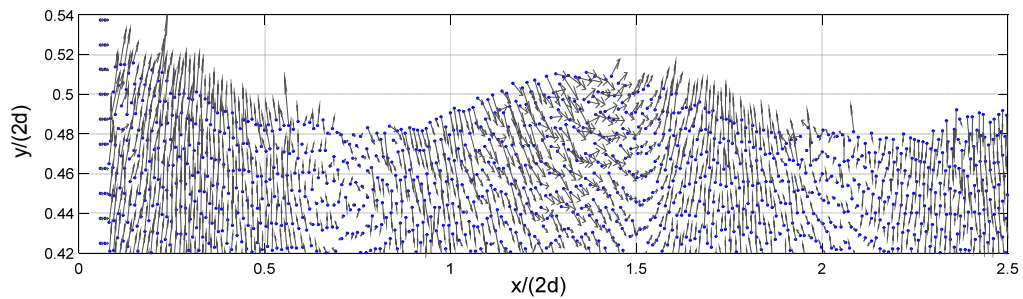
Figure 4-12 Velocity magnitude field of ISPH-CS at wave crest and wave trough. $H = 0.05$ **m**; $\lambda = 1.5$ m; $t = 14.75$ s.
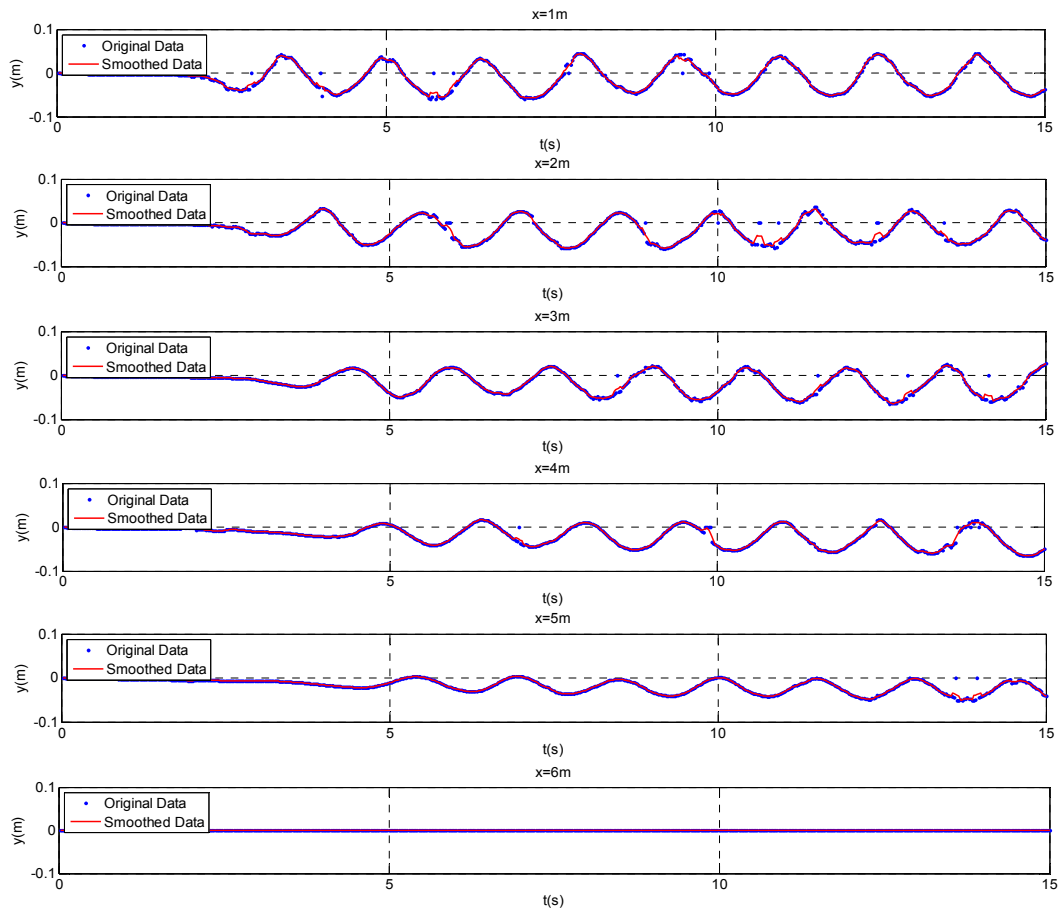
Figure 4-13 Time history of wave surface at different locations. $H = 0.10$ m; $\lambda = 3.0$ m; $t = 14.75$ s.

4.2.6 Incorporation of kernel renormalization (ISPH-R)

Although particle shifting may preserve a uniformity in a particle distribution, Oger et al. (2007) showed that the basic kernel gradient and divergence calculation of the standard ISPH may lead to errors due to the approximation procedures in the discrete form. The discretized convolution approximations are insufficient for obtaining accurate pressure and velocity fields. The approximations do not yield such high accuracy though the kernel gradient systematically results in $O(h^2)$ convergence Oger et al. (2007). Fewer neighbouring points used to reduce the computational cost in the kernel limit the information from neighbouring particles to be exploited fully by the kernel support. Thus, a kernel correction term known as renormalization is applied in addition to a *collision* and *particle shifting* method to fulfil the higher order accuracy of convergence (Vila, 1999; Khayyer et al., 2008). The expression for the kernel normalisation is

$$\nabla_a W_{ab} = \mathbf{L}(\mathbf{r}) \cdot \nabla_a \omega_{ab} \tag{4.18}$$

where

$$\mathbf{L}(\mathbf{r}) = \begin{pmatrix} \sum \dfrac{m_b}{\rho_b}(x_b - x)\dfrac{\partial \omega_{ab}}{\partial x} & \sum \dfrac{m_b}{\rho_b}(x_b - x)\dfrac{\partial \omega_{ab}}{\partial y} \\ \sum \dfrac{m_b}{\rho_b}(y_b - y)\dfrac{\partial \omega_{ab}}{\partial x} & \sum \dfrac{m_b}{\rho_b}(y_b - y)\dfrac{\partial \omega_{ab}}{\partial y} \end{pmatrix}^{-1} \tag{4.19}$$

This operator is used to normalise the kernel first derivative, both in gradient and divergence calculation as in equation (3.19) and equation (3.30). However, this technique is not applied to the pressure term in Poisson equation due to its complexity.
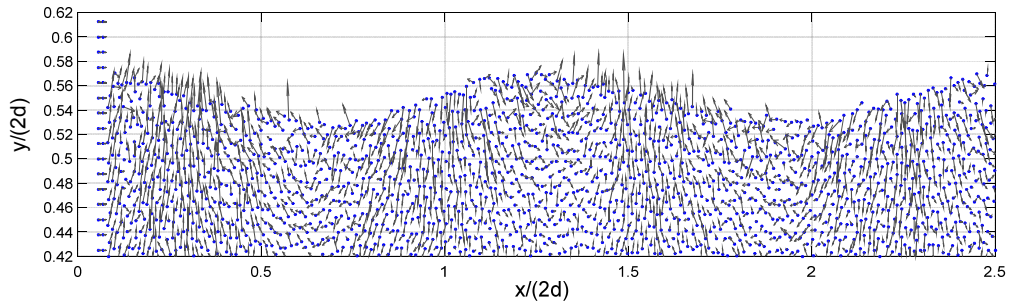
Figure 4-14 Velocity magnitude field of ISPH-R at wave crest and wave trough. $H = 0.05$ m; $\lambda = 1.5$ m; $t = 14.75$ s.
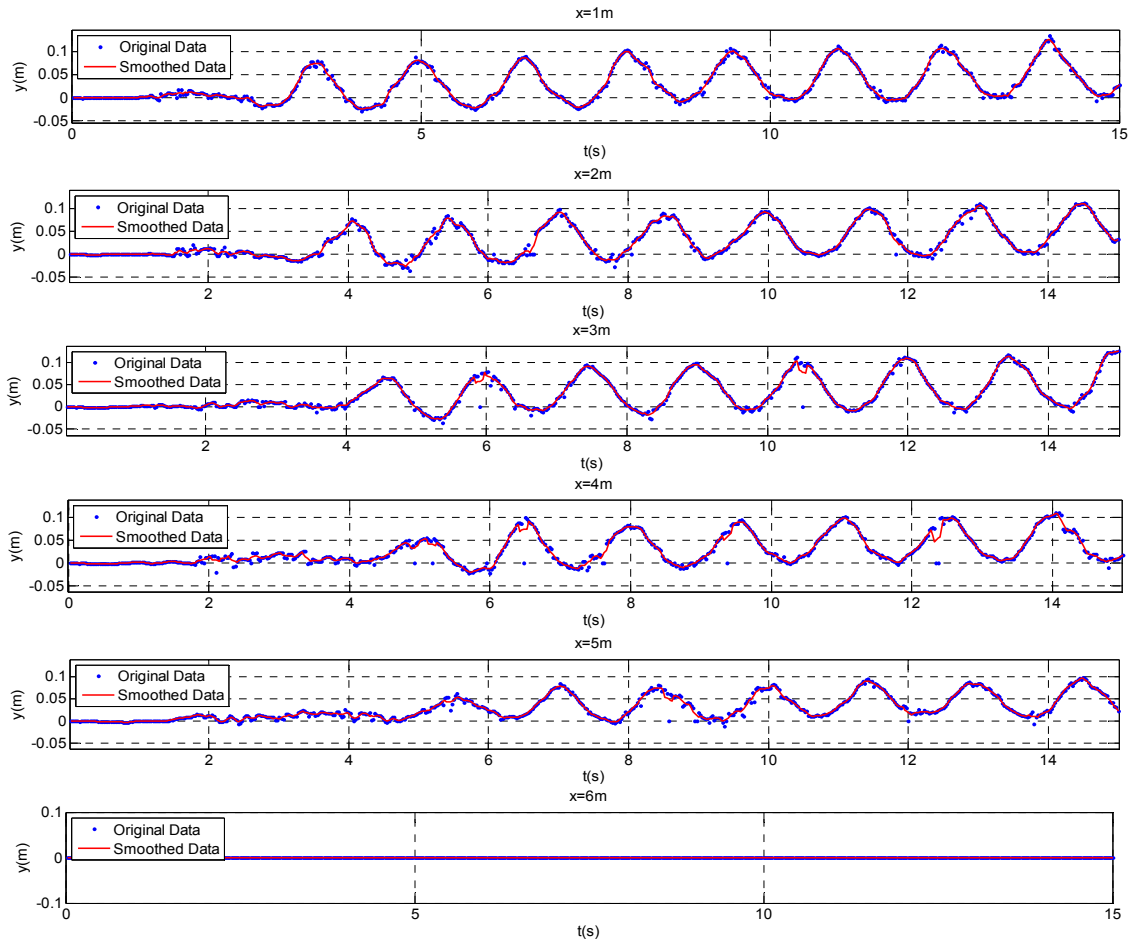
Figure 4-15 Time history of wave surface at different locations. $H = \mathbf{0.10}$ m; $\lambda = 3.0$ m; $t = 14.75$ s.

In Fig.4.15, the mean depth of the fluid domain seems to rise from time to time at every location and only settles at the origin depth when the waves reach the damping zone. The reason is due to the noisy free surface where free surface particles are incapable of maintaining their stable position even in hydrostatic conditions. Even with the occurrence of instability on the free surface, this modification is observed to be more reliable in maintaining the wave propagation with some nonlinear behaviour in some wave crests and wave troughs. Fig.4.16 and Fig.4.17 show comparisons of free surface predictions from all modified methods of ISPH with the potential flow at $t = 14.75$ s for two different wave heights, $H = 0.05$ m and $H = 0.10$ m, respectively. A simplified notation is used in the graphs to denote the methods for the results and further details of the improvements involved for each result can be found in Table 4.1. It can be observed that for smaller wave heights, waves are noticeably non-sinusoidal when using collision model and the shifting model. Overall, both methods do not agree well with the prediction from potential theory and have lost almost 50% of the wave height half way through the numerical tank. Similar trend is also observed in the case of relatively larger wave height. Prediction from potential flow with increased depth is introduced to obtain insight on the behaviour of prediction from higher order model and surprisingly a good agreement between these two predictions is obtained. This explained that the higher order scheme somehow slightly affecting the interaction between particle spacing particularly on the free surface. It also suggests that accumulated errors at each time step are not small leading to an increased distance from the initial depth. Ideas about suppressing the free surface instability and preventing noisy free surface will be explained later in chapter 4.2.7 which may compromise the accuracy of the simulation.

Particle velocity and pressure distributions for both wave heights are demonstrated in Fig.4.18 and Fig.4.19. Pressure distributions agree well with potential theory for both cases with nearly zero vertical velocity values under the wave trough. However, discrepancies are recorded for almost all points under the wave crest in all modification models, particularly in comparatively larger wave heights. The behaviour of this discrepancies can be related back to velocity magnitudes of free surface particles which can be observed fluctuating in random directions in Fig.4.14. This explains why some particles of horizontal velocities are observed to have large velocities despite being located away from free surface particles. With instability on the free surface, the approximation of pressure and velocity affects the distribution of inner fluid particles which makes it difficult to track the correct location of particles under the wave crest and the wave trough.
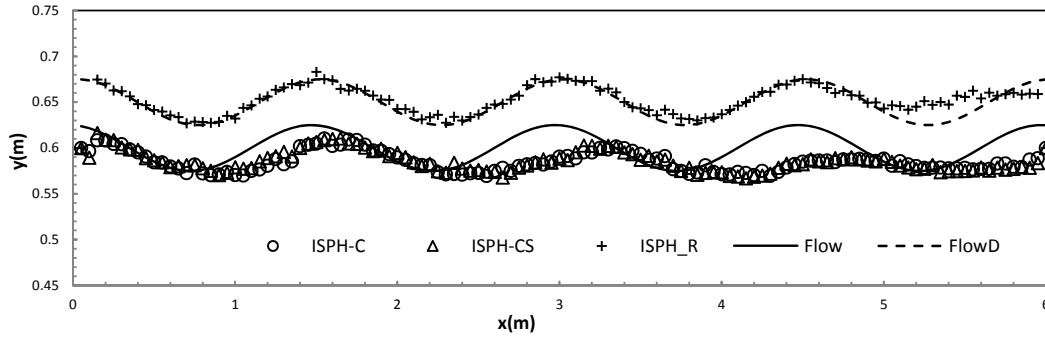
Figure 4-16 Comparison of free surface predictions between ISPH-C, ISPH-CS and ISPH-R. $H = 0.05 \text{ m}; \lambda = 1.5 \text{ m}; t = 14.75 \text{ s}.$
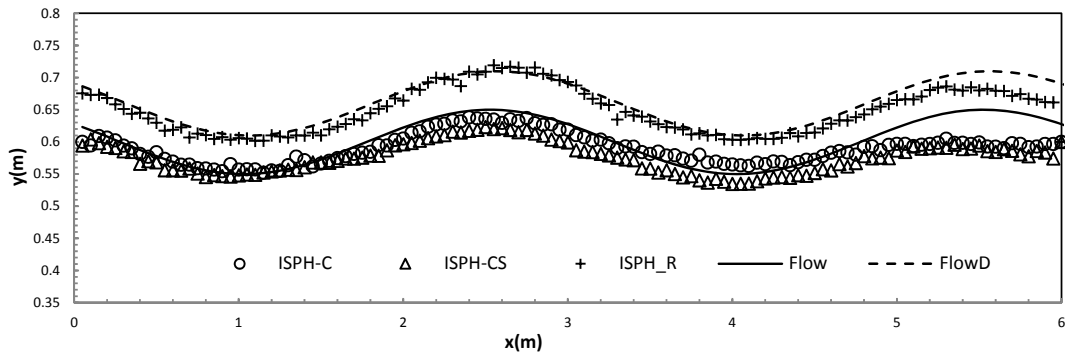
Figure 4-17 Comparison of free surface predictions between ISPH-C, ISPH-CS and ISPH-R. $H = 0.10 \text{ m}; \lambda = 3.0 \text{ m}; t = 14.75 \text{ s}.$
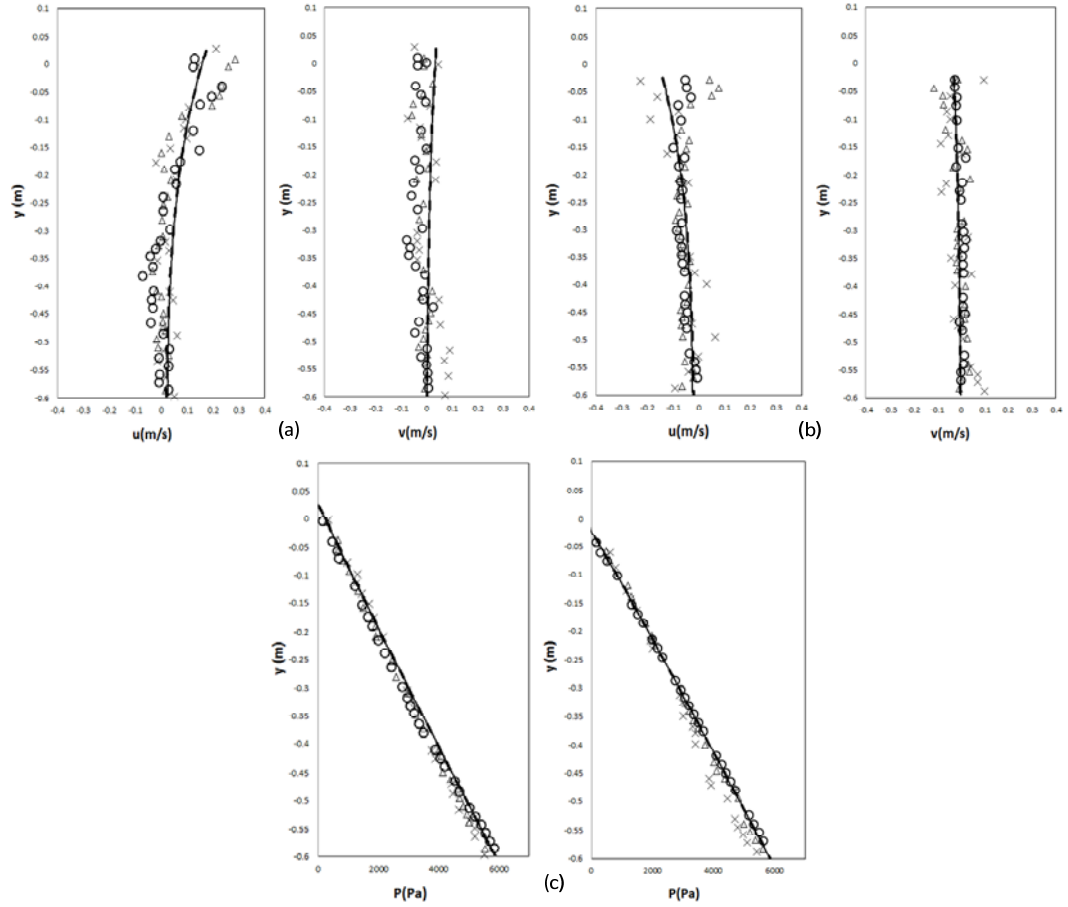
Figure 4-18 Comparison of velocity and pressure predictions between collision model, particle shifting and higher order convergence. (a)(b)Horizontal and vertical velocity profiles under wave crest and trough; (c) Pressure distribution under wave crest and trough. Wave height $\boldsymbol{H} = \boldsymbol{0.05}$ **m**; wave length $\lambda = 1.5$ m; water depth $d = 0.6$ m; $t = 14.75$ s; tank length $L = 6.0$ m.○ : prediction from ISPH-C; Δ : prediction from ISPH_CS; × : prediction from ISPH-R; $-$: prediction from Flow; $--$: prediction from potential FlowD.
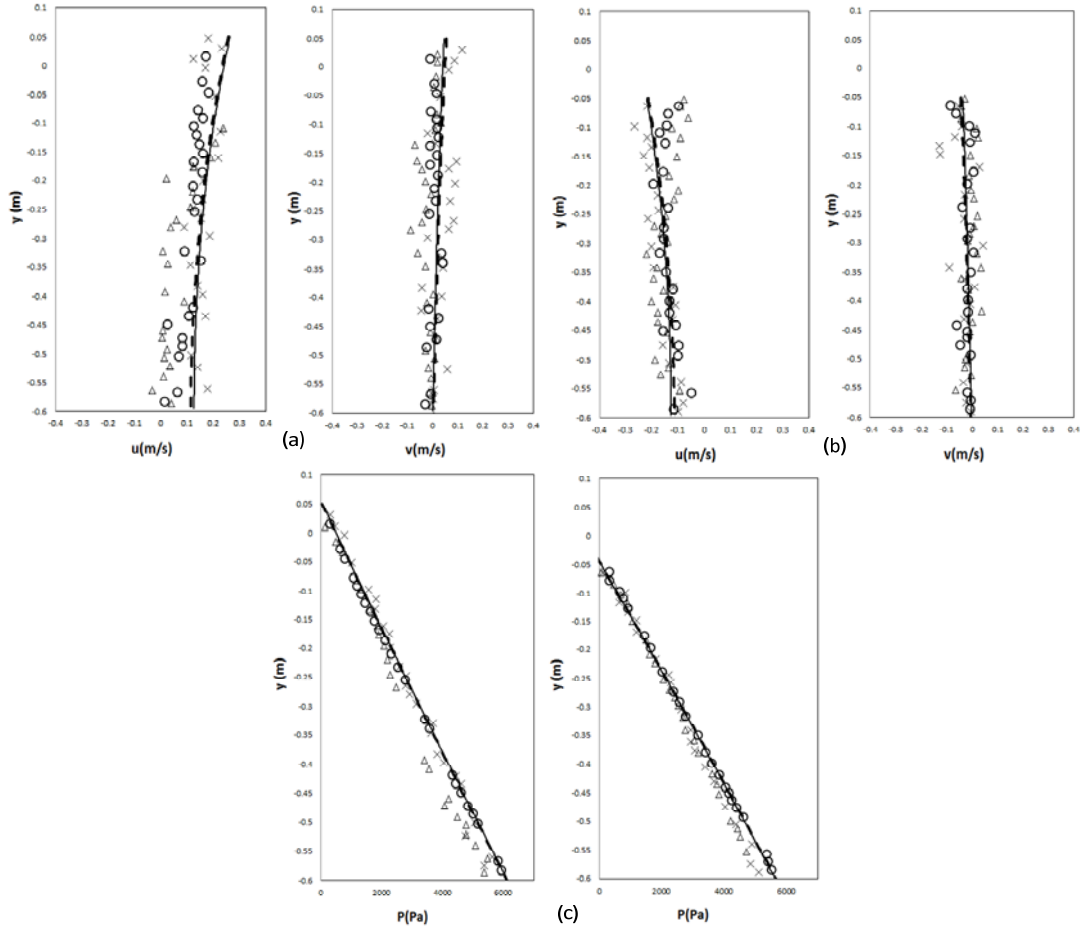
Figure 4-19 Comparison of velocity and pressure predictions between collision model, particle shifting and higher order convergence. (a)(b)Horizontal and vertical velocity profiles under wave crest and trough; (c) Pressure distribution under wave crest and trough. Wave height $H = 0.10$ m; wave length $\lambda = 3.0$ m; water depth $d = 0.6$ m; $t = 14.75$ s; tank length $L = 6.0$ m.∘ : prediction from ISPH-C; $\triangle$: prediction from ISPH-CS; × : prediction from ISPH-R; − : prediction from Flow; − − : prediction from FlowD.

4.2.7 Free-surface damping (ISPH-RD)

According to Xu Rui (2009), the deficiency and noise on the free surface can be smoothed by artificially increasing the viscosity around free surface particles and particles adjacent to the free surface without strongly influencing the free surface predictions. This is important to prevent excessive instability on the free surface. This numerical treatment is called free-surface damping which is determined by the following equation,

$$v_d = \frac{u_{max}dx}{Pe_{max}} \tag{4.20}$$

where Pe_{max} is the global maximum Peclet number; u_{max} is the global maximum velocity estimated as $\sqrt{2gH}$ and dx is the initial particle spacing. The values of viscosity v_d from equation (4.20) corresponding to different Peclet numbers are listed in Table 4.4 and it is noted that these viscosity v_d values are higher than initial kinematic viscosity $v = 10^{-6}$ m^2/s.

Table 4-4 Relation between global Peclet number and free surface viscosity

Pe_{max}	v_d
7	7.35714e-3
30	1.71667e-3
50	1.03000e-3
70	7.35714e-4
100	5.15000e-4
120	4.29167e-4
150	3.43333e-4

It has been shown through numerical experiments (Xu et al., 2009) that the Peclet number value should be in the range $7 \le Pe_{max} \le 150$. This is to ensure that if the surface viscosity is too high, the artificial diffusion will influence the free-surface prediction, while values that are too low cannot provide enough artificial damping for the truncated-kernel error. Fig.4.20 and Fig.4.21 demonstrate the comparison of time history between higher order models that employ free surface damping with a previous higher order model in subchapter 4.2.6 without any free surface damping. In this simulation, Peclet numbers of *7, 30* and *150* are used for comparison after several preliminary runs. Two locations of x are selected, $x = 1$ m when the wave elevation receives a higher energy transmission from the paddle motion and at $x = 4$ m when the wave starts to move into the damping layer. The instabilities on the free surface are well suppressed particularly in

comparatively large wave height but with little significant improvements in the velocity and pressure distribution for both wave heights shown in Fig.4.22 and Fig.4.23.

x = 1 m

x = 4 m
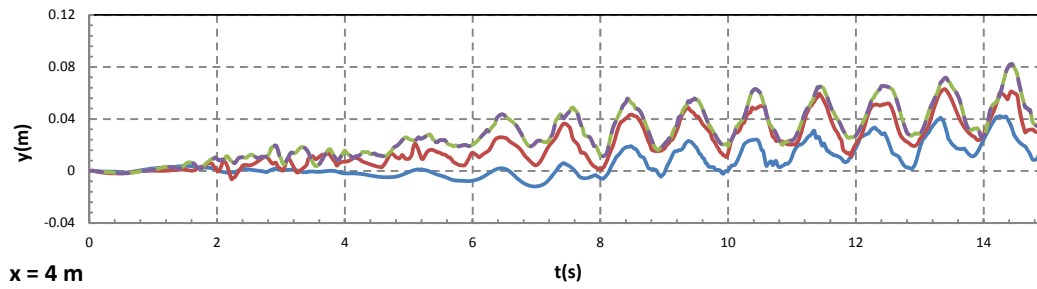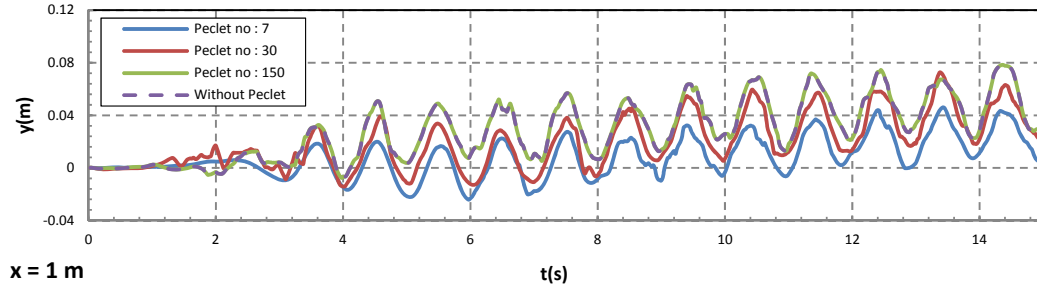
Figure 4-20 Comparing time history of wave surface at different locations. Wave height $H = 0.05$ m; wave length $\lambda = 1.5$ m; water depth $d = 0.6$ m; $t = 14.75$ s ; tank length $L = 6.0$ m.

x = 1 m

x = 4 m
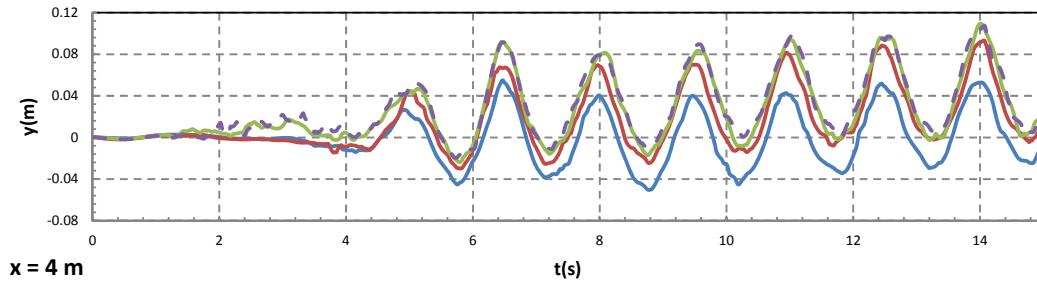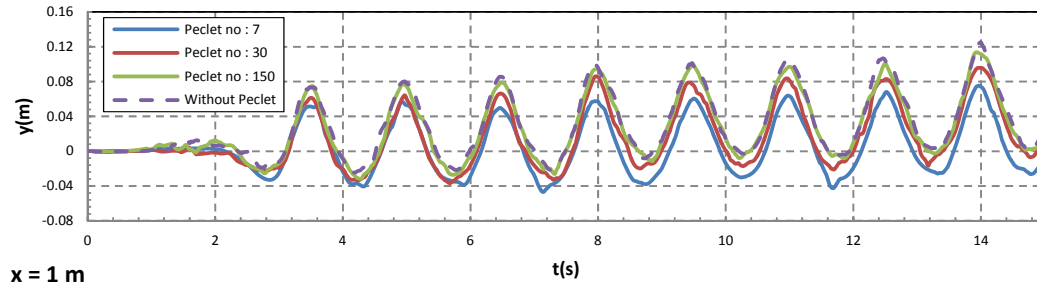
Figure 4-21 Comparing time history of wave surface at different locations. Wave height $H = 0.10$ m; wave length $\lambda = 3.0$ m; water depth $d = 0.6$ m; $t = 14.75$ s; tank length $L = 6.0$ m.
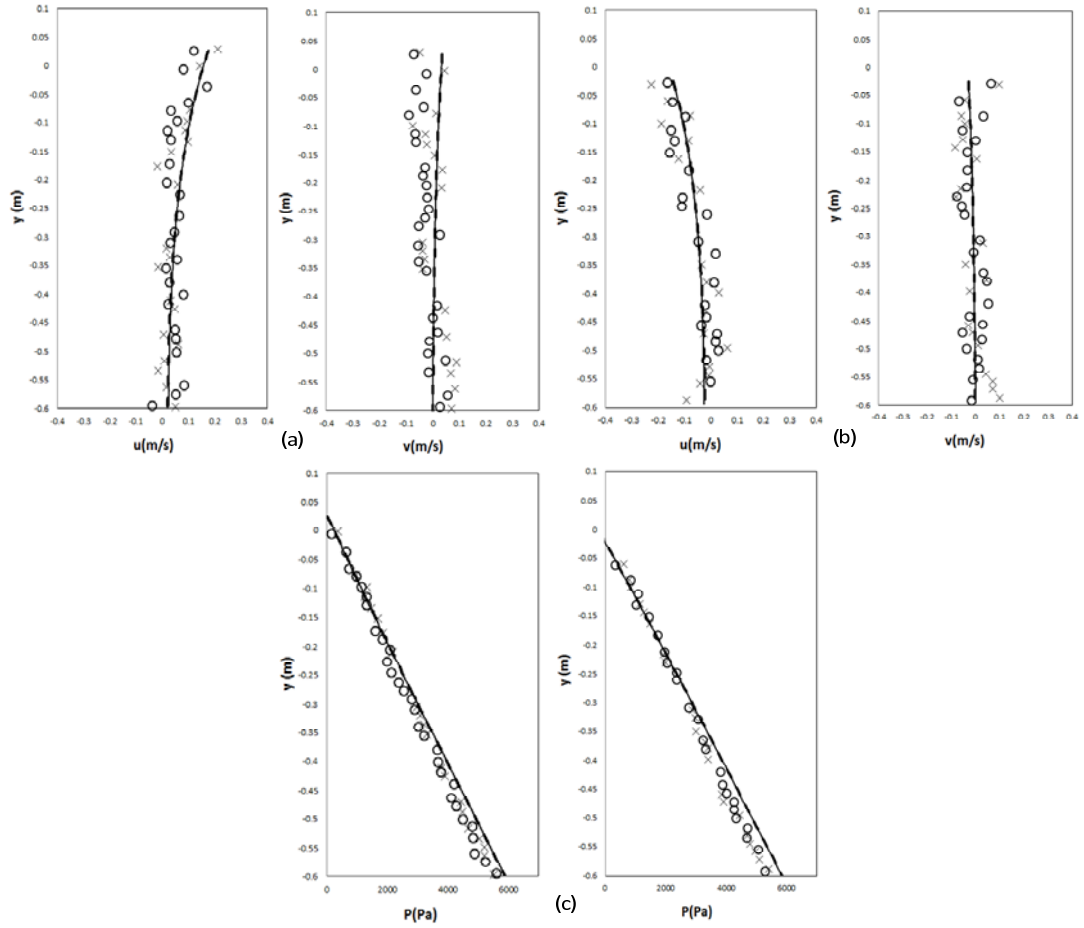
Figure 4-22 Comparing velocity and pressure predictions. Wave height $H = 0.05$ m; wave length $\lambda = 1.5$ m; water depth $d = 0.6$ m; $t = 14.75$ s; tank length $L = 6.0$ m. ∘ : prediction from ISPH-RD with $Pe_{max} = 30.0$; × : prediction from ISPH-R; − : prediction from Flow; − − : prediction from FlowD.
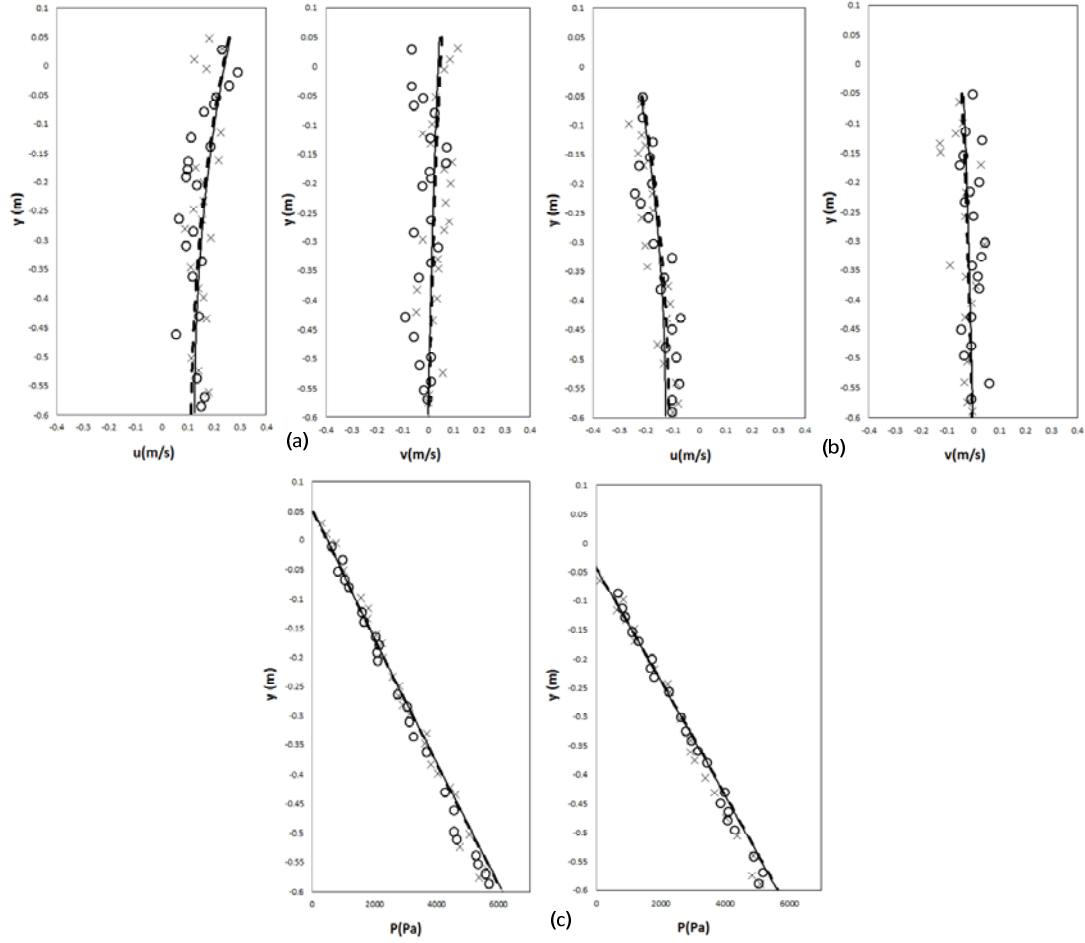
Figure 4-23 Comparing velocity and pressure predictions. Wave height $H = 0.10$ m; wave length $\lambda = 3.0$ m; water depth $d = 0.6$ m; $t = 14.75$ s; tank length $L = 6.0$ m. ∘ : prediction from ISPH-RD with $Pe_{max} = 30.0$; × : prediction ISPH-R; − : prediction from Flow; − − : prediction from FlowD.

4.2.8 Convergence analysis

In order to investigate the numerical stability in ISPH, convergence studies have been carried out in this section. Propagating waves need ample time to build up and to be steady. Therefore, the simulation runtime has been set to be 60 seconds for all cases. There are two factors that could influence the stability of propagating wave, namely particle spacing and total runtime. The particle distribution is refined to smaller initial particle spacing and the simulation runtime is set longer. In theory, ISPH simulation should be able to maintain a stable propagating wave unless errors accumulated from pressure and velocity calculation within the longer runtime lead to numerical instability. The model used for ISPH in this test incorporate the collision, shifting and higher order scheme with free surface damping technique (ISPH-RD). In Table 4.5, smaller initial particle spacing with a larger number of internal particles will have a higher resolution of simulation. All cases are run for 60 seconds but finished the simulation at different times. A stable simulation would last for 60 seconds, while many simulations with numerical instability break down halfway through the simulation. It has been shown from the result that highest resolution when dx=0.010 m will compromise ISPH stability. That is to say, with a larger number of particles, computational cost increases and errors could accumulate during pressure calculation (Dominguez et al., 2014). A higher frequency with large amplitude could also cause instability in the simulation due to the asymmetrical nonlinear effect, both on the wave crest and wave trough. All simulations settle at a slightly higher mean depth and from that, are able to maintain sufficiently accurate wave height until they begin to experience numerical instability. Even for a stable case, the particle refinement is still not enough to maintain a good wave profile. Hence, it is clear that running the simulation longer would not help in gaining a steady wave height and to prevent the waves from decaying.

Table 4-5 Total runtimes of CPU performance for different cases for convergence studies

Case	Initial particle spacing, dx (m)	No of Internal Particles	H (m)
1	0.030	3980	0.05
2	0.015	15880	0.05
3	0.010	35580	0.05
4	0.030	3980	0.10
5	0.015	15880	0.10
6	0.010	35580	0.10
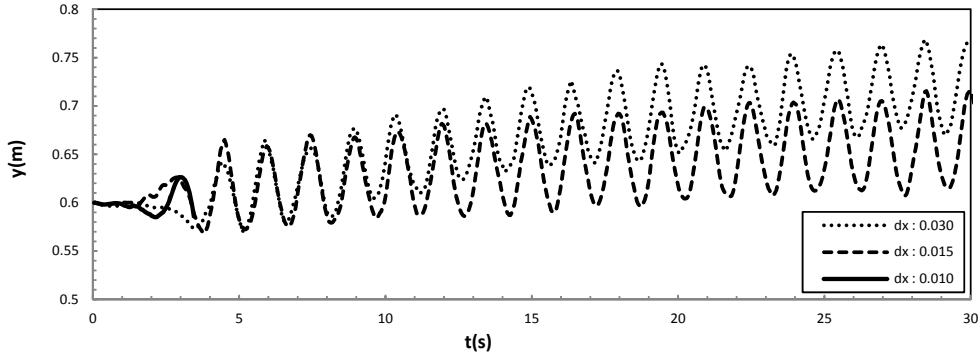
Figure 4-24 Comparison of free surface predictions. Wave height $H = 0.05$ m; wave length $\lambda = 1.5$ m; water depth $d = 0.6$ m; $t = 58.75$ s; tank length $L = 6.0$ m.

4.3 Simulation based on the WCSPH

In this section, the possible implementation of WCSPH is discussed. We have looked into a number of possibilities in modifying the standard ISPH formulation and all the works done had demonstrated some improvement in the free surface prediction. While all the modifications produced a satisfactory results, the inconsistency of estimation in velocity and pressure values, with chances of facing numerical instability in longer runtime still making ISPH model in this work a less reliable numerical tool for more complex hydrodynamic problems. In this work, additional algorithms are needed such as developing shifting particles according to Fick's law diffusion to be able to produce more accurate and stable free-surface profiles (Lind et al., 2012). From the perspective of computing technique, ISPH scheme should be modelled to execute through massively parallel processing which is not considered in this work. The interaction between large numbers of particles making ISPH run slowly compared to methods such as finite elements or finite volumes (Viccione at al., 2008). This will be time-consuming and computationally expensive. A large number of particles are needed to achieve sufficient accuracy and considering the possible complexities that we will face in the next 3-D cases with complex boundaries, an efficient algorithm with massively parallel computing resources is rather needed. Many engineering problems and applications in FSI has considered WCSPH as an alternative solution. Development on the Rieman solver (Monaghan, 1997; Molteni and Bilello, 2003; Varnousfaaderani and Ketabdari, 2014) or incorporating the delta-SPH (Crespo et al., 2015) so far has been proven to work well for WCSPH in producing accurate free-surface profiles. In order to overcome the limitations in free-surface profiles produced by ISPH-RD, research has been extended to examine how WCSPH performs in similar conditions. Hence, a free-surface fluid solver called DualSPHysics will be employed instead.

4.3.1 DualSPHysics open source software

DualSPHysics is a highly optimised code used for solving 2-D and 3-D Navier-Stokes equations using C++, OpenMP and CUDA for the simulation of potentially violent free-surface hydrodynamics. The code is based on WCSPH and can be modified to simulate various phenomena, including wave breaking, dam break flows, sloshing, floating objects, wave impact on a structure, multi-phase simulation (Mokos, 2014; Mokos et al., 2015) etc. In this section, the code is modified for wave generation problem to compare the results with ISPH done in section 4.2. Details of how WCSPH in DualSPHysics works can be found in Crespo et al., (2013, 2015). DualSPHysics incorporates a numerical diffusive term (Antuono et al., 2010; Antuono et al., 2011) which reduces the density fluctuations effectively. The version used in this study is 3.1. All simulations are run on graphics processing unit (GPU) that is 5 to 10 times faster than a single central processing unit (CPU) runs. GPU used in this study is GeForce GTX 970 and the specifications are provided in Table 4.6.

Table 4-6 Specifications of GeForce GTX 970 GPU card.

CUDA cores	1664
Base Clock (Mhz)	1050
Boost Clock (Mhz)	1178
Memory Clock	7.0 Gbps
Memory Interface	GDDR5
Memory Interface Width	256-bit
Memory Config	4 GB
Memory Bandwidth (GB/sec)	224
Bus Support	PCI Express 3.0
Max Digital Resolution	5120x3200

Figure 4-25 GTX 970 cards

4.3.2 Propagating free surface simulation

This study will use WCSPH formulation in order to simulate long non-breaking wave propagation. First, the structure and capabilities of the DualSPHysics code used are analysed. Propagating waves are absorbed by a numerical beach that is placed at the right end of the numerical tank as damping layer is not available in DualSPHysics. A similar wave maker is used to generate and propagate the waves. In this simulation, a sinusoidal movement is imposed on 2 layers of boundary particles which act like a piston. The computational setups, initial particle spacing and other parameters are set to be the same as the ISPH test cases in section 4.2.

The simulation is run by open source code and the results are obtained in binary files. The binary format is used to reduce the volume of the files and the time needed to generate them, allowing simulation with a high number of particles. The data from these binary files are then used as input to extract different physical quantities at a set of given points using the *MeasureTool.exe*. For example, in order to determine the position of the free surface, the numerical values are computed by means of a SPH interpolation of the values of the neighbouring particles around given points along the y-axis. At all these points a value of mass is computed and when this value of mass equals half the reference mass (0.4 in 2-D), that y position is assumed to be the free-surface position. Refinements with more points along the y-axis will result in more accurate free surface representation. The evolution of waves can be seen in Fig.4.26 and Fig.4.27 for wave height, $H = 0.05$ m and $H = 0.10$ m. The red contour shows the higher velocity values which propagate waves along the tank. Fig.4.28 and Fig.4.29 show the free surface predictions of WCSPH in comparison to ISPH method with different improvements for $H = 0.05$ m and $H = 0.10$ m. In both cases, WCSPH is able to maintain a stable propagating wave without the elevation of mean depth and numerical beach is observed to damp out all the incoming waves effectively. Overall, WCSPH agrees well with potential flow theory. The wave profiles of WCSPH can be observed to be in symmetrical indicating small influence of nonlinear effect. However, a slightly sharp wave peak and wave crest can be observed in the first 0.5 m and 1.0 m in Fig.4.28. This may be caused by the position of the moving piston. Horizontal movement of the piston pushes some of the particles nearby with large force at the initial stage before fluid particle redistribute themselves into a stable optimized particle distribution. Therefore, it is best to allow the fluid flow to initialise and become steady before the moving of the piston commences. A comparison of velocity and pressure under the wave crest and wave trough is made in Fig.4.30 and Fig.4.31. In general, results from DualSPHysics WCSPH show a good agreement with potential flow theory in both cases. Although in both cases the pressure values are slightly higher near the wave crest, the small

errors are assumed to be negligible and further investigation of how it affects the interaction between fluid-body will be conducted later.
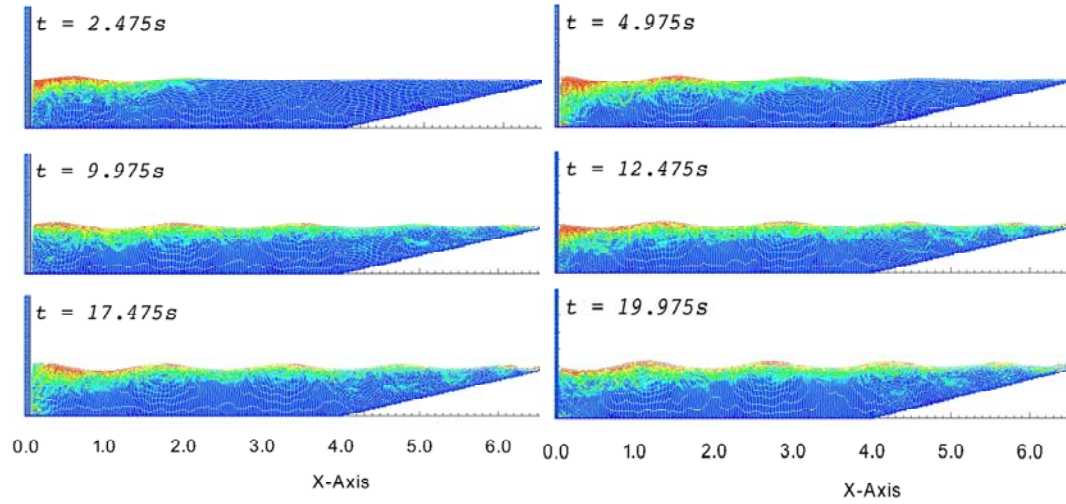
Figure 4-26 Kinematic distribution of WCSPH over time. Wave height $H = 0.05$ m; wave length $\lambda = 1.5$ m; water depth $d = 0.6$ m; tank length $L = 6.0$ m.

Figure 4-27 Kinematic distribution of WCSPH over time. Wave height $H = 0.10$ m; wave length $\lambda = 3.0$ m; water depth $d = 0.6$ m; tank length $L = 6.0$ m.
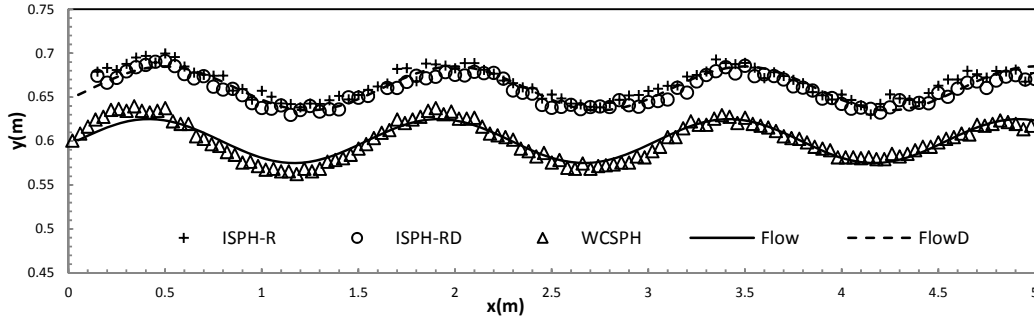
Figure 4-28 Comparison of free surface predictions between ISPH-R, ISPH-RD with $Pe_{max} = 30$ and WCSPH. Wave height $H = \mathbf{0.05\,m}$; wave length $\lambda = 1.5\,m$; water depth $d = 0.6\,m$; $t = 19.975$ s; tank length $L = 6.0$ m.
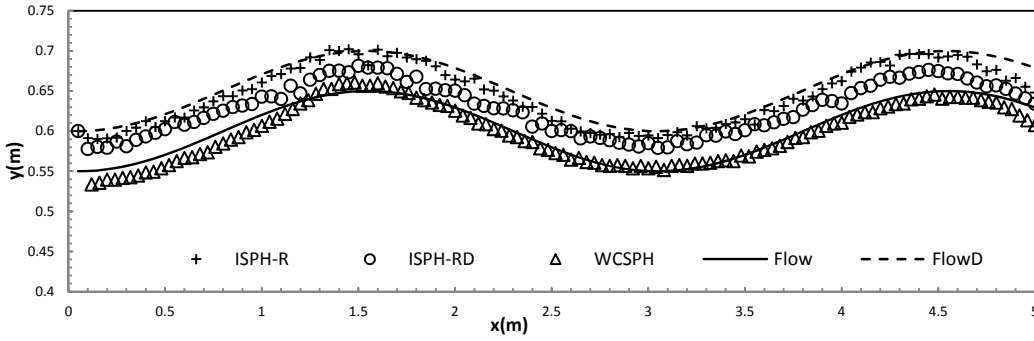
Figure 4-29 Comparison of free surface predictions between ISPH-R, ISPH-RD with $Pe_{max} = 30$ and WCSPH. Wave height $H = \mathbf{0.10\,m}$; wave length $\lambda = 3.0\,m$; water depth $d = 0.6\,m$; $t = 9.75$ s; tank length $L = 6.0$ m.
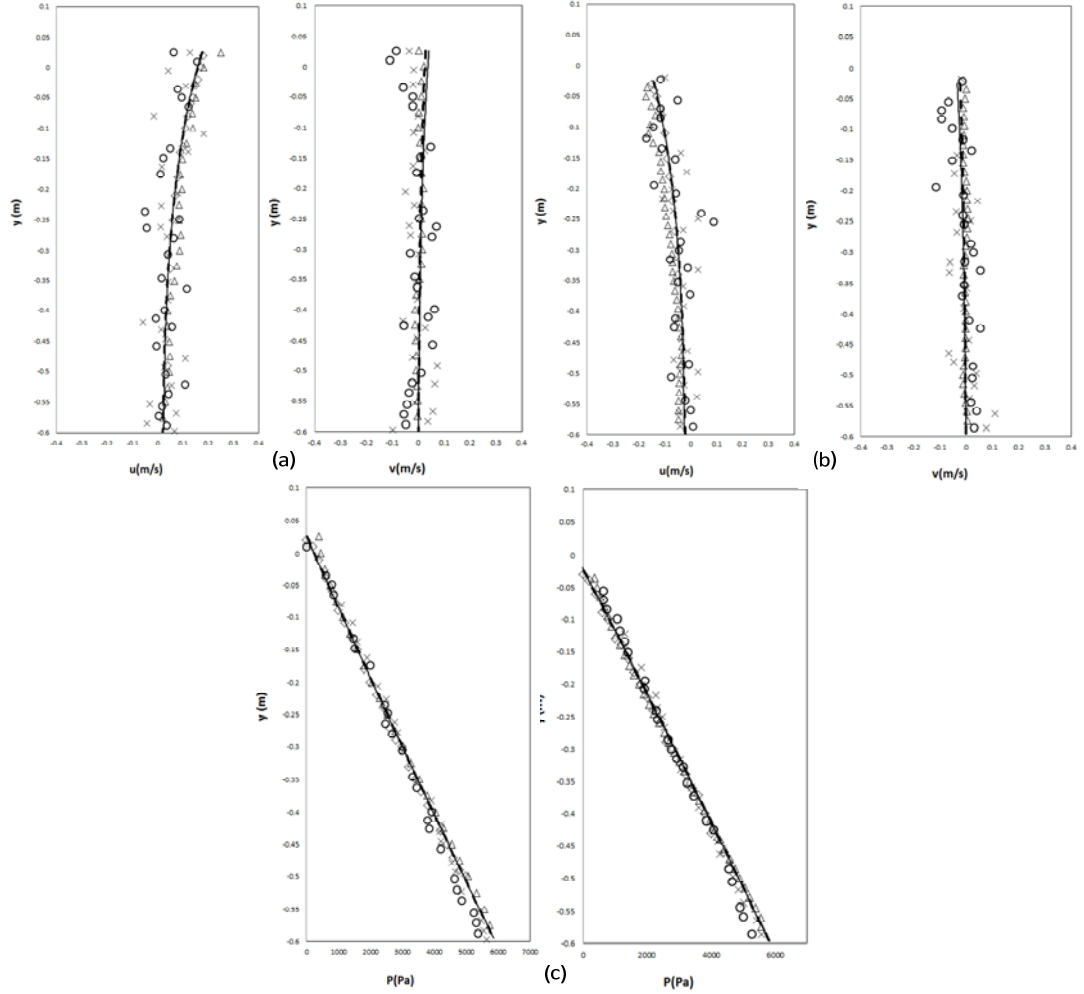
Figure 4-30 Comparing velocity and pressure predictions. Wave height $H = 0.05\text{m}$; wave length $\lambda = 1.5$ m; water depth $d = 0.6$ m; $t = 19.975$ s; tank length $L = 6.0$ m. ∘ : prediction from ISPH-RD with $Pe_{max} = 30.0$; × : prediction from ISPH-R; − : prediction from Flow; − − : prediction from FlowD; ∆ : prediction from WCSPH; ◇ : prediction from Xu Rui (2009).
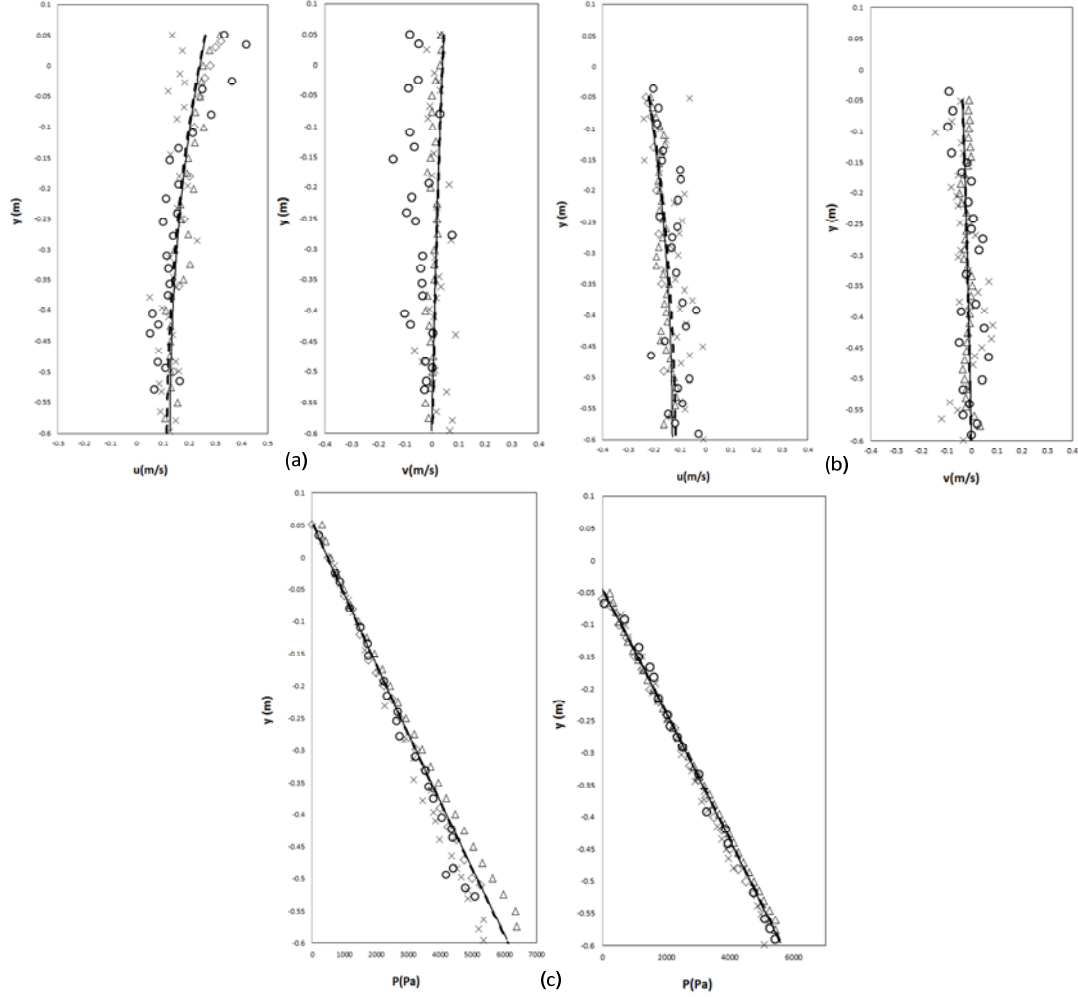
Figure 4-31 Comparing velocity and pressure predictions. Wave height $H = 0.10$ m; wave length $\lambda = 3.0$ m; water depth $d = 0.6$ m; $t = 9.75$ s; tank length $L = 6.0$ m. $\circ$: prediction from ISPH-RD with $Pe_{max} = 30.0$; $\times$: prediction from ISPH-R; $-$: prediction from Flow; $--$: prediction from FlowD; $\triangle$: prediction from WCSPH; $\diamond$: prediction from Xu Rui (2009).

4.3.3 Convergence analysis

For convergence studies, the same parameters as in section 4.2.8 are set and they are listed in Table 4.7. Smaller initial particle spacing indicates a larger number of internal particles and requires a much longer simulation run-time. dx = 0.010 m took 3 times longer to finish the simulation than dx = 0.015 m, which took only 8 minutes to complete. The reason behind this is the capability of the DualSPHysics code which is designed to run in a parallel environment, using 100% of CPU or GPU capacity. Three cases of different initial particle spacing are run with two different wave heights for 60 seconds and the results are shown in Fig.4.32 to Fig.4.35. Particle spacing of dx = 0.010 m and dx = 0.015 m show almost identical behaviour in terms of wave propagation at t = 58.75 s. The free-surface profiles are in good agreement with potential flow results. Particle spacing of dx = 0.030 m suffers from numerical errors in maintaining the wave height as error in the estimation of interpolation points accumulate within the time step due to an insufficient number of neighboring particles around free surface particles.

Fig.4.34 and Fig.4.35 show the comparison of the time history of free-surface at x = 3 m for different initial particle spacings. Due to the insufficient free surface prediction, the wave surface of dx = 0.030 m in longer run-times becomes numerically instable and waves experience a rapid damping particularly for H = 0.05 m. Particles on the free surface for H = 0.10 m also suffer from noisy prediction, leading to higher wave heights along the wave tank. Both dx = 0.015 m and dx = 0.010 m share a similar tendency for wave elevation, slightly rising from mean depth level starting from t = 30 s. This is probably caused by the length of the beach, which reflects back some of the incoming waves. In case with H = 0.10 m, it is observed that the waves are more symmetrical for dx = 0.015 m and maintain a steady wave height. In general, smaller particle spacing does result in more accurate results compromising a higher computational cost.

Table 4-7 Total runtimes of GPU performance for different cases for convergence studies

Case	Initial particle spacing, dx (m)	No of Internal Particles	H (m)	Runtime, simulation (s)	Runtime, real-time (s)
1	0.030	3309	0.05	60	489.68
2	0.015	13719	0.05	60	3500.12
3	0.010	31218	0.05	60	13109.18
4	0.030	3309	0.10	60	507.87
5	0.015	13719	0.10	60	3716.93
6	0.010	31218	0.10	60	11718.22
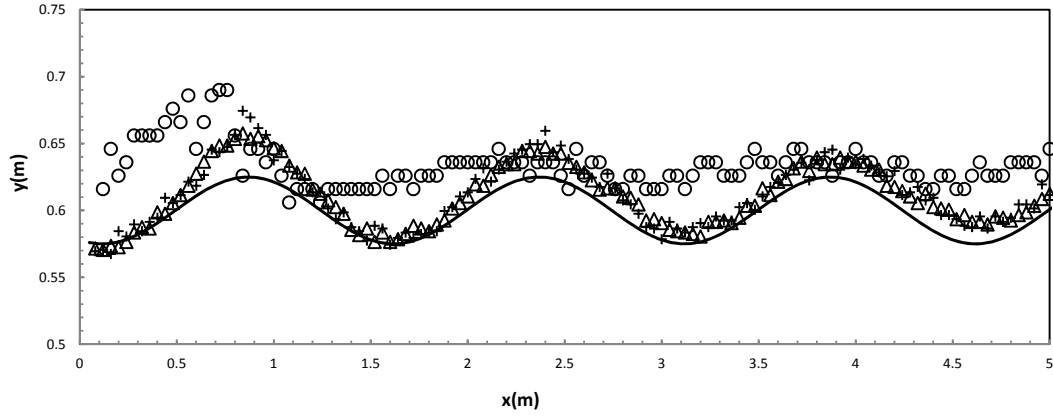
Figure 4-32 Comparison of free surface predictions. Wave height $H = \mathbf{0.05}$ **m**; wave length $\lambda = 1.5$ m; water depth $d = 0.6$ m; $t = 58.75$ s; tank length $L = 6.0$ m. $\circ$: dx of 0.030 m; $+$: dx of 0.015 m; Δ : dx of 0.010 m; $-$: prediction from Flow.
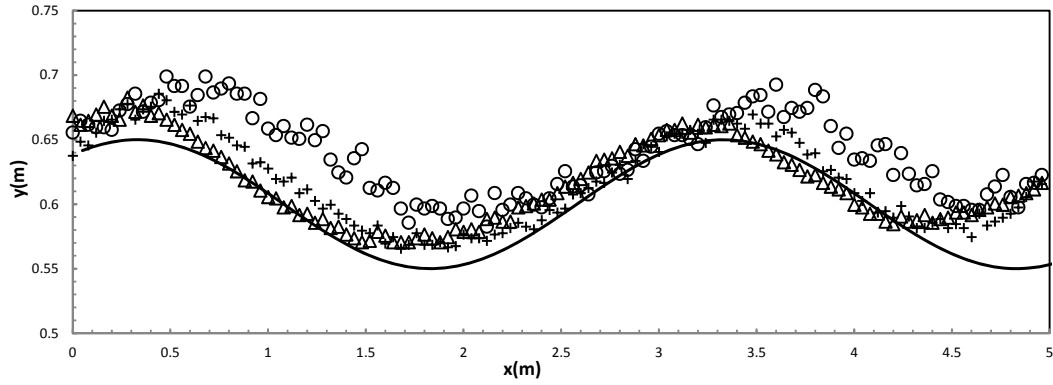
Figure 4-33 Comparison of free surface predictions. Wave height $H = \mathbf{0.10}$ **m**; wave length $\lambda = 3.0$ m; water depth $d = 0.6$ m; $t = 58.75$ s; tank length $L = 6.0$ m. $\circ$: dx of 0.030 m; $+$: dx of 0.015 m; Δ : dx of 0.010 m; $-$: prediction from Flow.
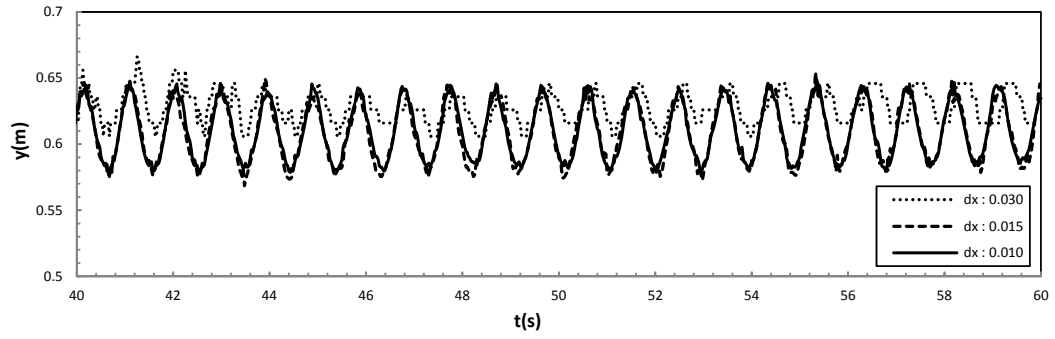
Figure 4-34 Comparing time history of free surface prediction. Wave height $H = 0.05$ m; wave length $\lambda = 1.5$ m; water depth $d = 0.6$ m; tank length $L = 6.0$ m.
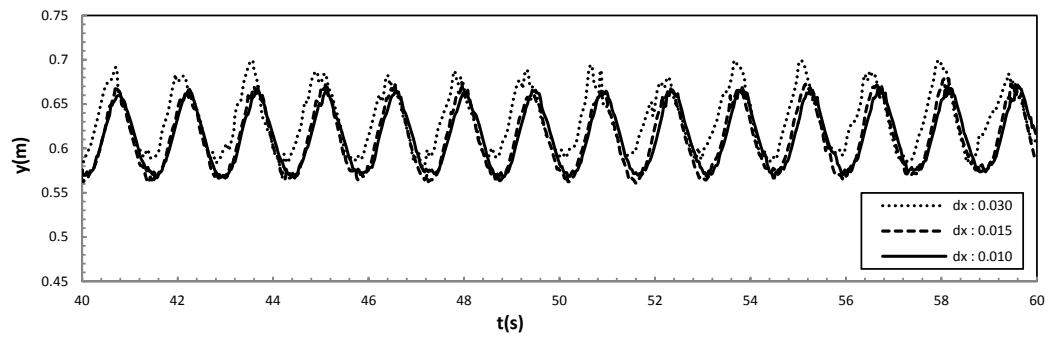
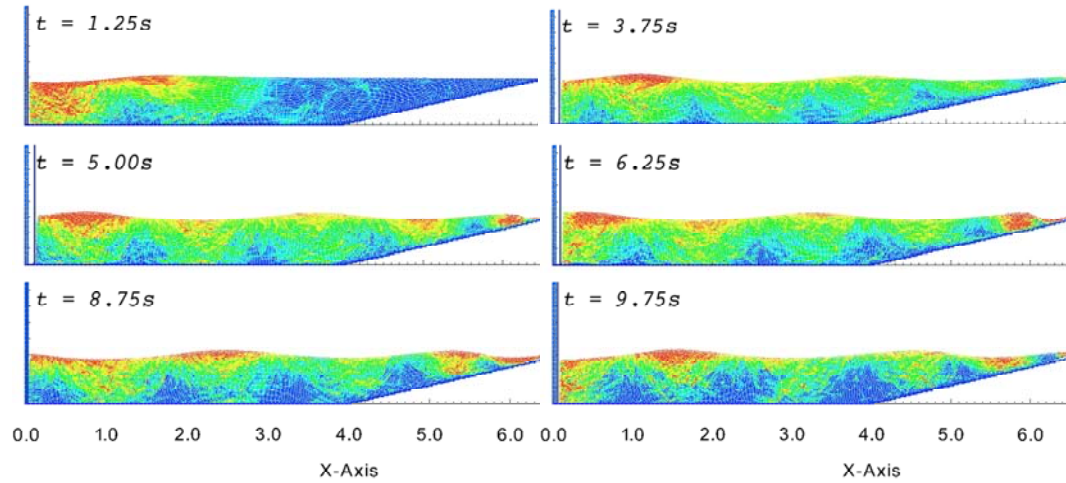Figure 4-35 Comparing time history of free surface prediction. Wave height $H = 0.10$ m; wave length $\lambda = 3.0$ m; water depth $d = 0.6$ m; tank length $L = 6.0$ m.

4.4 Concluding remarks

This section has focused on understanding the fundamental mechanism of SPH and how to incorporate ISPH in simulating free surface wave propagation. This is important in confirming SPH as a reliable numerical tool for the analysis of hydrodynamic problems. Therefore, efforts have been made to investigate various aspects of modifications in ISPH for suitability in producing accurate and stable free-surface profile. Several algorithms are proposed to improve the results, each with a different approach. The arc method is effective in preventing any misjudgement of free surface particles and collision control has proven to be effective between high-speed particles. The fundamental theory of ISPH demonstrates that uniform distribution of particles can reduce approximation errors. By incorporating particle shifting and the kernel renormalization, a good free-surface profile can be maintained in simulations. Additional viscosity on the free surface is shown to suppress the noisy configuration of fluid particles on the free surface. The general agreement for wave profiles between ISPH and potential flow is acceptable; accounting for the rise in mean depth, the pressure is predicted well, though velocity and pressure distributions are not consistent with potential flow results.

Further, in the convergence studies particularly in longer simulation runtime, ISPH has demonstrated less accurate results of free surface predictions. Other possible modifications to ISPH require additional algorithm and advanced computing techniques including parallel execution. This will be time-consuming and the main aim of this research in the application of SPH in seakeeping problem may not be achieved. Alternatively, an approach based on a WCSPH method from an open source code DualSPHysics could be employed for the same case of wave generation. The user-friendly nature of the code and software allows for easier adjustment and modifications of different parameters with parallel execution on GPU. Results from WCSPH show a good agreement in free surface profile, velocity and pressure distributions along the water depth. Obtaining more accurate results for the free surface profile would require a large number of particles. Refinement by increasing particle resolution i.e. smaller particle spacing, dx = 0.010 m was done though this would increase computational cost considerably.

Chapter 5

2-Dimensional validation and tests (WCSPH)

In the case of unsteady motion and unsteady flow around objects, it is essential to consider the additional force of fluid acting on the structure. Benchmark tests are used to verify the reliability of WCSPH code in predicting hydrodynamic loads acting on the body. Those loads are result from interaction between structure and waves considering the effects of broken/ non-breaking waves hitting the body. When the interaction between waves and floating bodies become significantly nonlinear, most of the potential theory methods perform less well. Violent behaviour between waves and floating bodies particularly on the free surface would be the subject of interest in WCSPH as the implementation of the nonlinear free surface condition is in general complicated. Three different types of forces namely radiation, diffraction and incident wave, in addition to the restoring force of hydrostatic origin are solved to provide motion, velocities as well as consequent loads induced on a body. Three rectangular sections with different dimensions are modelled in NWT. In the first test, radiation problem is investigated through a series of sensitivity analysis of sway, heave and roll motions under different wave frequencies. In the second test, diffraction problem of a fixed rectangular section in regular waves is demonstrated. While in the final test, WCSPH is utilised to simulate a floating body motion in 2 different wave heights of regular waves. Results in these three tests are compared to

experimental, theoretical and other numerical data. Convergence analyses are also carried out to test whether WCSPH method can maintain its performance at longer simulation runtime. Further, results from different refinements are also presented to give insight on the effect of particle number relative to domain size, damping zones, the motion of the rigid body and hydrodynamic loads around the rigid body.

5.1 Hydrodynamic coefficients predictions of a 2-D oscillating rectangular body

In seakeeping, it is important to evaluate hydrodynamic loads acting on the hull structure subject to incoming waves. Those loads that result from the interaction between structure and waves normally introduce nonlinearities considering the effects of broken and non-breaking waves hitting the structures. However, under the condition of less severe sea state, the contribution of hydrodynamic loads can be solved separately. Forces acting on the hull can be obtained by considering a linear approach of inviscid and irrotational fluid. It is worthwhile to mention that for motions in the transverse plane, and for particular ship hulls, viscous effects are not negligible. Motions of sway and roll are the most likely to be affected by viscosity around an oscillating body. This will be further discussed in the context of radiation problem where a rectangular section is moved with prescribed sinusoidal motion in the calm water. The hydrodynamic forces relating to the motion of a body in the fluid can be divided into components in phase with the acceleration and components in phase with the velocity of the body. The hydrodynamic force in phase with the acceleration of the body in a fluid is known as added mass force. The hydrodynamic force in phase with the velocity of the body in the fluid is known as damping force. These forces can be separated by their phases relative to the body motion. Forces in phase, but opposite in sign, with the motion, are in phase with the acceleration and hence are added mass forces. Forces 90 degrees out of phase with the motion are in phase with the velocity and hence are damping forces. In terms of complex number notation, the added mass is related to the real part of the measured force and the damping is related to the imaginary part of the measured force. Added-mass and damping coefficients are also important parameters for determining the amplitude of motion of the body. The dynamic characteristics of the bodies can be understood if these hydrodynamic coefficients are accurately predicted. However, it depends on the size and shape of the body, direction of motion, wave period and boundary conditions.

Using a simple rectangular section as a rigid body in calm water, the dynamic equilibrium of forces and moments can be determined by specifying sway, heave and roll motion. These cover the aspect of wave radiation problem of a simple 2-D rigid body in seakeeping. Hence, predicting the hydrodynamic coefficients of added mass and damping. The mathematical models for heave, sway and roll coefficients are explained in details in Vugts (1968).

5.1.1 Numerical setup

The numerical wave tank (NWT) is 16.0 m (including 3 m of damping beach on each side) long and 0.5 m deep. This case differs from the cases in chapter 4 because a space-fixed Cartesian coordinate system $O - XZ$ is used, with x-axis coincident with the bottom of the tank. The origin O is at the intersection of the bottom line and the vertical line, with x positive rightwards and z positive upwards. Beaches are installed at the ends of the wave tank to damp out the generated waves. About halfway down the length of the tank, a rectangular box is placed which is 0.40 m long and 0.40 meter wide, as shown in Fig.5.1. The box is placed at points (7.2, 0.5), slightly further away from the fixed wall on the left side of the tank. The box is homogeneous, and its centre of mass coincides with its geometric centre, so half of the box is immersed in water (Breadth to draught ratio, B/T = 2). The numerical simulation is performed using approximately 50,000 particles with an initial particle spacing dx of 0.010 m. A release time of 2 seconds allow particle distribution to settle before any movement commences. The layout of the discretized rectangular cross section is shown in Fig.5.2. The motion amplitude is 0.02 m for sway and heave, and 0.10 radians (5.73 deg.) for roll over frequency range between $\omega = 1$ rad/s to 9 rad/s as shown in Table 5-1.

5.1.2 Numerical parameters

Parameters in WCSPH code can be changed and tuned depending on different problems. Besides experimental value, Vugts also treated the flow field by classical potential theory of inviscid model. The inviscid model idealises the fluid flow by neglecting viscous effects. A few assumptions that were considered as the part of inviscid model are;

1. The fluid was incompressible and irrotational.
2. The amplitude of motion was small with respect to the section dimensions.
3. The generated waves have amplitudes which are small with respect to their wavelength.
4. Surface tension in the fluid domain is neglected.

These conditions are approximately fulfilled by WCSPH for comparison with the theoretical solution both qualitatively and quantitatively. Artificial viscosity in section 3.1.3 is used for numerical stability in WCSPH. Therefore, validating side by side with experimental results by Vugts would be beneficial as far as the influences of viscosity are concerned. The value of α_Π in viscosity term (equation 3.21) is set to 1×10^{-6} and 0.1 for delta-SPH (δ) term. Wendland quintic kernel is used for all simulation in this chapter as the interaction kernel unless stated otherwise. The initial time step is set to $dt = 2.5e^{-4}$ s and simulations are run for 20 seconds. In addition, fluid particles are not moved using XSPH (Monaghan, 1989) to avoid additional viscosity in the fluid domain. The filtering technique used for force calculation is similar to that discussed in section 4.2.4.
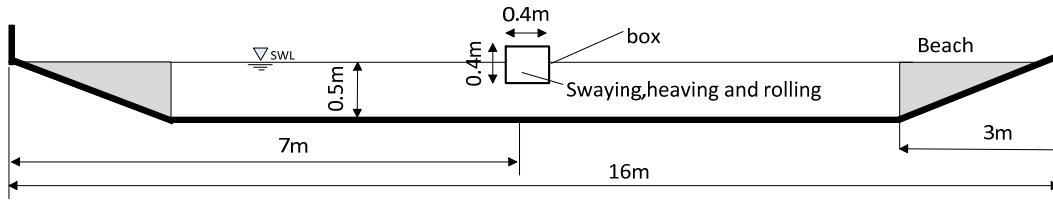
Figure 5-1 Setup of the numerical model
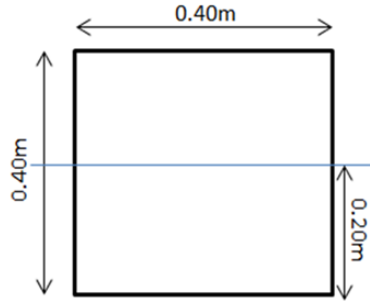
Figure 5-2 The cross-section of the rectangular box

Table 5-1 Frequencies used for added mass and damping coefficient analysis

$\omega\sqrt{B/2g}$	ω(rad/s)	T(s)	λ(m)
0.28056	1.97	3.20	15.8
0.50	3.50	1.80	5.0
0.79103	5.54	1.10	2.0
1.00	7.00	0.90	1.3
1.1385	7.97	0.79	0.97
1.2916	9.05	0.69	0.75

5.1.3 Results and discussion

The results of a rectangular section harmonically oscillating at a free surface are presented in this section. The relation between added mass and damping can be represent by equation (5.1). The computation of the hydrodynamic load due to the fluid-structure interaction is carried out using Fouries decomposition via MATLAB script to express the total fluid force in terms of a non-dimensional complex-valued hydrodynamic function, which real and imaginary parts identify added mass and damping coefficients, respectively. Total force is obtained from the SPH momentum equation by first computing the acceleration vector of each water particle in the first layer of fluid surrounding the rigid body. This value is then multiplied by the fluid particle's mass and reversed in sign so that the resulting vector is sought as the force exerted by the water on the boundary layer (Mokos, 2013; Meringolo, 2015; Tafuni, 2016). For swaying, only the x component of the acceleration is considered in the computation of the hydrodynamic force. Details on force calculation can be referred in subchapter 3.2.2. The unit of total force is N/m and is commonly referred to as the '*unit width of force*'. Both results from WCSPH and experiment can be non-dimensionalized with $\rho g dA$(N/m).

$$Force = \frac{a_{yy}}{\rho A} \cdot \rho A \cdot (-\omega^2 y_a sin\omega t) + \frac{b_{yy}}{\rho A}\sqrt{\frac{B}{2g}} \cdot \frac{\rho A}{\sqrt{B/2g}} \cdot \omega y_a cos\omega t \qquad (5.1)$$
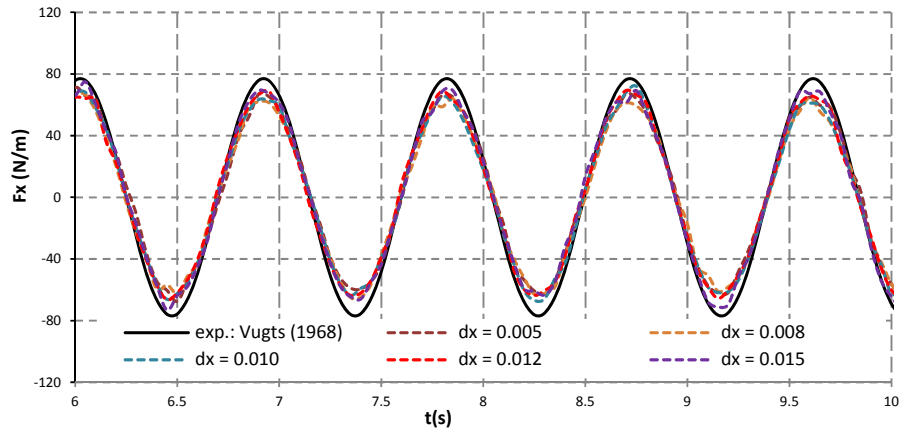
Figure 5-3 Force by acceleration and mass at 7.00 rad/s with different dx.

Predictions using WCSPH are compared against findings from Vugts (1968). Vugts has used 2 different approaches for his predictions of hydrodynamic coefficients, one of which is a theoretical estimation using potential theory and the other uses experiments. For this particular model, the most suitable comparison should be made using his theoretical estimation. The

experiments show to what extent the predictions invalidates the theoretical estimation which is of significant comparison to WCSPH when viscosity and small motion amplitudes are concerned.

Fig.5.3 shows convergence studies of horizontal force, F_x in sway motion at ω = 7.00 rad/s for different particle refinement. The preliminary tests were done to show convergence of the force computation. All tests are allowed to run for sufficient time for the motion to stabilize and the forces computed to be reliable. As mentioned for swaying motion, hydrodynamic coefficients are evaluated directly from the force around the body in the x direction. While in the case of heaving and rolling motions, computation from WCSPH will result in the total force experienced by the body. Therefore, static force need to be excluded for comparison with Vugts. Static condition is assumed to be the body in the initial buoyancy with initial vertical force. Static force is subtracted from total force to obtain the dynamic force.

5.1.3.a Sway motion

For each different frequency in sway simulation, the rectangular cross section experiences a horizontal forced oscillation with small influence of vertical forces. The simulation is run for 20 seconds for the fluid flow to become steadier before the calculation of body forces commences. The particle snapshot of the horizontally oscillating box is shown in Fig.5.4 at different oscillation frequencies. In (a) the box is at the maximum leftward position at T = 12.8 s and T = 11.3 s while in (b) the box is at the maximum rightward position at T = 14.5 s and T = 11.6 s. For lower frequency in (a), the formation of propagating waves is less visible due to a longer wavelength. The added mass and damping in sway, together with the coupling coefficients in the roll are shown in Fig.5.5 and Fig.5.6. Both graphs share the same legend. The solid line from Vugts represents calculations based on the best section fit (theoretical value) while the circle denotes the experimental results done by Vugts. The agreement in added mass, a_{yy} and mass coupling coefficients, $a_{\varphi y}$ of WCSPH agrees well with the best section fit line and the experiment at high frequencies motion. However, few discrepancies are observed at comparatively low frequencies. Meanwhile, the higher the frequency, the larger deviation of damping coefficients, b_{yy} and damping coupling coefficients, $b_{\varphi y}$ from the potential theory, starting from $\omega\sqrt{(B/2g)} = 0.75$ to 1.25. The experiments done are observed to overestimate the value of b_{yy} and underestimate the value of $b_{\varphi y}$. Hence, the WCSPH results appear to be closer to the theoretical values. Since the frequency of the sway motion is low, it is believed that the influence of viscosity is not important. Numerical errors for WCSPH at lower frequencies are noticeable especially for ω = 1.97 rad/s with 20% error for added mass and nearly 40% for coupling coefficients. The computed horizontal force

(**Appendix A**) shows noisy oscillation, which is slightly higher than the force recorded in the experimental. Filtering technique provided in the MATLAB routine (Filter Design Toolbox) in the post-processing has been applied to all the computed points to suppress outlier of high peak fluctuation. In order to overcome this issue, further investigations are carried out by i) extending the domain and ii) implement smaller particle spacing. Rectangle mark in Fig.5.5 denotes an extension of 20 m length while diamond mark denotes particle spacing of 0.005 m. The implementation of the refined particle spacing and extended domain, however, do not improve the predictions significantly. In order to save the computational cost, it is preferable to employ *dx* = 0.010 m for heave and roll tests.

Figure 5-4 Particle snapshot of the horizontally oscillating box. (a) ω = 1.97rad/s, (b) ω = 9.05rad/s.
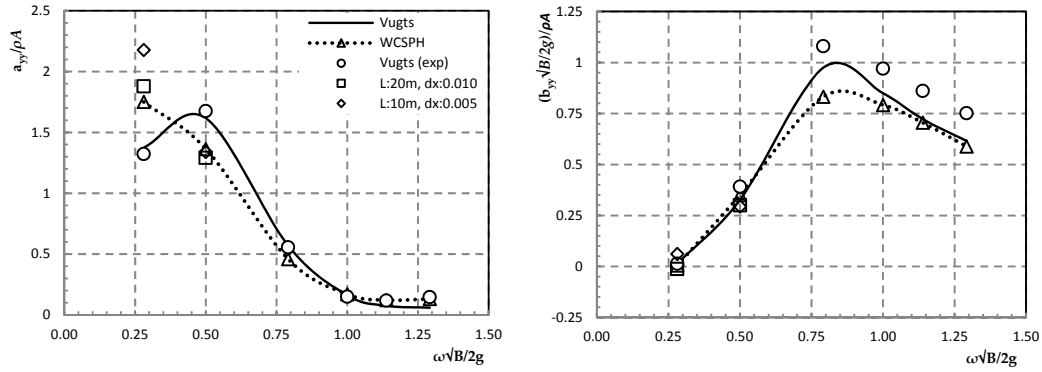
Figure 5-5 Added-mass and damping coefficient in swaying
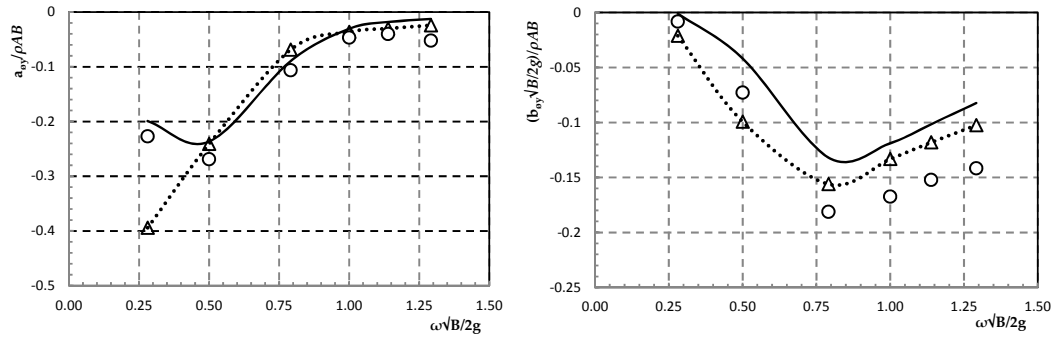
Figure 5-6 Coupling coefficients of sway into roll

5.1.3.b Convergence analysis for lower frequencies

Overall, good agreement is seen but not at relatively low frequencies or when the cross-coupling coefficients are involved. For ω = 1.97rad/s, it is very difficult to obtain accurate prediction. Long-crested wave demands a very steady condition in maintaining a good wave profile. Therefore, investigation using a number of different computation setup parameters are carried out. These parameters include different initial particle spacings, larger domain size, different initial time steps and different simulation runtimes. The main objective is to obtain insight into what could be the most influential parameter for the prediction of the hydrodynamic coefficients. Fig.5.7 shows the relative errors for different initial particle spacing used for the oscillating box. The domain is kept as 10 m to allow for damping of the reflected waves on both sides of the NWT. Refinement should be considered carefully based on the dimension of the rectangular section. The largest particle spacing used is 0.050 m, which in practice provide 8 particles on each side of the box. Insufficient neighbouring particles to provide detailed information could cause errors in pressure, density and velocity. This can be observed from the graph where accumulated relative errors increase with larger particle spacing. Particle spacing of 0.050 m produces at least 4 % more errors than other particle spacings. However, using smaller particle spacing to obtain a higher resolution does not guarantee as efficient due to the problems of single precision. It has been shown by Dominguez et al., (2014) that lack of precision to represent the position of the particles can lead to simulation breakdown. Therefore, it needs to be kept in mind when considering the suitable setup, that the initial particle spacing; dx should be small enough to represent the correct force but must not be too small or too large to cause instability between interacting particles.
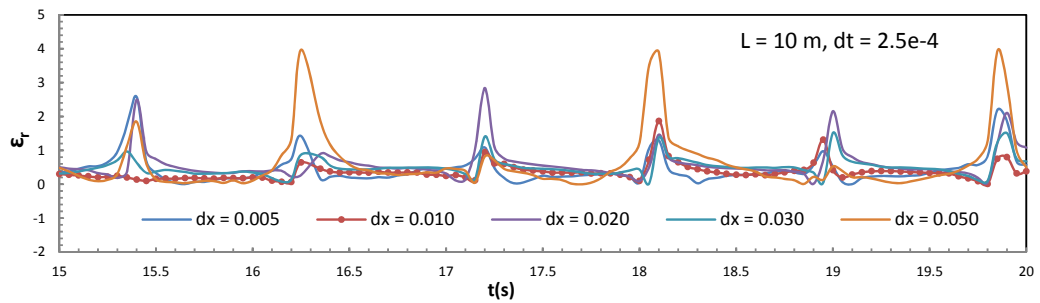
Figure 5-7 Relative errors for different particle spacing for horizontally oscillating box (sway motion).
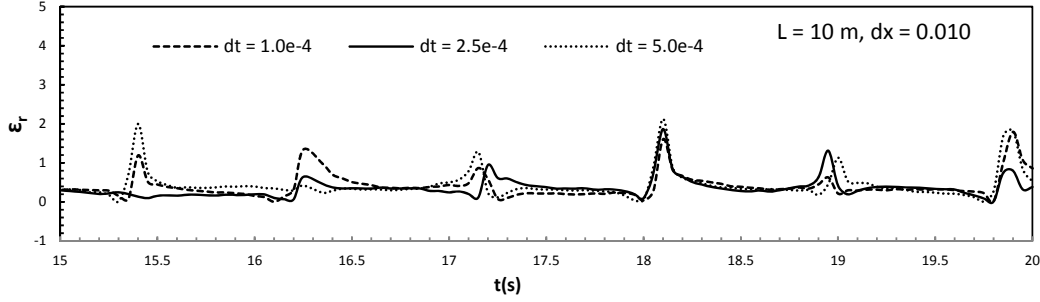
Figure 5-8 Relative errors for different initial time step for horizontally oscillating box (sway motion).

The results from different initial time steps are shown in Fig.5.8. In general, the time step is determined prior to the simulation by time-step constraints, as explained in 3.2.5. The time steps for each simulation were calculated ensuring that the Courant number was less than 1. As long as the time step is kept small, the error differences between the three initial time steps are negligible. Running time is also important for accurate predictions along the box boundary. It is best to allow the fluid flow to initialise and run the simulation for a longer period until it reaches its steady state before the calculation of force commences. At the release time, there is a possibility that force from fluid particles could suddenly be applied on the boundary and that could cause fluctuation of the data. A total of 1,200-time step is specified until the simulation is believed to be steady enough, as shown in Fig.5.9. Two graphs show predictions from two lower frequencies which suffer discrepancies from the experimental data in added mass, a_{yy} and mass coupling coefficients, $a_{\varphi y}$. Based on previous analysis, both frequencies implement the most suitable initial particle spacing time step and simulation runtime. Even after 60 s of simulation runtime, the prediction of force for $\omega = 1.97$ rad/s can be observed to be over-predicted while the force is under-predicted for case $\omega = 3.50$ rad/s. Considering the wavelength when $\omega = 1.97$rad/s, the domain is extended up to 20 m to cover at least 3 wavelengths or three oscillation cycles. As it is not practical to eliminate reflected waves and their effects on the prediction, the damping beach at both ends of NWT is also extended, along with the domain (a total of 26 m including the damping beach). Fig.5.10 demonstrate the effect of having too much fluid particles exposed as free surface due to wide domain. Wider free surface mean fewer particles in the summation of kernel near the free surface. The interpolation which round up to single precision is insufficient in determine the precise location of each fluid particle on or adjacent to the free surface. Thus accumulating errors at each time step creating unphysical movement of pressure and velocity near the damping zone. Similar conditions can be found in Dominguez et al., 2014. Therefore, the use of an extended domain did not significantly change either prediction of the hydrodynamic coefficients.
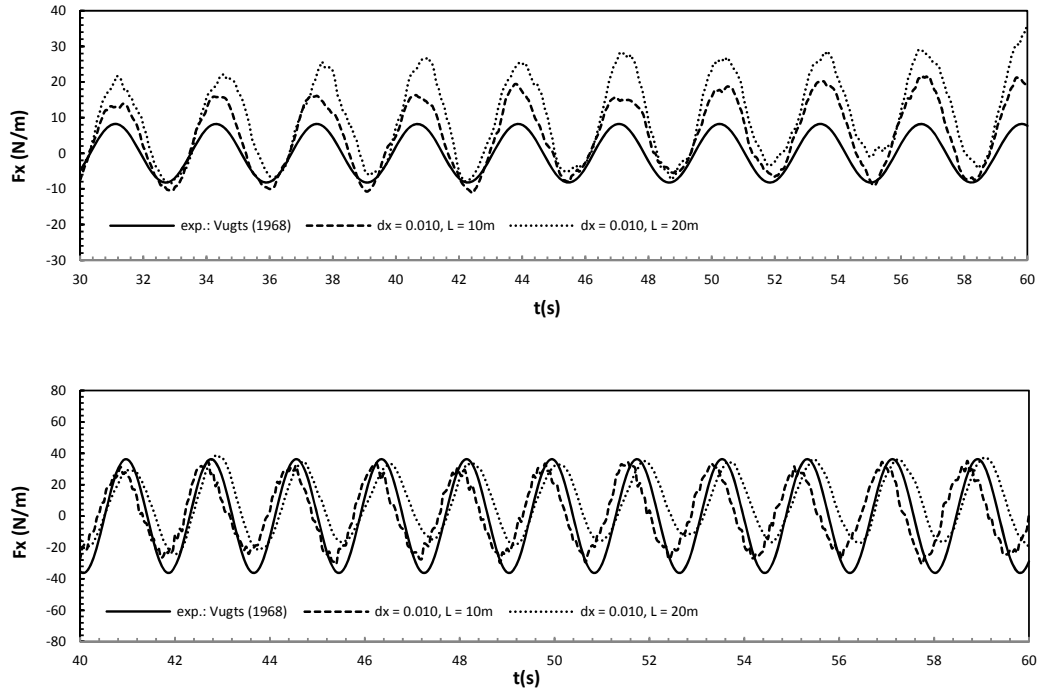
Figure 5-9 Time history of horizontal force for horizontally oscillating box. *upper*) 1.97rad/s and *lower*) 3.50rad/s.

(a)

(b)

Figure 5-10 Red boxes show the area where unphysical errors appear in the NWT due to single precision inaccuracy for larger domain size of (a) L = 20 m and (b) L = 30 m.
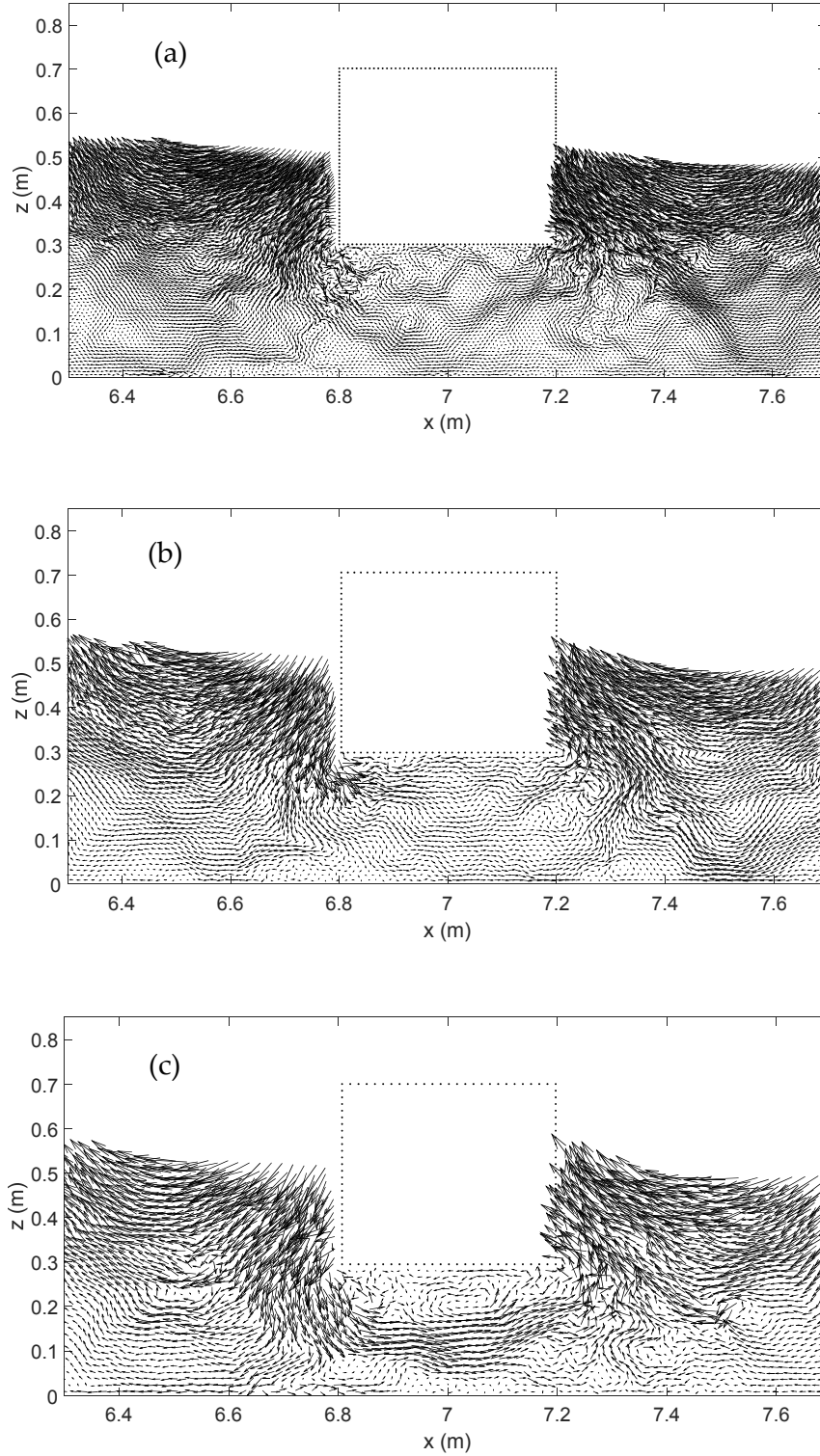
Figure 5-11 Generation of vortices around sharp corners in swaying shows convergence for different particle refinement at T = 11.0 s, ω = 7.00 rad/s. (a) dx = 0.008 m, (b) dx = 0.010 m and (c) dx = 0.012 m.

5.1.3.c   Heave motion

In this test, the rectangular section is restricted so that it oscillates only in a vertical direction, and therefore the influence of a horizontal force exerted by the fluid should be minimal. The particle snapshots of the vertically oscillating box for 2 different frequencies are presented in Fig.5.12. The box sinks to the lowest position at both T = 9.6 s and T = 18.4 s and rises to the highest position at T = 9.9 s and T = 20.0 s. In both cases, a coarse pressure field can be seen around the rigid boundary between fluid-boundary particles. Boundary near the free surface has asymmetry integral domains resulting in the neighbour particles deficiency. Therefore, when the fluid particles move along the rigid boundary, the densities of the boundary particles fluctuate, resulting in an unstable pressure field around the rigid body. Fig.A.4 shows the affected prediction of vertical force at 1.97rad/s by random fluctuations of high-frequency pressure develop around boundary particles. Although the dimension is extended to 20 m, maximum of 30% discrepancy is estimated for a_{zz} (**Appendix A**). However, these pressure fluctuations are observed to be small and can be smoothed out in the case of comparatively high frequencies.

Similarly, in swaying, WCSPH results show a good agreement in general with the experiments for added mass, a_{zz} and damping, b_{zz} particularly at high frequencies of motion (Fig.5.13). Deviations appear only in the low-frequency range, especially in a_{zz} (ω = 1.97 rad/s) where WCSPH share similar discrepancies with the experimental values of Vugts. The individual plot of vertical force for each frequency can be seen in **Appendix A**. The influence of breadth-draught (B/T) ratio to a_{zz} and b_{zz} is also quite large where it determines the immersed area of the rectangular section for heaving.
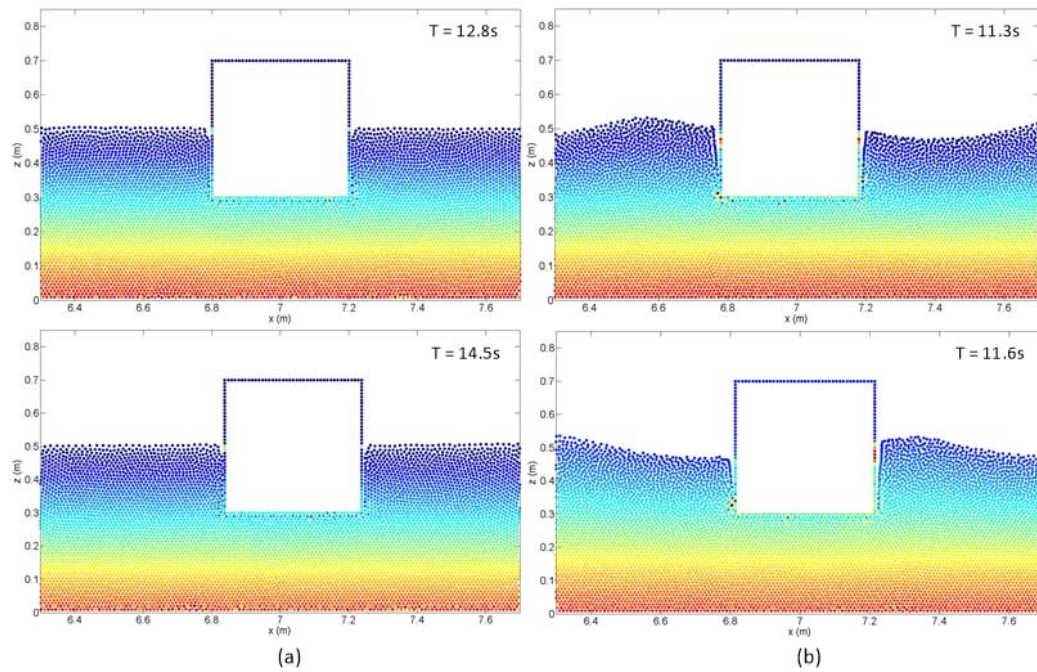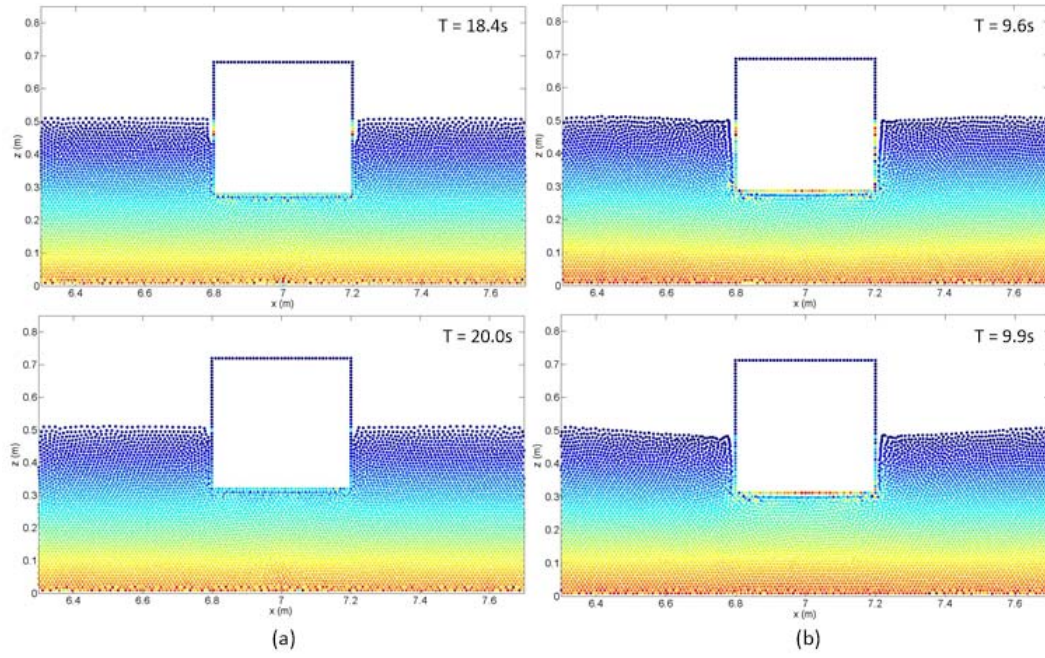
Figure 5-12 Particle snapshot of the vertically oscillating box. (a) ω = 1.97rad/s, (b) ω = 9.05rad/s
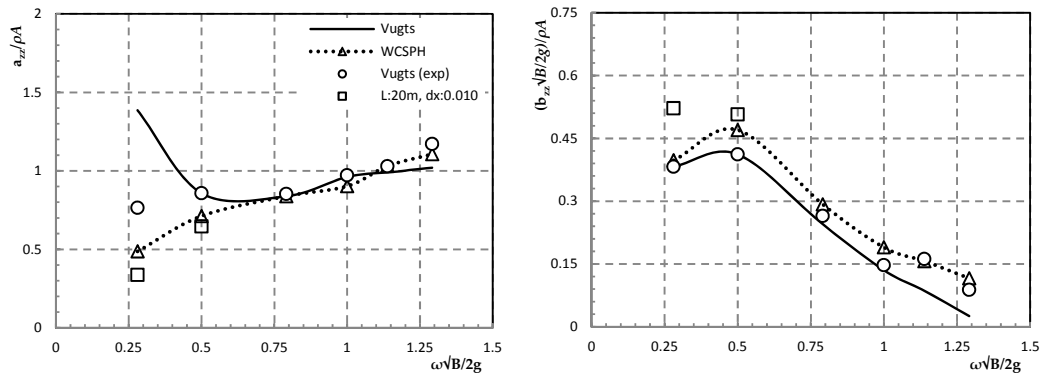
Figure 5-13 Added-mass and damping coefficient in heaving

### 5.1.3.d   Roll motion

In this analysis, the rectangular section is rolled at 6 different frequencies by the amplitude of 0.10 radians. Both roll moments and cross coupling forces of sway into roll are investigated. A particle snapshot of the rolling oscillating box is shown in Fig.5.14(a). The box rolls in an anti-clockwise direction to reach the rightward maximum position at T = 10.6 s and then turn in a clockwise direction to reach the leftward maximum position at T = 10.95 s. Comparison of the dynamic force for individual frequencies at lower frequencies can be found in **Appendix A**. In Fig.5.15 and Fig.5.16, predictions from WCSPH agree fairly well with experiments and potential theory in added moment of inertia, $a_{\varphi\varphi}$ and mass coupling, $a_{y\varphi}$ except for the lower frequency, $\omega\sqrt{(B/2g)} =$ 0.28. Here, nearly whole influence is focused on the energy dissipating terms that are coefficients $b_{\varphi\varphi}$ and $b_{y\varphi}$. Damping in coupling coefficient, $b_{y\varphi}$ also seems to fit the trend with both experimental and theoretical results. However, it can be observed that the roll damping coefficients, $b_{\varphi\varphi}$ are over-predicting the potential theory beyond the peak value at $\omega\sqrt{(B/2g)}$ = 0.2 at comparatively high frequencies. There is a large contribution of viscosity in $b_{\varphi\varphi}$ by WCSPH though they fit the trend line. It is known that viscous roll damping is the dominant damping mode in the roll motion of the forced motion box, representing the effect of vortex shedding of the box with sharp corners. Although sway, heave and particle velocities may also have affect in the vortex damping of the box, these contributions were found to be very small in the case of determining roll damping from forced-roll (Standing, 1991). Vortex damping term is directly depends on roll velocity only, which justify the gradual increase of intensity of nonlinear forces and moments experienced by the box at comparatively higher frequencies. These nonlinear forces are due to viscous effects which can lead to flow separation and generation of vortices. Magnitude of vortices near the immersed sharp corners of the box are presented in Fig.5.14(b). Similar scenario is also mentioned by Vugts in his experimental measurements. According to him, the viscosity had an effect on the measurement of $b_{\varphi\varphi}$, while $a_{\varphi\varphi}$ also suffers from experimental errors, which under predict the values from the theoretical counterpart. The errors in $a_{\varphi\varphi}$ in the experiment were also due to inaccuracies encountered in determining the inertia, I of the cylinders which resulted in lower added inertia coefficients. Hence, we can say that the roll added inertia using WCSPH is consistent with the experimental results for the case $\omega\sqrt{(B/2g)}$ > 0.28. Moreover, both coupling coefficients from sway and rolling share satisfactory results for both added mass and damping coefficients. In this analysis, extended dimension and refinement of particle spacing are not carried out based on previous studies done on sway motion and to prevent any possibility of

numerical instability in the fluid domain that could affect the prediction of hydrodynamic coefficients.

(a)   (b)
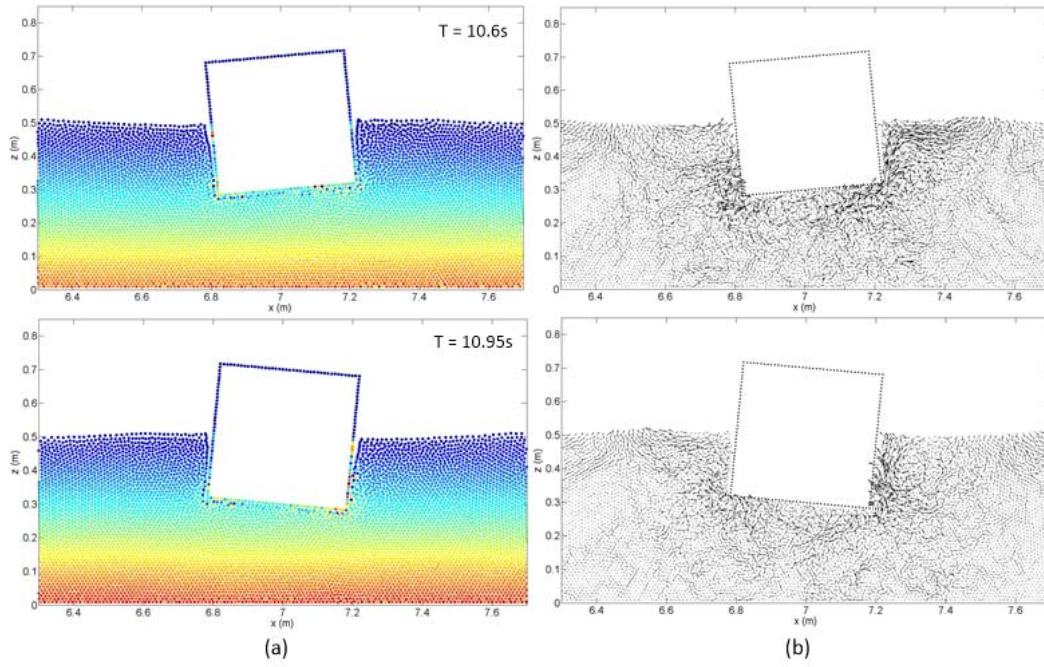
Figure 5-14 (a) Particle snapshot and (b) velocity vector speed around a rolling body at $\omega = 9.05$rad/s.
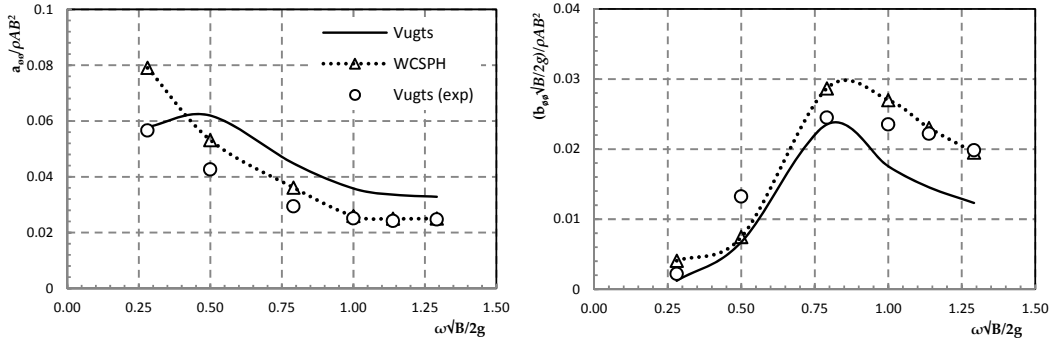
Figure 5-15 Added-mass moment of inertia and damping coefficient in roll
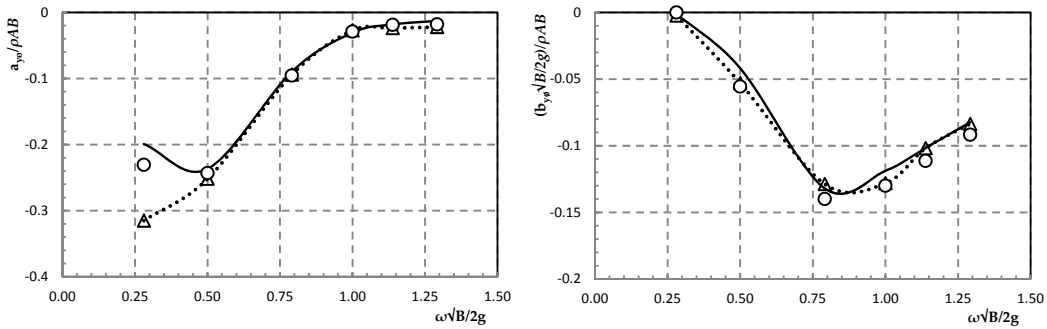
Figure 5-16 Coupling coefficients of roll into sway

5.1.4 Concluding remarks

WCSPH code from DualSPHysic is employed as a numerical tool to predict the hydrodynamic coefficients in sway, heave and roll. This is a 2-D hydrodynamic test to validate the capability of the WCSPH method in predicting the hydrodynamic coefficients, namely added mass and damping coefficients of a radiation problem. Here in WCSPH, the flow is modelled and compared to potential flow and experimental results from Vugts. The results from WCSPH and experimental data has shown to what extent numerical and experimental predictions differ in comparison to the theoretical solution, assuming that the potential theory can be a reliable prediction for all the hydrodynamic coefficients involved as long as flow separation is not concerned. However, results from damping coefficients particularly in roll damping suggests that viscosity effects do exists in both experiment and WCSPH which creates flow separation and generation of vortices at sharp corners of the box. It also showed that roll damping due to eddy making and radiation cannot be separated. These effects increase with frequency of the forced oscillation indicating nonlinear forces and moments.

Furthermore, it can be observed that the prediction of hydrodynamic coefficients for both added mass and damping around a moving rectangular section agrees well with the prediction from experimental data and potential theory with some discrepancies at the lower frequencies. Discrepancies of added mass and mass coupling coefficients are observed between $\omega = 1.97$ rad/s and $\omega = 3.50$ rad/s where wavelengths are particularly long. More detailed analysis is then carried out just for sway motion to investigate the discrepancies by i) implementing different particle spacings, ii) using different time steps and iii) extending the domain with a longer runtime. In theory, a better prediction of hydrodynamic coefficients can be obtained with reduced relative errors by refining the whole domain with careful consideration of the number of particles involved to minimise the numerical errors. However, the results do not change significantly for either ii) or iii). Generation of vortices were also observed for different particle refinement in sway to show convergence. Generally, WCSPH has shown a satisfactory results with discrepancies in the case with long wave evolution. As long as the targeted analysis is significant around reasonable ratio value of λ/L, WCSPH is proven to be a reliable numerical tool in predicting the hydrodynamic coefficients, which will be useful in the next study of dynamic characteristics of 3-D bodies. The result might be improved with boundary treatment to smooth out some pressure fluctuation between fluid and rigid particles, which is not discusses in this study. Improvements could also be made using double precision for particle position or variable particle distribution near the vicinity of the rectangular section.

5.2 Regular waves on a 2-D fixed rectangular box

While the previous section dealt with radiation problem by looking in details at the prediction of hydrodynamic coefficients of sway, heave and rolling motion, this section demonstrates the analysis of diffraction problem. It is one of the important hydrodynamic aspects to be verified by WCSPH and further to be utilised in the 3-D simulation. In this section, the behaviour of a fixed rectangular box in regular waves is investigated. The incoming waves generated by a piston-type wavemaker would encounter the body creating a diffraction phenomenon or interference of waves. The interaction between waves and fixed body is shown through transmission of forces from the waves to the body and vice versa. Hydrodynamic forces of horizontal force, vertical force and overturning moment from waves are then analysed individually. Each force is then validated with analytical solution accordingly. Wave profiles for the different case of wave heights are confirmed prior without the body in the numerical tank.

5.2.1 Numerical setup

The NWT shown in Fig.5.17 is 10 m long and 2.0 m high with a water depth of 1.2 m. Distances are measured from the left-lower corner of the NWT. A rectangular box of breath $B = 0.80$ m and height $H = 0.40$ m is constrained and semi-immersed, and its centroid is located at point (4.6 m, 1.2 m). Approximately 106,000 particles including 3,142 fixed boundary particles and 480 moving boundary particles are used in the simulations, with initial particle spacing of 0.010 m. The rigid boundary of the rectangular box is simulated by 2 layers of boundary particles for optimum boundary repulsion. An active piston-type wavemaker is set at $x = 0.2$ m initially to generate propagating waves. At the right end of the NWT, a beach with a length equal to one wavelength is used to absorb the incoming waves.

Simulations are carried out for 2 different wave heights with the same frequencies as shown in Table 5.2. The objective is to obtain insight into domain size, beach zone and free surface behaviour when interacting with the fixed box for each wave amplitude. In the preliminary runs, if severe free surface breaking occurs around the rigidly fixed box, then particle refinement or the distance of the fixed box from the wavemaker would be reconsidered. Wave profiles for each case are measured and confirmed at $x = 4.6$ m before the box is placed in the NWT.

Value of 0.5 is used for α_Π in the viscosity term (equation 3.21) and 0.1 for delta-SPH (δ) term. Simulations are performed using WCSPH and the results are compared with the available

numerical and analytical estimations. Initial time step is set to dt = 2.5e^{-4} s with time 0.05 seconds between output files. Simulations are then run for 20 seconds with 0.5 seconds of release time. In addition, fluid particles are moved using XSPH scheme with ε = 0.5. The XSPH regularize the WCSPH treatment of fluid to further prevent fluid particles inter-penetration while reducing particle disorder (Monaghan, 1992; 2005).
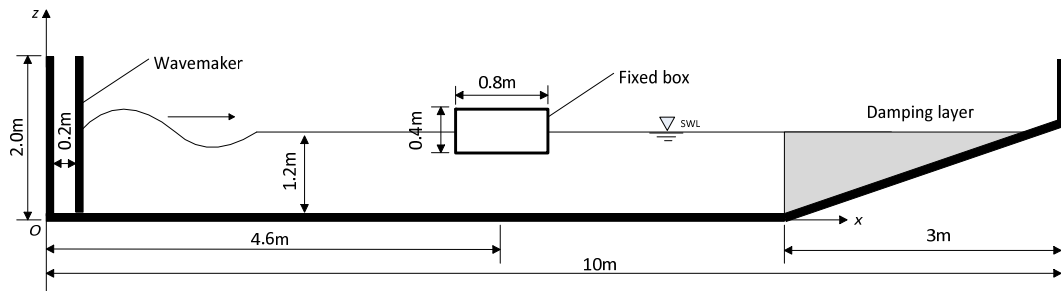
Figure 5-17 Simulation setup

Table 5-2 Numerical conditions used in the simulation

Case	H(m)	T(s)	ω(rad/s)	λ(m)
Examination of wave	0.06	1.2	5.24	2.25
forces on fixed box	0.20	1.2	5.24	2.25

5.2.2 Results and discussion

The results of the stationary rectangular box under the influence of regular waves, at a free surface, are presented in this section. Fig.5.18 shows the comparison of forces and moment between WCSPH, WCSPH predicted by Ren (2015) and the analytical solution obtained by Mei and Black (1969) for comparatively small wave height. The solid line denotes data from WCSPH, the dashed line denotes results from WCSPH by Ren and dot lines represent the analytical solution. The red rectangular frame highlights the results of 5 seconds window from Ren and Mei that are comparable to our computed results. The 5 seconds window does not necessarily share the same real-time with the computed result from WCSPH as we allowed the simulation to reach its steady state condition before comparison takes place. For case $H = 0.06$ m, time from 4 seconds to 9 seconds is observed to be steady enough for comparison and the same time frame is replotted in Fig.5.19 for further analysis. Similar graph and technique for comparatively large wave height of $H = 0.20$ m, T = 1.2 s can be found in **Appendix A**. The analytical solution of linear diffraction using the frequency domain method represented in Mei and Black (1969), which are converted to duration curved by multiplying it by a time function $\cos(\omega t)$. Nonlinear effects are hopefully to be achieved under two different wave heights that are used for comparison.

From the graph ($H = 0.06$ m) in Fig.5.19, the peak amplitude of wave elevation from WCSPH agrees well with the analytical solution and Ren's. Discrepancies in the elevation remain small and within one particle spacing which indicates the incoming waves can be nearly regarded as a linear wave. Moreover, the horizontal wave force F_x, the vertical force F_y, and the overturning moment M, about the centroid have a better agreement with the analytical solution than the overall results by Ren. Vertical force demonstrates some nonphysical fluctuation showing influence of sharp edge at bottom corner of the fixed rectangular body.

In the case of $H = 0.20$ m, the incoming waves generated from the piston cannot be considered as linear waves. The poor agreement can be observed where most of the computed results demonstrate significant asymmetry in their profile. A similar pattern can be observed in the investigation of regular wave loading on a fixed cylinder by Lind et al., (2016). However, the wave height is not large enough in leading to a breaking event. Both WCSPH and Ren have almost identical wave elevation profile with distinctive sharp wave crest and flat wave trough that conforms the surface character of a nonlinear wave and this differs from the sinusoidal curve of the analytical solution. The same nonlinearities can be observed in the plot of horizontal force and overturning moment. Sharp wave trough with the double hump of curve on the wave crest

in vertical wave force also imply significant nonlinearity of wave forces. However, it is seen that result from computed WCSPH predicts forces and moment with relatively better accuracy than Ren with much smaller discrepancies. The cause for discrepancies is investigated further with different particle refinement in the convergence analysis. The extended domain is not considered for convergence studies because as observed in previous studies, it made only small or insignificant improvements to the results.
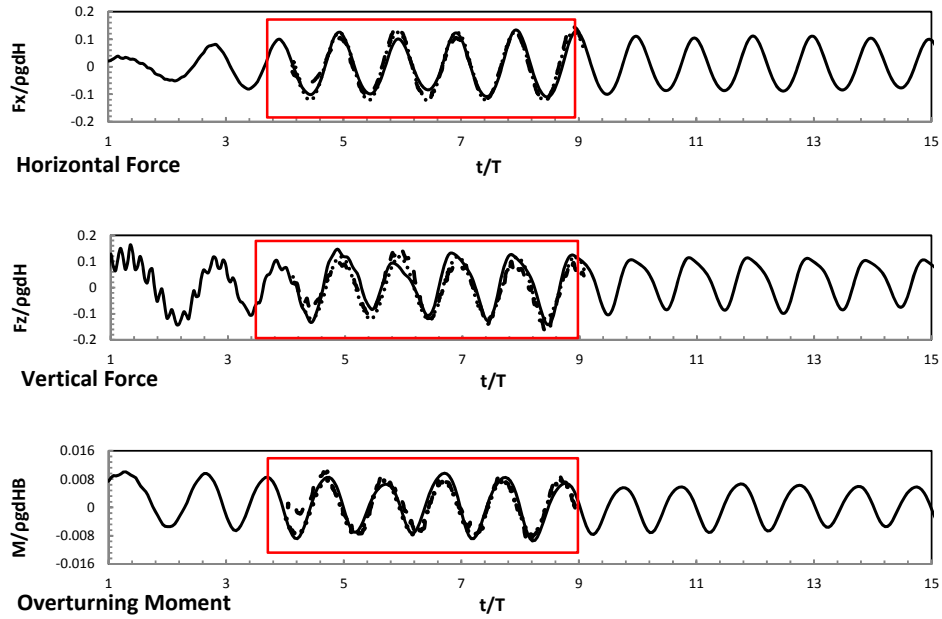
Figure 5-18 Time histories of forces and moment (H = 0.06 m, T = 1.2 s).
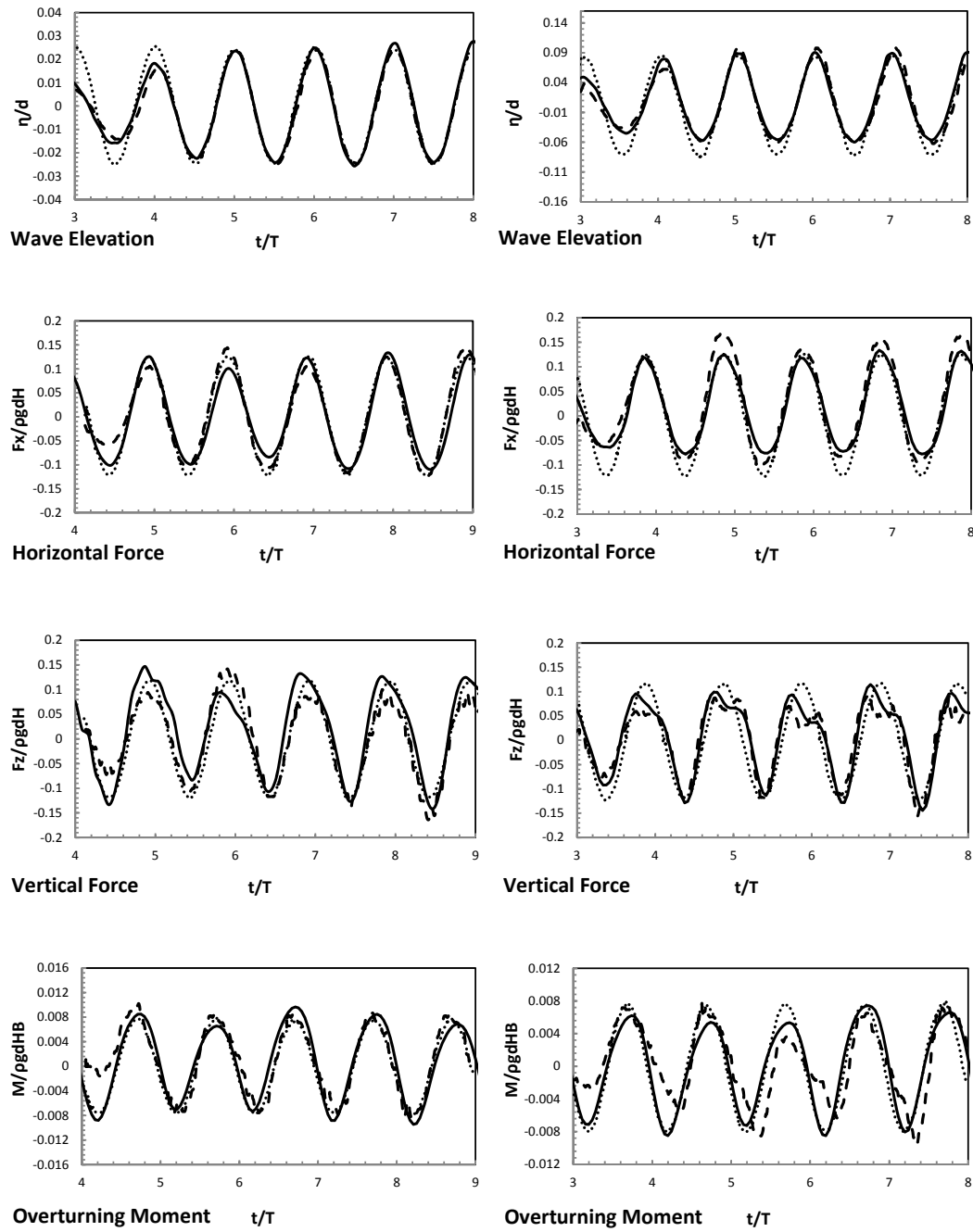
Figure 5-19 Comparison of wave elevation and filtered wave forces on a fixed rectangular box. − − SPH (Ren, 2015), ⋯ Analytical (Mei and Black, 1969),− WCSPH. Left (H = 0.06 m), right (H = 0.20 m).

5.2.3 Convergence analysis

Discrepancies are noted in vertical force and overturning moment especially in the case with comparatively larger wave height. Although we know the discrepancies would indicates nonlinear effect from the incoming waves, the consistensy between the two numerical methods should be investigated. Therefore, refinement on the fixed body and fluid domain are considered. This is because particle method like SPH sometimes rely on a sufficiently fine particle spacing to be able to predict the accurate result and it is important to have a good idea on the effect of particle spacing on the results and how the results would converge. A refinement with initial particle spacing ranging from 0.005 m to 0.040 m are used for the whole domain as the variable particle mass distribution method used by Omidvar et al., (2013) is not yet developed in current DualSPHysics. The implementation of particle refinement resulted in increasing and decreasing number of particles. For example, in the case of 0.005 m, the total number of particle increases to 417,112 and in the case of 0.040 m, the number decreases to 7,112 .

Fig.5.20 shows the average amplitudes of wave loading (horizontal force F_x, vertical force F_y, and overturning moment M) at the wave crest and wave trough of different initial particle spacing. Only data in the selected windows in Fig.5.19 are involved in computing the mean amplitude values. Mean amplitude is separated into 2 values. The positive values refer to mean peak while the negative values refer to mean trough, each being compared to the same analytical value which represented by solid line. Time histories from different particle spacing of the wave forces for both $H = 0.06$ m, T = 1.2 s and $H = 0.20$ m, T = 1.2 s can be found in the **Appendix A**.

In both cases of wave heights, particle spacing of 0.010 m, 0.015 m and 0.020 m share similar trend of forces and moment predictions in comparison to 0.005 m and 0.04 m. For 0.010 m, the different in vertical force and overturning moment from the computed results is less than 10%. While both horizontal forces demonstrate some inconsistency in different particle spacing particularly near the wave trough. Domain size also plays a major role when determining a suitable particle spacing. A number of neighbouring particles inside a kernel must be able to contain information for accurate computation. Choosing 0.04 m for initial particle spacing for a 0.3 m × 0.2 m box will only produce 4 particles to predict the horizontal forces and 8 particles to predict the vertical force which is clearly insufficient. This aspect of particle number in the interactions between fluid particles and boundary particles on the interface are shown in Table 5.3 with other different particle spacing. An insufficient number of particles is also proven leads to poor wave profile

which is explained in section 4.3.3. Results on wave forces for each different particle spacing can be found in **Appendix A**.
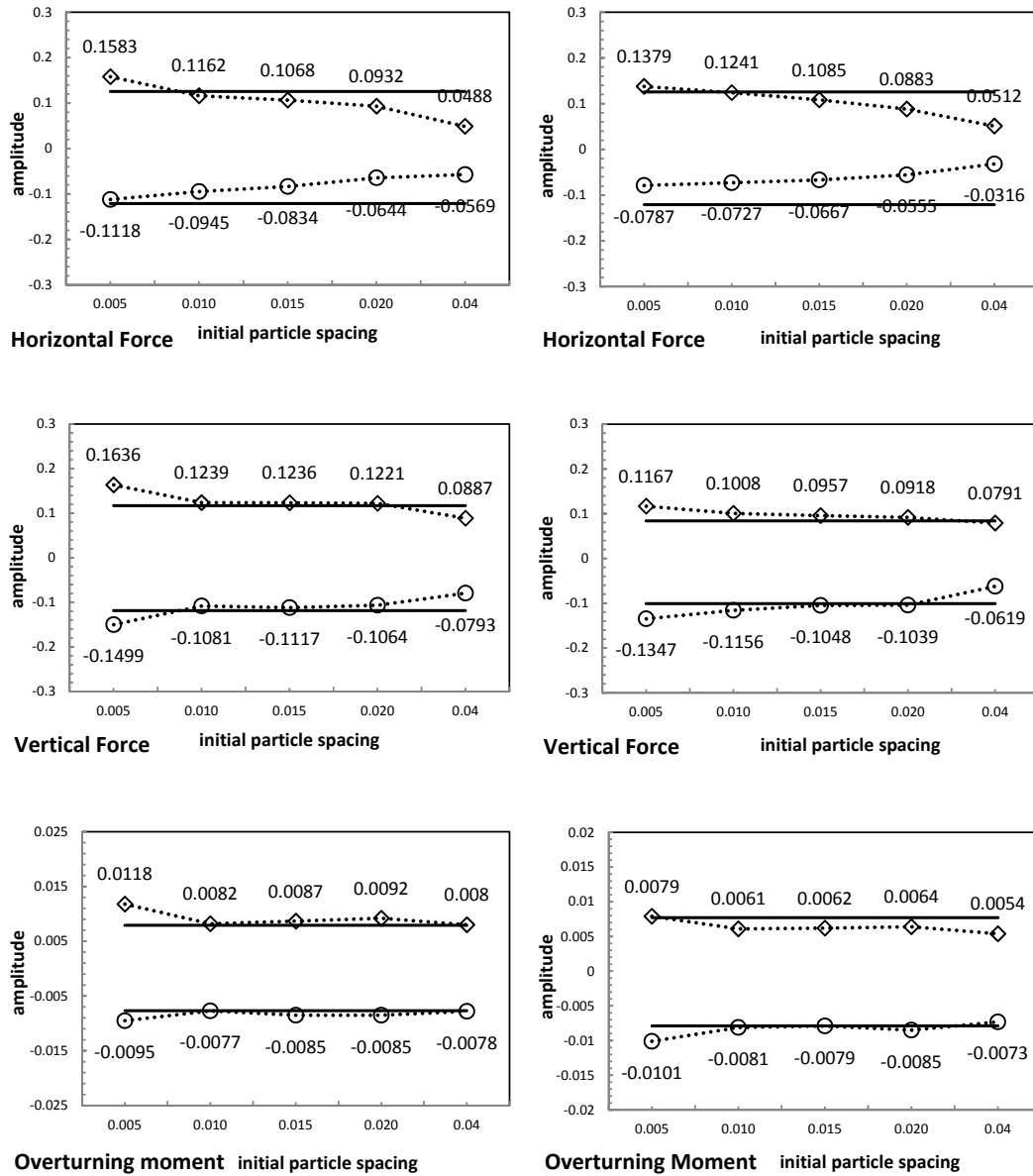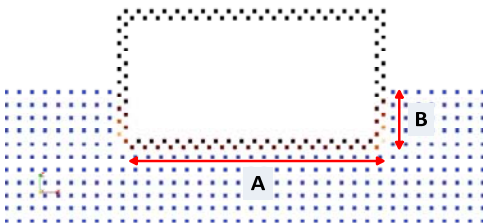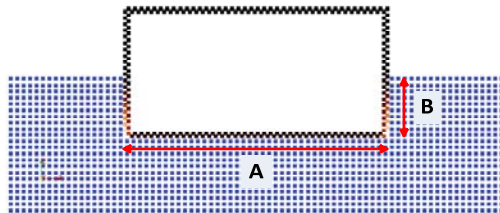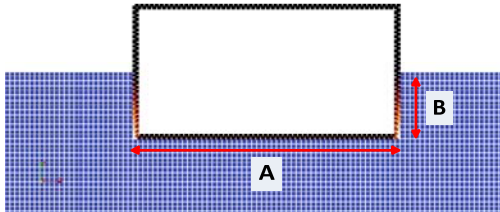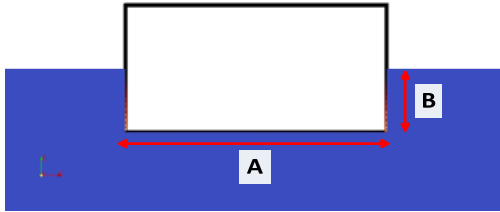
Figure 5-20 Convergence analysis (mean amplitude vs initial particle spacing. ⋯ WCSPH,− Analytical (Mei and Black, 1969). Left (H = 0.06 m), right (H = 0.20 m).

Table 5-3 Illustrations of different particle refinements

Initial particle spacing	Maximum number of particle interaction between fluid and boundary
$dx = $ 0.040 m	In A = 20 In B = 5
$dx = 0.020$ m	In A = 40 In B = 10
$dx = 0.015$ m	In A = 53 In B = 13
$dx = 0.005$ m	In A = 160 In B = 40

5.3   Dynamic coupling between waves and 2-D free-floating box

A floating body with a combination of sway, heave and roll motion is a challenging fluid structure interactions problem for numerical simulation. There are limited publications in the literature using particle method to study the behaviour of floating body in extreme waves, which would need extensive validation based on physical experimentation or sea trial (Ulrich and Rung, 2012; Omidvar et al.,2013; Ren et al., 2015). Most of the cases, standard approaches such as linear and second order wave diffraction theory is unable to capture details of nonlinearity associated with reasonably large waves. In this section, the interaction between incident waves and a free floating rectangular box is investigated. The floating box is placed within a wavelength near to the piston to fully interact with the wave. The incoming waves with given significant wave height generated by a piston-type wavemaker would encounter the floating body in real-time, pushing the body to the right side of the NWT near the damping zone. Forces exerted onto the entire body by surrounding waves are then summed up and analysed to determine the motion response of the floating box accordingly. Different hydrodynamic loadings can lead to different motion response of the floating box. Motion responses include the swaying, heaving and rolling of the box. A range of particle resolution, between 0.005 m and 0.010 m, are used to examine their effects on motion response of the floating box with particular reference to different wave heights. All results are then compared with experimental data and numerical data (Ren et al., 2015) accordingly. Wave profiles for the different case of wave heights are confirmed prior without the floating box in the NWT.

5.3.1   Numerical setup

For free-floating box, NWT with a water depth of 0.4 m is used as shown in Fig.5.21. This is less than half of the depth used in fixed box in section 5.2. The floating box is 0.30 m in breadth and 0.20 m in height. Its centroid initially locates at point (2.0 m, 0.4 m) and it can move in three degrees of freedom as sway, heave and roll without any constraint. Approximately 38,500 particles including 2,600 fixed boundary particles, 400 moving boundary particles and 200 floating particles are used in the simulations, with initial particle spacing of 0.010 m. An active piston-type wavemaker is set at x = 0.2 m initially to generate propagating waves. A beach is located at the right-hand side of the NWT to absorb the waves. The length of the beach is approximately equal to one wavelength. The motion trajectories of a free-floating box under regular waves are calculated with 2 different wave heights (Table 5.4). A reference system O-XZ

is defined, with x positive rightwards and z positive upwards. The θ in this section donates the roll angle which is positive in the clockwise direction. Wave profiles for each case are measured and confirmed at $x = 2.0$ m before the floating box is placed in the tank.
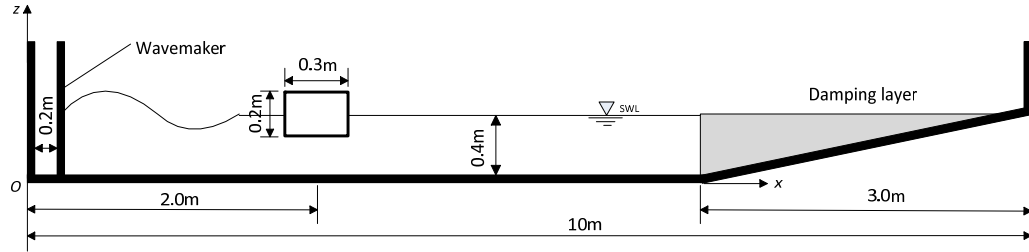
Figure 5-21 Simulation setup

Table 5-4 Numerical conditions used in the simulation

Case	H (m)	T(s)	ω(rad/s)	λ(m)
Coupling between	0.04	1.2	5.24	2.25
waves and floating box	0.10	1.2	5.24	2.25

5.3.2 Numerical parameters

Simulations are performed by WCSPH code and parameters in WCSPH can be changed and tuned depending on different problems. Artificial viscosity is important for numerical stability in WCSPH. Value of α_Π in viscosity term (equation 3.21) is set to 0.005 after some preliminary runs and 0.1 is used for delta-SPH (δ) term. Results are compared with the available experimental estimations. Initial time step is set to $dt = 2.5\mathrm{e}^{-4}$ s with time between output files of 0.05 seconds. Simulations are then run for 20 seconds with 0.5 seconds of release time. In addition, fluid particles are moved using XSPH scheme (Monaghan, 1989) with $\varepsilon = 0.5$. Filtering technique used for force prediction is similar to the one used in section 4.2.4.

Prior to simulating the interaction between waves and free floating box, it is important for the fluid and the floating box to attain the correct steady equilibrium state which is not subjected to excitation. Hydrostatic equilibrium sometimes becomes an issue in a numerical simulation where pressure tends to fluctuate near the free surface. This is due to the nature of pressure fluctuation in SPH and to determine the extent to which the particle spacing influences the fluctuation is the

key objective of this analysis. That is to say, the capability of WCSPH is tested in maintaining in time the equilibrium of a simple floating box. The initial static force on the box is calculated on the mean free surface where the immersed surface of the body contributes to the buoyancy force. The results of horizontal force, F_x and vertical force, F_z are shown in Fig.5.22. Different particle spacing is used to obtain insight into the particle refinements and the effect of the static floating box on its hydrodynamic load. In particular, it is shown that increasing the number of particles would reduce numerical errors on the box motions (Bouscasse, 2013). However, increasing too much the number of particles would lead to force fluctuation in the flow field. It is a matter of tuning the number of particles to the total domain size. Particle spacing of 0.010 m is proven to be suitable and will be used for numerical tests in the analysis in this section. The simulation with most refined particle spacing of 0.005 m suffers from force fluctuation which is as bad as other coarser particle spacing. This problem occurs due to errors accumulated from using single precision when the refinement used in the simulation is too small. This will be explained further later.
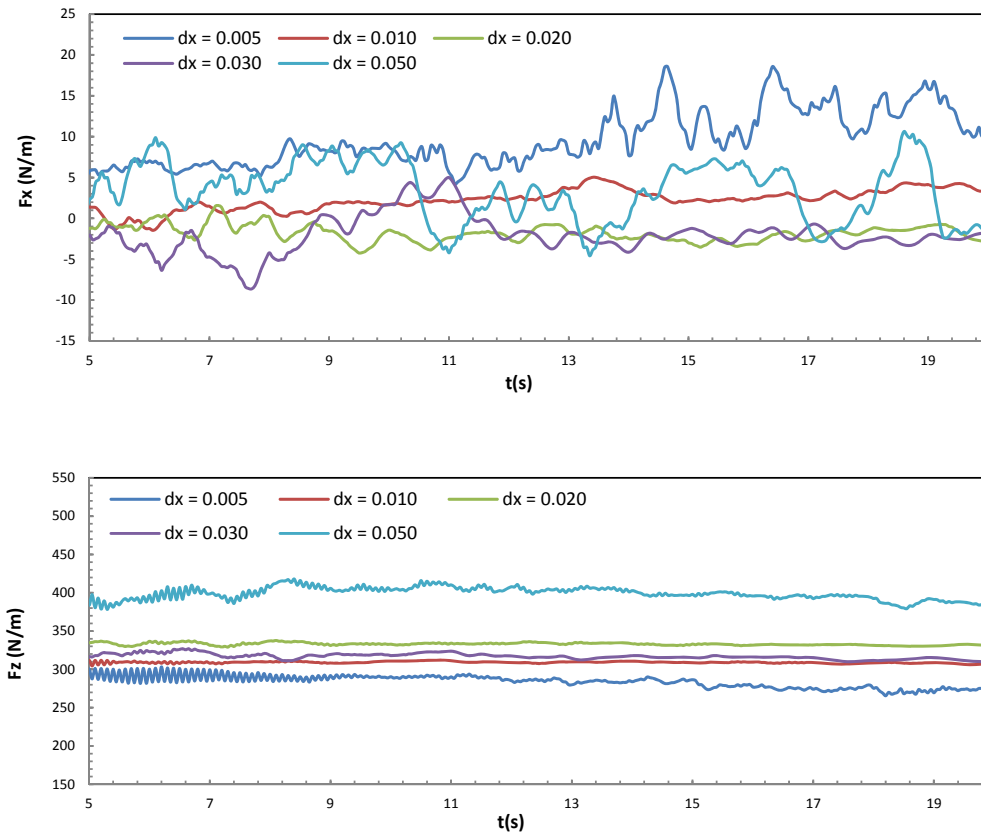
Figure 5-22 Horizontal and vertical force around stationary box for different particle spacing.

5.3.3 Results and discussion
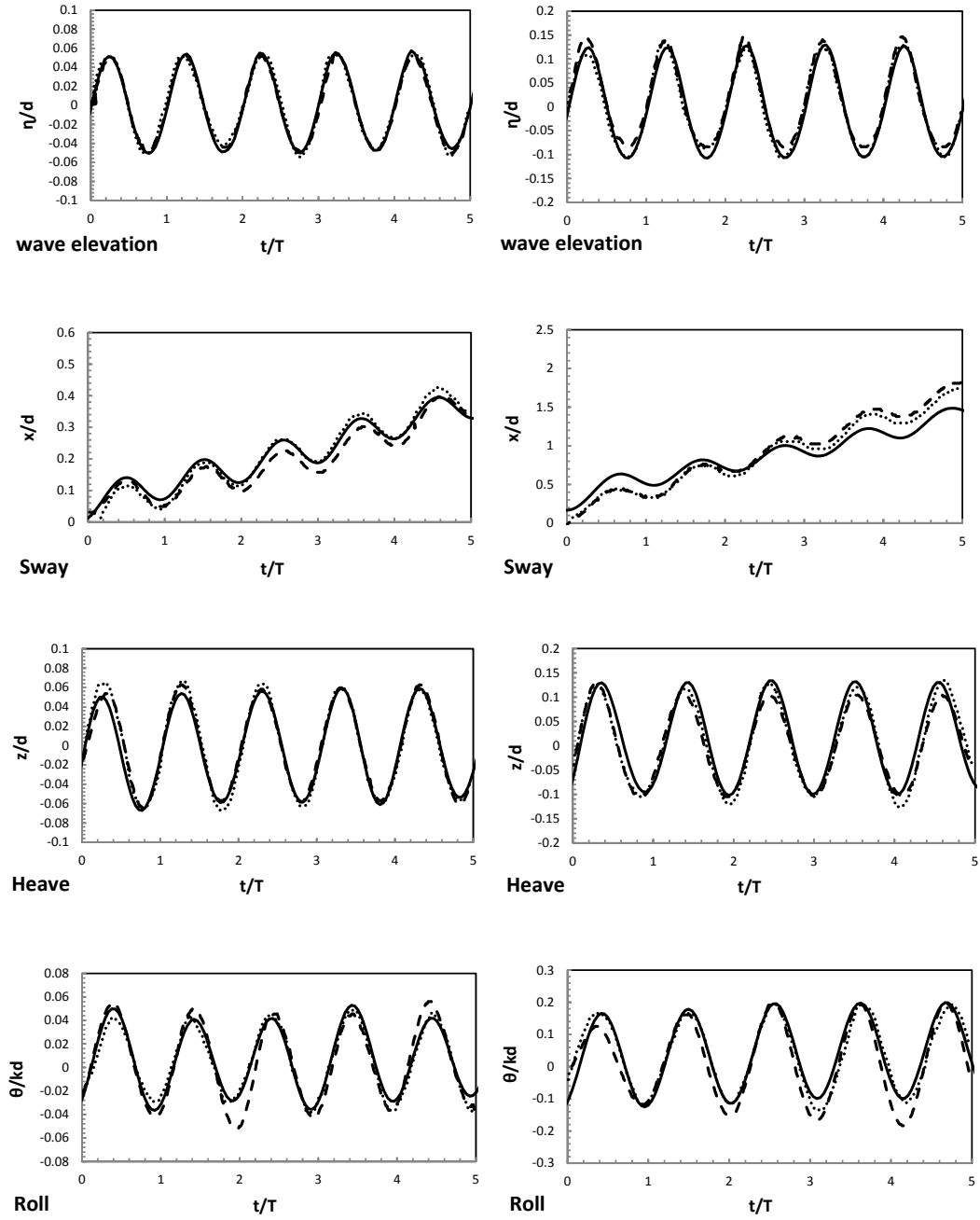
Figure 5-23 Time histories of the motion trajectories of the free-floating box under regular waves. − − SPH (Ren, 2015), ⋯ Experimental (Ren, 2015),− WCSPH. Left (H = 0.04 m), right (H = 0.10 m).

Fig.5.23 shows the time histories of the motion trajectories of a free floating box under regular waves. The solid line represents results from WCSPH, dash line represent SPH results from Ren and dot line denotes experimental data from Ren. All results for H = 0.04 m are on the left side and results for H = 0.10 m are on the right side. The comparison on the wave elevation is made for both cases first. As mentioned earlier, the wave profile is confirmed before placing the floating body inside the NWT to make sure the wave height is maintained along the tank. Waves are generated for several seconds where unsteady motion trajectories in the initial stage are abandoned. Then, time for wave elevation is recorded for 10 seconds and the same time is used in the floating case for consistency. Wave elevation from WCSPH simulation agrees well with the experimental result for both wave heights.

The centre point of floating box is used to track the motion trajectories of the floating box. All axes are not fixed for floating case so the body should move towards the right side of the NWT near the damping zone at the end of every simulation. Sway motion of WCSPH results show a good agreement with the experimental result for H = 0.04 m with similar nonlinearities. However, sway motion is slightly different in H = 0.10 m where the floating box seems to drift away faster when compared to the experimental result of the first 2 seconds after wave encounter. Possible reason is the difference in the prediction of wave elevation which is slightly higher at the wave trough than experimental result around 1.5 to 2 seconds which could introduce extra horizontal force for the additional sway motion of floating box.

Heave motion does not seem to be affected by this additional sway motion. For the case H = 0.04 m, both WCSPH and Ren's share the same trend though its position deviates slightly at the first 2 seconds of motion. Meanwhile, it is seen that WCSPH for H = 0.10 m has better agreement with the experimental in comparison to Ren's. In rolling, small nonlinearities are observed at the wave peak and trough where the floating box is unable to maintain a good sinusoidal rolling motion. However, the same tendency is observed in the experimental result and Ren's. Therefore, it is likely that poor predicted overturning moment could lead to such rolling motion. For small wave height, WCSPH results fit well with the experimental data and they are better than Ren's. A similar pattern is also observed for comparatively larger wave height. The position of floating box at various representative instants can be seen in Fig.5.24 and Fig.5.25. All the frames will add up to form a complete motion response of one period where t_0 is the initial time when the box is in horizontal position. The figures are placed side by side to the images from the experiments to show the similarity of the motion responses.
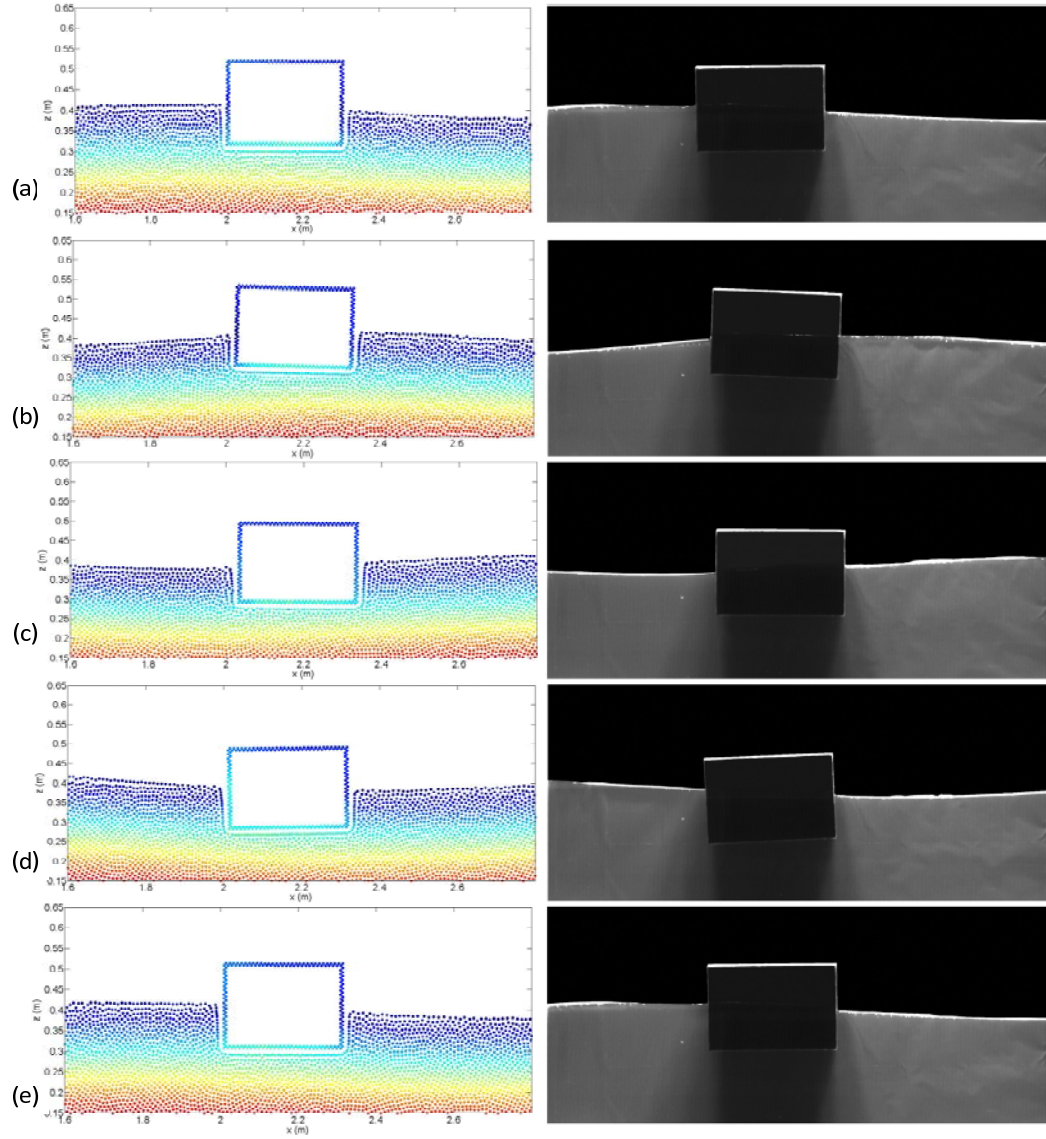
Figure 5-24 (a)$t = t_0$, (b)$t = t_0 + T/4$, (c)$t = t_0 + T/2$, (d)$t = t_0 + 3\,T/4$, (e)$t = t_0 + T$. Floating box locations and ambient wave surfaces of SPH compared with Ren (experimental). (H = 0.04m, T = 1.2s)
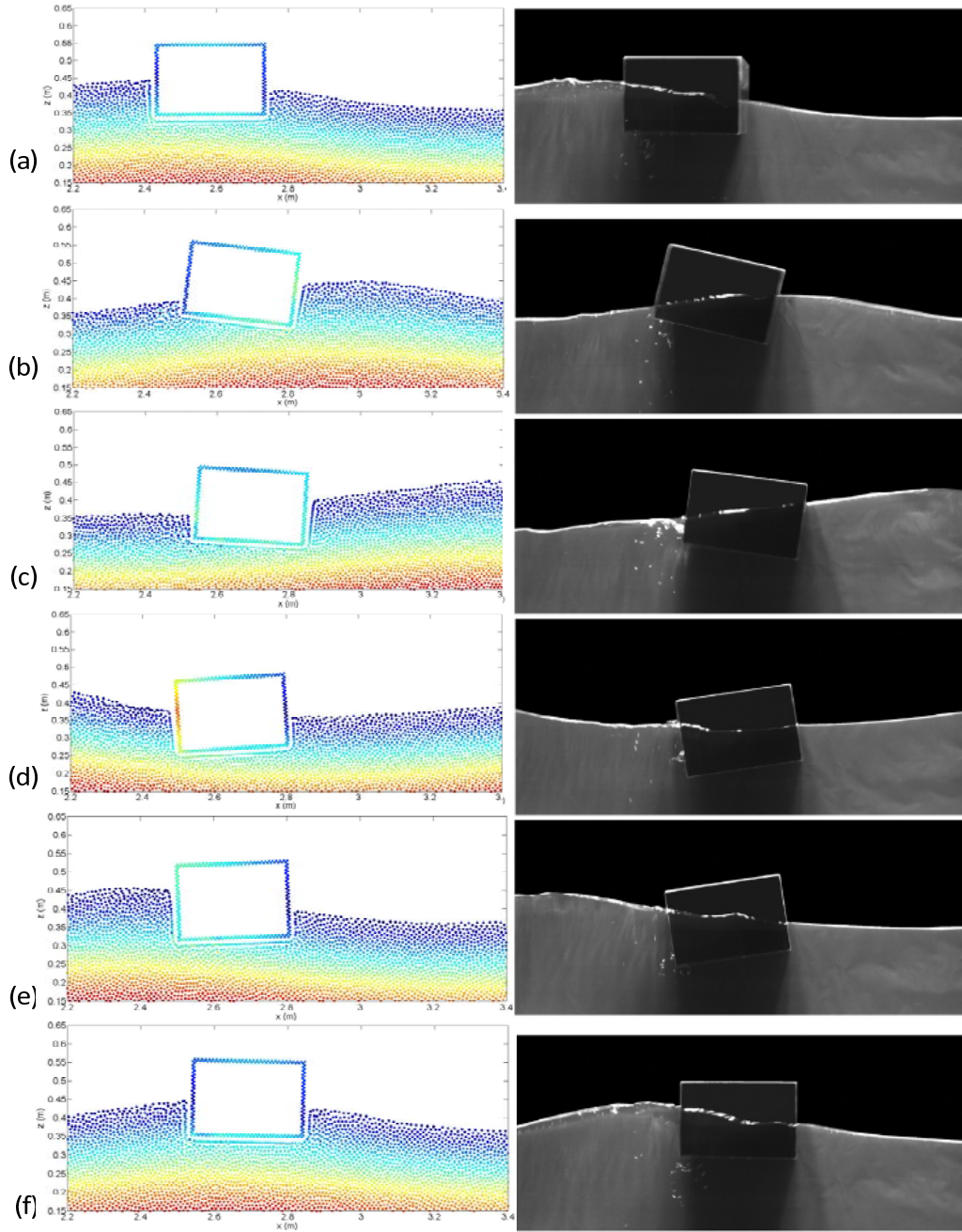
Figure5-25 (a)$t = t_0$, (b)$t = t_0 + T/4$, (c)$t = t_0 + T/2$, (d)$t = t_0 + 3T/4$, (e)$t = t_0 + T$, (f)$t = t_0 + 1.04T$.

Floating box locations and ambient wave surfaces of SPH compared with Ren (experimental). ($H = 0.10$ m, T = 1.2 s)

When there is interference between incoming and reflected waves from the floating body, nonlinearity or asymmetry in wave profile might occur. This could lead to drift motion in the horizontal direction and roll motion. To be specific, they are affected by the mean drift force and the mean roll moment imposed by the wave to the body. For a floating body, the mean drift force can be determined by the following equation (Longuet-Higgin, 1977; Ren et al., 2015).

$$\bar{F} = \frac{1}{8}\rho g H_\sigma^2 \left(1 + \frac{2kd}{\sinh 2kd}\right)$$ (5.2)

In the formulation, H_σ is the sum of the reflected wave and scattered wave height due to moving body. Referring to Fig.5.26, the first figure on the left presents the relation between drift speeds and different incident wave heights. It is reasonable to conclude that the drift speed is increasing with higher wave amplitude used. While the second figure on the right shows that the constant drift speed decreases with the increasing wave period. Since intense heave and roll motions occur around the resonance frequency, the damping reach their maximum values at the same time as drift force, effectively attenuates the drift speed.
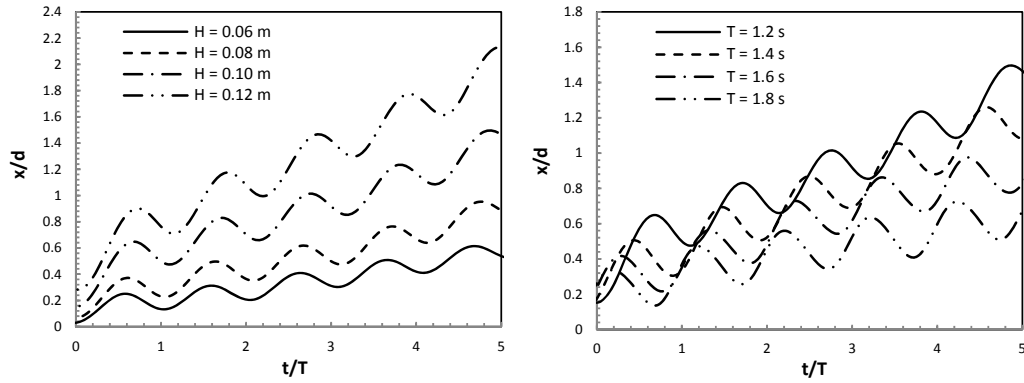
Figure 5-26 Relation between drift speed with incident wave heights and time periods

Fig.5.24 shows the motion behaviour of the floating box on the free surface when wave height is relatively small (H = 0.04 m, T = 1.2 s). Comparison of wave forces and velocities in Fig.5.27 can be related to this motion response for each time instant. It is worthwhile to mention that the positive and negative values denote the direction of forces and moment applied to the floating body. Looking at Fig.5.27, maximum positive horizontal force, F_x and negative vertical force, F_z with zero roll moment, M_y act on the floating box at its equilibrium state at t_0. At the same time, horizontal velocity, U_x is nearly zero while vertical, U_z and roll velocities, U_r approaching their maximum value. Then, the floating box starts to move towards upper left from t_0 to $t_0 + T/4$ in a clockwise rotation. At this interval, F_z reaches its peak while F_x and M_y gradually start to

approach their maximum value. Within the same time, U_z and U_r gradually increase along with maximum U_x.

Then, from $t_0 + T/4$ to $t_0 + T/2$, the floating box rotates in clockwise direction and in the next $T/4$, the floating box moves towards downright position with a clockwise rotation as seen in Fig.5.24(b)(c). At this time, F_x and M_y are at their maximum values. The floating box starts to rotates in clockwise direction from $t_0 + 3T/4$ to $t_0 + T$. An upward F_x and F_z increase and decrease, respectively, while M_y decreasing to zero. These increase the value of U_x and U_z. Finally, to complete one periodic cycle, the floating box returns to its original point at $t_0 + T$ with small displacement to the right comparing to the initial position at t_0.

A similar trend of results can be observed in wave height of $H = 0.10$ m. The only different is the longer time for the floating box to incline and perfect complete a cycle until the instant of $t_0 + 1.04T$, before finally settle down at a displacement slightly to the right from the original position at t_0. Wave forces around the floating box and its velocities show a consistent periodic change. It can be observed that the hydrodynamic loads in $H = 0.10$ m is quite similar to $H = 0.04$ m but demonstrate much higher velocities. A much higher amplitude of free surface can lead to slamming effect onto the floating box that would affect the movement. As the result, the period of wave forces on the floating box and its velocities settle around 1.04T.
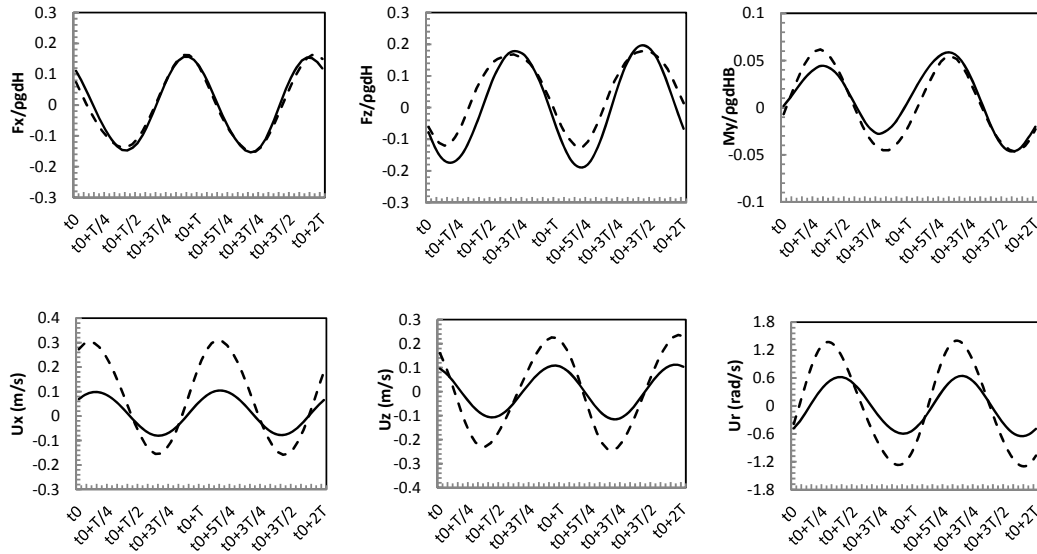
Figure 5-27 Comparison of wave forces on the floating box and its velocities.
— $H = 0.04$ m, − − $H = 0.10$ m.

5.3.4 Convergence analysis
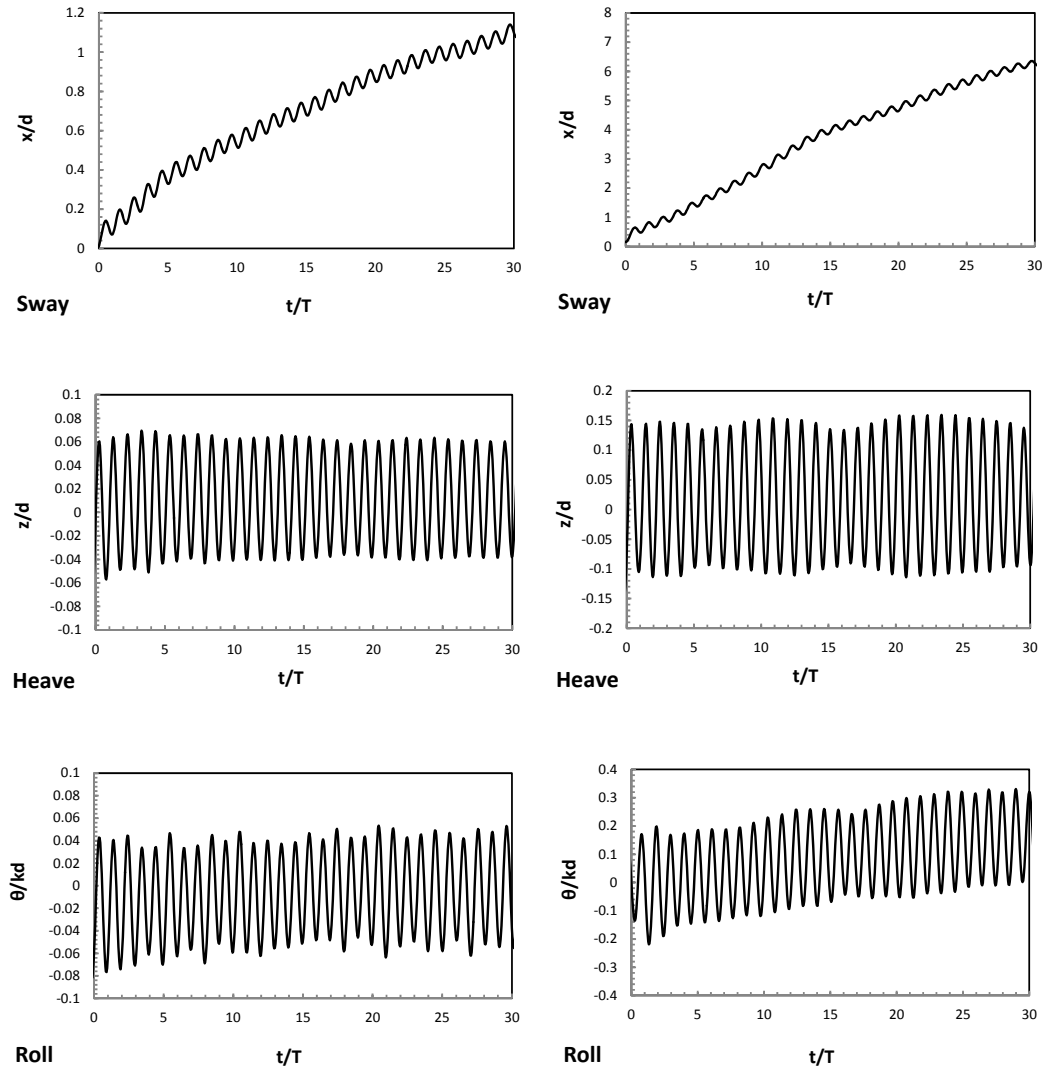
Figure 5-28 Free floating box in longer simulation runtime. Left ($H = 0.04$ m), right ($H = 0.10$ m).

WCSPH has shown good performances in the interaction of waves and floating bodies. Motion responses and forces around the entire body are well predicted against experimental values. However, to further confirm the capability of WCSPH from the perspective of stability, simulations for both wave heights are run for longer time up to 60 seconds as shown in Fig.5.28. As the floating box tends to drift away into the damping zone within the time duration, only 30 seconds of the total results are plotted for further analysis. Particular interests are given on how the floating box maintains the same pattern of motion responses without any numerical instability and the effect of the floating box on its hydrodynamic load.

Overall, the floating box is able to demonstrate good motion responses in sway, heave and roll motion. There are nonlinearities observed within time step particularly in roll motion for large wave height. As mentioned before, approximation at the interpolation process would likely introduce significant problems dealing with longer physical time as accumulated errors at each time step are inevitable. However, these are small and can be considered negligible. Therefore, to be able to perform in longer simulation runtime in a steady manner definitely would be beneficial in the intensive process of analysis particularly in the larger scale of simulation i.e. 3-D simulations.

Fig.5.29 shows the differences of mean amplitude of wave crests and troughs in heaving and rolling for different particle spacing. As each test would have an unsteady peak at several seconds during the initial runtime, only values after the first 2 seconds are considered for calculation. This test would give a better insight on the particle resolution used in the simulation. The solid line represents experimental result from Ren (2015) and the dot lines are for results from WCSPH. Every peak and trough of each result are added up and mean amplitude of the results at wave peaks and wave troughs are determined. Then, each mean amplitude is plotted against the experimental value. By doing this, the effect of particle spacing can be deduced easily. From the graph, it is seen that particle spacing of dx = 0.010 m, 0.015 m and 0.020 m produce similar values with a very small difference in the heave result for comparatively small wave height. Similarly, in section 5.2.3, a coarser resolution is not enough to capture details of forces and motion around the floating box, particularly near the free surface. The smaller spacing of 0.005 m over-predicts the mean value in roll motion for both wave heights indicating a series of inconsistent movement of the floating box. Therefore, the initial particle spacing should be small enough for precision but large enough to prevent numerical instability. Time histories of motion trajectories for different particle spacing can be found in **Appendix A**.
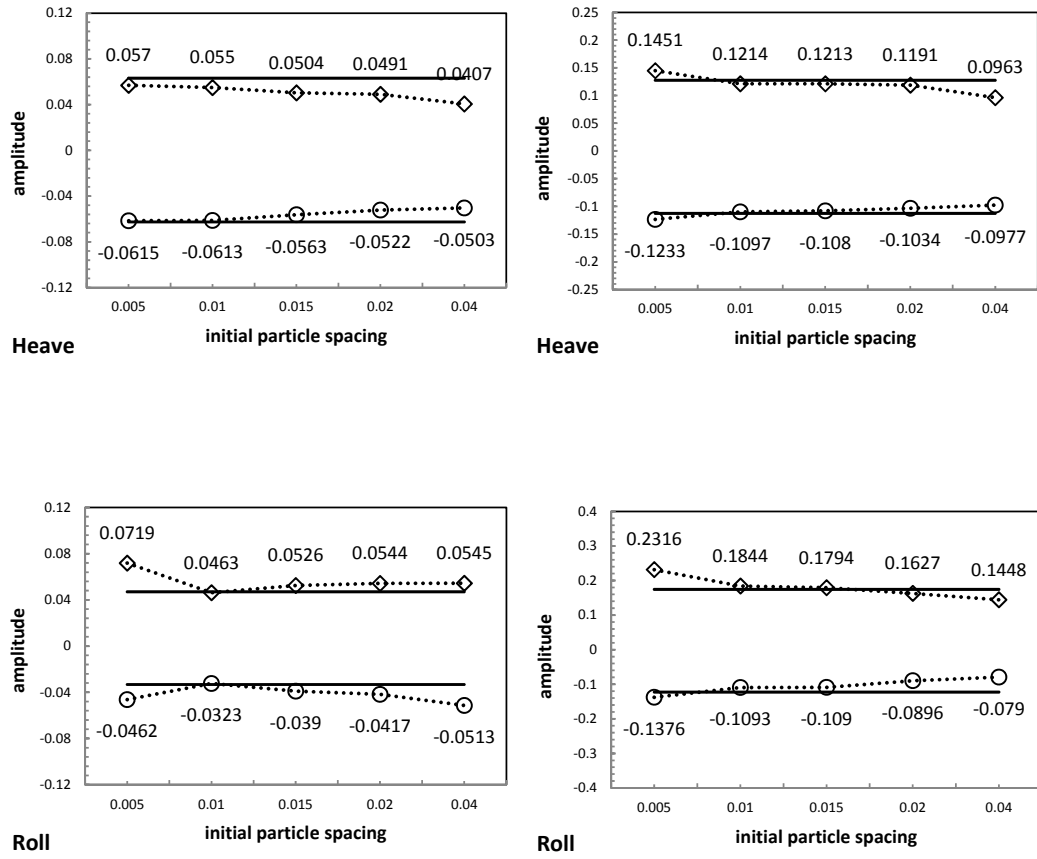
Figure 5-29 Free floating box for different particle spacings. ⋯ WCSPH,− Experimental (Ren, 2015). Left (*H* = 0.04 m), right (*H* = 0.10 m).

5.3.5 Concluding remarks

In this section, WCSPH codes from DualSPHysic are used for the interaction between 2-D simple rectangular boxes under progressive regular waves. 2 benchmark tests were carried out to validate the hydrodynamic loads acting on the body using WCSPH method. The first test dealt with diffraction problem, involving a rectangular box that was stationary in the simulation. Waves generated by the piston-type maker made a direct contact with the stationary body and the diffracted waves are damped by a damping zone. Simulations were carried out for 2 different wave heights and wave forces and moment was verified with analytical and other numerical results. Good agreement with the analytical solution of linear diffraction was seen in comparatively small wave height with discrepancies at larger wave height. This is because the surface character of the discrepancies do imply significant nonlinearity effect of wave forces which are successfully captured by the two numerical methods (WCSPH and WCSPH by Ren). Further, the interaction between waves and floating rectangular box was studied in the second test. In this work, two different conditions with different wave heights were carried out to test the slightly nonlinear effect on the motion of the floating box. Evaluations of motion response were made using experimental result and other available numerical result. Results of WCSPH agree well with experimental results with discrepancies noted in the sway and roll motions. These are mainly due to drift motion caused by the nonlinearity of the waves. The drift force would increase proportionally with increasing value of wave height and shorter wavelength. Predicted box motions were also shown side by side with the experimental result for the location of the box in one complete period of time. It can be seen that prediction of forces and motion responses around moving boundary depends on refinement on the free surface. Discrepancies at certain area might be improved by particle refinement and this factor was investigated in the convergence studies. Particle spacing refinements were made on the box and fluid domain, range from 0.005 m to 0.040 m. Refinement shows consistent results for 0.010 m, 0.015 m and 0.020 m. Coarser refinement like 0.040 m was not enough to predict all forces while smaller refinement (<0.005m) introduced numerical instability. By considering the proper particle number with the domain size depending on different case, WCSPH will be reliable enough to be used for next validation of 3-D cases.

Chapter 6

3 Dimensional validation and tests

The interaction between water waves and floating structures poses problems to different areas of marine sector especially to seakeeping for ships. Numerical predictions for such interactions involving rigid and elastic body could provide useful knowledge in the possibility of implementing particle method in seakeeping. This chapter is divided into two parts wherein the first part WCSPH is applied to simulate rigid body motion of a barge in regular waves. 3-D regular waves are generated by a piston-type wavemaker prior to the barge test; similar to the case presented in subchapter 4.3. Vertical displacements of barge under different wave conditions are calculated and their Response Amplitude Operators (RAOs) and vertical bending moments (VBMs) are determined. Results are then compared to experimental and 2 other numerical data sets. Moreover, a comprehensive study is conducted on the influence of wavelength to the numerical efficiency of WCSPH by varying particle refinement. On the other hand, the second part focuses on the investigation of the effect of domain size and particle refinement on modelling of the 3-D radiation problem using WCSPH. The oscillation of the flexible barge is prescribed based on the relevant mode shape and, in time, following a simple harmonic motion imposed to its velocity. These include the motion of heave, pitch, 2 node and 3-node distortion mode shapes. As the result, radiation forces on the body, namely added mass and fluid damping, are obtained. The predictions from WCSPH are compared with results from 3-D potential flow boundary element method and 3-dimensional RANS CFD simulations.

6.1 Rigid-body analysis of a barge in regular waves

In this study, a suitable barge is selected based on the consideration of available validation data although there are relatively few available experimental data sets that can be used for validation. The experimental model of a flexible barge by Remy et al., (2006) is adopted where numerical prediction by Lakshmynarayanana et al., (2015) also treat the barge as a rigid body for significant validation against WCSPH. Details of the segmented model used in their experiments and its structure are depicted in Fig.6.1. The barge is made of 12 segmented caissons and each caisson is clamped to a steel rod which is placed at 57 mm above deck level. The rod has a square cross-section of 1 cm × 1 cm. All the caissons are rectangular sections, except for the foremost caisson; which is slightly modified to have a bevelled shape as shown in Fig.6.2. The NWT dimensions used were 30 m × 16 m × 1 m and characteristics of the barge and the flexible rod is given in Table 6.1. Vertical horizontal and torsional bending were allowed for the flexible barge model based on modes of deformation accordingly. Tests were performed in regular and irregular waves in head waves without any forward speed. Tracking systems were located in 6 different locations of the barge, recording the barge motion responses and deformations. The 6 reference positions are shown in Table 6.2 where x, y and z measured from the stern, centreline and the keel of the barge. In the case of the regular wave, the barge motions were measured for a number of wave periods. Further details of the experiment can be found in the work by Remy et al., (2006).

Table 6-1 Barge characteristics

Length of barge,L_{pp} (caisson + clearance)	2.445 m
Beam	0.6 m
Depth	0.25 m
Draft	0.12 m
KG	0.163 m
Total mass (caissons + equipment)	172.5 kg
Length of each caisson	0.19 m
Mass of 11 caissons (except bow)	13.7 kg
Mass of 1 bow caisson	10 kg
Moment of inertia of rod	8.33×10^{-10} m^4
Bending stiffness of rod	175 Nm^2
Young's modulus of rod	2.1×10^{11} N/m^2
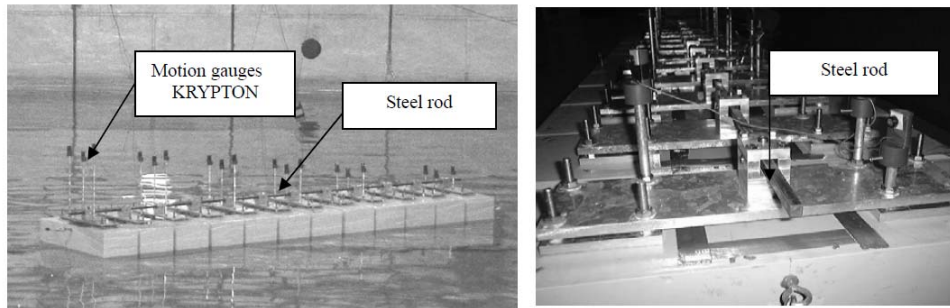
Figure 6-1 Experimental setup by Remy (2006).

Table 6-2 Measuring points from aft to fwd of barge

Location	x(m)	y(m)	z(m)
1	2.445	0.0	0.25
3	2.035	0.0	0.25
5	1.625	0.0	0.25
7	1.225	0.0	0.25
9	0.805	0.0	0.25
12	0.190	0.0	0.25
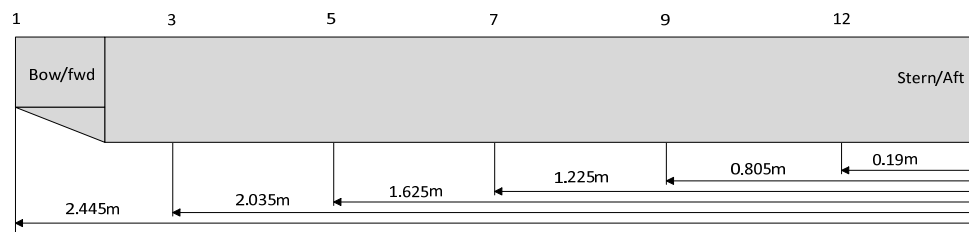
Figure 6-2 Reference points for measurements (bevelled shape for bow)

6.1.1 Numerical setup

In the 3-D case of WCSPH, boundary, and fluid domain are discretized into small particles using the same technique used in 2-D cases. The barge is represented by discrete boundary particles which directly interact with fluid particles in the NWT. Each boundary particle contributes to the properties of the floating barge and moves with the barge depending on the motion response. Data exchange between boundary particles and fluid particles take place in every iteration within a time step. However, in this case, where the boundary is not a symmetrical rectangular form, the discretization process can be tedious. Therefore, instead of using the standard technique of replacing every plane of the boundary with layers of boundary particles in the pre-processing, fill point technique is used (DualSPHysics team, 2016). Fill points technique generates the boundary particles from a single point and redistribute the point accordingly to the shape of the boundary throughout the domain (Fig.6.3). By this, any difficult frame can be easily discretized while maintaining a good refinement of particle mesh.

A 3-D domain is used for all WCSPH computations, with x along the barge and y and z in the athwartships and vertical directions, respectively. In DualSPHysics, symmetry boundary condition is not yet applicable where only half of the dimension is modelled. Therefore, barge and fluid domain must be modelled in full dimension making it computationally expensive. The lengths of the domain and side walls are determined based on wavelengths (λ) of each individual case. As shown in Fig.6.4, the barge is located at about 1.5λ from the wavemaker with the numerical beach at the end of the NWT to damp out the incoming waves. The numerical beach is set to 1.5 times of barge length, assuming 5 m as the longest wavelength produced in this test. The distance of barge's centroid to each of the side wall is fixed at 2.2 m for all cases. Three probes are located around the barge to confirm the wave elevation and to track wave reflections from the side walls. Displacement in x direction is fixed, allowing only the motion of heaving and pitching.

For this rigid body simulation in head waves, particle mesh is determined by considering the actual size of both barge and NWT. In finite volume method, it is possible to use NWT the size of 30 m × 16 m × 1 m due to variable mesh use in the vicinity of the barge. This is different with WCSPH where only uniform particle distribution can be applied. The NWT used in this study is large enough for the generation of the waves near the floating body and for the wave to be completely damped in the far field damping zone. Besides overall dimension, selection of suitable particle spacing for fluid domain and boundary also depends on the number of particles

produced, the computational cost involved and prevention of numerical instability. Based on previous convergence test of different particle spacings, 3 particle spacings are found to be the most consistent especially in maintaining a good wave profile. They are dx = 0.010 m, dx = 0.015 m and dx = 0.020 m. Any particle spacing range between these numbers is also considered suitable and can be used in the simulation. However, particle spacing of 0.010 m leads to particle number up to 25M, bigger than a maximum number can be handled by current GPU. Therefore, dx = 0.020 m is employed for all cases, with total 4M particles (3.5M fluid particles and 0.5M boundary particles). Particle spacings of 0.012 m and 0.015 m are used in the convergence studies for motion response in comparatively lower frequencies. Boundary particles are selected for each wall to mimics the real conditions of an NWT and at each iteration, the position of piston wavemaker is updated by a sinusoidal function. For the test conditions, the response of the barge treated as a rigid body in head regular waves is calculated for the five wave periods, shown in Table 6.3. The objective is to gain insight into the effect of domain size, damping beach, motion of the rigid body, and particle refinement around the body and free surface for the simulation at each wave period. The rigid body responses calculated using WCSPH is compared with results from 3-D finite volume CFD method (Star CCM+) by Lakshmynarayanana et al., 2-D numerical (MARS) and experimental observation by Remy.

The flexibility of the barge in the structural modelling can be simulated by treating the barge as a non-uniform Timoshenko beam allowing only the deformation in the vertical plane. Considering the beam with the flexural rigidity EI, the mass per unit length m, the mass moment of inertia mr^2, shear modulus G, the cross-sectional area $A(x)$, and the constant dependent on the cross-section geometry k, the equation of motion (Jensen, 2001) is given as:

$$\frac{\partial}{\partial x}\left[EI\left(1 + \mu\frac{\partial}{\partial t}\right)\frac{\partial \phi}{\partial x}\right] + kGA\left(1 + \varepsilon\frac{\partial}{\partial t}\right)\left(\frac{\partial v}{\partial x} - \phi\right) - mr^2\frac{\partial^2 \phi}{\partial t^2} = 0 \tag{6.1}$$

$$\frac{\partial}{\partial x}\left[kGA\left(1 + \varepsilon\frac{\partial}{\partial t}\right)\left(\frac{\partial v}{\partial x} - \phi\right)\right] - m\frac{\partial^2 v}{\partial t^2} = -f(x,t) \tag{6.2}$$

where $v(x,t)$ denotes the vertical deflection and $\phi(x,t)$ denotes the angular displacement. The right hand side term of $f(x,t)$ represents the load or impact due to external force on the barge which is fluid force in this study. Modal superposition method (Jensen, 2001) is used to solve deflection and angular displacement for the case when the dry mode shapes of the beam used to describe the barge deformation have been predetermined.

Table 6-3 Selected numerical test conditions

T (s)	ω(rad/s)	λ(m)	H(m)
1.8	3.490	5.058	0.1
1.6	3.926	3.996	0.1
1.2	5.235	2.248	0.1
1.0	6.283	1.561	0.1
0.9	6.981	1.264	0.1
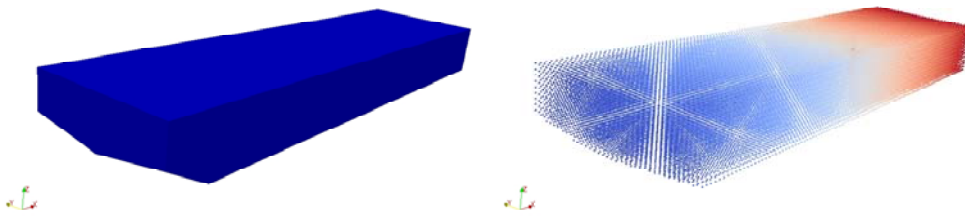
Figure 6-3 Conversion from solid to particles interface
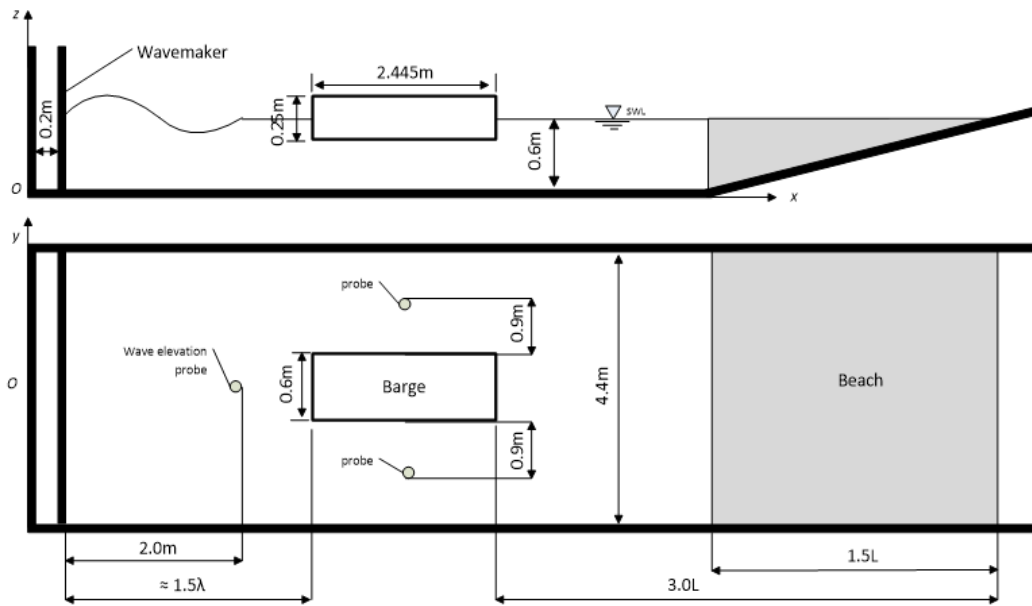
Figure 6-4 Setup of the computational domain with top and side views

$$v(x,t) = \sum_{j}^{n} u_j(x)w_j(t) \tag{6.3}$$

$$\phi(x,t) = \sum_{j}^{n} \varphi_j(x)w_j(t) \tag{6.4}$$

The orthogonality between the dry mode shapes can be written as

$$A_j = \int_0^L \left(mr^2\varphi_j^2 + mu_j^2 \right) dx \tag{6.5}$$

Damping coefficients μ and ε can be assumed to be the equal, i.e. $\mu = \varepsilon$ and are independent of the longitudinal position x. Thus, by applying the orthogonality condition, the time dependent weighting functions $w_j(t)$ and corresponding moment can be determined as

$$\ddot{w}(t) + \mu\omega_j^2\dot{w}_j(t) + \omega_j^2 w_j(t) = \frac{1}{A_j}\int_0^L u_j(x)f(x,t)\,dx \equiv F_j(t) \tag{6.6}$$

$$M_m = -EI\frac{\partial^2 v}{\partial x^2} \tag{6.7}$$

where EI is the vertical bending stiffness or flexural rigidity. In this study, the non-uniform Timoshenko barge is modelled based on finite element method in Lakshmynarayanana et al., (2015). The total mass is distributed along the particles without having to divide the length of the barge into smaller beam elements. Due to the simplicity of the barge, rotary inertia and shear are negligible. Therefore, the eigenfunctions u_j and φ_j of dry mode shapes can be determined by Euler beam theory approximated by polynomials function (Kim et al., 2014). Solving a two-way coupling (*implicitly*) is known to be complex and another way to evaluate hydroelasticity in this analysis is to consider the deformation in a one-way coupling approach (*explicitly*). That is to say the hydrodynamic and hydrostatic load distributions are computed from a rigid body simulation. There is no passing back and forth of information between barge and fluid particles at each time step during simulation. This process will be done as post processing procedure where external force from the fluid particle is computed to estimate the load distributions and moments for different mode shapes of the barge. The feasibility of implementing this approach will be discussed in the results section by presenting the comparison to rigid body results and 3-D predictions of STAR-CCM+ (Lakshmynarayanana et al., 2015).

6.1.2 Numerical parameters

This section describes the parameters and variables that have to be tuned to optimise the simulation. Similar to previous 2-D tests, artificial viscosity is important for numerical stability in WCSPH. Value of α_Π in viscosity term (equation 3.21) is set to 0.008 and delta-SPH (δ) term is set to 0.001. Initially, a high value of delta-SPH (δ) was tested for a few frequencies. This had caused penetration of fluid particles into the floating body. Small value of delta-SPH can also lead to a noisy free surface. Hence, a balanced combination of artificial viscosity and delta-SPH are selected. Wendland kernel is employed as the interaction kernel. After few tests, it is found to be best to allow the fluid flow around the barge to initialise and to become steady before the piston motion commences. Initial time step is set to $dt = 1.0e^{-4}$ s with release time of 2 seconds. Simulations are then run for 22 seconds. At the release time, it has been observed that pressure in the flow will fluctuate as the fluid particles redistribute themselves from the initial distribution. Therefore, to minimise this effect and facilitate a more robust solution by reducing unphysical oscillations, a ramp time of 40 time steps is allocated. Time step is chosen according to Courant number but it will be adjusted automatically depending on the value of coefficient of sound used. In addition, fluid particles are moved using XSPH scheme (Monaghan, 1989) with $\varepsilon = 0.5$. Filtering technique used for force calculation is similar to that used in section 4.3.2. Similarly in wave generation analysis, the smoothing length h used is 1.3 times of the initial particle spacing in all simulation unless stated otherwise.

6.1.3 Results and discussion

6.1.3.a Wave generation by paddle motion

In this section, the wave profiles generated by piston wavemaker before the instalment of barge model are presented. The tests are carried out to fulfil 2 main objectives. The first objective is to confirm the wave heights of generated regular waves for varying frequencies. Wave height is tracked along the NWT in each time step as the wave propagates. The second objective is to determine the location of the barge where the loss of wave height is at the minimum while allowing gap between the barge and wave maker for periodic solutions without reflection contamination. A similar test has been carried out in the 2-D case previously with satisfactory result from WCSPH. However, those 2-D cases did not consider wave reflections from the side walls where wave height could be affected (Lakshmynarayanana et al., 2015). Additional 6 wave probes are added to the initial 3 probes shown in Fig.6.4. The initial 3 probes are used in the

second test with the presence of barge model. All 6 tracking probes are presented in Table 6.4. In the table, each probe is assumed to correspond to the reference point on the barge denotes by Pt 1 to Pt. 12. Tracking points are fixed within 1.5λ from the wave maker depending on different frequencies and then wave heights are recorded in every iteration. Tests were done for different locations and it has come to the conclusion that locations listed in the table may produce the most optimised result.

Mean wave height for different conditions used in this test can be found in Fig.6.6. The dotted lines represent results from WCSPH and they are compared to the analytical result with a fixed wave height of 0.10 m along the NWT. In the literature review, the issue of maintaining wave height in WCSPH simulations has been discussed and further explained in chapter 4. From Fig.6.6, the wave profiles are observed to be in a good agreement with the analytical solution with small discrepancies for comparatively low frequency. Time history of wave elevation for $\omega = 3.490$ rad/s revealed little wave dissipation at each tracking probes, with a maximum decrease in wave height around 12% as the simulation progressed (Fig.A.15). Wave elevation at different time step can be found in Fig.6.5. The visualisation is improved by representing the particles by surface using *IsoSurface.exe* provided by DualSPHysics (Crespo et al., 2015).
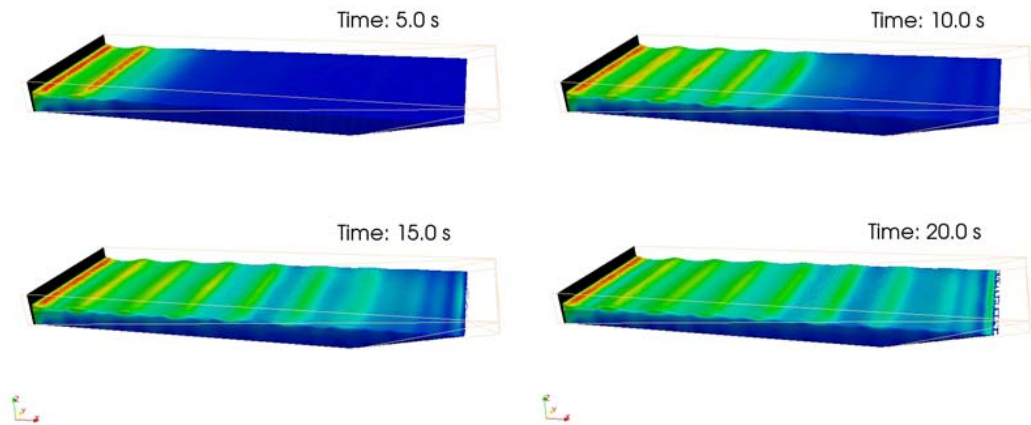
Figure 6-5 Different instants of wave elevation simulation at $\omega = 6.283$ rad/s. Color represent celerity of wave.

Table 6-4 Recommended location of barge represented by 6 tracking probes at different frequencies.

Tracking probes	Corresponding points on the barge	Locations (x, y, z)				
		T = 1.8 s ω = 3.490 rad/s λ = 5.058 m	T = 1.6 s ω = 3.926 rad/s λ = 3.996 m	T = 1.2 s ω = 5.235 rad/s λ = 2.248 m	T = 1.0 s ω = 6.283 rad/s λ = 1.561 m	T = 0.9 s ω = 6.981 rad/s λ = 1.264
1	Pt. 1	3.36, 0.0, 0.6	4.51, 0.0, 0.6	3.61, 0.0, 0.6	3.31, 0.0, 0.6	3.31, 0.0, 0.6
2	Pt. 3	3.77, 0.0, 0.6	4.92, 0.0, 0.6	4.02, 0.0, 0.6	3.72, 0.0, 0.6	3.72, 0.0, 0.6
3	Pt. 5	4.18, 0.0, 0.6	5.33, 0.0, 0.6	4.43, 0.0, 0.6	4.13, 0.0, 0.6	4.13, 0.0, 0.6
4	Pt. 7	4.58, 0.0, 0.6	5.73, 0.0, 0.6	4.83, 0.0, 0.6	4.53, 0.0, 0.6	4.53, 0.0, 0.6
5	Pt. 9	5.00, 0.0, 0.6	6.15, 0.0, 0.6	5.25, 0.0, 0.6	4.95, 0.0, 0.6	4.95, 0.0, 0.6
6	Pt. 12	5.62, 0.0, 0.6	6.77, 0.0, 0.6	5.87, 0.0, 0.6	5.57, 0.0, 0.6	5.57, 0.0, 0.6

T = 1.8 s, ω = 3.490 rad/s

T = 1.6 s, ω = 3.926 rad/s

T = 1.2 s, ω = 5.235 rad/s

T = 1.0 s, ω = 6.283 rad/s

T = 0.9 s, ω = 6.981 rad/s
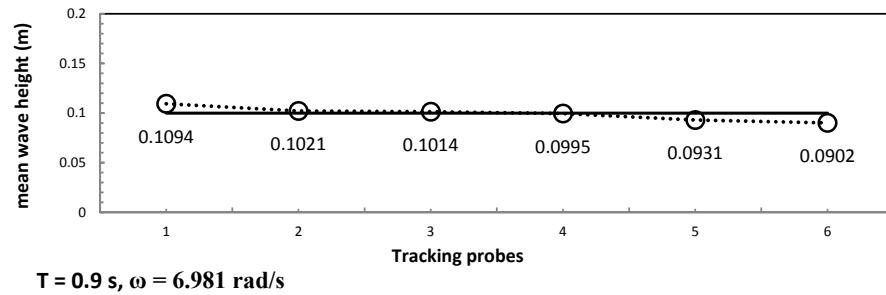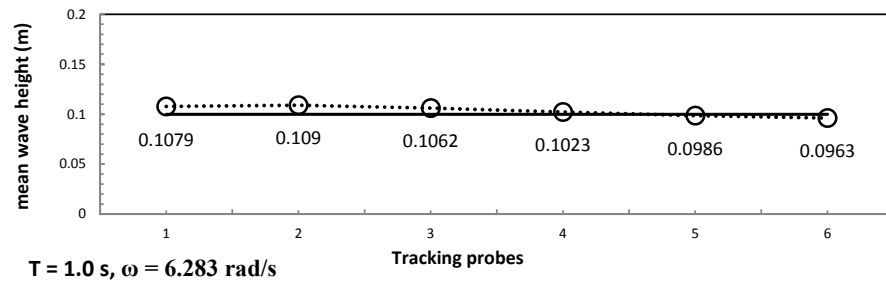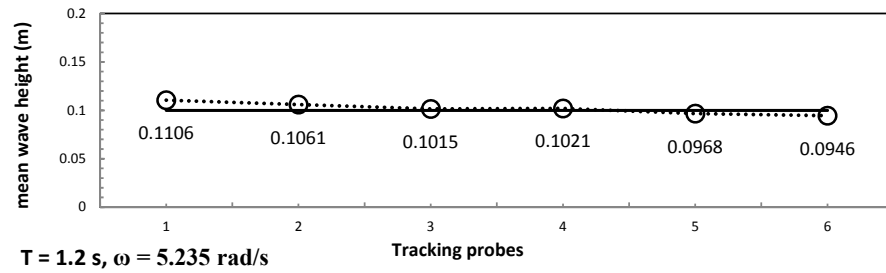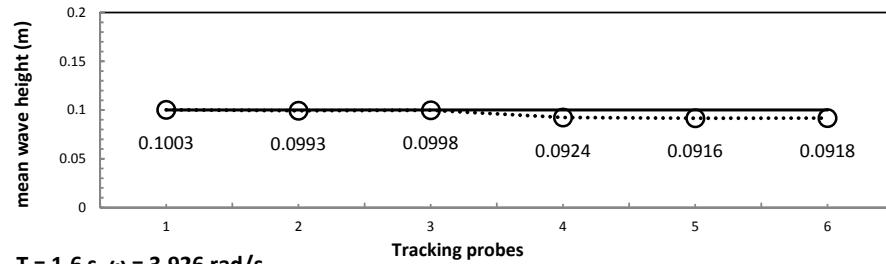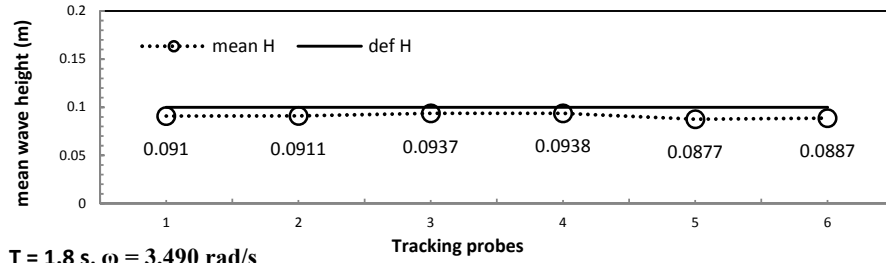
Figure 6-6 Mean wave height at each tracking probes (before the instalment of the barge) for different frequencies.

6.1.3.b   Motion response of rigid body in head waves

In this section, WCSPH results are compared with other numerical and experimental data and the motion responses of the barge when treated as a rigid body in regular waves is assessed. As shown in Fig.6.4, wave profile in the vicinity of the barge is checked using data from 3 wave probes. By comparing the wave elevations, it is noted that the wave dissipation and wave reflection are insignificant as the simulation progresses. The Response Amplitude Operators (RAOs) obtained from WCSPH are shown in Fig.6.8. Time history of vertical displacement at each reference point can be found in **Appendix A (**Fig.A.16 to Fig.A.18**)**. The amplitude of the results over 4 to 6 wave period is averaged to determine the value of RAOs. The responses are from a 2-D linear potential flow using strip theory and Timoshenko beam theory denoted as MARS (Bishop and Price, 1979) and two-way coupling between a finite volume CFD method, by STAR-CCM+, and a finite element method (FEM), by ABAQUS denoted by STAR. Excluding the distortions, the displacement comprises only rigid body motion of heave and pitch denoted by MARS_Rigid and STAR_Rigid. Overall, a good qualitative agreement is observed with MARS_Rigid and STAR_Rigid but with small discrepancies noted around point 7 and point 9 at comparatively low frequencies. Additional hydroelastic measurement from Remy et al., (2006) is plotted to show the relation between deformations and motion responses. It is worthwhile to mention that the prediction of the 2-D flexible barge by MARS is not included in this analysis (Lakshmynarayanana et al., 2015). Results from the experimental data reflect the behaviour of a flexible barge, giving insight on how it differ in comparison to the rigid barge.

First, observations are done at relatively high-frequency ranges where $\omega > 5.235$ rad/s. There is an overestimation by WCSPH in pt.1, pt.3, and pt.5 which indicate that the barge experiences 3-D effects from instantaneous wave contour around the body (Fig.6.7). The effects are mainly due to the strong localised nonlinear wave systems, which are not well modelled in a 2-D linear potential flow theory. However, predictions from WCSPH are recorded lower than those from STAR-CCM+ particularly at $\omega = 5.283$ rad/s with a maximum difference of 30%. Possible reasons of these lower predictions may be the breaking wave on the free surface around the forward section and repulsive nature of the dynamic boundary particles, which could lead to fluctuation of pressure affecting the flow fields. Looking at the highest frequency, most of the predictions from WCSPH and STAR-CCM+ are observed to have better agreement with experimental data at all points. In this case, the diffraction effects become dominant where the wave approaches the bow, perturbing the free surface at the vicinity of the barge regardless of its flexible or rigid condition, and therefore contributes only a small change.
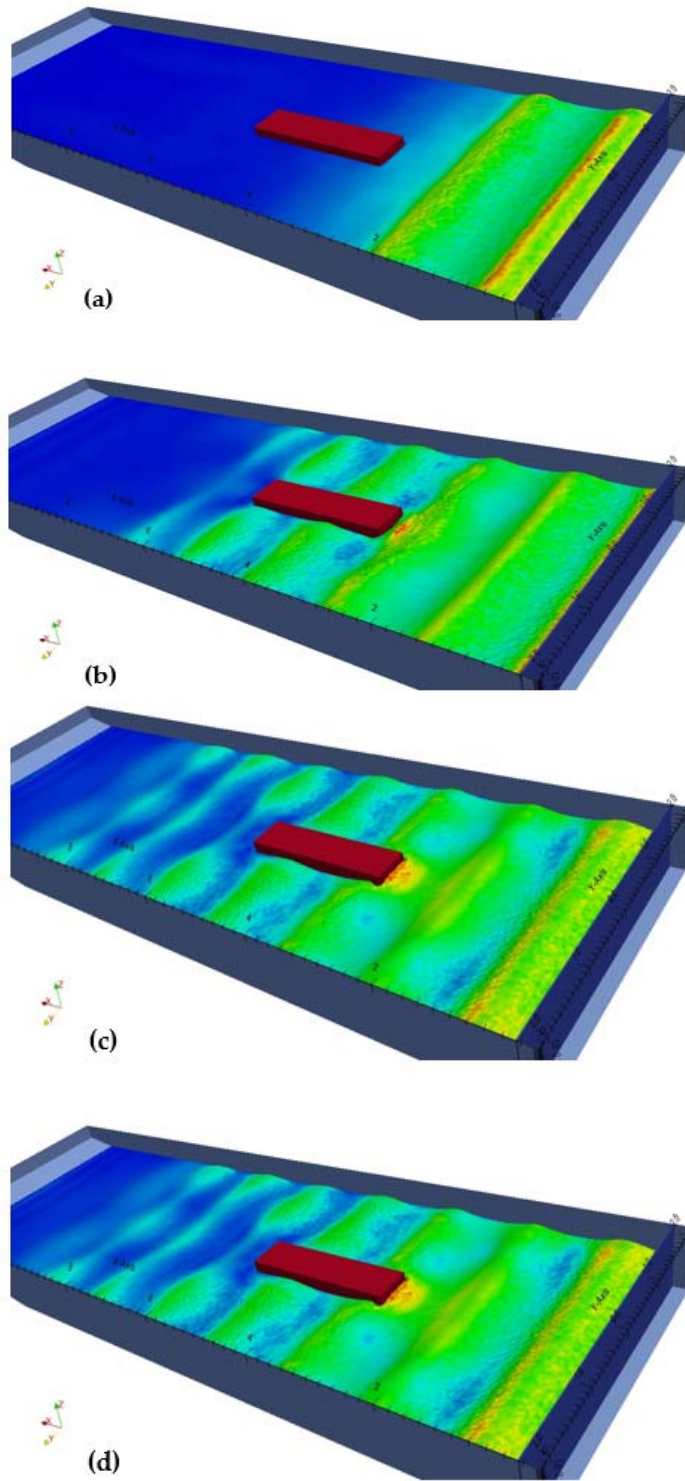
Figure 6-7 Development of wave profile hitting the floating barge for $\omega = 6.981$ rad/s.
(a) $t = 5.0$s, (b) $t = 5.0$s, (c) $t = 5.0$s dan (d) $t = 5.0$s.
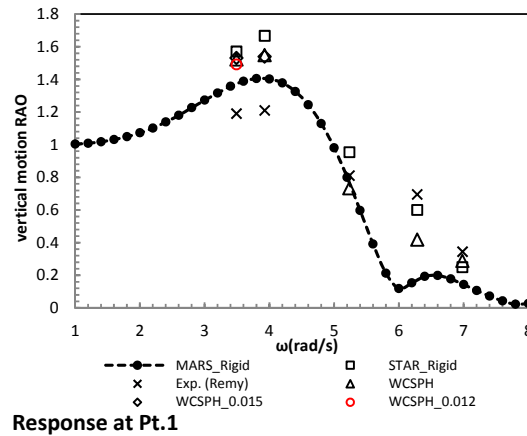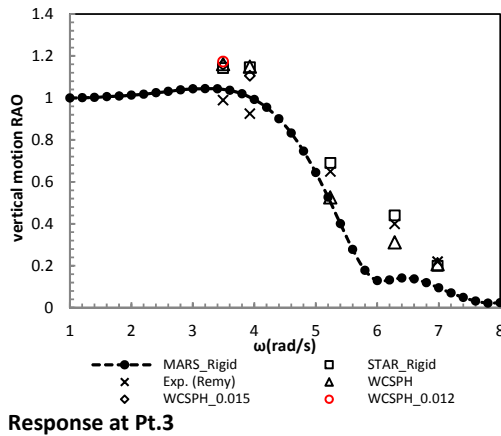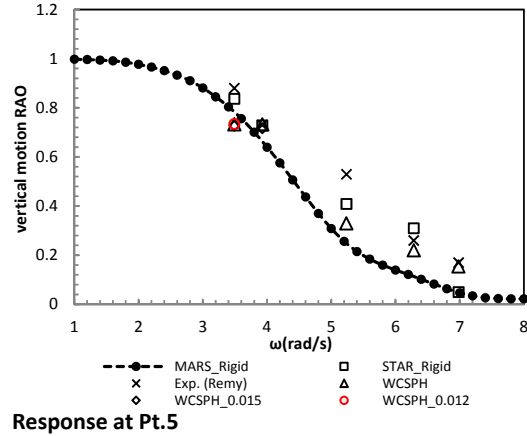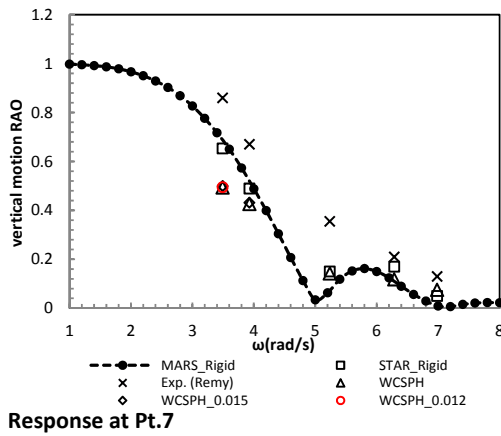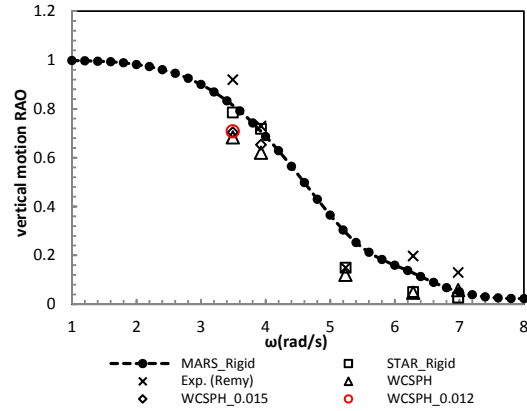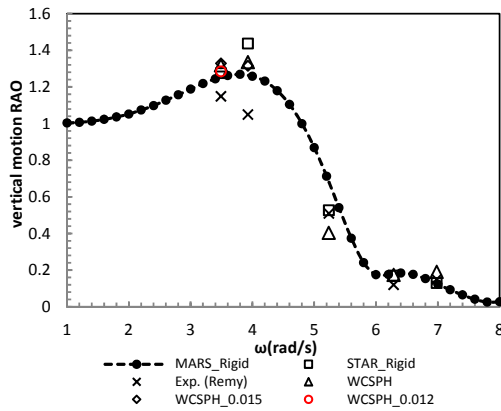
Figure 6-8 RAOs of vertical displacements along the barge, point 12 near the stern and point 1 near the bow, for both rigid and flexible body analyses

Most deviations from potential theory are demonstrated when ω < 5.235 rad/s. In pt.1, pt.3 and pt.12, vertical displacements by WCSPH are found to be over predicted while in pt.5, pt.7 and pt.9, the values are under predicting the potential theory. Clearly, rigid body mostly related to the influence of strong bow and stern waves due to motion when operating in pitch motion. However, most of the predictions seem to agree well with STAR_Rigid except for pt.7 and pt.9. This deviation is due to their location and will further explain. In locations near bow and stern, results of the flexible body from the experimental can be seen to deform following the wave elevation and therefore, recorded a smaller value of responses than the rigid body. The opposite responses demonstrated by experimental data in pt.5, pt.7 and pt.9 suggest a similar behaviour of the flexible body.

One notes that for pt. 7 and pt. 9, the characteristics of the predictions are slightly vary from MARS_Rigid and STAR_Rigid due to the location of the points which is at the amidships. In general, motion around amidships is mainly influenced by the heave motion of the barge. It is worthwhile to mention that similar phenomenon is observed in heaving rectangular section in chapter 5, where the obtained added mass coefficient from WCSPH did not agree well with experimental and theoretical data for low-frequency ranges. The similar issue continues for this 3-D case and this might be attributed to the fact that there is a possibility of pressure fluctuation between the fluid–structure interfaces.

A comprehensive comparison between RAOs at different frequencies is presented in Fig.6.9 and Fig.6.10. Colours represent the velocity of the generated waves. As one can observe in ω = 3.926 rad/s, long-crested wave i.e. $\lambda \geq 2.245$ m (length of the barge) allows for bow to reflect most of the incoming waves, one after another. Higher velocity around bow suggests high impact of slamming due to higher vertical displacement. This creates a continuous strong localised wave contour along the barge which affects the vertical displacement of the barge particularly at the amidships (Pt.7 to Pt.9). Similar pattern is shown in Fig.6.10 whereas slamming event takes place at the bow. This effect distinguishes the 3-D motion in the simulation from its 2-D motion counterpart. Shorter wave generated in higher frequency seems to be able to overcome the reflected incoming wave, preventing major wave dissipation. Thus, vertical displacement on the vicinity at the amidships is less affected due to the weak localised wave contour.
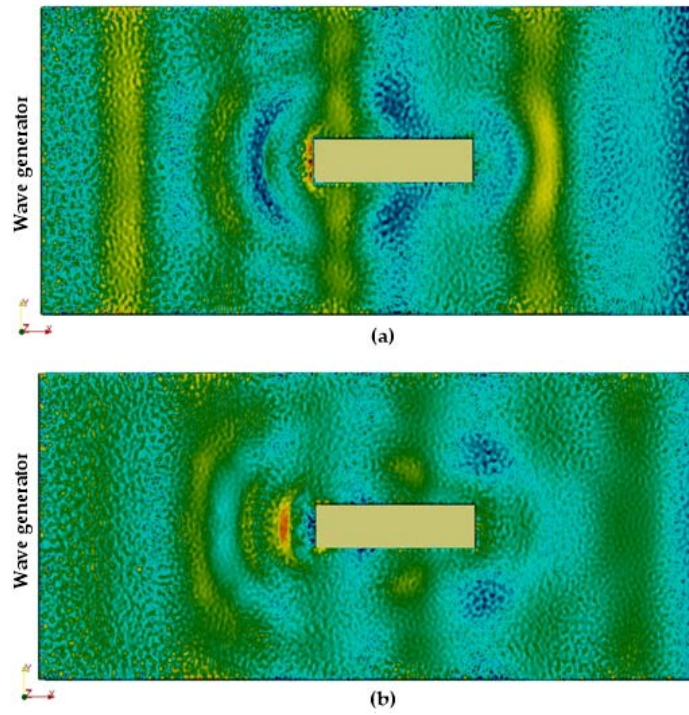
Figure 6-9 Diagram of instantaneous wave contour around the rigid body at 9.15 s and 9.85 s for ω = 3.926 rad/s.
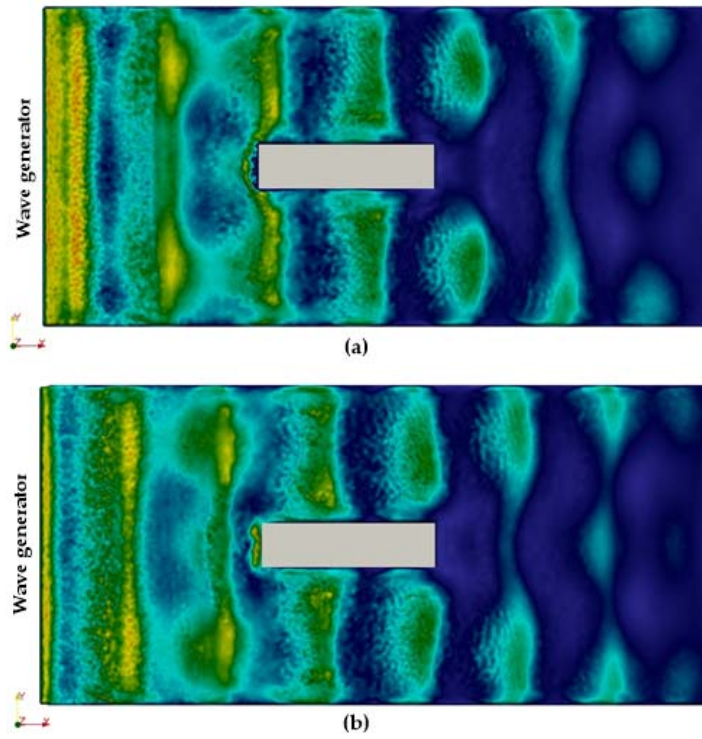
Figure 6-10 Diagram of instantaneous wave contour around the rigid body at 13.95 s and 14.5 s for ω = 6.283 rad/s.

To better assess the dependence of prediction accuracy of RAOs on the initial particle spacing, refinements with larger particle numbers are made for simulations with ω = 3.490 rad/s and ω = 3.926 rad/s. In contrast to the wave generation case where refinement has yielded a better prediction, the case is different here. Even after using particle spacing of dx = 0.012 m with 18M particles and dx = 0.015 m with 9M particles, the results do not show any significant changes. The same issue is reported not just for particle method, Zhou and Ma (2010) in their work on violent sloshing waves by MLPG method conclude that pressure could not be improved by simply increasing the resolution. However, the size of the computational domain do affect the quality of the solution due to the presence of boundary effects and therefore it must be selected carefully in order to balance the overall computational cost. In order to understand further the role of refinement in WCSPH, tests on the effect of different particle spacings under different wavelengths are carried out and the results are presented in Fig.6.11. It is worthwhile to mention that the maximum and minimum numbers of particles used in this simulation are chosen relative to the wavelength, wave height and domain size employed in every case to prevent any numerical instability. The longest wavelength investigated is 16 m while the shortest is around 1.5 m. By investigating the peaks in free surface elevation, the accumulated simulation errors increase with increasing values of wavelength, regardless the number of particles used. However, the errors are found to change gradually with highest relative error recorded at 60%. An increase of error for λ < 2 m in all cases particularly in case dx> 0.020 m indicates some numerical instability in free surface at comparatively high frequency simulations. No further investigation is conducted to improve results at lower frequencies as all simulations conducted in the scope of this section are still in the range (1.2 m < λ < 5 m) where accumulated errors are under 10%.
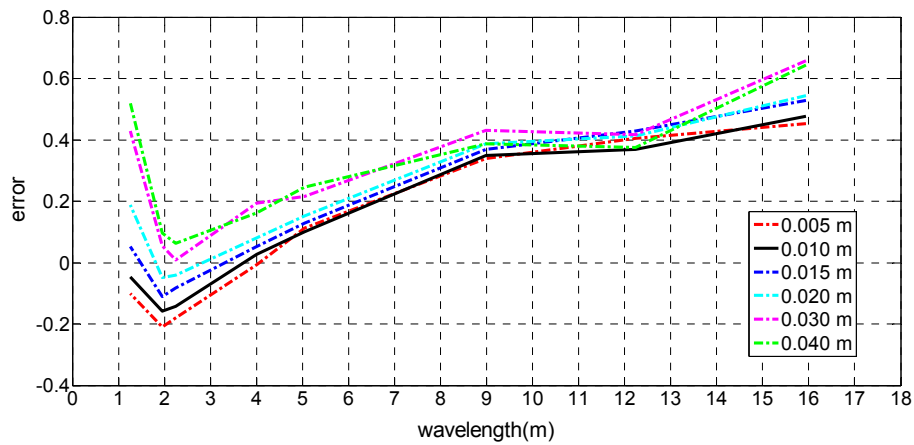
Figure 6-11 Relation between accumulated simulation errors with different wavelengths over a period of time.

6.1.3.c Vertical bending moment (VBM) of 1 way coupled solution

This analysis is conducted using information of the FE model reported by Lakshmynarayanana et al., (2015). In his work, modal analysis is performed in Abaqus to obtain dry hull natural frequencies for the first 4 flexible modes shown in Table 6.5. With the assumption of using the same model as Lakshmynarayanana, the same natural frequencies could be employed in this analysis. As for the mode shapes, they are determined by assuming that the non-uniform beam can be simplified as Euler beam. Thus, 2-node to 5-node modes can be derived directly from the polynomial function shown in Fig.6.12. Here, zero structural damping is employed due to the fact that the frequency range used in the experiments and simulations is below the first resonance. Moreover, in the case of one-way coupling approach, obtaining the damping ratio for flexible mode can be a difficult procedure and it may lead to a large uncertainty in the estimations. It has been shown that the structural damping will not affect the result significantly as the contribution from structural damping is usually small compared to the effect of the hydrodynamic damping (Seng et al., 2012).

Table 6-5 Dry hull natural frequencies

Mode	ω(rad/s)
2-node	6.01
3-node	16.43
4-node	32.00
5-node	52.66
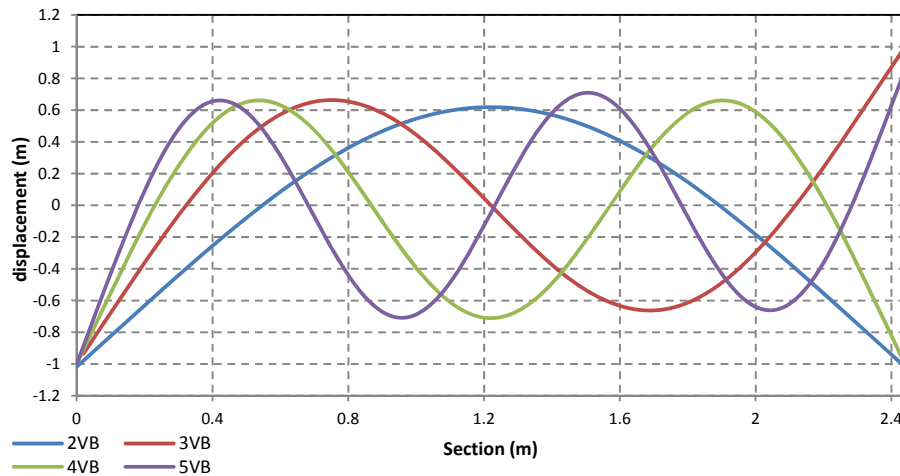
Figure 6-12 Mode shapes for the model scale

In order to determine the hydroelasticity response, the generalised external force from the fluid solver in equation (6.6) is computed via MATLAB routine. One may say that there are two fundamentally different ways to calculate wave induced forces on structures in the sea. In one method the pressure distribution around the surface of the structure is computed with due consideration to the water motion distorted by the structure itself and subsequently integrated around the structure. In the other method, one considers the structure as a whole and assesses the total wave force from empirical or computed coefficients using water velocities and accelerations in the undistorted wave motion. The latter approach is employed in this analysis. At each time step, fluid forces in three dimensions are converted to one-dimensional line loads. This can be achieved by dividing the barge into discrete panels and summing all forces corresponding to each longitudinal point in the 122 panels along the barge. This will provide the data for the term on the right-hand side of the equation and later the equation can be solved at each iteration using Newmark method (Newmark, 1959; Sun et al., 2016). The detailed procedure of the solution process can be found in the **Appendix C**. As the solution only take place as post-processing task, the body will not experience hogging or sagging in the initial condition, making it steady in calm water. The incident wave is applied almost instantaneously by the wave generator to enable a sufficient number of waves to propagate from the wave maker to the rigid barge. Only vertical wave loads are assumed to be importance, for the structural deformation of the barge. Fig.6.13 and Fig.6.14 show the required time for the rigid barge to reach a steady heave and pitch motions. Ratio of $\lambda/L \approx 2$ and $\lambda/L \approx 1$ should yield a large pitch motion. Pt.7 located in the middle of the barge shows most motion influenced by heave while pitch motion due to slamming is mostly recorded at Pt.1. From both graphs, it is seen that a start-up time of 5 seconds is needed for a steady motion response at each point once the incident wave reaches the barge. Consistency in the periodic height demonstrates the small interference from wave reflected by each side walls. There is, however, the possibility that the motion in the fluid domain will never become steady due to the behaviour of free surface particle which may lead to pressure fluctuation particularly in the case of high frequencies. This is mentioned in section 6.1.2 which closely associates with the value of delta-SPH and artificial viscosity chosen. Smaller amplitude is recorded at Pt.7 as longer time is needed for the incident wave to travel from bow to the centre point of the barge. It is worthwhile to mention that particle refinement does not change the prediction significantly, thus the results from almost all refinements show a similar trend in motion response in the case of T = 1.2 s (Fig.6.8). It is also important to stress that although WCSPH inherit some difficulties from the classical SPH formulation in obtaining accurate

periodic result related to wave generation and boundary condition, forces around the rigid barge in this simulation is observed to be well-predicted by each of the rigid boundary particles.
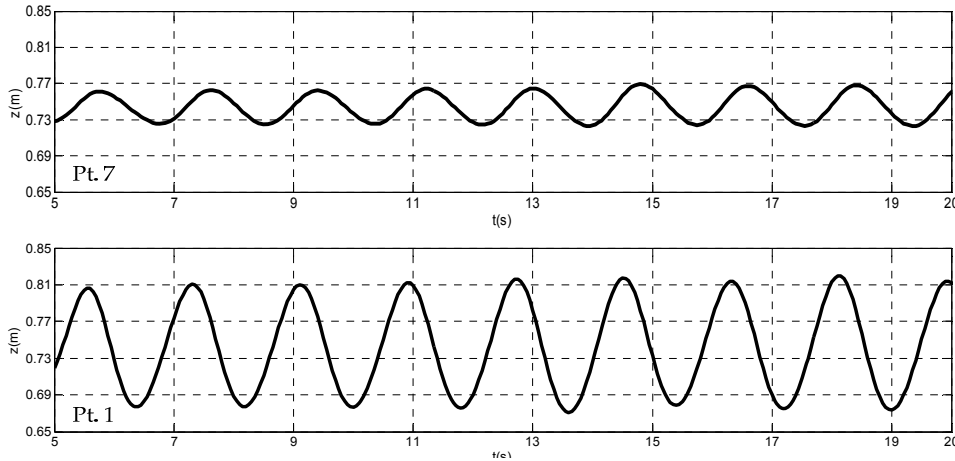
Figure 6-13 Vertical displacement of heave (Pt. 7) and pitch (Pt. 1) at each measuring points on barge. T = 1.8 s, λ = 5.058 m for dx = 0.012 m, dx = 0.015 m and dx = 0.020 m.
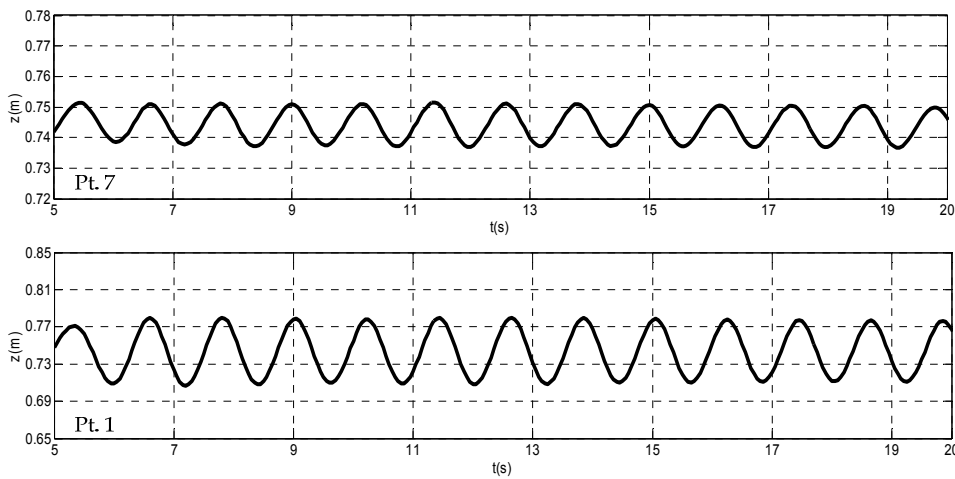
Figure 6-14 Vertical displacements of heave (Pt. 7) and pitch (Pt. 1) at each measuring points on barge. T = 1.2 s, λ = 2.248 m for dx = 0.020 m.

Fig.6.15 shows the principal coordinate plot for each mode shapes. The principal coordinate is used for scaling purposes for the model used in this study. These principal coordinates are obtained from 2-D hydroelasticity simulation using MARS (Bishop et al., 1979). MARS has been proven to be a suitable tool for hydroelastic analysis since the results are in agreement with FEA as well as theoretical data. From the graph, it is apparent that the response in 2nd mode is the largest and it influences greatly the whole distortion of the barge. Another noticeable characteristic is that higher order modes tend to decrease more rapidly and the magnitudes are close to zero. Therefore, the contribution of the higher modes can be considered small and negligible. In equation (6.3), the total deflection of the barge will then consist of only the information from the 2-node contribution.
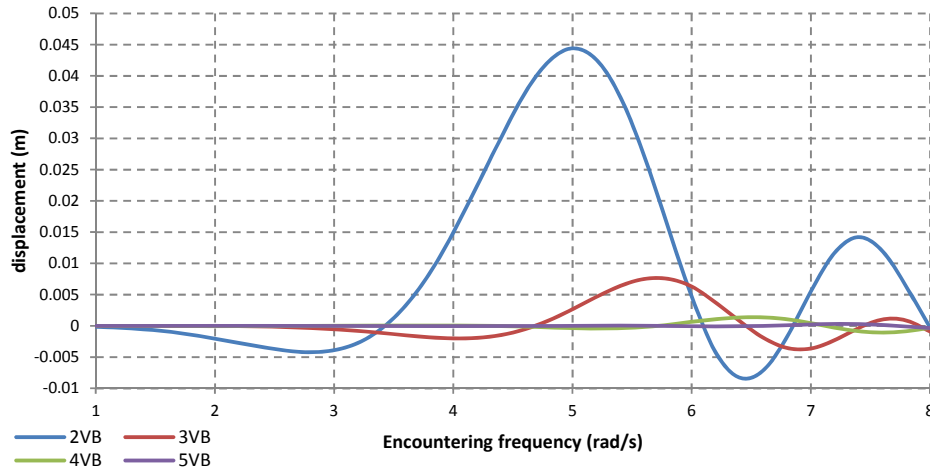
Figure 6-15 Principal coordinates for different distortion modes

In order to obtain the bending moment at amidships, the following calculation using principal coordinate is conducted. Principal coordinate is the generalised coordinate corresponding to wave excited vibration.

$$\left| M_{(x=\text{amidship})} \right| = \sum_{r=2}^{3} P_r M_r \tag{6.8}$$

where M_r is a real number whilst P_r is a complex number. Therefore, in order to evaluate the magnitude of, modulus of the principal coordinate is computed.

$$|P_r| = |X + Yi| \tag{6.9}$$

$$|P_r| = \sqrt{X^2 + Y^2} \tag{6.10}$$

Response at Pt.9

Response at Pt.5

Response at amidship
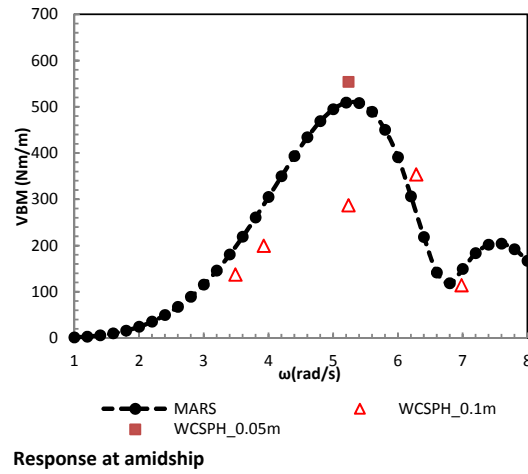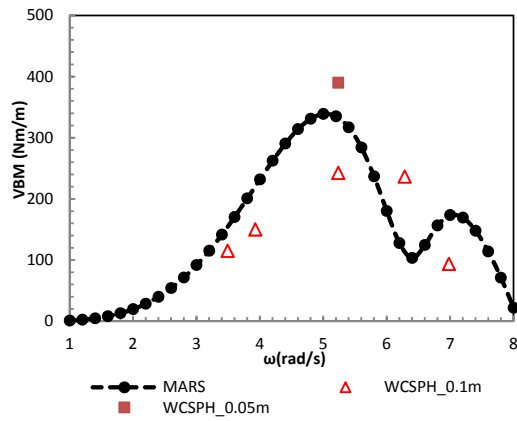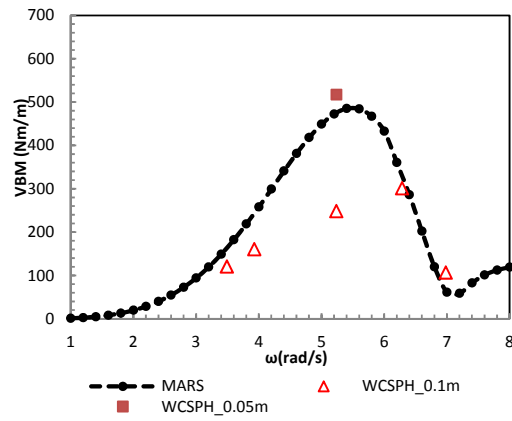
Figure 6-16 RAOs of VBM between MARS and 1-way coupling approach at amidships, point 9 (0.805m) near the stern and point 5 (1.625m) near the bow, for flexible body analyses.
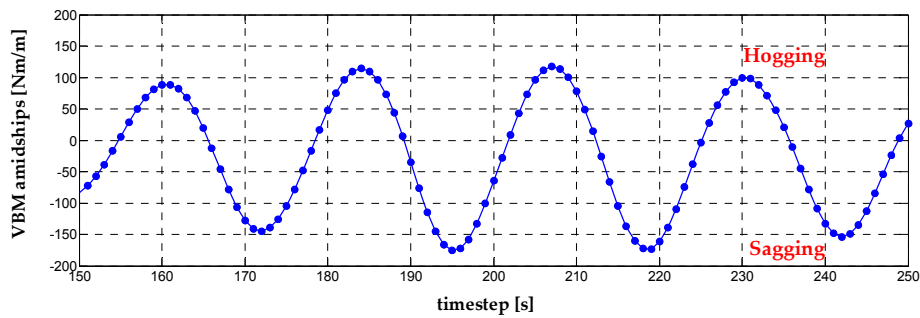
Figure 6-17 Time series of VBM at amidships of WCSPH 1-way coupled at ω = 5.235 rad/s, λ = 2.248 m.

140

The RAOs of VBM between WCSPH results and 2-D hydroelastic predictions from MARS are shown in Fig.6.16. For consistency purposes, incident wave in the free surface used for the RAO calculations is defined similarly as seen in the prediction of rigid body motion. Responses are recorded in 3 places where the flexible barge experiences the most bending moment from a 2VB distortion modes. The barge experiences an increasing bending moment starting from ω = 1.0 rad/s up until ω = 5 rad/s where the wavelength is close to the barge length, before gradually decreasing for the higher frequency range. In the range of frequencies studied using WCSPH, it can be observed that most of the predictions share similar trend of VBM responses with MARS, particularly in the first 2 low frequencies. However, WCSPH gives an underestimation of approximately 40% for the first VBM peak value particularly at the amidship. This is probably caused by the 3-D nonlinear effect of external force acting on the barges which cannot be captured in the 2-D hydroelasticity by MARS. Natural frequency of the barge in 2VB distortion is close to the wave frequency between 5 rad/s < ω < 6 rad/s. This suggests resonance of rigid body which may cause the deviation. Another test is run by changing the height of the regular incident wave in order to reduce the non-linearity effect. Wave height of 0.05 m denotes by WCSPH_0.05m can be considered small enough so the simulation can be assumed to be linear and the result are observed to agree well with the prediction of 2-D linear data from MARS by less than 10% of difference at amidships.

Fig.6.17 shows the time series of VBM at amidships at ω = 5 rad/s. The sign convention applied is that hogging VBM is positive and sagging VBM is negative. The comparison is not made with MARS as we know MARS calculation yields VBM amplitude of approximately 250 Nm/m. It can be seen in the graph that maximum sagging bending moment is larger than the maximum hogging bending moment by 30% (peak to peak value). Because the present model only involves one-way coupling where the local deformation of the barge is not transferred back to the fluid particles, the added mass associated with the local vibrations is completely missing in the external force in equation (6.6). Therefore, the prediction of the one-way coupling approach can be improved by modelling explicitly the missing added mass in equation (6.2). Moreover, it is worthwhile to mention that no severe slamming is observed in the 3-D simulation for wave configuration used. As demonstrated in the RAOs, the classical one-way coupling approach is not able to predict the hydroelastic effect of the barge accurately and the results are underestimated when to compare with the 2-D hydroelastic prediction. However, validations using other experimental data and two-way coupling approach are necessary for further analysis.

6.1.4 Concluding remarks

In this section, investigation of a rigid barge in regular waves is carried out. The rigid body is modelled according to a numerical prediction by Lakshmynarayanana et al., (2015) which is based on a hydroelastic experiment done by Remy et al., (2006). A numerical technique used is based on the WCSPH code, both for rigid floating body and fluid domain. Rigid body is discretized into particles whose properties are similar to those of fluid particles. Two sub-studies of wave generation and motion response of rigid body in head waves have been discussed. Prior to the test, wave dissipation along the NWT is investigated and a maximum decrease of 12% in the wave height is observed. In the study of motion responses, results from WCSPH are compared with the 3-D prediction from STAR_Rigid, 2-D prediction of MARS_Rigid and experimental data. Overall, results from WCSPH agrees well with both numerical results with some discrepancies at lower frequencies around the amidships section of the barge. These discrepancies are mainly influenced by heave motion which is believed to be affected by strong localised wave along the barge and regular long-crested wave. Additional computations have been carried out using two more particle refinements for ω = 3.490 rad/s and ω = 3.926 rad/s. In both cases, refinements do not change the predictions significantly. Further, it has been shown that motion responses from WCSPH in bow regions are also over-predicted, similar to STAR_Rigid or comparatively higher frequencies. In some of these cases, the reason is the 3-D effects around the vicinity of the bow mainly caused by a continuous slamming event of pitch motion which are captured in WCSPH. This proves the consistency in predicting the motion between these 2 numerical solvers. Comparison with experimental data also provides insight in motion difference between rigid body and deformable structure. An analysis based on varying the particle resolution has been carried out to investigate the behaviour of each simulation under different wave lengths. Accumulated errors less than 8% are observed for range of frequencies used in this section including the case where the wave length is close to the length of the barge. Further investigations have been conducted to evaluate hydroelastic effect using one-way coupling approach. VBMs are calculated as post processing task and the outcome is compared with results for a 2-D flexible model from MARS. Discrepancies are observed between the predictions from WCSPH as the one-way coupling cannot capture the hydroelastic effect accurately. Moreover, it is hard to say what causes the large discrepancy between these results without proper validation with other 3-D hydroelastic numerical results or experimental data. Further improvement is to adopt added mass explicitly in the method which can help in improving the prediction of the one-way coupling scheme.

6.2 Added-mass and damping coefficients for a uniform flexible barge

In this section, WCSPH code is used in the simulation where the barge is treated as a flexible body. The DualSPHysics code described so far is only able to simulate rigid body cases, significantly restricting its usability and application. By applying a flexible model, the computation of a stationary uniform rectangular barge, in still water, undergoing forced simple harmonic oscillations in symmetric rigid body and distortion modes can be carried out. Forced oscillation tests are chosen to be investigated as they provide a direct evaluation of the hydrodynamic coefficients in the 3-D radiation problems. Hydrodynamic theory of linear seakeeping is used to estimate the hydrodynamic coefficients and for a given encounter frequency, use these values to calculate the ship motions in a seaway. These hydrodynamic coefficients, namely added mass and damping coefficients are solved in rigid body motion of heave and pitch, 2 node (2VB) and 3 node (3VB) distortion mode shapes. Coupling terms for 2VB-heave and 3VB-pitch and vice versa are also included. Sizes of the domains, particle numbers and damping zones are modified based on different cases of wavelengths, allowing the free surface to be well captured in WCSPH. Finally, simulation results and discussions are presented in the comparison of WCSPH with 3-D CFD predictions and results from potential flow boundary element method.

6.2.1 Numerical setup

Using the boundary and fluid geometry as described by Kim et al., (2014), a uniform rectangular barge is modelled with main particulars as presented in Table 6.6. Both boundary and fluid domain are discretized using particles whose size and number depending on the initial particle spacing. For the boundary, 2 layers of boundary particles are adopted to model the conditions of a NWT. The domain is modelled in three dimension where y axis is in the athwarthships and x and z axis is along the barge and in vertical directions, respectively. Unlike VOF model, WCSPH code in DualSPHysics does not have the option to model only half of the barge about its longitudinal axis to reduce the computational cost. Therefore, due to the large dimension, several considerations need to be made in determining the appropriate particle spacing and particle number. Among them is that the number of particles needed particularly in the vicinity of the barge and flow field near the free surface in high frequencies. Particle spacing of 1.0 m with particle number shown in Table 6.7 is considered adequate in capturing details of forces along

the oscillating barge. The modelled boundary for a particular case, with particle number over 3.9 million is shown in Fig.6.18 while each axis of the barge is presented in Fig.6.19. All simulations are carried out in a range of frequencies shown in Table 6.7 with each wavelength and wave height. The size of the numerical domain changes with the wavelength of individual frequencies.

Additional to the barge dimension, the NWT is extended from each side of x and y direction that includes two zones, namely wave zone and damping zone. Wave zone allows enough time for radiated wave from the oscillating barge to travel before being slowly damped by the beach at the end of the domain. Ideally, the lengths of both these zones should be set equal to the wavelength of the radiated wave. However, considering the number of particles used, wave zone and damping zone for all frequencies are first determined based on the characteristics of the wave with a frequency of 1.0 rad/s. Here the wave zone is twice of its wavelength and damping zone is equal to the wavelength. The water depth is kept large enough to avoid shallow water influence to the radiated wave for each individual frequency. The excitation amplitude is set to 1 m for frequencies $\omega \leq 1.0$ rad/s and 0.2 m for frequencies $\omega > 1.0$ rad/s. This large value of amplitude is assigned to lower frequencies case to ensure that the dynamic components are not too small compared to the static components.

Table 6-6 Main particulars of the barge

Main particulars	Barge
Length, L	120 m
Breadth, B	14 m
Depth, D	11.15 m
Draft	5.575 m

Table 6-7 Simulation conditions

ω (rad/s)	λ (m)	H/2 (m)	Wave zone (m)	Damping zone (m)	Depth (m)	dx (m)	Particles number
0.2	1540.9	1.0	132.12	60.0	61.64	1.0	7.8 M
0.4	384.24	1.0	132.12	60.0	61.64	1.0	7.8 M
0.6	171.22	1.0	123.28	60.0	61.64	1.0	7.8 M
0.8	96.309	1.0	123.28	60.0	30.69	1.0	3.9 M
1.0	61.638	1.0	123.28	60.0	30.69	1.0	3.9 M
1.2	42.804	0.2	123.28	60.0	30.69	1.0	3.9 M
1.4	31.448	0.2	123.28	60.0	30.69	1.0	3.9 M
1.6	24.077	0.2	123.28	60.0	30.69	1.0	3.9 M
1.8	19.024	0.2	123.28	60.0	30.69	1.0	3.9 M
2.0	15.410	0.2	123.28	60.0	30.69	1.0	3.9 M
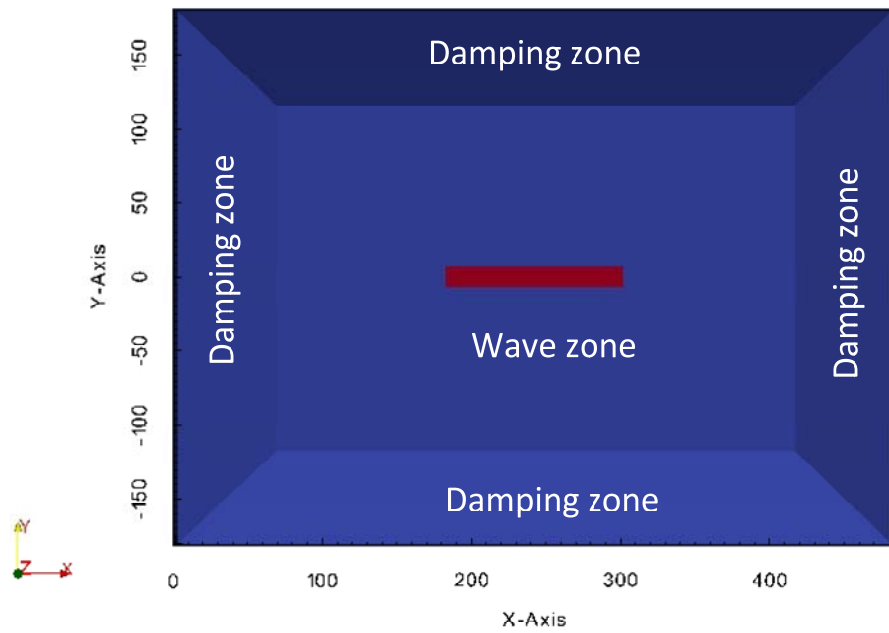
Figure 6-18 Overall size of NWT including wave zones and damping zones.
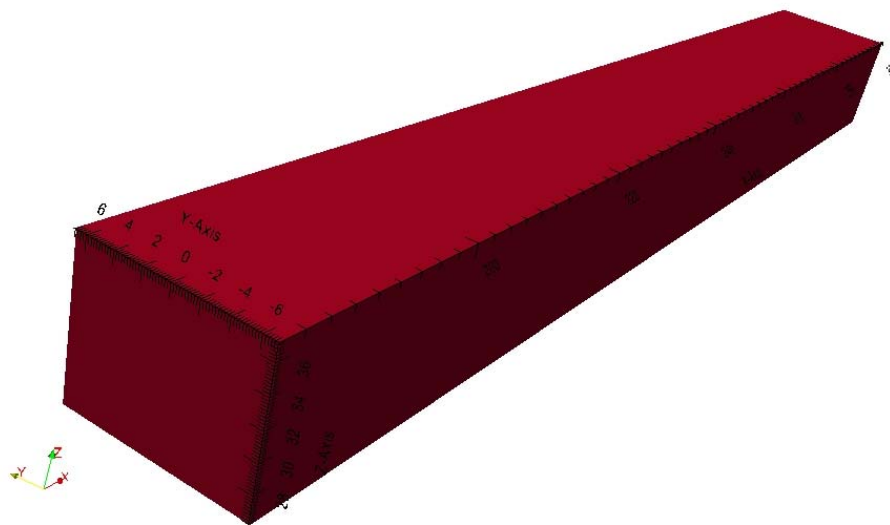
Figure 6-19 The size of the numerical barge.

6.2.2 Numerical parameters

Simulations are carried out with damping beaches set in both the horizontal and vertical direction as shown in Fig.6.18. Similarly with simulations in the previous section, delta-SPH (δ) term is set to 0.1. Wendland kernel is chosen for the interaction between neighbouring particles while the sympletic scheme is used for the step algorithm. Particles are then initialised on a regular grid of particle spacing. Subsequently, after several preliminary tests, viscosity value of 0.01 is used to prevent any instability in the flow field. Fluid particles are not moved using XSPH to minimise the viscosity effect in the fluid domain. The initial SPH smoothing length is then set at $h = 1.3dx$. WCSPH in DualSPHysics provides prescribed motion to be assigned to a body using <*mvrectsinu*> option for sinusoidal rectilinear movement. However, this prescribed motion cannot be applied to heave motion to estimate the value of generalised force along the oscillating barge. In order to implement the flexible mode model, modifications of motions for pitch, vertical 2- and 3- node of distortion modes are applied directly to the velocity in the source code. Following the velocity of a body undergoing a simple harmonic motion,

$$\dot{z} = \omega z_a cos\omega t \tag{6.11}$$

where $\dot{z}$ is the velocity, ω is the oscillation frequency (rad/s), z_a the amplitude and t is the time (s). Velocity of each barge particle is imposed as a vector by multiplying the velocity with the eigenvector for individual rigid body motions or distortions. The eigenvectors for the distortion modes are calculated using Euler beam theory approximated using polynomials. Implementing Euler beam in this simulation ensure that the displacements changes in the z direction. Displacement of each barge particle is updated with new velocity at the end of every time step. These steps can be simplified as follows;

1st step: $\dot{z} = \omega z_a cos\omega t * eigenvector$

2nd step: $\dot{z} = \begin{pmatrix} u \\ v \\ w \end{pmatrix} * \begin{pmatrix} R_y \\ 0 \\ T_z \end{pmatrix}$

where $[R_y, 0, T_z]$ is equal to $[0,0,1]$ in heave and $[1/60, 0, (x - 60)/60]$ in pitch.

Time step sizes of all simulations are kept to $1.0e^{-4}$ s due to some high frequencies wave propagation. Time of simulation varies depending on individual wavelengths with similar time between output files of 0.1 seconds.

6.2.2.a   Hydrodynamic coefficients

The computation of the hydrodynamic force, $F(t)$ is carried out using results from the application, *PartVTK.exe* where all the information on the particle properties at each time step is recorded. Related data are then used to obtain the added mass and damping coefficients of the barge by utilising post-processing techniques. Different from pressure integration technique, here the force is determined by first computing the acceleration vector of each fluid particle in the vicinity of the oscillating barge and making use of Newton's second law, force is obtained by multiply this value with mass of each fluid particle. Referring back to equation (3.35), the resulting vector is assumed as the force exerted by the fluid on the barge with opposite sign. Since changes in x and y directions are negligible, only the z component of the acceleration is considered in obtaining the total hydrodynamic force, $F(t)$. However, in order to compute the dynamic force, the static force is subtracted from the total hydrodynamic force. Similarly in STAR-CCM+, buoyancy of the barge is obtained when the vertical force on the body reach its equilibrium condition. The static forces on the body for rigid body motions and distortions are computed on the mean free surface. In order to obtain the generalised force, $F_{rs}(t)$, the dynamic force for each particle is multiplied with the sth eigenvector where r denotes the index of the motion including both the rigid body motion and distortion mode. Using this relation, one can also extract generalised forces from the cross-coupling motion i.e. diagonal terms of Heave-2VB, 2VB-Heave, Pitch-3VB and 3VB-Pitch. For example, using data from barge oscillating in pitch motion,

$$F_{rs}(t) = ma \cdot \begin{bmatrix} R_y \\ 0 \\ T_z \end{bmatrix} = ma \cdot \begin{bmatrix} 1/60 \\ 0 \\ (x-60)/60 \end{bmatrix} = F_{rs}^{Pitch} \tag{6.12}$$

$$F_{rs}(t) = ma \cdot \begin{bmatrix} R_y \\ 0 \\ T_z \end{bmatrix} = ma \cdot \begin{bmatrix} 3.1405e^{-12}x^6 \dots \dots \\ 0 \\ 3.3021e^{-9}x^5 \dots \dots \end{bmatrix} = F_{rs}^{Pitch-3VB} \tag{6.13}$$

Instantaneous values of the hydrodynamic coefficient are obtained by Fourier analysis of time history of the generalised force $F_{rs}(t)$ using discrete windows approach for one period, $T = 2\pi/\omega$, of oscillation, namely

$$A_{rs} = \frac{2}{T\omega^2} \int_{t-T/2}^{t+T/2} F_{rs}(t) \sin(\omega t)\, dt \tag{6.14}$$

$$B_{rs} = -\frac{2}{T\omega} \int_{t-\frac{T}{2}}^{t+\frac{T}{2}} F_{rs}(t) \cos(\omega t)\, dt \tag{6.15}$$

6.2.3 Results and discussion

This section presents results of oscillating uniform barge at different mode shapes on the free surface. The predictions from WCSPH are compared to those obtained from 3-D predictions of STAR-CCM+ and 3-D potential flow using the Green's function of pulsating source (Bishop et al., 1986). In contrast to STAR-CCM+/ABAQUS used in section 6.1 , the STAR-CCM+ from Kim et al., (2014) is the imposition of a boundary that oscillates simply harmonically in the shape of selected modes. Both simulations still using potential flow but are nonlinear. Each eigenvector relevant to the motion of the barge is determined by approximating the polynomial solution based on Euler beam idealisation. Ideally, the displacement in vertical axis has a larger contribution than the displacement in horizontal axis to the motion for each mode shapes in Euler beam. It is worthwhile to mention that results from STAR-CCM+ used for the comparisons can be categorised into two sets. The first set is the initial setup of the numerical model while the second set is obtained by refinement of the mesh corresponding only to relatively low frequencies. Results from the extension of the domain are not included due to the small significant improvements (Kim et al., 2014).

Fig.6.20 shows the generalised added mass and damping coefficients for rigid body motion of heave and pitch. The variables are plotted with respect to each frequency and are not nondimensionalized. Overall, both added mass and fluid damping from WCSPH predictions agree well with STAR-CCM+ and potential flow theory with small discrepancies below 10% in added mass of heave motion. At $\omega = 1.6$ rad/s, a trend of overestimation can be observed. The facts that both numerical methods have similar predictions on that particular frequency confirm the irregular frequency which is believed to be difficult to capture by a potential theory method. In almost all points of results, damping shows an increasing trend for $\omega < 0.8$ rad/s before starting to decline gradually for shorter waves. Additional case at $\omega = 0.7$ rad/s is carried out just for the pitch motion where damping is at the peak value. Moreover, added mass by WCSPH which includes up to 8 million particles is in closer agreement with a refined grid of STAR-CCM+ at low frequencies in Fig.6.20(c) which also consist of almost 10 million cells. In the case of $\omega = 0.8$ rad/s, small discrepancy is noted in Fig.6.20(d) which suggests the insufficient amount of force prediction around the oscillating barge.

2-node (2VB) and 3-node (3VB) distortion mode are represented in Fig.6.21. For frequencies greater than 0.4 rad/s, 2VB and 3VB have better agreement with both STAR-CCM+ and potential flow. In 2VB and 3VB results, similar irregularity can be observed between $\omega = 1.6$ rad/s and $\omega =$

148

1.8 rad/s. For 2VB, differences between WCSPH and potential theory are smaller in fluid damping than in added mass. Added mass from WCSPH shows a slightly higher value for ω = 0.2 rad/s and ω = 0.4 rad/s. The same trend in 3VB simulation is noted where there is a better agreement of added mass from WCSPH than results from refined grid of STAR-CCM+. However, the deviation in damping is recorded to be about 10 times bigger from STAR-CCM+ and potential flow at the lowest frequency. Primarily, this is due to the complexity of 3VB motion and insufficient length of radiated wave in the NWT. Additional measurements are also added where simulation at ω = 0.9 rad/s is carried out in 3VB motion. This is to make sure that the peak in fluid damping for 3VB motion is covered for evaluation. Initially, the size of NWT is planned to be large enough to cover at least three period of the radiated wave based on each individual wavelength. However, simulating such large domain with uniform particle spacing of 1.0 m would lead to the total number of fluid particles to exceed 25 million, which is the limitation of the current graphic card. The domain size is scaled down by a factor of 8 for ω = 0.2 rad/s and by a factor of 2 for ω = 0.4 rad/s. The results are based on some preliminary runs and these sizes are believed to be enough in providing accurate results and to avoid precision problems (Dominique et al., 2014). Scaling down the domain would not eliminate reflected waves efficiently and the effect can be seen in cases where the predictions deviated from the potential flow results.
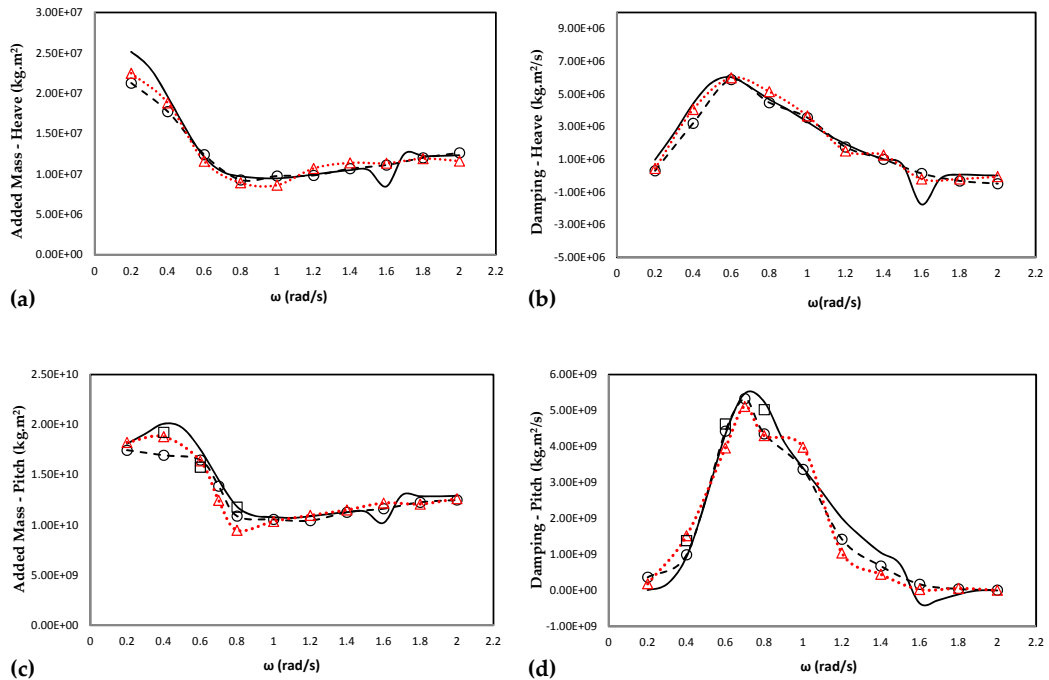
Figure 6-20 Comparison between generalised added mass and damping coefficients. (a) and (b) : Heave motion, (c) and (d) : Pitch motion. − : Predictions from potential flow, ○ : predictions from STAR-CCM+, □ : predictions from STAR-CCM+_fine and △ : predictions from WCSPH.
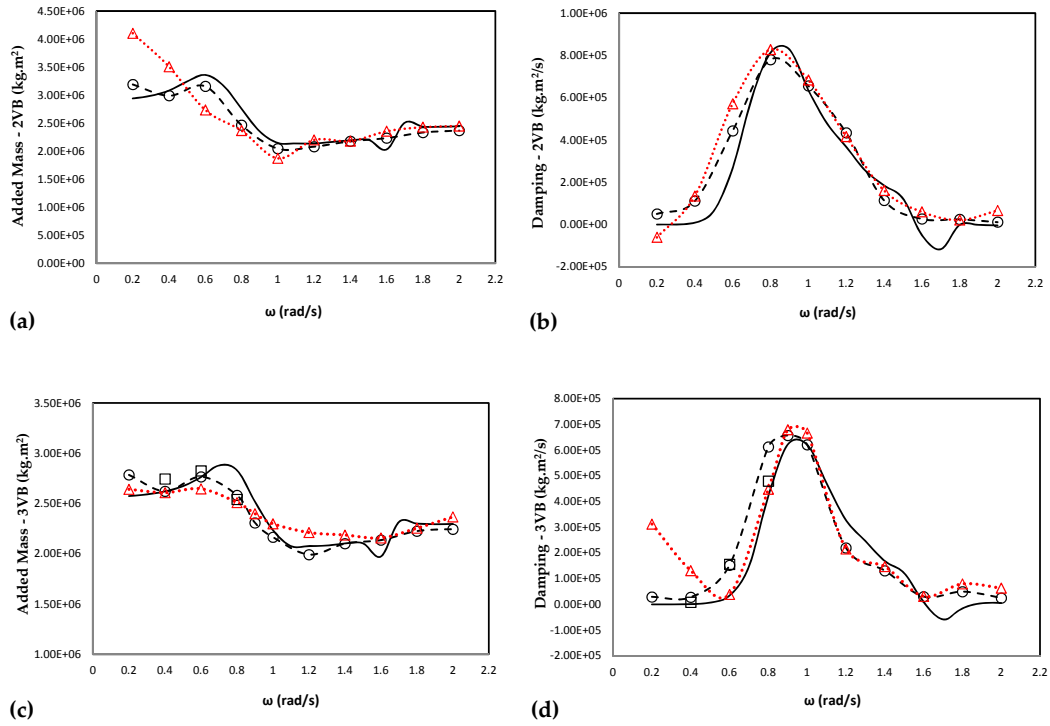
Figure 6-21 Comparison between generalised added mass and damping coefficients. (a) and (b) : 2VB motion, (c) and (d) : 3VB motion. − : Predictions from potential flow, ○ : predictions from STAR-CCM+ , □ : predictions from STAR-CCM+_fine and △ : predictions from WCSPH.

The comparisons of hydrodynamic coefficients for the cross-coupling terms in the 2VB distortion modes are shown in Fig.6.22. Apart from the predictions at lower frequencies, Heave-2VB and 2VB-Heave terms show a consistent trend with each other, agreeing well with both STAR-CCM+ and potential flow results. In heave-2VB, the first discrepancy point is observed at ω = 0.4 rad/s in added mass and the errors continue to increase further for ω = 0.2 rad/s. The error bound recorded is nearly 20% when compared to the potential flow results. While for the 2VB-Heave term, large discrepancies started to show at ω = 0.2 rad/s. The added mass by WCSPH is over predicted, similar with the STAR-CCM+ while the agreement with potential flow results is better in damping than STAR-CCM+. Results with a refined grid using STAR-CCM+ are only available for ω = 0.4 rad/s, due to the fact that higher computer power is needed as mentioned before at ω = 0.2 rad/s for both WCSPH and STAR-CCM+. As discussed earlier, it is possible that there is an additional effect resulting from reflective fluid acting on the structure when the body is oscillating at relatively low frequencies. The viscosity term in WCSPH may lead to a better prediction of the damping term. However, it is difficult to say which prediction is better without proper validation with experimental data when taking into account of the 3-D effect.
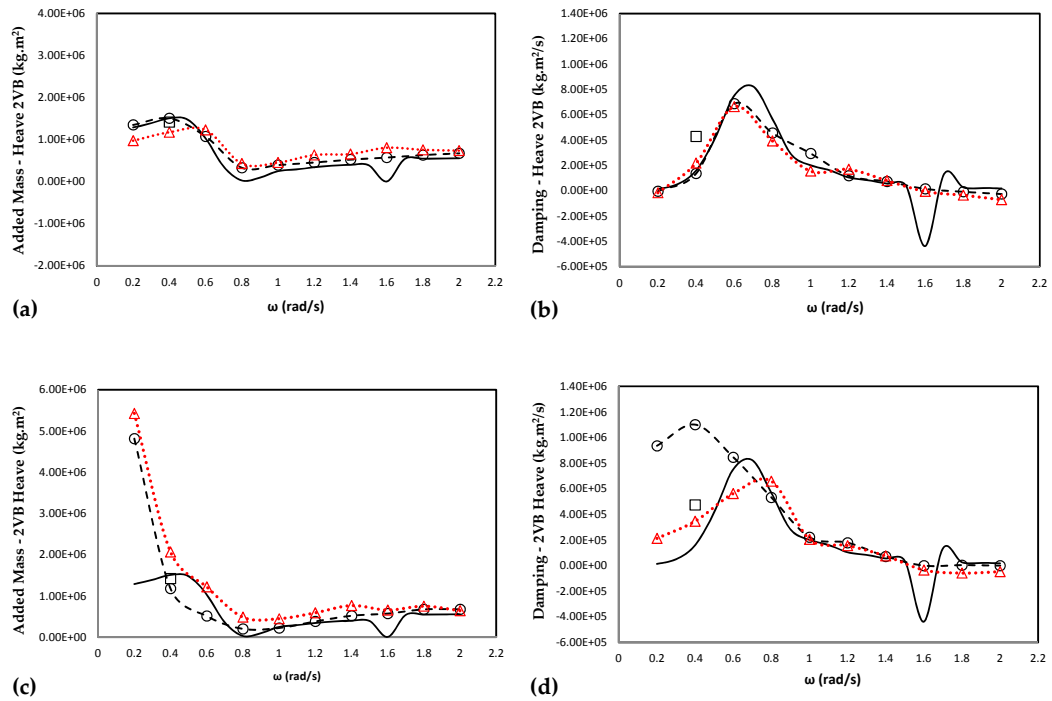
Figure 6-22 Comparison between generalised added mass and damping coefficients. (a) and (b) : Heave-2VB motion, (c) and (d) : 2VB-Heave motion. − : Predictions from potential flow, ○ : predictions from STAR-CCM+ , □ : predictions from STAR-CCM+_fine and △ : predictions from WCSPH.
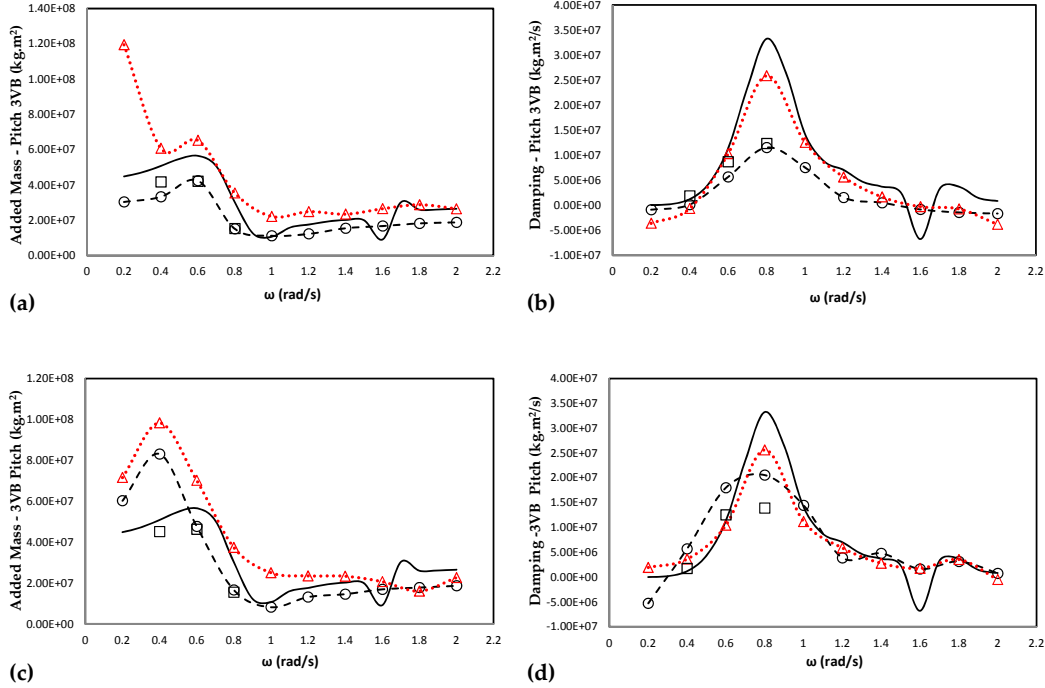
Figure 6-23 Comparison between generalised added mass and damping coefficients. (a) and (b) : Pitch-3VB motion, (c) and (d) : 3VB-Pitch motion. − : Predictions from potential flow, ○ : predictions from STAR-CCM+ , □ : predictions from STAR-CCM+_fine and △ : predictions from WCSPH.

Fig.6.23 shows the comparison of hydrodynamic coefficients for the cross-coupling terms in the 3VB distortion modes. For relatively high frequencies ($\omega > 0.8$ rad/s), pitch-3VB and 3VB-pitch terms are observed to follow the trend similar with STAR-CCM+ and potential flow although small discrepancies can be observed in nearly all points. The deviation in predictions of WCSPH and potential flow results, particularly for added mass in Pitch-3VB and 3VB-Pitch terms become larger towards lower frequencies. Overall, WCSPH overestimated added mass value for most individual frequency. This overestimation somehow explains the complexity in obtaining the generalised force for 3VB motion in comparison to the rigid body motion due to a higher nonlinearity involved when the body oscillates. As emphasised before, the rigid body in STAR-CCM+ is modelled by employing half of symmetry plane boundary condition, making it less exposed than WCSPH to the surrounding 3-D nonlinearities. Refinement from STAR-CCM+ denotes by STAR_CCM+_fine are plotted together to show the sensitivity of the force prediction around the oscillating body. The results from the refinement of STAR-CCM+ at $\omega = 0.4$ rad/s suggests that added mass for both terms can be closer to potential flow theory (Kim et al., 2014). This suggests that force contribution around the body is very sensitive to the mesh refinement. Similarly, the same improvement may be achieved by WCSPH method if smaller particle spacing

is used. However, as mentioned before, in order to use much smaller particle spacing, it is necessary to use double precision in the simulation. Furthermore, in Fig.6.23(b)(d), both WCSPH and STAR-CCM+ can be seen underestimate the value of damping at ω = 0.8 rad/s. The results from STAR-CCM+_fine suggest that it could be due to 3-D irregularity and therefore the predictions are smaller. The discrepancies computed in 3VB-Pitch is observed to be larger than the one computed in Pitch-3VB term. One of the reasons could be the difficulty in obtaining generalised force as dynamic components is small compared to static where time window is longer in lower frequencies. Although WCSPH is not expected to predict well at this particular frequency, WCSPH is able to show the consistency of trend in damping for both Pitch-3VB and 3VB-Pitch terms. This is because both cross-coupling terms should be the same for a stationary symmetrical body, like the barge used in this study.

Motion responses at different time instant by WCSPH for 2VB and 3VB modes are shown in Fig.6.24. Pressure distribution is observed to be higher where the particles move at its maximum displacement along with the highest dynamic force, $F_{rs}(t)$. The interaction between boundary particles and fluid particles are very sensitive for the case where magnitude of dynamic force is small in lower frequencies. Fig.6.25(c to f) depict the contour lines and motion of the waves radiated away from the oscillating body for pitch and 3VB respectively. The contour lines are plotted via MATLAB routines with contribution of fluid particles near free surfaces where the colours show the pressure distributions of the flow field. The distributions are scattered throughout the fluid domain as pressure values on free surface particles does fluctuate. Observation on the behaviour of flow field around the oscillating barge are then made by comparing the wave contour between pitch motion in Fig.6.25(a)(c) and 3VB motion in Fig.6.25(b)(d) by WCSPH and STAR-CCM+_fine (Kim et al., 2014), respectively. In pitch motion, wave contours in WCSPH shows similar wave pattern with STAR_CCM+_fine except that fluctuations arise near each wall. These fluctuations are the results of radiated wave which reached the damping zone and were reflected back. The effect could be in the accuracy of the prediction of the dynamic force. In the 3VB motion, WCSPH shows significant wave pattern around the oscillating barge. Due to the movement of 3-node distortion, radiated wave seems to disperse in the vicinity of the barge and mostly cancelling each other before reaching the damping zones. The large domain used in the simulation plays a role in the 3-D effect on the flow field which somehow also contribute to the increasing number of accumulated errors in the prediction of the hydrodynamic coefficients.
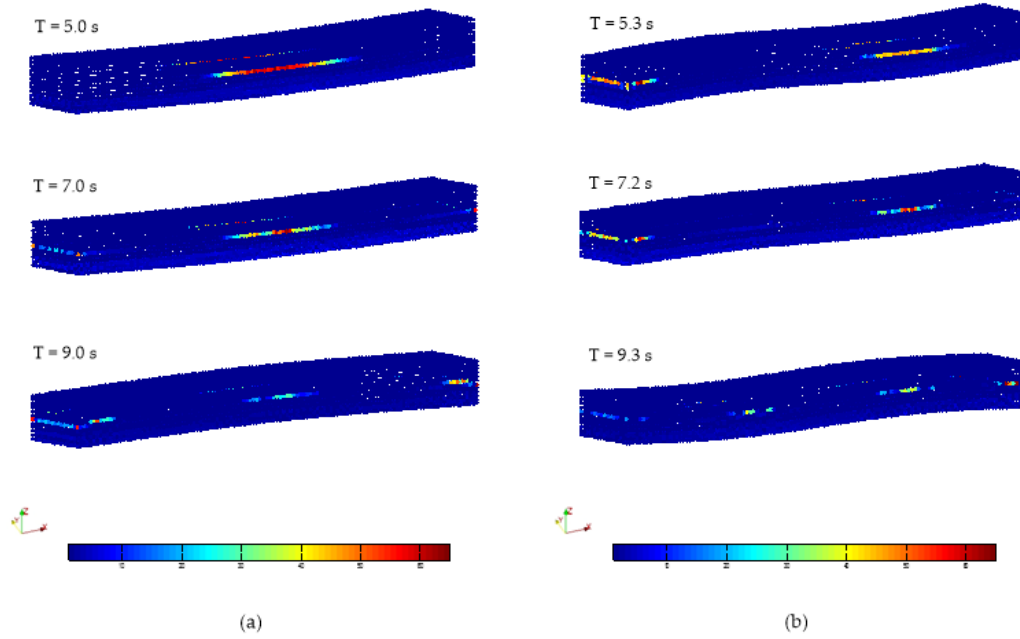
Figure 6-24 Motion of the barge at different time instance for different distortion mode shapes at ω = 0.8 rad/s. (a) 2VB and (b) 3VB.

Table 6-8 Computing performance of different solver for 3VB at ω = 0.2 rad/s

Version	Number of cores	Computed step per seconds	Speedup vs CPU single core
CPU single core	1	0.09275	1.0x
GPU GTX 970	1664	3.88972	1664x
STAR-CCM+	160	1.48392	160x
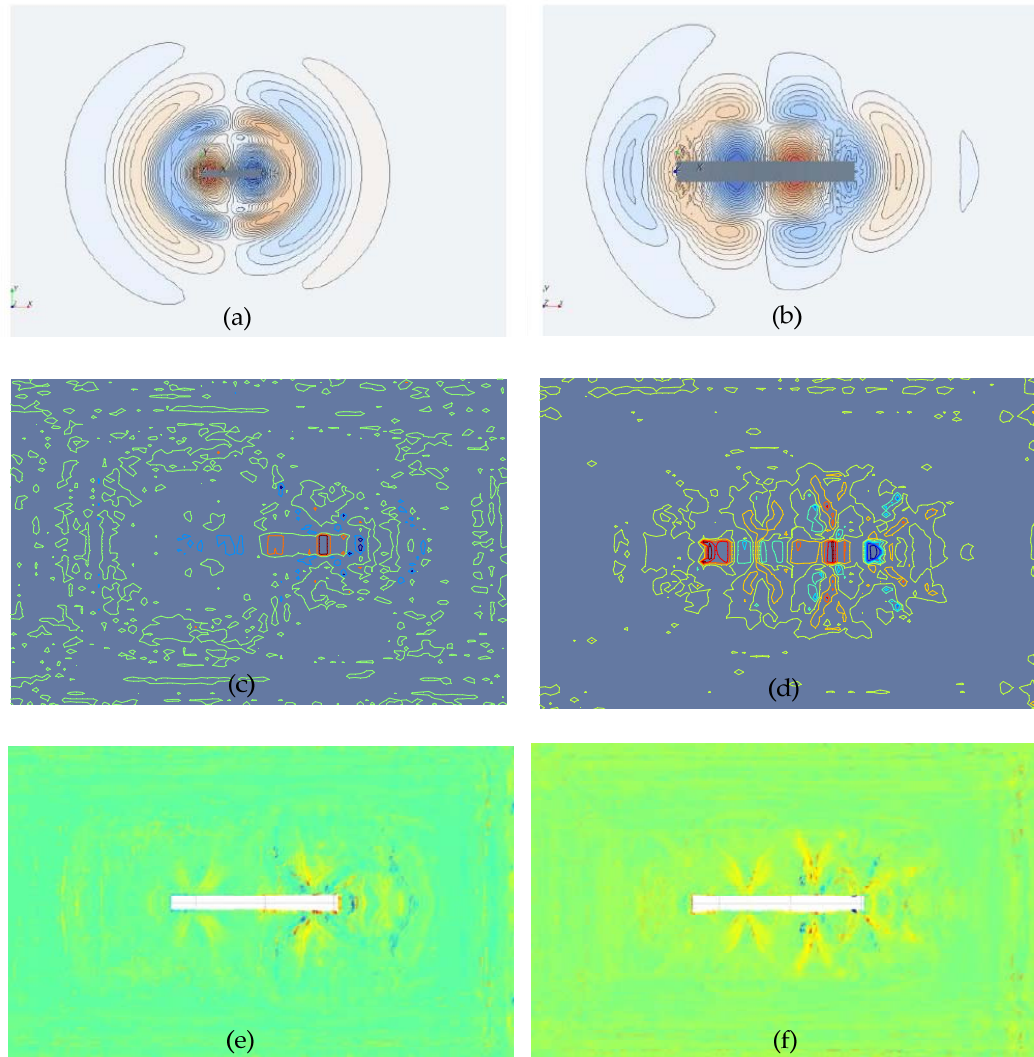
Figure 6-25 Wave lines and pressure contours for different mode shapes at ω = 0.8 rad/s. (a)(b)pitch and 3VB motion, STAR-CCM+ (Kim et al., 2014), (c)(d) wave contours of pitch and 3VB motion, WCSPH and (e)(f) pressure distribution of pitch and 3VB motion, WCSPH.

6.2.4 Concluding remarks

The accuracy of WCSPH in predicting the hydrodynamic coefficients of a stationary barge harmonically oscillating in still water is validated. The model has been successfully applied to the symmetric rigid body with 4 different mode shapes, namely heave and pitch motion of the rigid body, 2-node and 3-node distortion mode shapes. Numerical tests have found that WCSPH agrees wells with most cases investigated and can predict the fluid actions equally well in comparison to STAR-CCM+ and potential flow method. Both numerical methods have been found to possess similar features including few discrepancies in the area of relatively low frequencies. These discrepancies occurred due to the complexity of force computation in long-crested radiated waves which demands large domains and damping zones in preventing any wave reflections. The extracting dynamic force from the total generalised force in such large time window in the case of low frequency could become complicated, which is likely to increase the errors within the calculation of added mass and damping.

Moreover, some major poor performance in WCSPH particularly for the cross-coupling coefficients of Pitch-3VB modes and vice versa similarly may be related to the insufficient particle refinement and scaling down of the total fluid domain although it has been shown in STAR-CCM+ that extending the domain does not improve significantly the quality of the results at low frequencies. Further, in order to investigate the behaviour of discrepancies between numerical methods in the cross-coupling terms, observation on the pressure distributions and wave contours of the radiated wave are successfully compared to the refined results of STAR-CCM+.

Simulation of fluid and structure interaction involving flexible body using WCSPH method employed in this chapter has shown that WCSPH code is a reliable numerical tool in the prediction of added mass and damping coefficients. Although it is limited to the radiation problem, the conclusions drawn for this chapter is that this method is applicable to the modelling of the behaviour of the 3-D ship in regular waves.

Chapter 7

Conclusion and Future Work

7.1 Conclusion

In this PhD thesis, implementation of Smoothed Particle Hydrodynamics (SPH) model was used to investigate seakeeping problems where a number of 2-D and 3-D validation tests were conducted. The model was selected based on the capability of particle method to tackle a range of highly non-linear hydrodynamic problems involving severe flow surface discontinuities. Furthermore, simplicity, robustness and relative accuracy are other advantages of using SPH for complex problems such as surface waves interacting with bodies. Here, SPH method in the modelling dynamic behaviour of flow and motion responses of rigid and flexible 3-D bodies in waves was investigated. In order to simulate the free surface motion efficiently, the initial works have been focusing on understanding the fundamentals classical SPH formulations where several improvements in ISPH have been identified in order to simulate successful progressive waves.

7.1.1 Progressive waves in a 2-D NWT

Wave propagation in an intermediate depth has been investigated using standard SPH formulations, comparing with linear wave theory. This investigation showed that using standard SPH equations would lead the waves to decay along the NWT. The chronology of modifications involved are as follows;

- A new scheme for free surface particle identification was introduced to prevent inner fluid particles from being misjudged as free surface particles and particle collision control method has been tested to reduce the numerical instability caused by collisions between high-speed particles in the simulation.

- Particle shifting method to distribute particles more uniformly was employed to reduce the approximation errors by ensuring that kernel domain is fully supported for more accurate integration.

- Lack of neighbouring points used to reduce the computational cost in the kernel particularly on the free surface has limited the information from neighbouring particles to be exploited fully by the kernel support. It does actually compromise the ISPH ability to predict velocity and pressure value accurately. Thus, a kernel correction term known as renormalization is applied in order to overcome this drawback. However, numerical instabilities are observed on the free surface as a result of the increased kernel interpolation error.

- It is later found that these free surface instabilities could be solved by artificially increasing the viscosity of particles on or adjacent to the free surface without strongly influence the free surface predictions. Effect of different values of viscosity is investigated in producing the accurate and stable free surface profiles.

- While this approach produced a reliable result, convergence studies show most simulations were not able to maintain a consistent free surface profile in a longer run-time simulation where propagating waves were gradually decayed. Velocity and pressure distributions were also poorly predicted in comparison to the potential theory.

Many complex engineering problems that implement SPH as an operational tool requires massive computational power where parallel processing system is also desirable for optimisation. Due to limited knowledge in parallel computing and time constraints, with the objectives of SPH application become the priority than improving the method numerically for seakeeping analysis, searching for an alternative approach was the best decision.

7.1.2 Progressive waves in a 2-D NWT by WCSPH

Open source code of Weakly Compressible SPH (WCSPH) provided by DualSPHysics presents some attractive features and can be designed to suit different purposes. The GPU implementation offered great performance and helps in reducing the CPU computing cost. The WCSPH model was applied to the similar problem of wave generation and the results were compared with the results from the modified ISPH model and linear wave theory. Based on the comparative study, validations in terms of wave profiles, velocity fields, and pressure distributions of each method were discussed. It turned out that results by WCSPH showed good agreement with potential theory. Contrary to ISPH method, there was no indication of severe pressure fluctuations on the free surface and the results were steady enough in longer run-time simulations. Therefore, WCSPH is rather applied in the later study of wave-body interactions.

7.1.3 2-D FSI problems

In chapter 5, WCSPH model has been successfully applied to simulate well-defined 2-D hydrodynamic tests of radiation, diffraction and wave-induced motion. Both fluid and solid models were discretised by particles in all simulations.

- For radiation test, WCSPH showed a good overall agreement in the prediction of hydrodynamic coefficients, namely added mass and damping when compared with theoretical and experimental data. Convergence analysis was carried out considering most small discrepancies recorded were observed at comparatively low frequencies. Similar discrepancies were also found with other numerical modelling approach.
- For wave loading on a half-submerged fixed rectangular, WCSPH agrees well with the analytical solution by Mei and Black (1969).
- While for progressive waves interacting with floating rectangular section, WCSPH was proved to be able to demonstrate a good motion responses with experimental data of Ren (2015) for 2 different wave heights.

It was later found in the convergence study that refining procedure by decreasing the particle size and employing more computational points (particles) would not improve the accuracy of the predictions significantly unless new algorithm is developed in the precision of particle location and neighbouring searching scheme.

7.1.4 3-D FSI problems

The main objective of this PhD thesis was to study the implementation of SPH method in 3-D seakeeping problems of hydrodynamics and hydroelasticity. Here, two well-defined test cases of rigid body and flexible body were considered.

- In the analysis of rigid body in waves, three different tests have been investigated using WCSPH. Progressing waves without dissipation was studied in the first test and the results were in good agreement with linear wave theory. For the second test, RAOs of the barge in waves fits well with predictions from MARS and STAR-CCM+ except for some discrepancies at amidships. The relationship between wavelength and particles' number has shown that the particle spacing used in the test was adequate along with lower computational costs. The last test investigated one-way coupling approach in barge deformation. Deviations were observed in comparison to other available numerical methods. Using smaller wave height has shown to work well with the prediction by linear theory particularly at $\omega = 5.235$ rad/s.

- In the last part of this work, flexible barge was successfully applied in the original 2-D rigid body radiation problem. This is also one of the attempts to fulfil the core objectives of this study where SPH may provide significant advantages in the modelling of the behaviour of 3-D ship in waves. The barge was forced to oscillate in rigid body motions of heave and pitch, 2-node and 3-node distortion modes. The effects of domain size and particle density were closely observed particularly in larger domain and longer wavelengths.

The WCSPH solutions followed most of the expected trends from CFD and potential flow theory, indicating a trustworthy numerical tool in predicting the added mass and damping coefficients, given enough particle refinements. To the author's knowledge, these are the first extensive studies on the seakeeping problem by particle method involving such large dimension. In doing so, the novelty of the present study can be considered in the i) techniques employed for different applications and ii) validation in 3-D tests which also has been explained in section 1.4.

7.2 Future works

In general, the works covered in this study has proven the implementation of SPH in seakeeping problems with satisfactory accuracy. However, to be able to extend this method further to a large set of applications, improvements in term of methodology and implementations are essential.

It has been shown that present model demonstrated some deviations, particularly at relatively lower frequencies. This is due to the issue of precision that occurs in problems involving very large domains at a very high resolution. The issue arises from using single precision to represent the position of the particles. This issue can be overcome by using particles of small mass and small kernel support in regions where high definition is needed and particles of larger mass elsewhere. As previously discussed, double precision technique (Dominguez et al., 2014) or variable resolution technique (Vacondio et al., 2013) could improve the results while optimising the computational cost.

One of the challenges in this study was to calculate the correct force on bodies which can be evaluated by summing the force exerted on the boundary particles for the entire body. For this work, the correct force magnitude is found to be sensitive to the repulsive boundary condition. Alternative *interface technique or boundary treatment* between rigid bodies and fluid motion where treatment of boundary can smooth out pressure fluctuation on the structure particularly when dealing with 3-D problems is indeed essential.

In chapter 6, simulations of the 3-D floating bodies have been shown employing only a rigid barge. It is recommended that flexible barge in waves should be simulated and compared with flexible results by STAR-CCM+/ABAQUS and experiment (Remy et al., 2006). Besides RAOs of each mode, non-linear effects on wave induced motions and loads for flexible bodies should also be investigated. It is also recommended that the two ways of weak or strong hydroelastic coupled solutions in the VBM should be solved in order to address the hydroelastic effects due to flexible bodies. The weak coupling approach involves active interaction between fluid and body where the deformation of the body is transferred to the fluid once in every time step while two-way strong coupling requires information to be passed back and forth between fluid and body solver in a single time step. Strong coupling scheme is usually applied to maximise the stability of the numerical solution (Seng and Jensen, 2012). Then, the feasibility of applying these options should be discussed by making a comparison against other available numerical results and experimental measurements.

Further, extensive study of 3-D floating bodies with much more complex geometries of the ship-like structure should be carried out in order to investigate the behaviour of repulsive boundary and motion response of complex bodies. With the implementation of much more complex bodies, the investigation should be done involving coupled antisymmetric hydrodynamic coefficients where horizontal bending and twisting are concerned. The investigation would likely to introduce further nonlinearities in the flow field of radiated waves.

List of References

[Akbari and Namin, 2013] Akbari, H., & Namin, M. M. (2013). Moving particle method for modelling wave interaction with porous structures. *Coastal Engineering*, *74*, 59-73.

[Adami et al., 2012] Adami, S., Hu, X. Y., & Adams, N. A. (2012). A generalized wall boundary condition for smoothed particle hydrodynamics. *Journal of Computational Physics*, *231*(21), 7057-7075.

[Altomare et al., 2015] Altomare, C., Crespo, A. J., Domínguez, J. M., Gómez-Gesteira, M., Suzuki, T., & Verwaest, T. (2015). Applicability of Smoothed Particle Hydrodynamics for estimation of sea wave impact on coastal structures. *Coastal Engineering*,*96*, 1-12.

[Antuono et al., 2010] Antuono, M., Colagrossi, A., Marrone, S., & Molteni, D. (2010). Free-surface flows solved by means of SPH schemes with numerical diffusive terms. *Computer Physics Communications*, *181*(3), 532-549.

[Antuono et al., 2011] Antuono, M., Colagrossi, A., Marrone, S., & Lugni, C. (2011). Propagation of gravity waves through an SPH scheme with numerical diffusive terms. *Computer Physics Communications*, *182*(4), 866-877.

[Antuono et al., 2012] Antuono, M., Colagrossi, A., & Marrone, S. (2012). Numerical diffusive terms in weakly-compressible SPH schemes. *Computer Physics Communications.*

[Antuono et al., 2016] Antuono, M., Marrone, S., Colagrossi, A., & Bouscasse, B. (2015). Energy balance in the δ-SPH scheme. *Computer Methods in Applied Mechanics and Engineering*, *289*, 209-226.

[Ahmadzadeh et al., 2013] Ahmadzadeh, M., Saranjam, B., Hoseini Fard, A., & Binesh, A. R. (2013). Numerical simulation of sphere water entry problem using Eulerian–Lagrangian method. *Applied Mathematical Modelling*.

[Ahn and Kallinderis, 2006] Ahn, H. T., & Kallinderis, Y. (2006). Strongly coupled flow/structure interactions with a geometrically conservative ALE scheme on general hybrid meshes. *Journal of Computational Physics*, *219*(2), 671-696.

[Baum and Taylor, 2009] Bai, W., & Taylor, R. E. (2009). Fully nonlinear simulation of wave interaction with fixed and floating flared structures. *Ocean engineering*, *36*(3), 223-236.

[Baum et al., 2006] Baum, J. D., Mestreau, E., Luo, H., Löhner, R., Pelessone, D., Giltrud, M. E., & Gran, J. K. (2006). Modelling of near-field blast wave evolution. In *44th AIAA Aerospace Sciences Meeting and Exhibition* (pp. 2006-191).

[Batchelor, 2000] Batchelor, G. K. (2000). An introduction to fluid dynamics.

[Beeman, 1976] Beeman, D. (1976). Some multistep methods for use in molecular dynamics calculations. *Journal of Computational Physics*, 20:130-139.

[Belytschko and Liu, 1999] Belytschko, T., Moran, B., & Liu, W. K. (1999). *Nonlinear finite element analysis for continua and structures* (Vol. 1). Wiley.

[Belibassaki, 2010] Belibassakis, K. A. (2010). Roll response of ship-hull sections in variable bathymetry regions by a hybrid BEM - Vortex particle method, 8 Da Hui Si Road, Beijing, 100081, China, China Ocean Press.

[Benson, 1992] Benson D.J. (1992). Computational methods in Lagrangian and Eulerian hydrocodes. *Computer Methods in Applied Mechanics and Engineering*, 99:235-394.

[Benz and Asphaug, 1994] Benz, W., & Asphaug, E. (1995). Simulations of brittle solids using smooth particle hydrodynamics. *Computer physics communications*, *87*(1), 253-265.

[Biausser et al., 2004] Biausser, B., Fraunié, P., Grilli, S. T., & Marcer, R. (2004). Numerical analysis of the internal kinematics and dynamics of 3-D breaking waves on slopes. *International Journal of Offshore and Polar Engineering*, *14*(4).

[Biesel and Suquet, 1954] Biesel F. and Suquet F. (1954). Laboratory wave generating apparatus. *St. Anthony Falls Hydraulic Laboratory Proj. Rep. No. 39*.

[Bishop et al., 1979] Bishop, R. E. D., Price, W. G., & Temarel, P. (1979). *A unified dynamical analysis of antisymmetric ship response to waves* (No. Paper No. W15).

[Bishop and Price, 1979] Bishop R.E.D and Price W.G. (1979). Hydroelasticity of ships. *Cambridge University Press*.

[Bishop et al., 1986] Bishop, R. E. D., Price, W. G., & Wu, Y. (1986). A general linear hydroelasticity theory of floating structures moving in a seaway.*Philosophical Transactions of the Royal Society of London A: Mathematical, Physical and Engineering Sciences*, *316*(1538), 375-426.

[Bonet and Lok, 1999] Bonet, J., & Lok, T. S. (1999). Variational and momentum preservation aspects of smooth particle hydrodynamic formulations. *Computer Methods in applied mechanics and engineering*, *180*(1), 97-115.

[Bonet et al., 2004] Bonet, J., Kulasegaram, S., Rodriguez-Paz, M. X., & Profit, M. (2004). Variational formulation for the smooth particle hydrodynamics (SPH) simulation of fluid and solid problems. *Computer Methods in Applied Mechanics and Engineering*, *193*(12), 1245-1256.

[Bouscasse et al., 2013] Bouscasse, B., Colagrossi, A., Marrone, S., & Antuono, M. (2013). Nonlinear water wave interaction with floating bodies in SPH. *Journal of Fluids and Structures*, *42*, 112-129.

[Brackbill et al., 1992] Brackbill, J. U., Kothe, D. B., & Zemach, C. (1992). A continuum method for modelling surfaces tension. *Journal of computational physics*, *100*(2), 335-354.

[Broglia et al., 2009] Broglia, R., Bouscasse, B., Di Mascio, A., Lugni, C., & Atsavapranee, P. (2009, January). Experimental and numerical analysis of the roll decay motion for a patrol boat. In *The Nineteenth International Offshore and Polar Engineering Conference*. International Society of Offshore and Polar Engineers.

[Bui et al., 2007] Bui, H. H., K.Sako, et al. (2007). "Numerical simulation of soil-water interaction using smoothed particle hydrodynamics (SPH) method." *Journal of Terramechanics* 44: 339-346.

[Carrica et al., 2007] Carrica, P. M., Wilson, R. V., & Stern, F. (2007). An unsteady single-phase level set method for viscous free surface flows. *International Journal for Numerical Methods in Fluids*, *53*(2), 229-256.

[Cartwright et al., 2004] Cartwright, B., Groenenboom, P. H. L., & McGuckin, D. (2004). Examples of Ship Motion and Wash Predictions by Smoothed Particle Hydrodynamics (SPH). In *9th Symposium on Practical Design of Ships and Other Floating Structures, Luebeck-Travemuende, Germany*.

[Cartwright et al., 2006] Cartwright B., Xia J., Cannon S., McGuckin D., Groenenboom P. (2006). Motion prediction of ships and yachts by smoothed particle hydrodynamics*. In: Proc. 2nd high-performance yacht design conference, Auckland*. 14–16 February.

[Castiglione et al., 2011] Castiglione, T., Stern, F., Bova, S., & Kandasamy, M. (2011). Numerical investigation of the seakeeping behaviour of a catamaran advancing in regular head waves. *Ocean Engineering*, *38*(16), 1806-1822.

[Chapchap et al., 2011] Chapchap, A., Ahmed, F. M., Hudson, D. A., Temarel, P., & Hirdaris, S. E. (2011). The influence of forward speed and nonlinearities on the dynamic behaviour of a container ship in regular waves. *Trans. RINA*, *153*(2), 137-148.

[Chapchap, 2015] Cerello Chapchap, A. (2015). *Unstructured MEL modelling of non-linear 3D Ship hydrodynamics* (Doctoral dissertation, University of Southampton).

[Chen et al., 2013] Chen, Z., et al. (2013). "A comparative study of truly incompressible and weakly compressible SPH methods for free surface incompressible flows." *International Journal for Numerical Methods in Fluids* **73**(9): 813-829.

[Chen and Doolen, 1998] Chen, S., & Doolen, G. D. (1998). Lattice Boltzmann method for fluid flows.*Annual review of fluid mechanics*, *30*(1), 329-364.

[Chen et al., 1996] Chen, J. S. Pan, C., Wu, C.-T., and Liu, W. K. (1996) "Reproducing kernel particle methods for large deformation analysis of non-linear structures," *Computer Methods in Applied Mechanics and Engineering* Vol. 139, pp.195-228

[Chen et al., 1997] Chen, J.S., Pan, C., andWu, C.T. (1997) "Large deformation analysis of rubber based on a reproducing kernel particle method," *Computational Mechanics*, Vol. 19, pp. 153-168

[Chen et al., 1999] Chen, J. K., Beraun, J. E., & Jih, C. J. (1999). An improvement for tensile instability in smoothed particle hydrodynamics. *Computational Mechanics,23*(4), 279-287.

[Chen et al., 2014] Chen, L. F., Zang, J., Hillis, A. J., Morgan, G. C. J., & Plummer, A. R. (2014). Numerical investigation of wave–structure interaction using OpenFOAM. *Ocean Engineering*, *88*, 91-109.

[Chen and Beraun, 2000] Chen, J. K., & Beraun, J. E. (2000). A generalised smoothed particle hydrodynamics method for nonlinear dynamic problems. *Computer Methods in Applied Mechanics and Engineering*, *190*(1), 225-239.

[Ciappi et al., 2003]Ciappi, E., Dessi, D., & Mariani, R. (2003). Slamming and whipping response analysis of a fast monohull via a segmented model test. In *Proceedings of the Third International Conference on Hydroelasticity in Marine Technology*(pp. 143-153).

[Crespo et al., 2007] Crespo, A. J. C., Gomez-Gesteira, M., and Dalrymple, R. A. (2007). Boundary conditions generated by dynamic particles in sph methods. *Computers,Materials & continua*, 5:173-184.

[Crespo et al., 2007] Crespo, A. J. C., Gómez-Gesteira, M., & Dalrymple, R. A. (2007). 3D SPH simulation of large waves mitigation with a dyke. *Journal of Hydraulic Research,45*(5), 631-642.

[Crespo et al., 2008] Crespo, A.J.C., Gómez-Gesteira, M., Dalrymple, R.A. (2008). Modelling dam breaks behaviour over a wet bed by a SPH technique. J. Wtrwy. *Port, Coastal and Ocean Engrg*. 134(6).

[Crespo et al., 2013] A.J.C. Crespo, J.M.Dominguez, Gómez-Gesteira, B.D.Rogers, S.Longshaw, R.Canelas, R.Vacondio. (2013). User guides for DualSPHysics code. DualSPHysics_v3.0 guide.

[Crespo et al., 2015] Crespo, A. J. C., Domínguez, J. M., Rogers, B. D., Gómez-Gesteira, M., Longshaw, S., Canelas, R., ... & García-Feal, O. (2015). DualSPHysics: Open-source parallel CFD solver based on Smoothed Particle Hydrodynamics (SPH). *Computer Physics Communications*, *187*, 204-216.

[Cummins and Rudman, 1999] Cummins, S. J. and Rudman, M. (1999). An sph projection method. *Journal of Computational Physics*, 152:584-607.

[Colagrossi and Landrini, 2003] Colagrossi A. and Landrini M. (2003). Numerical simulation of interface flows by smoothed particle hydrodynamics, *Journal of Computational Physics*. 191, 448-475.

[Colagrossi et al., 2009] Colagrossi, Andrea, Matteo Antuono & David Le Touze (2009), Theoretical considerations on the free-surface role in the smoothed-particle-hydrodynamics, *PHYSICAL REVIRE E 79*.

[Colagrossi et al., 2013] Colagrossi, A., A. Souto-Iglesias, M. Antuono and S. Marrone (2013). Smoothed-particle-hydrodynamics modelling of dissipation mechanisms in gravity waves. *Physical Review E - Statistical, Nonlinear, and Soft Matter Physics* **87**(2).

[Cottet, 1999] Cottet, G. H. (1999, November). 3D vortex methods: achievements and challenges. In *International Conference on Vortex Methods*.

[Cottet and Poncet, 2004] Cottet, G. H., & Poncet, P. (2004). Advances in direct numerical simulations of 3D wall-bounded flows by Vortex-in-Cell methods. *Journal of Computational Physics*, *193*(1), 136-158.

[Cummins and Rudman, 1999] Cummins, S. J., & Rudman, M. (1999). An SPH projection method. *Journal of computational physics*, *152*(2), 584-607.

[Dalrymple and Rogers, 2006] Dalrymple R. A. and Rogers B.D. (2006). Numerical modelling of water waves with the SPH method. *Coastal Engineering* **53**(2-3): 141-147.

[Dalrymple et al., 2011] Dalrymple, R. A., Herault, A., Bilotta, G., & Farahani, R. J. (2011). GPU-accelerated SPH model for water waves and free surface flows. *Coastal Engineering Proceedings*, *1*(32), 9.

[Darwish, 1993] Darwish, M. S. (1993). A new high-resolution scheme based on the normalised variable formulation. *Numerical Heat Transfer, Part B Fundamentals*, *24*(3), 353-371.

[Das and Cheung, 2012] Das, S., & Cheung, K. F. (2012). Hydroelasticity of marine vessels advancing in a seaway. *Journal of Fluids and Structures*, *34*, 271-290.

[Dean and Dalrymple, 1991] R.G.Dean and R.A. Dalrymple.(1991). Water wave mechanics for engineers and scientist, Advanced Series on Ocean Engineering, vol. 2: 172-185.

[Di Mascio et al., 2007] Di Mascio, A., Broglia, R., & Muscari, R. (2007). On the application of the single-phase level set method to naval hydrodynamic flows. *Computers & fluids*, *36*(5), 868-886.

[Didier and Neves, 2012] Didier, E., & Neves, M. G. (2012). A semi-infinite numerical wave flume using smoothed particle hydrodynamics. *International Journal of Offshore and Polar Engineering*, *22*(03).

[Didier et al., 2014] Didier, E., Neves, D. R. C. B., Martins, R., & Neves, M. G. (2014). Wave interaction with a vertical wall: SPH numerical and experimental modelling. *Ocean Engineering*, *88*, 330-341.

[Dilts, 2000] Dilts, G. A. (2000). Moving least-squares particle hydrodynamics II: conservation and boundaries. *International Journal for Numerical Methods in Engineering*, *48*(10), 1503-1524.

[Dominuque et al., 2014] Dominuque J.M., Crespo A.J.C., Barreiro A., Gomez-Gesteira M., (2014). Efficient implementation of double precision in GPU computing to simulate realistic cases with high resolution. *9th international SPHERIC workshop*, 140-145.

[Doring et al., 2004] Doring, M., Oger, G., Alessandrini, B., & Ferrant, P. (2004, January). Sph simulations of floating bodies in waves. In *ASME 2004 23rd International Conference on Offshore Mechanics and Arctic Engineering* (pp. 741-747). American Society of Mechanical Engineers.

[Dowell and Kenneth, 2001] Dowell E. H., Kenneth C. H., (2001). Modelling of Fluid-Structure Interaction. *Annu. Rev. Fluid Mech*. 33:445-90.

[DualSPHysics team, 2016] User Guide for DualSPHysics v4.0.

[Drews and Horst, 2001] Drews J. E., Horst P. (2001). Fluid-structure interaction of high lift devices at low Mach numbers. In *Computational fluid and solid mechanics* (ed. K. J. Bathe), pp. 1139-1142. Elsevier.

[Faltinsen, 1977] Faltinsen, O. M. (1977, September). Numerical solution of transient nonlinear free-surface motion outside or inside moving bodies. In *Proceedings 2nd Int. Conf. on Num. Ship Hydrodynamics, UC Berkeley* (pp. 257-266).

[Faltinsen, 2001] Faltinsen O.M. (2001) Hydroelastic slamming. *Journal of Marine Science and Technology*, 5: 49-65.

[Faltinsen et al., 1991] Faltinsen, O., Zhao, R., & Umeda, N. (1991). Numerical Predictions of Ship Motions at High Forward Speed [and Discussion]. *Philosophical Transactions of the Royal Society of London A: Mathematical, Physical and Engineering Sciences*, *334*(1634), 241-252.

[Fanfan, 2013] Fanfan S. (2013) Investigations of Smoothed Particle Hydrodynamics method for fluid-rigid body interactions. *Final Thesis*. University of Southampton.

[Farahani et al., 2009] Farahani, M. H., Amanifard, N., and Hosseini, S. M. (2009). A fluid-structure interaction simulation by smoothed particle hydrodynamics. Engineering Letter, 16.

[Fonseca and Guedes., 2002] Fonseca, N. and C. Guedes Soares (2002). "Comparison of numerical and experimental results of nonlinear wave-induced vertical ship motions and loads." *Journal of Marine Science and Technology* **6**(4): 193-204.

[Fontaine, 2000] Fontaine, E. (2000). On the use of smoothed particle hydrodynamics to model extreme waves and their interaction with structures. *Proc., Rogue Waves 2000*.

[Fourey et al., 2010] Fourey, G., Oger, G., Le Touzé, D., & Alessandrini, B. (2010, June). Violent Fluid-Structure Interaction simulations using a coupled SPH/FEM method. In*IOP Conference Series: Materials Science and Engineering* (Vol. 10, No. 1, p. 012041). IOP Publishing.

[Fossen, 2002] Fossen, Thro I. (2002), Marine control systems: guidance, navigation, and control of ships, rigs and underwater vehicles: Marine Cybernetics AS.).

[Gao et al., 2012] Gao, R., B. Ren, G. Wang and Y. Wang (2012). Numerical modelling of regular wave slamming on subface of open-piled structures with the corrected SPH method. *Applied Ocean Research* **34**(0): 173-186.

[Giron et al. 2005] Giron-Sierra, J. M., Esteban, S., Recas, J., Andres-Toro, B., De la Cruz, J. M., Riola, J. M., & Velasco, F. (2005, July). Overview of a research on actuators controls for better seakeeping in fast ships. In *World Congress* (Vol. 16, No. 1, pp. 1948-1948).

[Gomez and Dalrymple, 2004]Gómez-Gesteira, M., & Dalrymple, R. A. (2004). Using a three-dimensional smoothed particle hydrodynamics method for wave impact on a tall structure.*Journal of waterway, port, coastal, and ocean engineering*, *130*(2), 63-69.

[Gomez et al., 2005] Gomez-Gesteira M, Cerqueiro D, Crespo C, Dalrymple RA. (2005). Green water overtopping analysed with a SPH model. *Ocean Engineering* ;32(2): 223–38.

[Gotoh et al., 2004] Gotoh, H., Shao, S., Memita, T. (2004). SPH-LES model for numerical investigation of wave interaction with partially immersed breakwater. *Coastal Engrg. J.* 46(1), 39–63.

[Gotoh et al., 2014] Gotoh, H., Khayyer, A., Ikari, H., Arikawa, T., & Shimosako, K. (2014). On enhancement of Incompressible SPH method for simulation of violent sloshing flows. *Applied Ocean Research*, *46*, 104-115.

[Gingold and Monaghan, 1977] Gingold, R. A. and Monaghan, J. J. (1977). Smoothed particle hydrodynamics: Theory and application to non-spherical stars. *Monthly Notices of the Royal Astronomical Society*, 181:375-389.

[Greco et al., 2013] Greco, M., et al. (2013). "3D domain decomposition for violent wave-ship interactions." *International Journal for Numerical Methods in Engineering* **95**(8): 661-684.

[Greco and Lugni, 2012] Greco, M. and C. Lugni (2012). "3-D seakeeping analysis with water on deck and slamming. Part 1: Numerical solver.*" Journal of Fluids and Structures* **33**: 127-147.

[Gretarsson et al., 2011] Gretarsson J.T., Kwatra N., Fedkiw R. (2011). Numerically stable fluid-structure interactions between compressible flow and solid structures. *Journal of Computational Physics*. 230:3062-3084.

[Hadžić et al., 2005] Hadžić, I., Hennig, J., Perić, M., & Xing-Kaeding, Y. (2005). Computation of flow-induced motion of floating bodies. *Applied mathematical modelling*, *29*(12), 1196-1210.

[Hans, 1999] Hans U.M. (1999). Review: hydrocodes for structure response to underwater explosions, *Shock and Vibration*, 6(2): 81-96.

[Hashemi et al., 2012] Hashemi, M. R., Fatehi, R., & Manzari, M. T. (2012). A modified SPH method for simulating motion of rigid bodies in Newtonian fluid flows. *International Journal of Non-Linear Mechanics*, *47*(6), 626-638.

[Hayasi et al., 2000] Hayashi, M., Gotoh, H., Memita, T., Sakai, T. (2000), 16–21 July. Gridless numerical analysis of wave-breaking and overtopping at upright seawall. *Proc. 27th Int. Conf. Coast. Eng., Sydney Australia*, pp. 2100–2113.

[Heil et al., 2008] Heil, M., Hazel, A. L., & Boyle, J. (2008). Solvers for large-displacement fluid–structure interaction problems: segregated versus monolithic approaches.*Computational Mechanics*, *43*(1), 91-101.

[Hernquist and Katz, 1989] Hernquist L. and Katz N. (1989). TreeSPH- A unification of SPH with the hierarchical tree method. *The Astrophysical Journal Supplement Series*, 70: 419-446.

[Hirdaris et al., 2003] Hirdaris, S. E., Price, W. G., & Temarel, P. (2003). Two-and three-dimensional hydroelastic modelling of a bulker in regular waves. *Marine Structures*, *16*(8), 627-658.

[Hirdaris and Temarel, 2009] Hirdaris, S. E., & Temarel, P. (2009). Hydroelasticity of ships: recent advances and future trends. *Proceedings of the Institution of Mechanical Engineers, Part M: Journal of Engineering for the Maritime Environment*,*223*(3), 305-330.

[Hirdaris et al., 2010] Hirdaris, S. E., White, N. J., Angoshtari, N., Johnson, M. C., Lee, Y., & Bakkers, N. (2010). Wave loads and flexible fluid-structure interactions: current developments and future directions. *Ships and Offshore Structures*,*5*(4), 307-325.

[Hirt and Nichols, 1981] Hirt, C. W., & Nichols, B. D. (1981). Volume of fluid (VOF) method for the dynamics of free boundaries. *Journal of computational physics*, *39*(1), 201-225.

[Hirt et al., 1974] Hirt C.W.,Amsden A.A. and Cook J.L. (1974). An arbitrary Lagrangian-Eulerian computing method for all flow speeds, *Journal of Computational Physics*, 14:227-253.

[Hochkirch and Mallol, 2013] Hochkirch, K., & Mallol, B. (2013). On the importance of full-scale CFD simulations for ships. In *11th International conference on computer and IT applications in the maritime industries, COMPIT*.

[Holmes et al., 2011] Holmes, D. W., Williams, J. R., & Tilke, P. (2011). Smooth particle hydrodynamics simulations of low Reynolds number flows through porous media. *International Journal for Numerical and Analytical Methods in Geomechanics*, *35*(4), 419-437.

[Hosseini et al., 2007] Hosseini, S. M., Manzari, M. T., & Hannani, S. K. (2007). A fully explicit three-step SPH algorithm for simulation of non-Newtonian fluid flow.*International Journal of Numerical Methods for Heat & Fluid Flow*, *17*(7), 715-735.

[Hu and Adams, 2007] Hu, X. Y. and N. A. Adams (2007). "An incompressible multi-phase SPH method." *Journal of Computational Physics* **227**(1): 264-278.

[Huang et al., 1998] Huang, Y., & Sclavounos, P. D. (1998). Nonlinear ship motions. *Journal of ship research*, *42*(2), 120-130.

[Hubner et al., 2004] Hubner B., Walhorn E., and Dinkler D. (2004). A monolithic approach to fluid-structure interaction using space-time finite elements. *Comput. Methods Appl. Mech. Engineering.*, 193: 2087-2104.

[Huerta and Fernandez-Mendez, 2000] Huerta, A., and Fernandez-Mendez, S. (2000), "Enrichment and coupling of finite element and meshless methods," *International Journal for Numerical Methods in Engineering*, Vol. 48, pp. 1615-1536.

[Hughes and Graham, 2010] Hughes, J. P. and D. I. Graham (2010). "Comparison of incompressible and weakly-compressible SPH models for free-surface water flows.*" Journal of Hydraulic Research* **48**(SUPPL. 1): 105-117.

[Inutsuka, 2002] Inutsuka, S. I. (2002). Reformulation of smoothed particle hydrodynamics with Riemann solver. *Journal of Computational Physics*, *179*(1), 238-267.

[Huijsmans et al., 2004] Huijsmans, R. H. M., & Van Grosen, E. (2004). Coupling freak wave effects with green water simulations. *Proceeding of the 14th ISOPE*, 23-28.

[Jensen, 2001] Jensen, J. J. (2001). *Load and global response of ships* (Vol. 4). Elsevier.

[Jensen and Mansour, 2003] Jensen, J. J., & Mansour, A. E. (2003). Estimation of the Effect of Green Water and Bow Flare Slamming on the Wave-Induced Vertical Bending Moment Using Closed-Form Expressions. In *Proceedings of the 3rd International Conference on Hydroelasticity in Marine Technology*. The University of Oxford.

[Jensen et al., 1998] Jenssen, C. B., Kvamsdal, T., Okstad, K. M., & Amundsen, J. (1998, June). Parallel methods for fluid-structure interaction. In *International Workshop on Applied Parallel Computing* (pp. 263-274). Springer Berlin Heidelberg.

[Jensen et al., 2004] Jensen, J. J., Mansour, A. E., & Olsen, A. S. (2004). Estimation of ship motions using closed-form expressions. *Ocean Engineering*, *31*(1), 61-85.

[Jia, 1987] Jia, Shuhui. (1987), Rigid Body Dynamics: Gao deng jiao yu chu ban she, China).

[Johnson et al., 1996] Johnson, G. R., Stryk, R. A., and R., B. S. (1996). SPH for high-velocity impact computations. *Comput. Methods Appl. Mech. Engineering.*, 139:347-373.

[Johnson and Beissel, 1996] Johnson, G. and Beissel, S. (1996). Normalised smoothing functions for sph impact computations. *Int J Numer Meth Eng*, 39:2725-41.

[Kawamura et al., 2016] Kawamura, K., Hashimoto, H., Matsuda, A., & Terada, D. (2016). SPH simulation of ship behaviour in severe water-shipping situations. *Ocean Engineering*, *120*, 220-229.

[Kazuya et al., 2007] Kazuya S., Katsuji T. and Seiichi K. (2007). Numerical analysis of coupling between ship motion and green water on deck using MPS method. *Proceeding of International Conference on Violent Flows*.

[Kevin et al., 2010] Kevin M., Dominic J.P. and Donghee L. (2010). Fluid Structure interaction during ship slamming. *Fifth OpenFOAM Workshop*.

[Khayyer et al., 2008] Khayyer, A., Gotoh, H., & Shao, S. D. (2008). Corrected incompressible SPH method for accurate water-surface tracking in breaking waves. *Coastal Engineering*, *55*(3), 236-250.

[Kim et al., 2014] Kim, J. H., Lakshmynarayanana, P. A., & Temarel, P. (2014). Added-mass and damping coefficients for a uniform flexible barge using VOF.

[Koh et al., 2012] Koh, C. G., Gao, M., & Luo, C. (2012). A new particle method for simulation of incompressible free surface flows problems. *International Journal for Numerical Methods in Engineering*, *89*(12), 1582-1604.

[Koshizuka et al., 1995] Koshizuka, S., Tamako, H., Oka, Y. (1995). A particle method for incompressible viscous flow with fluid fragmentation. Comput. Fluid Dyn. J. 4 (1), 29–46.

[Korvin-Kroukovsky and Jacobs, 1957] Korvin-Kroukovsky, B. V., & Jacobs, W. R. (1957). *Pitching and heaving motions of a ship in regular waves* (Vol. 659). STEVENS INST OF TECH HOBOKEN NJ EXPERIMENTAL TOWING TANK.

[Krongauz and Belytschko, 1996] Krongauz, Y. and Belytschko, T. (1996) "Enforcement of essential boundary conditions in meshless approximations using finite elements," Computer Methods in Applied Mechanics and Engineering Vol. 131, pp. 133-145

[Krysl and Belytschko, 1996] Krysl, P. and Belytschko, T. (1996) "Analysis of Thin Shells by the Element-free Galerkin Method," *International Journal of Solids and Structures*, Vol. 33, pp. 3057-3080.

[Lafaurie et al., 1994] Lafaurie, B., Nardone, C., Scardovelli, R., Zaleski, S., & Zanetti, G. (1994). Modelling merging and fragmentation in multiphase flows with SURFER. *Journal of Computational Physics*, *113*(1), 134-147.

[Lakshmynarayanana et al., 2015] Lakshmynarayanana, P., Temarel, P., & Chen, Z. (2015). Hydroelastic analysis of a flexible barge in regular waves using coupled CFD-FEM modelling. *Analysis and Design of Marine Structures V*, 95.

[Landrini et al., 2003] Landrini M., Colagrossi A. and Faltisen O.M. (2003). Sloshing in 2D flows by the SPH method. Proceedings, *8th International Conference on Numerical Ship Hydrodynamic*.

[Landrini et al., 2007] Landrini M., Colagrossi A., Greco M., Tulin M.P. (2007). Gridless simulations of splashing processes and near-shore bore propagation. *J.Fluid Mech*. 591: 183-213.

Landrini et al., [2012] Landrini, M., et al. (2012). The fluid mechanics of splashing bow waves on ships: A hybrid BEMSPH analysis. *Ocean Engineering* 53: 111-127.

[Larsson et al.,2000] Larsson, L., Stern, F. & Bertram, V. (2000). 'Gothenburg 2000: a workshop on numerical Ship Hydrodynamics', Gothenburg, Sweden.

[Lee et al., 2008] Lee, E. S., et al. (2008). Comparisons of weakly compressible and truly incompressible algorithms for the SPH meshfree particle method. *Journal of Computational Physics* 227(18): 8417-8436.

[Le Touze et al., 2010] Le Touze D., Marsh A., Oger G., Guilcher M.P., Khaddaj-Mallat C., Alessandrini B., Ferrant P. (2010). SPH simulation of green water and ship flooding scenarios. *Journal of Hydrodynamics*. 22:231-236.

[Lee et al., 2008] Lee E. S., Moulinec C., Xu R., Violeau D., Laurence D. and Stansby P. (2008). Comparisons of Weakly Compressible and Truly Incompressible Algorithms for the SPH Mesh Free Particle Method. *J. Comput. Phys,* 227:8417-8436.

[Lee et al., 2010b] Lee, E.-S., VIOLEAU, D., ISSA, R., and PLOIX, S. (2010b). Application of weakly compressible and truly incompressible sph to 3-d water collapse in waterworks. *Journal of Hydraulic Research*, 48:50-60.

[Lee et al., 2011] Lee, B. H., Park, J. C., Kim, M. H., & Hwang, S. C. (2011). Step-by-step improvement of MPS method in simulating violent free-surface motions and impact-loads. *Computer methods in applied mechanics and engineering*, *200*(9), 1113-1125.

[Leimkuhler et al., 1996] Leimkuhler, B.J., Reich, S., Skeel, R.D. (1996). Integration Methods for Molecular dynamic IMA Volume in Mathematics and its application. Springer.

[Leveque, 2002] Leveque, R. (2002). *Finite Volume Methods for Hyperbolic Problems.* Cambridge University Press.

[LeVeque and Li, 1997] LeVeque, R. J., & Li, Z. (1997). Immersed interface methods for Stokes flow with elastic boundaries or surface tension. *SIAM Journal on Scientific Computing*, *18*(3), 709-735.

[Liang, 1991] Liang, P. Y. (1991). Numerical method for calculation of surface tension flows in arbitrary grids. *AIAA journal*, *29*(2), 161-167.

[Liang et al., 2012] Liang, C. X., C. Y. Zhang, H. Y. Liu, Z. R. Qin and Q. Wang (2012). "Modelling low Reynolds number incompressible flows with curved boundaries using SPH." *International Journal for Numerical Methods in Fluids* **68**(9): 1173-1188.

[Liao and Hu, 2013] Liao, K., & Hu, C. (2013). A coupled FDM–FEM method for free surface flow interaction with thin elastic plate. *Journal of Marine Science and Technology*, 1-11.

[Lighthill, 2001] J.Lighthill. (2001). Waves in Fluids, Cambridge University Press, New York.

[Li et al., 2000] Li, S., Qian, Q., Liu, W.K., and Belytschko, T. (2000) "A meshfree contact detection algorithm," *Computer Methods in Applied Mechanics and Engineering*, Vol. 190, pp. 7185-7206.

[Li et al., 2000] Li, S., W. Hao, and Liu, W. K. (2000) "Numerical simulations of large deformation of thin shell structures using meshfree methods," *Computational Mechanics*, Vol. 25 No. 2/3, pages 102-116

[Li et al., 2012] Li J., Liu H.X., Gong K., Tan S.K., Shao S.D. (2012) SPH modelling of solitary wave fissions over uneven bottoms. *Coast Eng* ;60:261–75.

[Lin et al., 1996] Lin, W. M., Zhang, S., & Yue, D. (1996). Linear and nonlinear analysis of motions and loads of a ship with forward speed in large-amplitude waves. In *Proceedings 11th International Workshop on Water Waves and Floating Bodies. Hamburg, Germany*.

[Lin et al., 2007] Lin, W. M., Collette, M., Lavis, D., Jessup, S., & Kuhn, J. (2007). Recent hydrodynamic tool development and validation for motions and slam loads on Ocean-Going High-Speed Vessels. In *10th International Symposium on Practical Design of Ships and Other Floating Structures.*

[Lin et al., 2009] Lin, M. Y. and L. H. Huang (2009). "Study of water waves with submerged obstacles using a vortex method with Helmholtz decomposition." *International Journal for Numerical Methods in Fluids* **60**(2): 119-148.

[Lind et al., 2012] Lind, S. J., Xu, R., Stansby, P. K., & Rogers, B. D. (2012). Incompressible smoothed particle hydrodynamics for free-surface flows: a generalised diffusion-based algorithm for stability and validations for impulsive flows and propagating waves. *Journal of Computational Physics*, *231*(4), 1499-1523.

[Lind et al., 2015] Lind, S. J., Stansby, P. K., Rogers, B. D., & Lloyd, P. M. (2015). Numerical predictions of water–air wave slam using incompressible–compressible smoothed particle hydrodynamics. *Applied Ocean Research*, *49*, 57-71.

[Lind et al., 2016] Lind, S. J., Stansby, P. K., & Rogers, B. D. (2016). Fixed and moored bodies in steep and breaking waves using SPH with the Froude–Krylov approximation. *Journal of Ocean Engineering and Marine Energy*, 1-24.

[Liu, 2010] Liu, G. R. (2010). *Meshfree methods: moving beyond the finite element method*. CRC press.

[Liu and Liu, 2003] Liu, G. R. and Liu, M. B. (2003). *Smoothed Particle Hydrodynamics: a meshfree particle method.* World Scientific.

[Liu and Quek, 2003] Liu, G. R. and Quek (2003). *The finite element method: a practical course*. Butterworth Herinemann.

[Liu and Papanikolaou, 2010] Liu, S., & Papanikolaou, A. D. (2011). Time-domain hybrid method for simulating large amplitude motions of ships advancing in waves.*International Journal of Naval Architecture and Ocean Engineering*, *3*(1), 72-79.

[Liu and Papanikolaou, 2011] Liu, S. K., & Papanikolaou, A. (2011). Application of Chimera grid concept to simulation of the free-surface boundary condition. In *Proceedings of the 26th International Workshop on Water Waves and Floating Bodies (IWWWFB'11).*

[Liu et al., 1997] Liu, W. K., Jun, S., Sihling, D.T., Chen, Y., Hao, W. (1997) "Multiresolution reproducing kernel particle method for computational fluid dynamics," *International Journal for Numerical Methods in Fluids*, Vol. 24, pp. 1391-1415.

[Liu et al., 1997] Liu, W.K., Hao, W., Chen, Y., Jun, S., and Gosz, J. (1997) "Multiresolution reproducing kernel particle methods," *Computational Mechanics*, Vol. 20, pp. 295-309.

[Liu et al., 2011] Liu, C., J. Zhang and Y. Sun (2011). The optimisation of SPH method and its application in simulation of water wave. *7th International Conference on Natural Computation, ICNC 2011, Shanghai, China, IEEE Computer Society.*

[Liu et al., 2013] Liu, X., Xu, H., Shao, S., & Lin, P. (2013). An improved incompressible SPH model for simulation of wave–structure interaction. *Computers & Fluids*, *71*, 113-123.

[Liu et al., 2014] Liu, M. B., Shao, J. R., & Li, H. Q. (2014). An SPH model for free surface flows with moving rigid objects. *International Journal for Numerical Methods in Fluids*,*74*(9), 684-697.

[Longuet-Higgins and Cokelet, 1976] Longuet-Higgins, M. S., & Cokelet, E. D. (1976, July). The deformation of steep surface waves on water. I. A numerical method of computation. In Proceedings of the Royal Society of London A: Mathematical, Physical and Engineering Sciences (Vol. 350, No. 1660, pp. 1-26). The Royal Society.

[Lo and Shao, 2002] Lo E.Y.M and Shao S. (2002). Simulation of near-shore solitary wave mechanics by an incompressible SPH method. *Applied Ocean Research*. 24-275.

[Lucy, 1977] Lucy, L. B. (1977). A numerical approach to the testing of the fission hypothesis. *Astron. J.*, 82 :1013-24.

[Lundgren and Koumoutsakos, 1999] Lundgren, T., & Koumoutsakos, P. (1999). On the generation of vorticity at a free surface. *Journal of Fluid Mechanics*, *382*(1), 351-366.

[Manenti et al., 2008] Manenti S, Panizzo A, Ruol P, Martinelli L. SPH simulation of a floating body forced by regular waves. *Proceedings of Third International SPHERIC Workshop*. 38–41.

[Marrone et al., 2011] Marrone, S., Antuono, M., Colagrossi, A., Colicchio, G., Le Touzé, D., & Graziani, G. (2011). δ-SPH model for simulating violent impact flows. *Computer Methods in Applied Mechanics and Engineering*, *200*(13), 1526-1542.

[Marrone et al., 2011] Marrone, S., Colagrossi, A., Antuono, M., Lugni, C., & Tulin, M. P. (2011). A 2D+t SPH model to study the breaking wave pattern generated by fast ships. *Journal of Fluids and Structures*, *27*(8), 1199-1215.

[Marrone et al., 2012] Marrone S., Bouscasse B., Colagrossi A. and Antuono M. (2012). Study of ship waves breaking patterns using 3D parallel SPH simulations. *Computers & Fluids* **69**: 54-66.

[Maruzewski et al., 2010] Maruzewski, P., Touzé, D. L., Oger, G., & Avellan, F. (2010). SPH high-performance computing simulations of rigid solids impacting the free surface of water. *Journal of Hydraulic Research*, *48*(S1), 126-134.

[Maurizio, 2006] Maurizio L. (2006). Strongly nonlinear phenomena in ship hydrodynamics. *Journal of Ship Research*. 50:99-119.

[Meringolo, 2015] Meringolo, D. D., (2015). *Weakly-compressible Smoothed Particle Hydrodynamics modelling of fluid-structure interaction problems* (Doctoral dissertation, UNIVERSITA DELLA CALABRIA).

[Meringolo et al., 2015] Meringolo, D. D., Aristodemo, F., & Veltri, P. (2015). SPH numerical modelling of wave–perforated breakwater interaction. *Coastal Engineering*, *101*, 48-68.

[Moe, 2000] G.Moe. Linear wave theory, NTNU, Trondheim, Norway, Part II: Chapter 6, Section 6.

[Mok et al., 2001] Mok, D. P., Wall, W. A. & Ramm, E. (2001). Accelerated iterative substructuring schemes for instationary fluid-structure interaction. In *Computational ° uid and solid mechanics* (ed. K. J.Bathe), pp. 1325-1328. Elsevier.

[Mokos, 2013] Mokos, A. D. (2013). *Multi-phase Modelling of Violent Hydrodynamics Using Smoothed Particle Hydrodynamics (SPH) on Graphics Processing Units (GPUs)*, (Doctoral dissertation, UNIVERSITY OF MANCHESTER).

[Mokos, 2014] Mokos, A. D. (2014). Multiphase modelling of violent hydrodynamics using Smoothed Particle Hydrodynamics (SPH) on Graphics Processing Units (GPUs).

[Mokos et al., 2015] Mokos, A., Rogers, B. D., Stansby, P. K., & Domínguez, J. M. (2015). Multi-phase SPH modelling of violent hydrodynamics on GPUs. *Computer Physics Communications*, *196*, 304-316.

[Moctar et al., 2011] El Moctar, O., Oberhagemann, J., & Schellin, T. E. (2011). Free surface RANS method for hull girder springing and whipping. In *Proceedings of the SNAME Annual Meeting, Houston, TX, Paper* (No. A56).

[Molteni and Bilello, 2003] Molteni, D., & Bilello, C. (2003). Riemann solver in SPH. *Memorie della Societa Astronomica Italiana Supplementi*, *1*, 36.

[Monaghan, 1982] Monaghan, J. J. (1982). Why particle methods work. *SIAM Journal on Scientific and Statistical Computing*, *3*(4), 422-433.

[Monaghan, 1989] Monaghan, J. J. (1989). On the Problem of Penetration in Particle Methods. *Journal Computational Physics*, 82:1-15.

[Monaghan, 1992] Monaghan, J. J. (1992). Smoothed Particle Hydrodynamics. *Annual Rev. Astron. Appl.*, 30:543-574.

[Monaghan, 1994] Monaghan, J. J. (1994). Simulating free surface flows with SPH. *Journal Computational Physics*, 110:399-406.

[Monaghan, 1996] Monaghan J.J. (1996). Gravity currents and solitary waves. *Physica D.* 98, 523-533.

[Monaghan, 1997] Monaghan, J. J. (1997). SPH and Riemann solvers. *Journal of Computational Physics*, *136*(2), 298-307.

[Monaghan, 2000] Monaghan J.J. (2000). Scott Russell`s wave generator. *Physics of Fluids.* 12: 622.

[Monaghan, 2000] Monaghan, J. J. (2000). SPH without a tensile instability. *Journal of Computational Physics*, *159*(2), 290-311.

[Monaghan, 2005] Monaghan, J. J. (2005). Smoothed Particle Hydrodynamics. *Reports on Progress in Physics*, 68:1703-1759.

[Monaghan, 2006] Monaghan, J. J. (2006). Time stepping algorithms for SPH. Technical report, Monash University.

[Monaghan and Kos, 1999] Monaghan J.J, Kos A. (1999). Solitary waves on a Cretan beach. *Journal of Waterway Port, Coastal and Ocean Engineering*. 125(3), 145-154.

[Monaghan et al., 2003] Monaghan JJ, Kos A, Issa N. (2003) Fluid motion generated by impact. *Journal of Waterway, Port, Coastal and Ocean Engineering*; 129(6):250–9.

[Monaghan and Gingold, 1983] Monaghan, J.J. and Gingold R.A. (1983) Shock simulation by the particle method SPH. *J. Comput. Phys*, 52: 374-89

[Monaghan and Lattanzio, 1985] Monaghan, J. J. and Lattanzio, J. C. (1985). A refined method for astrophysical problems. *Astron. Astrophys*, 149:135-143.

[Monaghan and Lattanzio, 1985] Monaghan, J. J. and H. Pongracic (1985). "Artificial viscosity for particle methods." *Applied Numerical Mathematics* **1**(3): 187-194.

[Monaghan and Kajtar, 2009] Monaghan, J. J., & Kajtar, J. B. (2009). SPH particle boundary forces for arbitrary boundaries. *Computer Physics Communications*, *180*(10), 1811-1820.

[Morris et al., 1997] Morris J.P., Fox P.J., and Zhu Y. (1997). Modelling low Reynolds number incompressible flows using SPH *J. Comput. Phys*, 136:214-226.

[Nakanishi and Kamemoto , 1993] Nakanishi, Y., & Kamemoto, K. (1993). Numerical simulation of flow around a sphere with vortex blobs. *Journal of Wind Engineering and Industrial Aerodynamics*, *46*, 363-369.

[Newmark, 1959] Newmark, N. M. (1959). A method of computation for structural dynamics.*Journal of the engineering mechanics division*, *85*(3), 67-94.

[Noh, 1964] Noh, W. (1964). Cel: a time-dependent, two-space dimensional, coupled eulerian-lagrangian code. *Methods in computational physics*, 3:117.

[Ni et al., 2014] Ni, X., Feng, W. B., & Wu, D. (2014). Numerical simulations of wave interactions with vertical wave barriers using the SPH method. *International Journal for Numerical Methods in Fluids*, *76*(4), 223-245.

[Oger et al., 2006] Oger G, Doring M, Alessandrini B. (2006) Two-dimensional SPH simulations of wedge water entries. *Journal of Computational Physics* ;213(2):803–22.

[Oger et al., 2007] Oger, G., Doring, M., Alessandrini, B., & Ferrant, P. (2007). An improved SPH method: Towards higher order convergence. *Journal of Computational Physics*,*225*(2), 1472-1492.

[Ojima and Kamemoto, 2000] Ojima, A., & Kamemoto, K. (2000). Numerical simulation of unsteady flow around three-dimensional bluff bodies by an advanced vortex method. *JSME international journal. Series B, fluids and thermal engineering*, *43*(2), 127-135.

[Omidvar, 2010] Omidvar, P. (2010). Wave loading on bodies in the free surface using Smoothed Particle Hydrodynamics (SPH).

[Omidvar et al., 2013] Omidvar, P., Stansby, P. K., & Rogers, B. D. (2013). SPH for 3D floating bodies using variable mass particle distribution. *International Journal for Numerical Methods in Fluids*, *72*(4), 427-452.

[Osher and Fedkiw, 2001] Osher, S. and R. P. Fedkiw (2001). "Level Set Methods: An Overview and Some Recent Results.*" Journal of Computational Physics* **169**(2): 463-502.

[Paik and Shin, 2006] Paik, J. K., & Shin, Y. S. (2006). Structural damage and strength criteria for ship stiffened panels under impact pressure actions arising from sloshing, slamming and green water loading. *Ships and Offshore Structures*, *1*(3), 249-256.

[Patel et al., 2009] Patel M.H., Vignjevic R., Campbell J.C. (2009). An SPH technique for evaluating the behaviour of ships in extreme ocean waves. *Int J Maritime Eng*. 151:39–47.

[Panizzo et al., 2007] Panizzo, A., Capone, T., and Dalrymple, R. A. (2007). Accuracy of kernel derivatives and numerical schemes in SPH. *Submitted to Journal of Computational Physics*.

[Panizzo and Dalrymple, 2004] Panizzo, A., Dalrymple, R.A. (2004). SPH modelling of underwater landslide generated waves. *Proc. ICCE 2004, ASCE.*

[Potapov et al., 2009] Potapov S., Maurel B., Combescure A., Fabis J. (2009). Modelling accidental-type fluid-structure interaction problems with the SPH method. *Comput Struct*. 87:721-734.

[Peskin and McQuenn, 1989] Peskin, C. S., & McQueen, D. M. (1989). A three-dimensional computational method for blood flow in the heart I. Immersed elastic fibres in a viscous incompressible fluid. *Journal of Computational Physics, 81*(2), 372-405.

[Rabzuk et al., 2000] Rabzuk, T., Xiao, S. P., and Saver, M. (2000). Coupling of meshfree methods with _nite elements: Basic concepts and test results. *Communications in Numerical Methods in Engineering*, 00:1-6.

[Rafiee et al., 2012] Rafiee, A., Cummins, S., Rudman, M., & Thiagarajan, K. (2012). Comparative study on the accuracy and stability of SPH schemes in simulating energetic free-surface flows. *European Journal of Mechanics-B/Fluids*, *36*, 1-16.

[Ren et al., 2014] Ren, B., Wen, H., Dong, P., & Wang, Y. (2014). Numerical simulation of wave interaction with porous structures using an improved smoothed particle hydrodynamic method. *Coastal Engineering*, *88*, 88-100.

[Ren et al., 2015] Ren, B., He, M., Dong, P., & Wen, H. (2015). Nonlinear simulations of wave-induced motions of a freely floating body using WCSPH method. *Applied Ocean Research*, *50*, 1-12.

[Rey et al., 1992] Rey, V., Belzons, M., & Guazzelli, E. (1992). Propagation of surface gravity waves over a rectangular submerged bar. *J. Fluid Mech*, *235*, 453-479.

[Rhee, 2005] Rhee, S. H. (2005). Unstructured grid based Reynolds-averaged Navier-Stokes method for liquid tank sloshing. *Journal of fluids engineering*, *127*(3), 572-582.

[Rider and Kothe, 1998] Rider, W. J., & Kothe, D. B. (1998). Reconstructing volume tracking. *Journal of computational physics*, *141*(2), 112-152.

[Rogers et al., 2010] Rogers B.D., Dalrymple R.A., Stansby P.K. (2010). Simulation of Caisson breakwater movement using 2-D SPH. *Journal of Hydraulic Research*. 48:85–93.

[Roubtsova and Kahawita, 2006] Roubtsova, V., & Kahawita, R. (2006). The SPH technique applied to free surface flows. *Computers & Fluids*, *35*(10), 1359-1371.

[Rubinstein and Kroese, 2011] Rubinstein, R. Y., & Kroese, D. P. (2011). *Simulation and the Monte Carlo method* (Vol. 707). John Wiley & Sons.

[Rudman et al., 2009] Rudman M, Prakash M, Cleary P. (2009). SPH modelling of liquid sloshing in an LNG tank. *ISOPE*; 21:3–220.

[Scardovelli and Zaleski] Scardovelli, R., & Zaleski, S. (1999). Direct numerical simulation of free-surface and interfacial flow. *Annual Review of Fluid Mechanics*, *31*(1), 567-603.

[Schuessler and Schmitt, 1981] Schuessler, I., & Schmitt, D. (1981). Comments on smoothed particle hydrodynamics. *Astronomy and Astrophysics*, *97*, 373-379.

[Seng et al., 2012] Seng, S., Andersen, I. M. V., & Jensen, J. J. (2012). On the Influence of Hull Girder Flexibility on the Wave. In *6th International Conference Hydroelasticity in Marine Technology* (pp. 341-353).

[Seng and Jensen, 2012] Seng, S., & Jensen, J. J. (2012). Slamming simulations in a conditional wave. In *ASME 2012 31st International Conference on Ocean, Offshore and Arctic Engineering* (pp. 359-368). American Society of Mechanical Engineers.

[Servan et al., 2016] Serván-Camas, B., Cercós-Pita, J. L., Colom-Cobb, J., García-Espinosa, J., & Souto-Iglesias, A. (2016). Time domain simulation of coupled sloshing–seakeeping problems by SPH–FEM coupling. *Ocean Engineering*, *123*, 383-396.

[Sethian, 1999] Sethian, J. A. (1999). Level set methods and fast marching methods: evolving interfaces in computational geometry.*Fluid mechanics, computer vision, and materials science* (Vol. 3). Cambridge university press.

[Sethian, 2001] Sethian, J. A. (2001). "Evolution, Implementation, and Application of Level Set and Fast Marching Methods for Advancing Fronts." *Journal of Computational Physics* **169**(2): 503-555.

[Shadloo et al., 2012] Shadloo, M. S., Zainali, A., Yildiz, M., & Suleman, A. (2012). A robust weakly compressible SPH method and its comparison with an incompressible SPH.*International Journal for Numerical Methods in Engineering*, *89*(8), 939-956.

[Shao, 2009] Shao, S. (2009). Incompressible SPH simulation of water entry of a free-falling object. *International Journal for numerical methods in fluids*, *59*(1), 91-115.

[Shao, 2010] Shao S.D. (2010). Incompressible SPH-flow model for wave interactions with porous media. *Coast Eng*. 57:304-16.

[Shao and Lo, 2003] Shao, S. and Lo, E. Y. M. (2003). Incompressible sph method for simulating Newtonian and non-Newtonian own with a free surface. *Advances in Water Resources*, 26:787-800.

[Shao and Gotoh, 2004] Shao, S., & Gotoh, H. (2004). Simulating coupled motion of progressive wave and floating curtain wall by SPH-LES model. *Coastal Engineering Journal*,46(02), 171-202.

[Shao et al., 2006] Shao, S.D., 2006. Simulation of breaking wave by SPH method coupled with k–ε model. J. Hydraul. Res. 44 (3), 338–349.

[Shao et al., 2012] Shao, J. R., Li, H. Q., Liu, G. R., & Liu, M. B. (2012). An improved SPH method for modelling liquid sloshing dynamics. *Computers & Structures*, *100*, 18-26.

[Shaofan and Liu, 2007] Shaofan Li. and Liu W.K (2007). Meshfree Particle Methods. Springer Berlin Heidelberg New York.

[Shibata et al., 2009] Shibata, K., Koshizuka, S., & Tanizawa, K. (2009). Three-dimensional numerical analysis of shipping water onto a moving ship using a particle method. *Journal of Marine Science and Technology*, *14*(2), 214-227.

[Sirotkin and Yoh, 2013] Sirotkin, F. V., & Yoh, J. J. (2013). A smoothed particle hydrodynamics method with approximate Riemann solvers for simulation of strong explosions.*Computers & Fluids*, *88*, 418-429.

[Skaar et al., 2009] Skaar, D., Vassalos, D., & Jasionowski, A. (2006). The use of a meshless CFD method in modelling progressive flooding and damaged stability of ships. In *Proceedings of the 9th International Conference on Stability of Ships and Ocean Vehicles* (pp. 625-632).

[Song et al., 1994] Song, J. Z., Ren, H. L., & Dai, Y. S. (1994). Hydroelastic analysis of non-linear wave-induced loads of ship hull. *Shipbuilding of China*.

[Sun and Faltinsen, 2009] Sun, H., & Faltinsen, O. M. (2009). Water entry of a bow-flare ship section with roll angle. *Journal of marine science and technology*, *14*(1), 69-79.

[Sun et al., 2016] Sun, Z., Djidjeli, K., Xing, J. T., & Cheng, F. (2016). Coupled MPS-modal superposition method for 2D nonlinear fluid-structure interaction problems with free surface. *Journal of Fluids and Structures*, *61*, 295-323.

[Standing, 1991] Standing, R. G. (1991, January). Prediction of viscous roll damping and response of transportation barges in waves. In *The First International Offshore and Polar Engineering Conference*. International Society of Offshore and Polar Engineers.

[St Dinis and Pierson, 1953]St Dinis, M., & Pierson Jr, W. J. (1953). *On the motions of ships in confused seas*. NEW YORK UNIV BRONX SCHOOL OF ENGINEERING AND SCIENCE.

[St-Germain et al., 2014] St-Germain, P., Nistor, I., Townsend, R., & Shibayama, T. (2014). Smoothed-particle hydrodynamics numerical modelling of structures impacted by tsunami bores. *Journal of Waterway, Port, Coastal, and Ocean Engineering*.

[Stilinger and Rahman, 1974] Stillinger, F. H., & Rahman, A. (2003). Improved simulation of liquid water by molecular dynamics. *The Journal of Chemical Physics*, *60*(4), 1545-1557.

[Svendsen, 1985] Svendsen I.A.(1985). Physical modelling of water waves, Physical Modelling in Coastal Engineering, AA Balkema, Rotterdam: 13-48.

[Swegle et al., 1995] Swegle, J. W., Hicks, D. L., & Attaway, S. W. (1995). Smoothed particle hydrodynamics stability analysis. *Journal of computational physics*, *116*(1), 123-134.

[Tafuni, 2016] Tafuni, A. (2016). *Smoothed Particle Hydrodynamics: Development and application to problems of hydrodynamics* (Doctoral dissertation, POLYTECHNIC INSTITUTE OF NEW YORK UNIVERSITY).

[Takeda et al., 1994] Takeda, H., et al. (1994). "Numerical Simulation of Viscous Flow by Smoothed Particle Hydrodynamics." *Progress of Theoretical Physics* **92**(5): 939-960.

[Tallec and Mouro, 2001] Tallec, P. L. and Mouro, J. (2001). Fluid-structure interaction with large structural displacements. *Computer Methods in Applied Mechanics Engineering*, 190:3039-3067.

[Tanizawa and Naito, 1998] Tanizawa, K., & Naito, S. (1998). An application of fully nonlinear numerical wave tank to the study on chaotic roll motions. In *The Eighth International Offshore and Polar Engineering Conference*. International Society of Offshore and Polar Engineers.

[Taylor, 2009] Taylor, R. E. (2009). Reflections on the structural dynamics of floating beams and ship hull in waves. *Proceedings of the Institution of Mechanical Engineers, Part M: Journal of Engineering for the Maritime Environment*, *223*(3), 257-273.

[Teymoori, 2013] Teymoori, F., et al. (2013). "Numerical analysis of fluid-structure interaction in water jet incremental sheet forming process using coupled Eulerian-Lagrangian approach." 1-8.

[Tezdogan et al., 2015] Tezdogan, T., Demirel, Y. K., Kellett, P., Khorasanchi, M., Incecik, A., & Turan, O. (2015). Full-scale unsteady RANS CFD simulations of ship behaviour and performance in head seas due to slow steaming. *Ocean Engineering*, *97*, 186-206.

[Tiwari, 2001] Tiwari, S. (2001). "A LSQ-SPH approach for solving compressible viscous flows." *Hyperbolic Problems: Theory, Numerics, Applications, Vols I and II* **140**: 901-910.

[Tucker and Pitt, 2001] Tucker M.J. and Pitt E.G. (2001). Waves in Ocean Engineering, Elsevier Science Ltd, Oxford, UK.

[Tuitman and Malenica, 2009] Tuitman, J. T., & Malenica, Š. (2009). Fully coupled seakeeping, slamming, and whipping calculations. *Proceedings of the Institution of Mechanical Engineers, Part M: Journal of Engineering for the Maritime Environment*, *223*(3), 439-456.

[Tuitman et al., 2013] Tuitman, J. T., T. N. Bosman and E. Harmsen (2013). "Local structural response to seakeeping and slamming loads." *Marine Structures* **33**: 214-237.

[Ubbink, 1997] Ubbink, O. (1997). *Numerical prediction of two fluid systems with sharp interfaces* (Doctoral dissertation, University of London).

[Ulrich and Rung, 2012] Ulrich, C. and Rung, T., (2012), July. Multi-Physics SPH Simulations of Launching Problems and Floating Body Interactions. In *ASME 2012 31st International Conference on Ocean, Offshore and Arctic Engineering* (pp. 685-694). American Society of Mechanical Engineers.

[Ursell et al., 1960] Ursell F., Dean R.G., and Yu Y.S. (1960). Forced Small Amplitude Water Waves: A Comparison of Theory and Experiment. *J. Fluid Mech, Vol.7, Pt. 1*.

[Vacondio et al., 2012] Vacondio, R., Rogers, B. D., Stansby, P. K., & Mignosa, P. (2012). SPH modelling of shallow flow with open boundaries for practical flood simulation.*Journal of Hydraulic Engineering*, *138*(6), 530-541.

[Vacondio et al., 2013] Vacondio, R., Rogers, B. D., Stansby, P. K., Mignosa, P., & Feldman, J. (2013). Variable resolution for SPH: a dynamic particle coalescing and splitting scheme. *Computer Methods in Applied Mechanics and Engineering*,*256*, 132-148.

[Varnousfaaderani and Ketabdari, 2014] Varnousfaaderani, M. R., & Ketabdari, M. J. (2014). Numerical simulation of solitary wave breaking and impact on seawall using a modified turbulence SPH method with Riemann solvers. *Journal of Marine Science and Technology*, 1-13.

[Veen, 2010] Veen, D. J. (2010). A smoothed particle hydrodynamics study of ship bow slamming in ocean waves.

[Veen and Gourlay, 2012] Veen, D., & Gourlay, T. (2012). A combined strip theory and Smoothed Particle Hydrodynamics approach for estimating slamming loads on a ship in head seas. *Ocean Engineering*, *43*, 64-71.

[Verlet, 1967] Verlet, L. (1967). Computer Experiments on Classical Fluids. I. Thermodynamical Properties of Lennard-Jones Molecules. *Phys. Rev.*, 159:98-103.

[Vossers et al., 1961] Vossers, G., Swaan, W. A., & Rijken, H. (1961). Vertical and lateral bending moment measurements on Series 60 models. Nederlandsch Scheepsbouwkundig Proefstation.

[Viccione at al., 2008] Viccione, G., Bovolin, V., & Carratelli, E. P. (2008). Defining and optimising algorithms for neighbouring particle identification in SPH fluid simulations.*International Journal for Numerical Methods in Fluids*, *58*(6), 625-638.

[Vila, 1999] Vila, J. P. (1999). On particle weighted methods and smooth particle hydrodynamics. *Mathematical models and methods in applied sciences*, *9*(02), 161-209.

[Vinje, 1982] Vinje, T. (1981). Nonlinear Ship Motions. In *Proc. of the 3rd. Int. Conf. on Num. Ship Hydro.* (pp. IV-3).

[Vugts, 1968] Vugts, J. H. (1968). *The hydrodynamic coefficients for swaying, heaving and rolling cylinders in a free surface* (No. Report No. 194).

[Weiss et al., 2011] Weiss, R., Munoz, A. J., Dalrymple, R. A., Herault, A., & Bilotta, G. (2011). Three-dimensional modelling of long-wave runup: Simulation of tsunami inundation with GPU-SPHysics. *Coastal Engineering Proceedings*, *1*(32), 8.

[Wendland, 1995] Wendland, H. (1995). *Computational aspects of radial basis function approximation*. Elsevier.

[Weymouth et al., 2005] G. Weymouth, R. Wilson, F. Stern (2005). RANS CFD predictions of pitch and heave ship motions in head seas**.** *Journal of Ship Research*, 49 (2), pp. 80–97.

[Wilson et al., 2006] Wilson, R. V., et al. (2006). Unsteady RANS method for ship motions with application to roll for a surface combatant. *Computers & Fluids* **35**(5): 501-524.

[Wilkins, 1999] Wilkins M. L. (1999). Computer simulation of dynamic phenomena. Springer Verlag Berlin Heidelberg.

[Wlhorn et al., 2005] Wlhorn E., Kolke A., Hubner B. (2005). Fluid-structure coupling within a monolithic model involving free surface flows. *Comput Struct*. 83:2100-2111.

[Wu et al., 2003]Wu, Y. S., Chen, R. Z., & Lin, J. R. (2003). Experimental technique of hydroelastic ship model. In *Proceedings of the 3rd International Conference on Hydroelasticity, Oxford* (pp. 131-142).

[Wu and Moan, 2005] Wu, M., & Moan, T. (2005). Efficient calculation of wave-induced ship responses considering structural dynamic effects. *Applied Ocean Research*,*27*(2), 81-96.

[Wu Qiaorui et al., 2014] Wu Qiao-rui, Tan M., Xing J.T., (2014). An improved moving particle semi-implicit method for dam break simulation.

[X.Y.Hu et al., 2014] X.Y. Hu, S. Littvinov, N.A. Adams (2014). Towards both numerical consistency and conservation for SPH approximation. 9th SPHERIC proceedings. 283-288.

[Xenakis et al., 2015] Xenakis, A. M., Lind, S. J., Stansby, P. K., & Rogers, B. D. (2015). An incompressible SPH scheme with improved pressure predictions for free-surface generalised Newtonian flows. *Journal of Non-Newtonian Fluid Mechanics*, *218*, 1-15.

[Xie et al., 2007] Xie J.S., Nistor I., Murty T., Shukla T. (2007). Numerical modelling of the Indian Ocean Tsunami-a review. *Int J Ecol Dev IJED*. 3(S05): 71-88.

[Xie et al., 2009] Xie, W., Liu, Z., & Young, Y. L. (2009). Application of a coupled Eulerian–Lagrangian method to simulate interactions between deformable composite structures and compressible multiphase flow. *International journal for numerical methods in engineering*, *80*(12), 1497-1519.

[Xing and Price, 1991] Xing, J. and Price, W. (1991). A mixed finite element method for the dynamic analysis of coupled fluid-solid interaction problems. *Proceedings of the Royal Society of London*, A433:235-255.

[Xing et al., 2003] Xing, J. T., Price, W. G., and Chen, Y. G. (2003). A mixed finite element finite-difference method for nonlinear fluid-structure interaction dynamics. *The Royal Society*, 459:2399-2430.

[Xu et al., 2009] Xu, R., P. Stansby and D. Laurence (2009). "Accuracy and stability in incompressible SPH (ISPH) based on the projection method and a new approach." *Journal of Computational Physics* 228(18): 6703-6725.

[Yan and Liu, 2010] Yan, H., & Liu, Y. (2010). Efficient computations of fully-nonlinear wave interactions with floating structures. In *ASME 2010 29th International Conference on Ocean, Offshore, and Arctic Engineering* (pp. 645-655). American Society of Mechanical Engineers.

[Yang and Stern, 2009] Yang, J., & Stern, F. (2009). Sharp interface immersed-boundary/level-set method for wave–body interactions. *Journal of Computational Physics*, *228*(17), 6590-6616.

[Yang et al., 2006] Yang, C., Löhner, R., & Lu, H. (2006). An unstructured-grid based volume-of-fluid method for extreme wave and freely-floating structure interactions. *Journal of Hydrodynamics, Ser. B*, *18*(3), 415-422.

[Yooil et al., 2009] Yooil K., Kyong H.K. and Yonghwan K. (2009). Analysis of hydroelasticity of floating shiplike structure in time domain using a fully coupled hybrid BEM-FEM. *Journal of Ship Research*. 53:31-47.

[Young, 1982] Youngs, D. L. (1982). Time-dependent multi-material flow with large fluid distortion. *Numerical methods for fluid dynamics*, *24*, 273-285.

[Young, 2001] Young, D. L., et al. (2001). "A coupled BEM and arbitrary Lagrangian-Eulerian FEM model for the solution of Two-dimensional laminar flows in external flow fields." *International Journal for Numerical Methods in Engineering* **51**(9): 1053-1077.

[Zhang et al., 2013] Zhang, A. M., Cao, X. Y., Ming, F. R., & Zhang, Z. F. (2013). Investigation on a damaged ship model sinking into water based on three-dimensional SPH method. *Applied Ocean Research*, *42*, 24-31.

[Zheng et al., 2012] Zheng, X., et al. (2012). "A new scheme for identifying free surface particles in improved SPH." *Science China Physics, Mechanics and Astronomy* **55**(8): 1454-1463.

[Zhou and Ma, 2010]Zhou J.T. and Ma Q.W. 2010. MLPG method Based on Rankine Source Solution for Modelling 3D Breaking Waves. Computer Modeling in Engineering and Sciences (56(2)), 179- 210.

[Zhu et al., 1999] Zhu, Y., Fox, P. J., & Morris, J. P. (1999). A pore-scale numerical model for flow through porous media. *International journal for numerical and analytical methods in geomechanics*, *23*(9), 881-904.

[Zienkiewicz and Taylor, 2000] Zienkiewicz, O. C. and Taylor, R. L. (2000). *The Finite Element*. Butterworth Herinemann, 5th edition.

Paper and conferences

Ramli, M.Z., Temarel, P., and Tan, M. (2014). An improved SPH method for wave generation in free surface flow simulations. *The 5th UK Marine Technology Postgraduate Conference, MTPC 2014, p 8.* **Sponsor:** Lloyd's Register Marine.

Ramli, M.Z., Temarel, P., and Tan, M. (2015). Smoothed particle hydrodynamics (SPH) for modelling 2-dimensional free-surface hydrodynamics. *Analysis and Design of Marine Structures - Proceedings of the 5th International Conference on Marine Structures, MARSTRUCT 2015*, p 45-52, 2015; **ISBN-13:** 9781138027893; **Conference:** 5th International Conference on Marine Structures, MARSTRUCT 2015, March 25, 2015 - March 27, 2015; **Sponsor:** Lloyd's Register Marine; **Publisher:** CRC Press/Balkema.

Appendix A

5.1.4 Sway motion
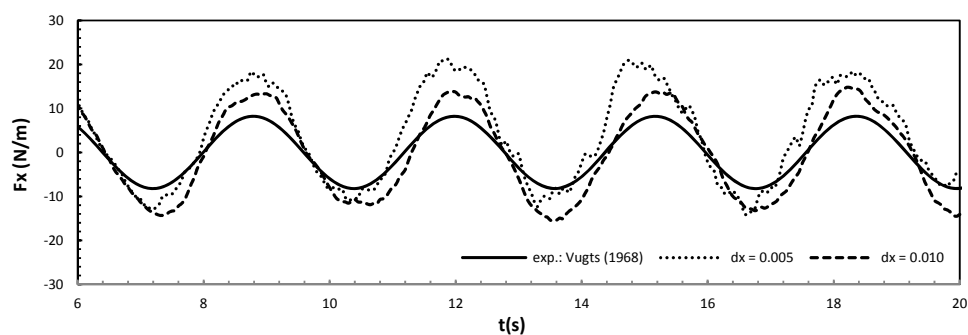
Figure A - 1 Horizontal force prediction of swaying motion at ω = 1.97 rad/s for different particle spacing.
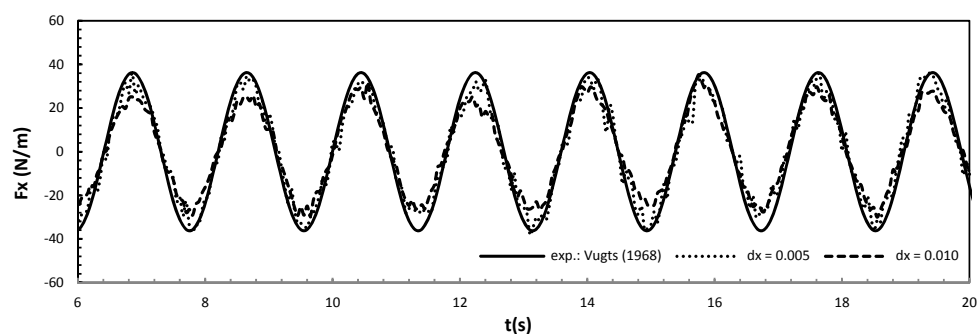
Figure A - 2 Horizontal force prediction of swaying motion at ω = 3.50 rad/s for different particle spacing.
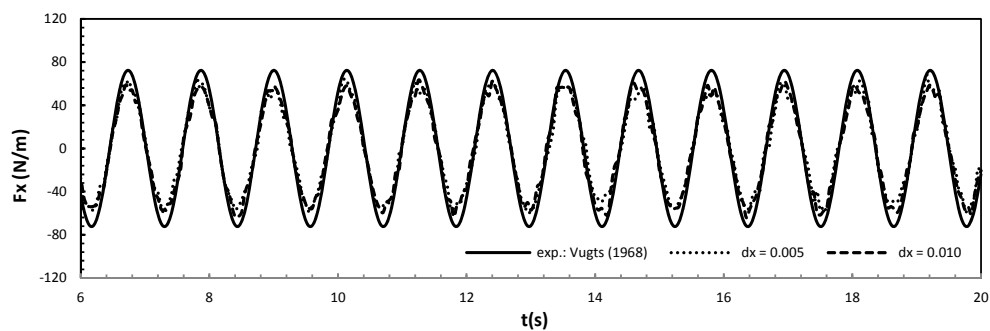
Figure A - 3 Horizontal force prediction of swaying motion at ω = 5.54 rad/s for different particle spacing.

Heave motion
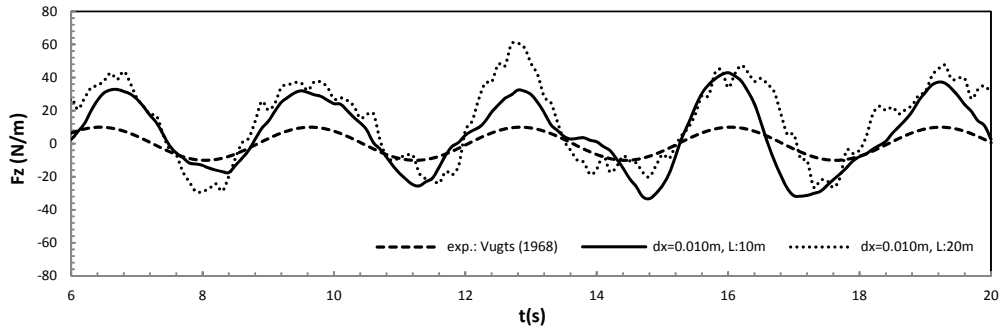
Figure A - 4 Vertical force prediction of heave motion at ω = 1.97 rad/s for different numerical tank length.
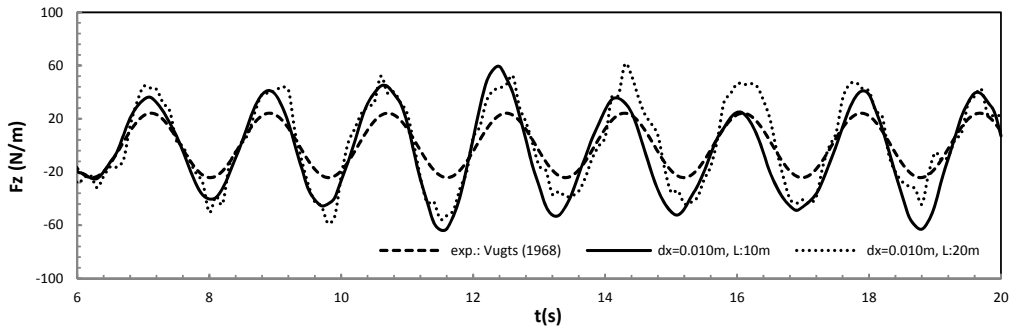
Figure A - 5 Vertical force prediction of heave motion at ω = 3.50 rad/s for different numerical tank length.
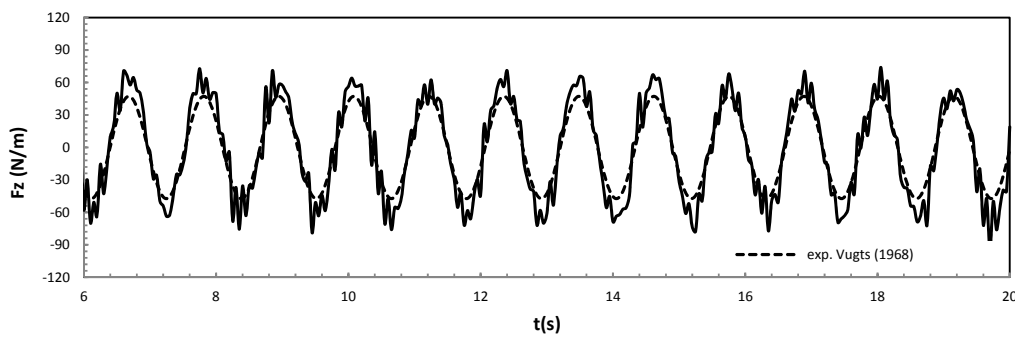
Figure A - 6 Vertical force prediction of heave motion at ω = 5.54 rad/s with less noise filter applied.

Roll motion
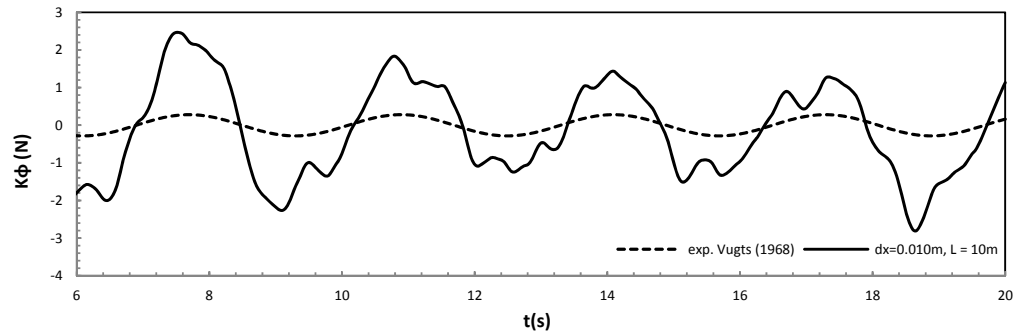
Figure A - 7 Dynamic force prediction of roll motion after disregarding the hydrostatic force at ω = 1.97 rad/s.
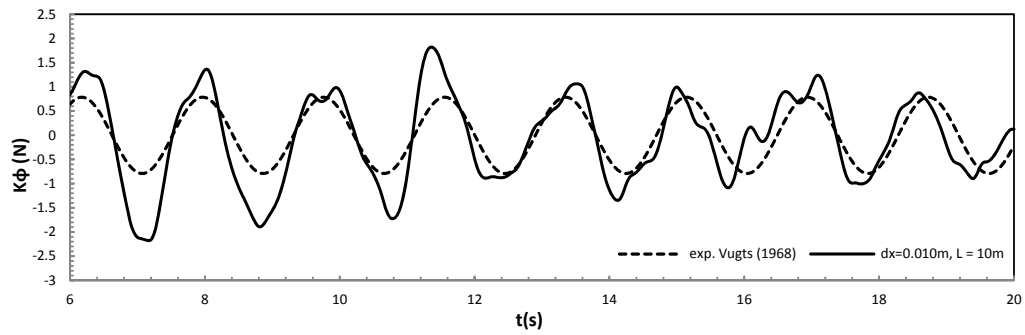
Figure A - 8 Dynamic force prediction of roll motion after disregarding the hydrostatic force at ω = 3.50 rad/s.
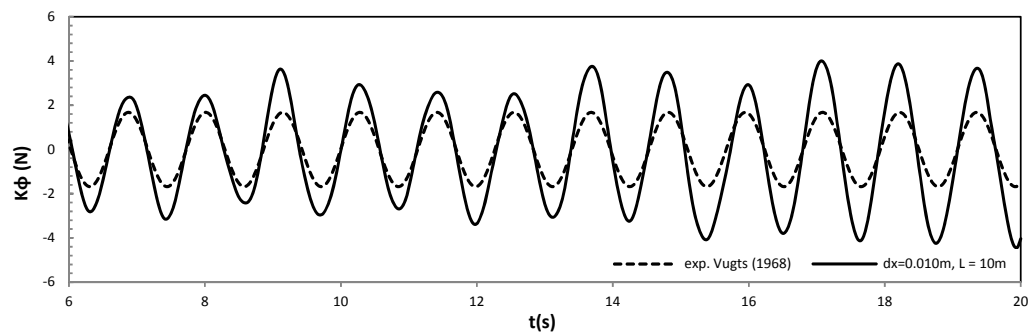
Figure A - 9 Dynamic force prediction of roll motion after disregarding the hydrostatic force at ω = 5.54 rad/s.

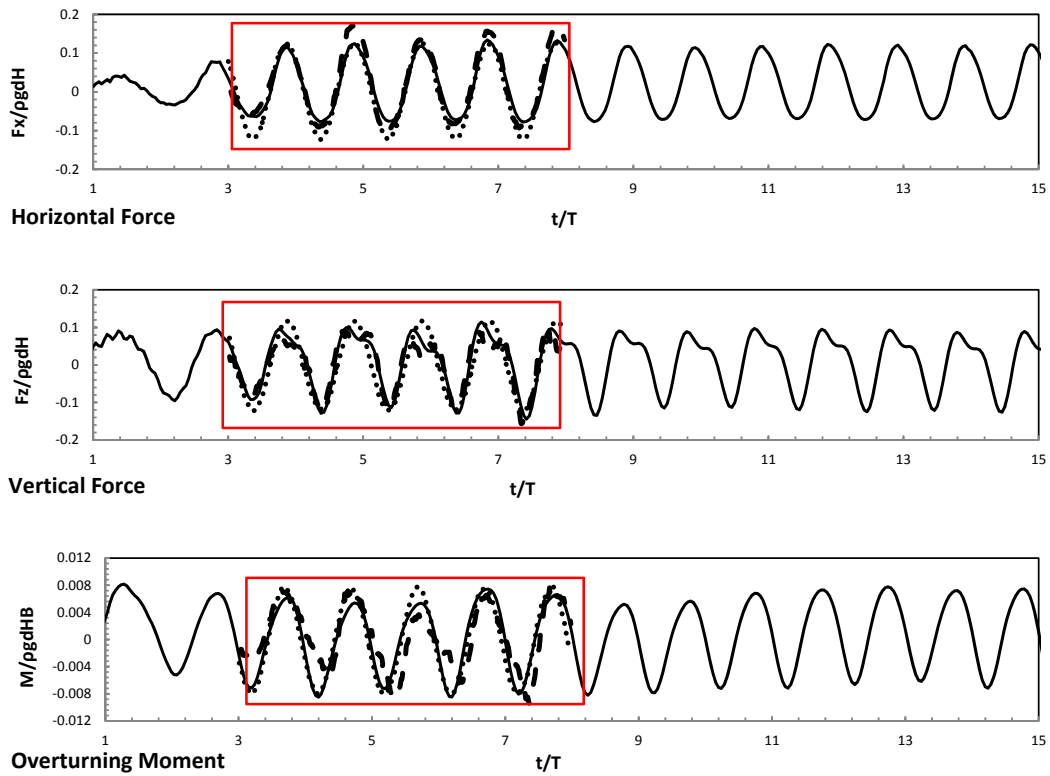## 5.2 Forces and moment predictions for 2D fixed rectangular box in regular waves.

Figure A - 10 Time histories of forces and moment (H = 0.06 m, T = 1.2 s). − − SPH [Ren, 2015], ⋯ Experimental (Ren, 2015),− WCSPH.
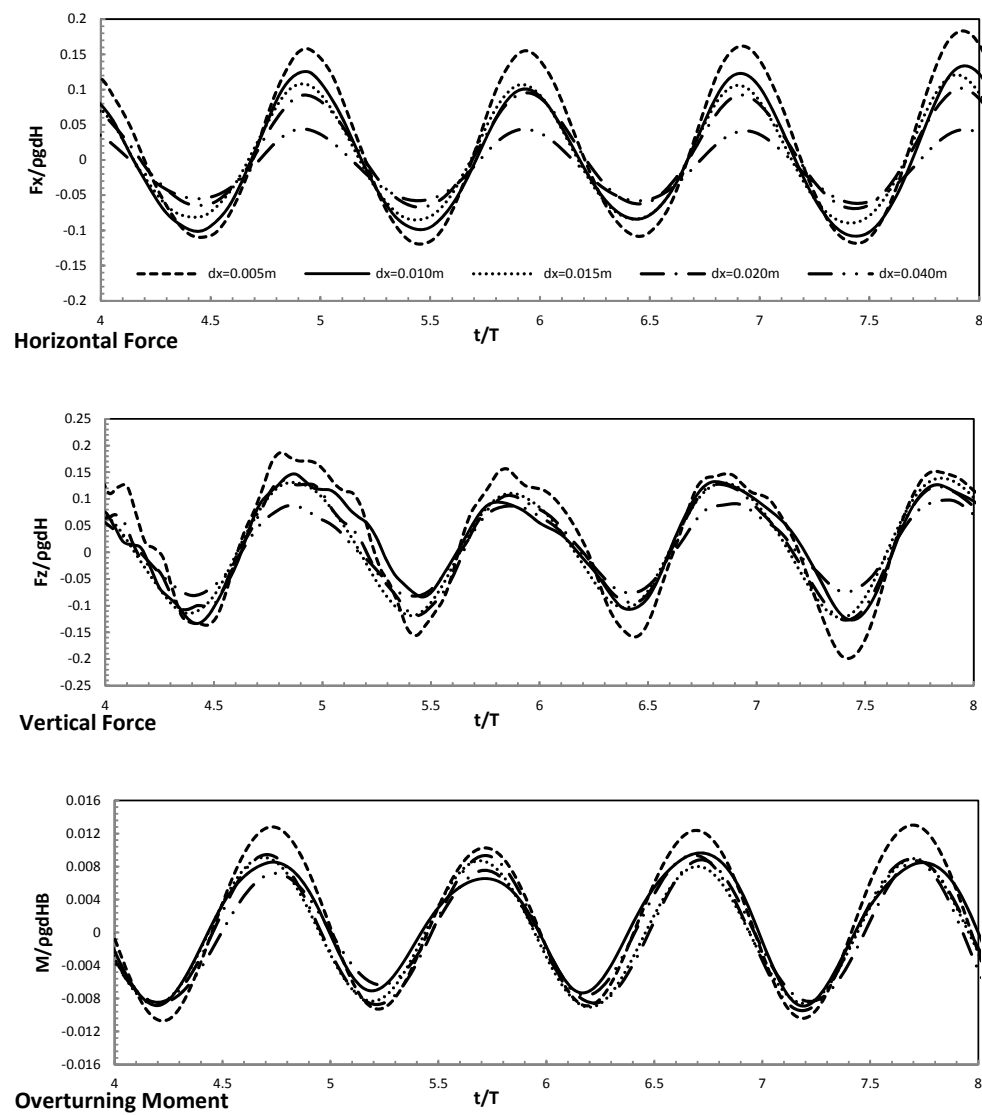
Figure A - 11 Convergence analysis: Time histories of forces and moment for different initial particle spacing (H = 0.06 m, T = 1.2 s).
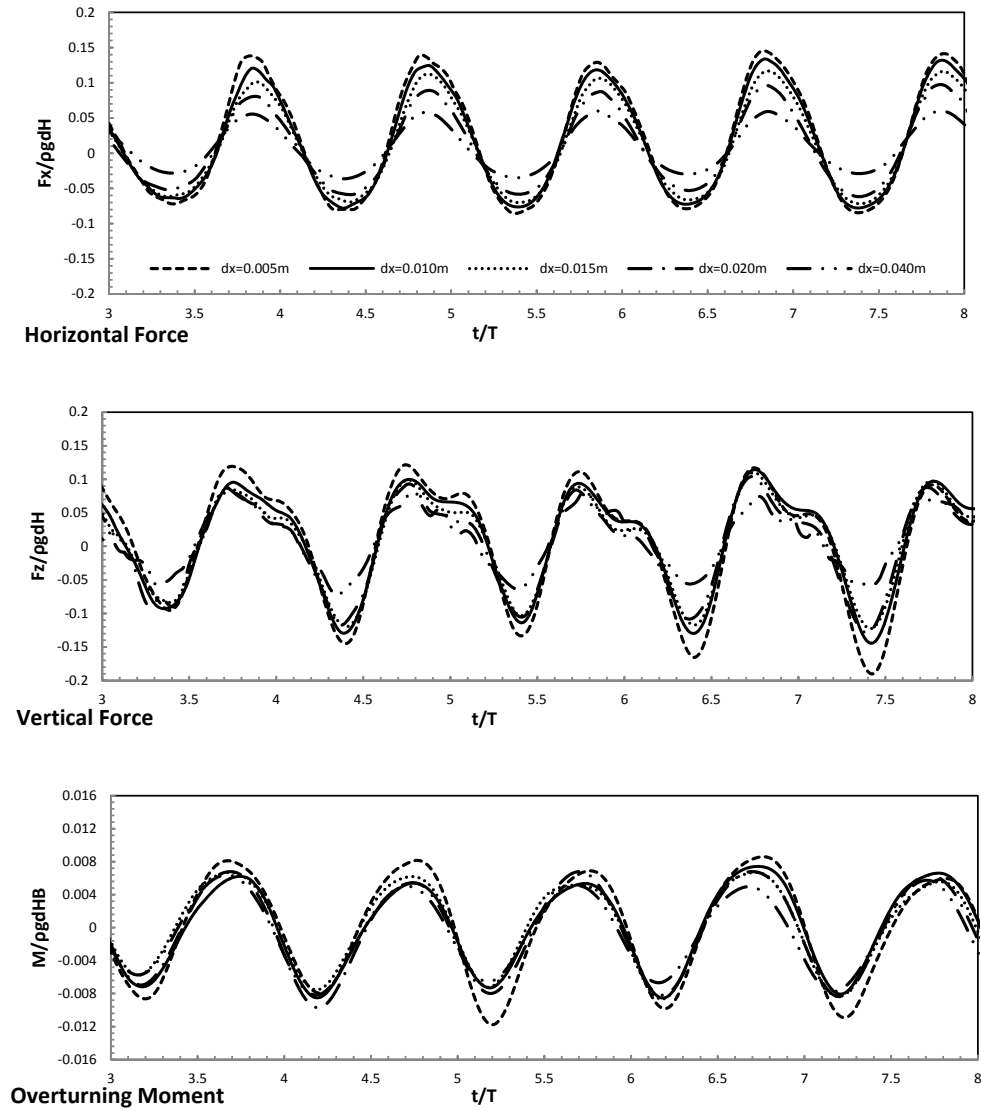
Figure A - 12 Convergence analysis: Time histories of forces and moment for different initial particle spacing (H = 0.20 m, T = 1.2 s).

5.2 Motion trajectories of free floating box under regular waves.
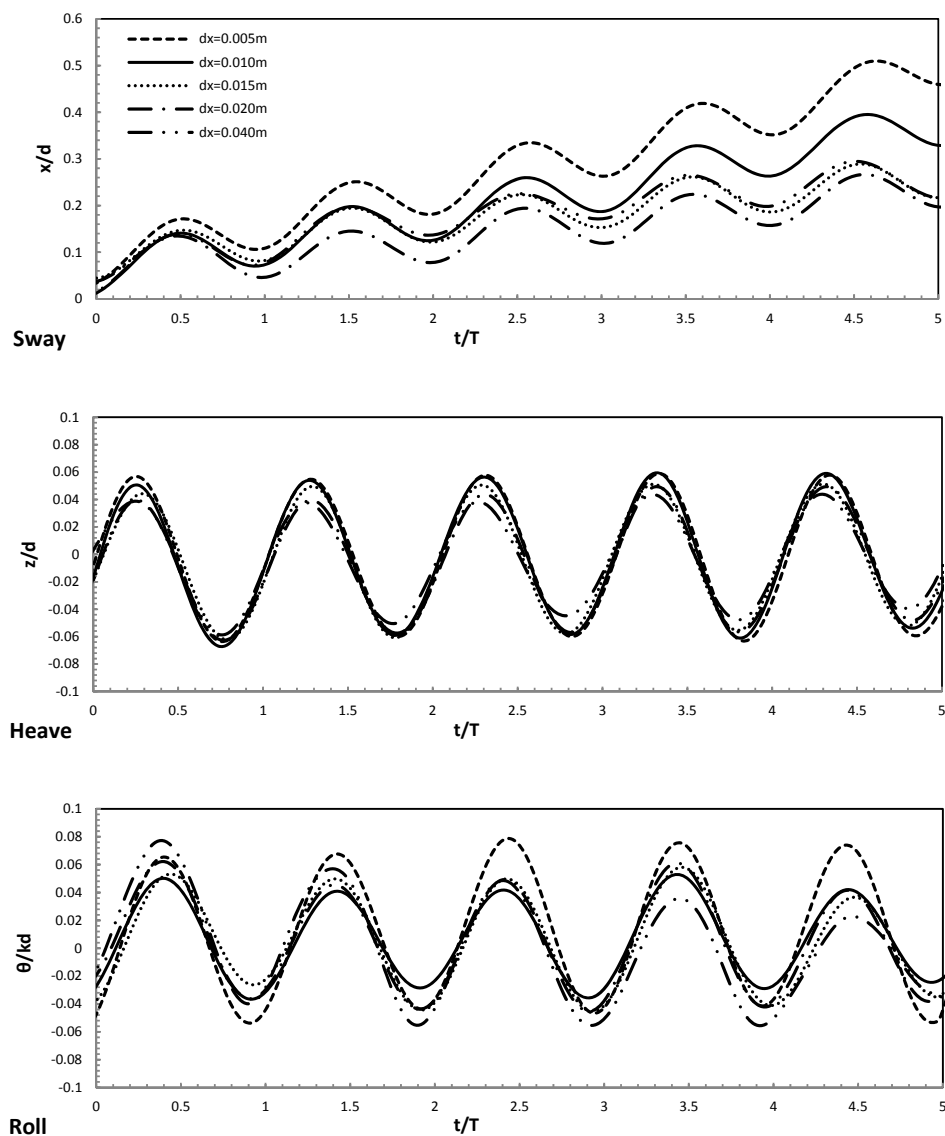

Figure A - 13 Convergence analysis: Time histories of motion trajectories for different initial particle spacing (H = 0.04 m, T = 1.2 s).
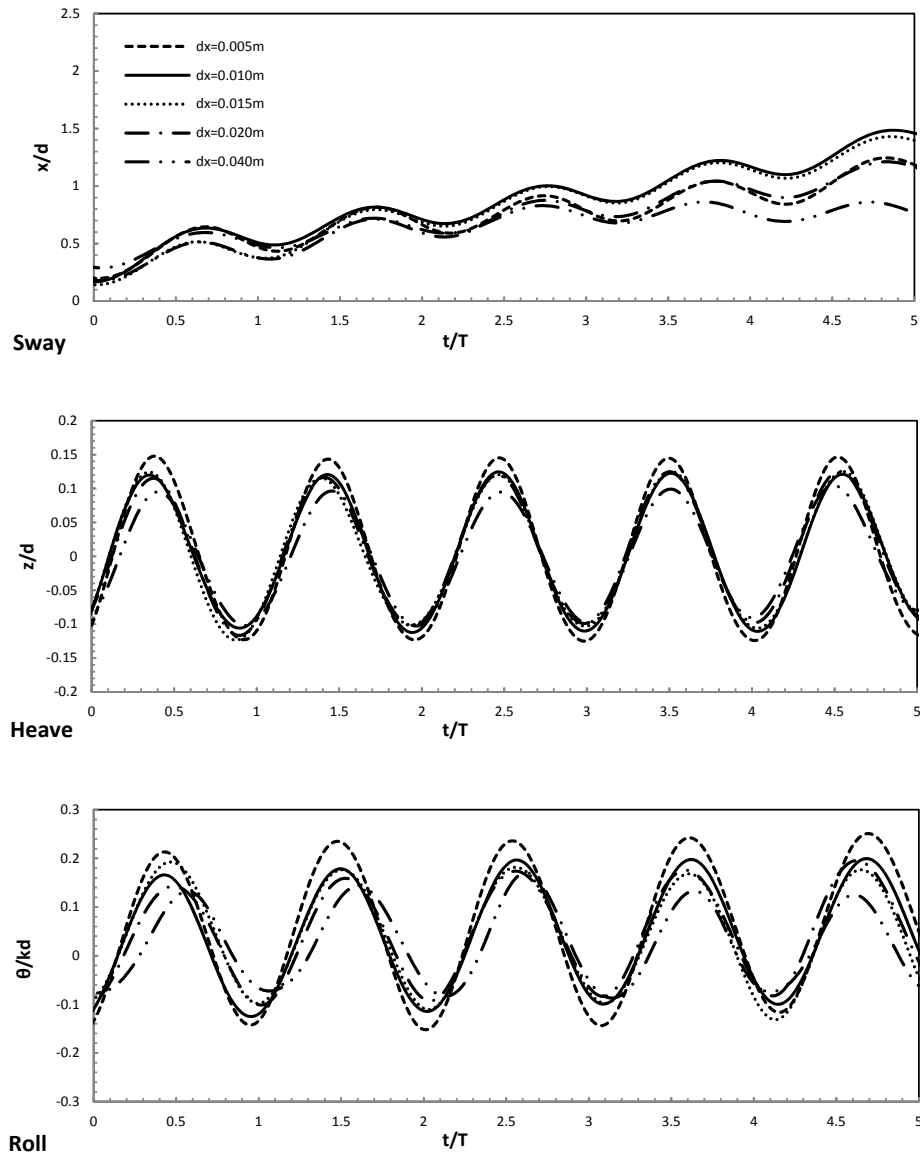
Figure A - 14 Convergence analysis: Time histories of motion trajectories for different initial particle spacing (H = 0.10 m, T = 1.2 s).

6.1.3a Wave profile at each measurement points for wave generation
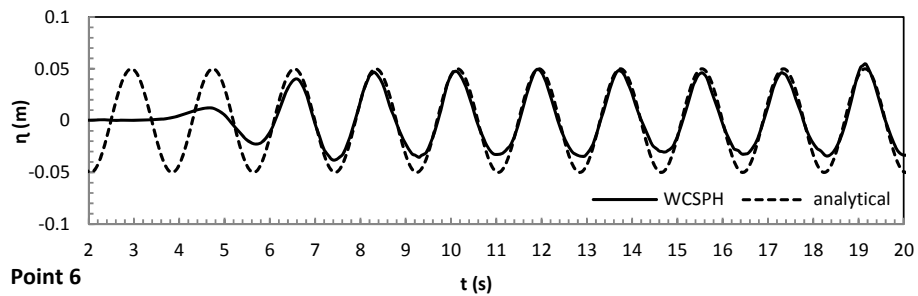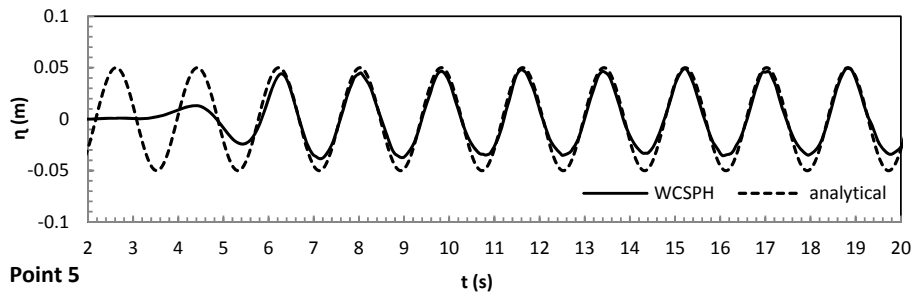

Point 1

Point 3

Point 5

Point 6

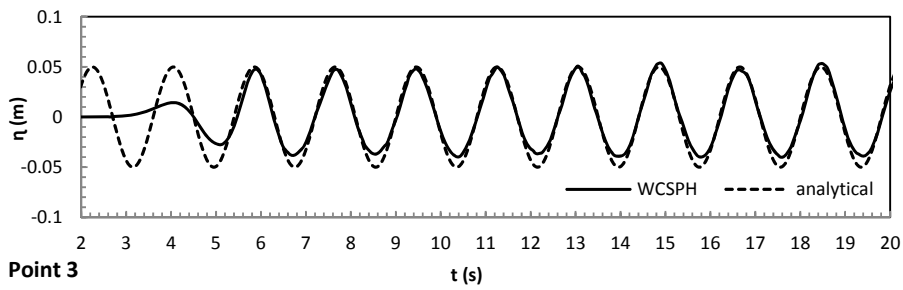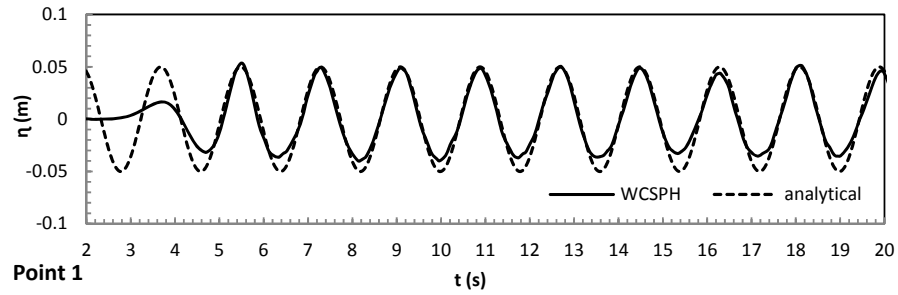Figure A - 15 Time history of wave elevation along numerical wave tank without barge. T = 1.8 s, λ = 5.058 m ($\cong$ 0.7λ) for dx = 0.012 m, dx = 0.015 m and dx = 0.020 m.

6.1.3c Vertical displacement of heave and pitch motion trajectories of each point on floating barge

Figure A - 16 Vertical displacement of heave (Pt. 7) and pitch (Pt. 1) at each measuring points on barge. T = 1.6 s, λ = 3.996 m for dx = 0.015 m and dx = 0.020 m.

Figure A - 17 Vertical displacement of heave (Pt. 7) and pitch (Pt. 1) at each measuring points on barge. T = 1.0 s, λ = 1.561 m for dx = 0.020 m.
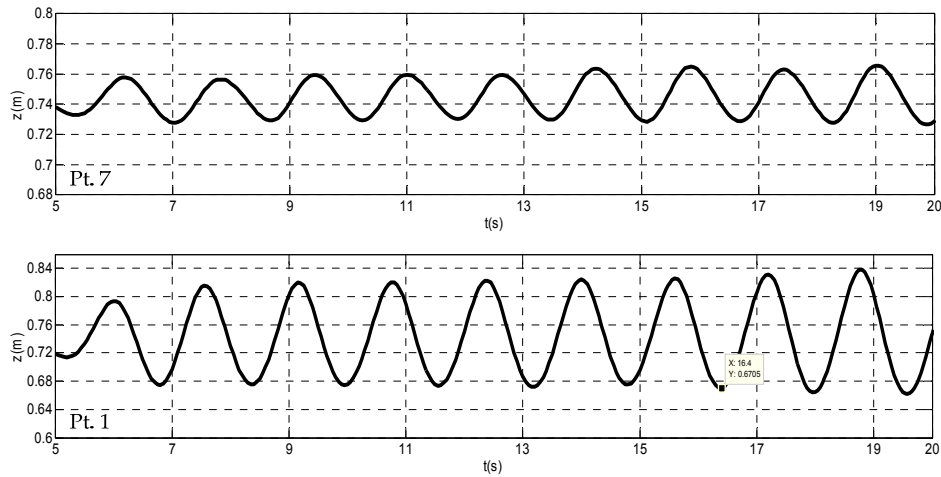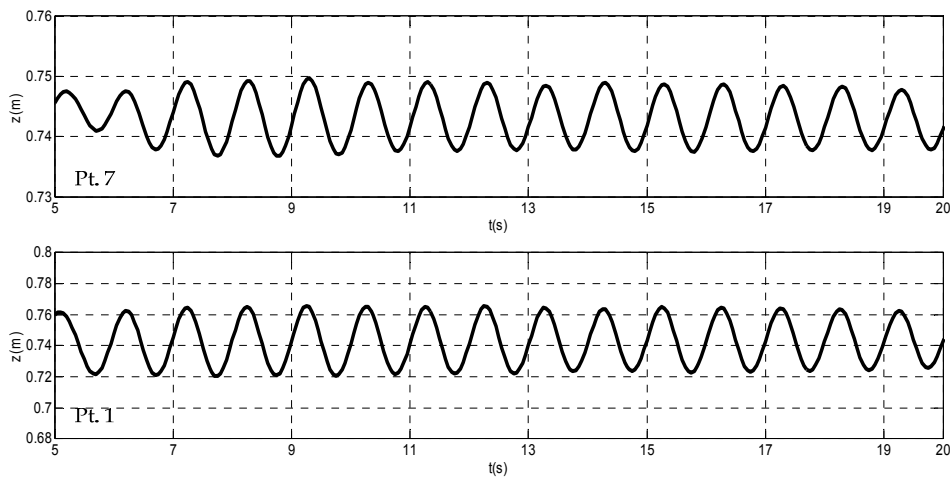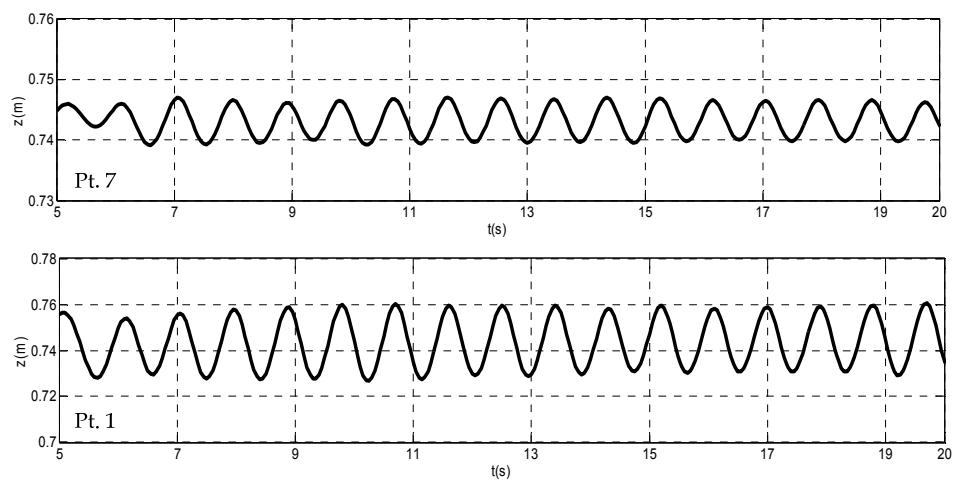
Figure A - 18 Vertical displacement of heave (Pt. 7) and pitch (Pt. 1) at each measuring points on barge. T = 0.9 s, λ = 1.264 m for dx = 0.020 m.

Appendix B

Formulation of SPH

The basic formulation of SPH will be discussed in this section. A general function $A(x)$ can be reproduced as

$$A(\mathbf{x}) = \int_\Omega A(\mathbf{x}') \, \delta(\mathbf{x} - \mathbf{x}') d\mathbf{x}' \tag{B.1}$$

where Ω is the volume of the integration, and $\delta(\mathbf{x} - \mathbf{x}')$ is the Dirac delta function defined as

$$\delta(\mathbf{x} - \mathbf{x}') = \begin{cases} \infty \dots \dots \dots \dots . \, \mathbf{x} = \mathbf{x}' \\ 0 \dots \dots \dots \dots . . \, \mathbf{x} \neq \mathbf{x}' \end{cases} \tag{B.2}$$

and it also satisfies the following unity condition

$$\int_{-\infty}^{\infty} \delta \, (\mathbf{x} - \mathbf{x}') d\mathbf{x} = 1 \tag{B.3}$$

Equation (B.1) is exact but not practically useful. The concept of SPH is to replace Dirac delta function with a kernel function to obtain an approximation [Monaghan, 1982; Monaghan and Gingold, 1983; Liu and Liu, 2003] and the kernel estimation denoted by $\langle A(\mathbf{x}) \rangle$, is defined as

$$\langle A(\mathbf{x}) \rangle = \int_\Omega A(\mathbf{x}') \, \omega(\mathbf{x} - \mathbf{x}', h) d\mathbf{x}' \tag{B.4}$$

where $\omega(\mathbf{x} - \mathbf{x}')$ is the kernel function and h is the smoothing length which defines the influence domain of the kernel function. Similar process can be applied to the gradient of function approximation

$$\langle \nabla \cdot A(\mathbf{x}) \rangle = \int_\Omega (\nabla \cdot A(\mathbf{x}')) \, \omega(\mathbf{x} - \mathbf{x}', h) d\mathbf{x}' \tag{B.5}$$

Via integration by part, this can be expressed as

$$\langle \nabla \cdot A(\mathbf{x}) \rangle = \int_\Omega \nabla \cdot (A(\mathbf{x}') \, \omega(\mathbf{x} - \mathbf{x}', h)) d\mathbf{x}' - \int_\Omega A(\mathbf{x}') \cdot \nabla \omega(\mathbf{x} - \mathbf{x}', h) d\mathbf{x}' \tag{B.6}$$

Applying divergence theorem [Batchelor, 2000] to the first integral in equation (B.6)

$$\langle \nabla \cdot A(\mathbf{x}) \rangle = \int_S A(\mathbf{x}') \, \omega(\mathbf{x} - \mathbf{x}', h) \cdot \mathbf{n} d\mathbf{x}' - \int_\Omega A(\mathbf{x}') \cdot \nabla \omega(\mathbf{x} - \mathbf{x}', h) d\mathbf{x}' \tag{B.7}$$

where is the unit vector normal to the surface, is the volume of the integral. The first item on the right-hand side is normally zero due to the compact property of kernel function. Therefore, equation (B.7) becomes

$$\langle \nabla \cdot A(\mathbf{x}) \rangle = - \int_{\Omega} A(\mathbf{x}') \cdot \nabla \omega(\mathbf{x} - \mathbf{x}', h) d\mathbf{x}' \qquad (B.8)$$

On the left-hand side of the equation (B.8) the derivative is taken with respect to $\mathbf{x}$ while one the right-hand side it is taken with respect to $\mathbf{x}'$. From the above equation, it can be seen that the differential operation on a function is transferred to a differential operation on the smoothing function. And the SPH integration allows the spatial derivative of a function to be calculated based on the values of the function and the derivative of the kernel function which can be calculated analytically, instead of the function derivative itself. This reduces the consistency requirement and produces more stable solutions for PDE [Liu, 2010].

In order to facilitate numerical approximation, the infinitesimal volume $d\mathbf{x}'$ in the integral equation (B.8) is replaced by the particle volume which can be expressed using mass m and density ρ,

$$\mathbf{dx}' = \frac{m_b}{\rho_b} \qquad (B.9)$$

The SPH particle approximation form can be derived if the integration is approximated by a summation over the neighbouring particles which are located within the smoothing length domain

$$\langle A(\mathbf{x}) \rangle_a = \sum_{b=1}^{N} m_b \frac{A(\mathbf{x}_b)}{\rho_b} \omega(|\mathbf{x} - \mathbf{x}_b|, h) \qquad (B.10)$$

The subscript a indicates the specific particle and b indicates neighbouring particles and N is the total number of particles inside the smoothing domain. Similarly, the approximation for spatial derivatives is obtained by representing the integration in equation (B.10) with the sum of the contribution from discrete particles

$$\langle \nabla A(\mathbf{x}) \rangle_a = \sum_{b=1}^{N} m_b \frac{A(\mathbf{x}_b)}{\rho_b} \nabla \omega(|\mathbf{x} - \mathbf{x}_b|, h) \qquad (B.11)$$

The minus sign in equation (B.8) is removed because the derivative is in terms of $\mathbf{x}_b$ instead of $\mathbf{x}_a$. This equation implies that the derivatives of any function can be found by differentiating the

kernel rather than by using grids. As a consequence, instead of solving partial differential equations for hydrodynamics problems, only ordinary differential equations need to be solved.

Besides kernels used in this thesis, there are several other common smoothing kernels used in SPH and some of them are explained below;

Gaussian

$$\omega(\mathbf{r}, h) = \alpha_D \cdot \exp(-q^2) \qquad 0 \le q \le 2 \tag{B.12}$$

where $q = \mathbf{r}/h$, $\mathbf{r}$ being the distance between particles a and b and α_D (the dimensional factor) is $1/(\pi h^2)$ in 2D and $1/(\pi^{3/2} h^3)$ in 3D.

This kernel has been used by [Gingold and Monaghan, 1977] in their original paper to simulate the non-spherical stars. This kernel approximates the Dirac delta function very well. However, it is computationally expensive as it is an infinite series (extend well beyond $2h$) and it has a point of maximum (extremum) in its gradient.

New quartic

$$\omega(\mathbf{r}, h) = \frac{1}{h} \left[\frac{2}{3} - \frac{9}{8} q^2 + \frac{19}{24} q^3 + \frac{5}{32} q^4 \right] \qquad 0 \le q \le 2 \tag{B.13}$$

This kernel has been implemented by [Liu et al., 2003] and has only one piece property. The stability properties are expected to be superior to the cubic function as it has a smoother second derivative than the piecewise linear second derivative of those function.

Quadratic

$$\omega(\mathbf{r}, h) = \alpha_D \left[\frac{3}{16} q^2 - \frac{3}{4} q + \frac{3}{4} \right] \qquad 0 \le q \le 2 \tag{B.14}$$

where α_D is $2/(\pi h^2)$ in 2D and $5/(4\pi h^3)$ in 3D. $q = |\mathbf{r}_{ij}|/k$. k is the kernel support size, $k = 1 \cdot h$, with $h = c \cdot \delta r$. δr is the initial particle distance and c is a constant, equal to 2.6. This kernel was used by [Johnson et al., 1996] to simulate the high velocity impact problem. This function prevents particle clustering in compression problems. It is low-order simple and therefore computationally cheap. However, because of the low-order property, this function is not suitable for physical processes needing higher-order interpolation to capture important effects.

Cubic spline

$$\omega(\mathbf{r}, h) = \alpha_D \begin{cases} 1 - \frac{3}{2}q^2 + \frac{3}{4}q^3 & 0 \leq q \leq 1 \\ \frac{1}{4}(2-q)^3 & 1 \leq q \leq 2 \\ 0 & q \geq 2 \end{cases} \tag{B.15}$$

where α_D is $10/(7\pi h^2)$ in 2D and $1/(\pi h^3)$ in 3D.

The cubic spline kernel which introduced by [Monaghan and Lattanzio, 1985] has been, so far, the most widely used smoothing function in the SPH literature since it approximates Gaussian kernel very closely while having a narrower compact support (computationally cheap). However, the second derivative of the cubic spline is a piecewise linear function, the stability properties can be inferior to those of smoother kernels.

Quadratic spline

$$\omega(\mathbf{r}, h) = \alpha_D \begin{cases} \frac{1}{24h}\left((q+2.5)^4 - 5(q+1.5)^4 + 10(q+0.5)^4\right) & 0 < q < 0.5 \\ \frac{1}{24h}\left((2.5-q)^4 - 5(1.5-q)^4\right) & 0.5 \leq q < 1.5 \\ \frac{1}{24h}(2.5-q)^4 & 1.5h \leq q < 2.5h \\ 0 & q \geq 2.5 \end{cases} \tag{B.16}$$

[Morris, 1994] introduced a higher order splines that are approximate Gaussian closer and more stable.

3.2 Time stepping algorithm

In DualSPHysics code, besides Symplectic scheme, Verlet scheme is also available in the package. The Verlet scheme is the fastest one and symplectic scheme is the most accurate with cost twice the cost of Verlet scheme. The symplectic scheme is recommended for simulation with long runtime and with moving objects. Other schemes can be found in Crespo et al., [2013].

Verlet scheme;

This algorithm by Verlet [1967] is split into two parts. In general, variables are calculated according to

$$\mathbf{v}_a^{n+1/2} = \mathbf{v}_a^{n-1} + 2\Delta t \mathbf{F}_a^n; \ \mathbf{r}_a^{n+1} = \mathbf{r}_a^n + \Delta t \mathbf{V}_a^n + 0.5\Delta t^2 \mathbf{F}_a^n \tag{B.17}$$

$$\rho_a^{n+1} = \rho_a^{n-1} + 2\Delta t D_a^n \tag{B.18}$$

Once every N_s time steps ($N_s \approx 50$), variables are calculated according to

$$\mathbf{v}_a^{n+1/2} = \mathbf{v}_a^n + \Delta t \mathbf{F}_a^n; \ \mathbf{r}_a^{n+1} = \mathbf{r}_a^n + \Delta t \mathbf{V}_a^n + 0.5\Delta t^2 \mathbf{F}_a^n \tag{B.19}$$

$$\rho_a^{n+1} = \rho_a^n + \Delta t D_a^n \tag{B.20}$$

which prevents the time integration diverging since the equations are no longer coupled.

Appendix C

Vertical bending moment (VBM) of 1 way coupled

For a variable w (i.e. each element in equations (6.6)), its first and second derivatives $\dot{w}_{n+1}$, $\ddot{w}_{n+1}$ at next time step $t = t_{n+1}$, can be expressed using Newmark method as:

$$\ddot{w}_{n+1} = \frac{1}{\beta \Delta t^2} w_{n+1} - \left[\frac{w_n}{\beta \Delta t^2} + \frac{\dot{w}_n}{\beta \Delta t} + \left(\frac{1}{2\beta} - 1\right)\ddot{w}_n\right]$$

$$\dot{w}_{n+1} = \frac{\gamma}{\beta \Delta t} w_{n+1} + \left(1 - \frac{\gamma}{\beta}\right)\dot{w}_n + \Delta t\left[(1 - \gamma) - \gamma\left(\frac{1}{2\beta} - 1\right)\right]\ddot{w}_n - \frac{\gamma}{\beta \Delta t} w_n$$

where $\gamma = \frac{1-2\alpha}{2}$, $\beta = \frac{(1-\alpha)^2}{4}$, and α is chosen to be -0.05 in this study.

In order to simplify the above equations, the following definitions are introduced;

$$C_1 = \frac{1}{\beta \Delta t^2}, C_2 = \frac{1}{\beta \Delta t}, C_3 = \left(\frac{1}{2\beta} - 1\right), C_4 = \left(1 - \frac{\gamma}{\beta}\right), C_5 = [(1 - \gamma) - \gamma C_3]$$

Therefore;

$$\ddot{w}_{n+1} = C_1 w_{n+1} - [C_1 w_n + C_2 \dot{w}_n + C_3 \ddot{w}_n]$$

$$\dot{w}_{n+1} = C_2 \gamma w_{n+1} + C_4 \dot{w}_n + \Delta t C_5 \ddot{w}_n - C_2 \gamma w_n$$

And taking $D_1 = -[C_1 w_n + C_2 \dot{w}_n + C_3 \ddot{w}_n]$ and $D_2 = C_4 \dot{w}_n + \Delta t C_5 \ddot{w}_n - C_2 \gamma w_n$. Using Newmark method to replace the velocity and acceleration terms with position values, the governing equations then become

$$C_1 w_{n+1} + D_1 + \mu \omega^2 [C_2 \gamma w_{n+1} + D_2] + \omega^2 w_{n+1} = RHS$$

$$w_{n+1} = \frac{RHS - D_1 - \mu \omega^2 D_2}{C_1 + \mu \omega^2 C_2 \gamma + \omega^2}$$